Pre-orogenic upper crustal softening by lower greenschist facies metamorphic reactions in granites of the central Pyrenees

Laura Airaghi, Nicolas Bellahsen, Benoît Dubacq, David M Chew, Claudio L Rosenberg, Emilie Janots, Maxime Waldner, Valérie Magnin

Journal of METAMORPHIC GEOLOGY

Pre-orogenic upper crustal softening by lower greenschist-facies metamorphic reactions in granites of the central Pyrenees

Journal:	*Journal of Metamorphic Geology*
Manuscript ID	JMG-19-0021.R1
Manuscript Type:	Original Article
Date Submitted by the Author:	27-Sep-2019
Complete List of Authors:	Airaghi, Laura; Institut des sciences de la terre de Paris, Sorbonne Université Bellahsen, Nicolas; Institut des sciences de la terre de Paris, Sorbonne Université Dubacq, Benoît; Institut des sciences de la terre de Paris, Sorbonne Université Chew, David; Trinity College Dublin, Geology Rosenberg, Claudio; Institut des sciences de la terre de Paris, Sorbonne Université Janots, Emilie; Observatoire des Sciences de l'Univers de Grenoble, Institut des Sciences de la Terre Waldner, Maxime; Institut des sciences de la terre de Paris, Sorbonne Université Magnin, Valérie; Observatoire des Sciences de l'Univers de Grenoble, Institut des Sciences de la Terre
Keywords:	U-Th/Pb anatase-titanite-monazite dating, mylonites, chlorite-white mica thermobarometry, Bielsa, Axial zone

Pre-orogenic upper crustal softening by lower greenschist-facies metamorphic reactions in granites of the central Pyrenees

Laura Airaghi[1*], Nicolas Bellahsen[1], Benoît Dubacq[1], David Chew[2], Claudio Rosenberg[1], Emilie Janots[3], Maxime Waldner[1], Valérie Magnin[3]

[1] Sorbonne Université, CNRS-INSU, Institut des Sciences de la Terre de Paris, ISTeP UMR 7193, F-75005 Paris, France

[2] Department of Geology, Trinity College Dublin, Dublin 2, Ireland

[3] Université Grenoble Alpes, CNRS, IRD, IFSTTAR, ISTerre, 38000 Grenoble, France

*corresponding author:laura.airaghi@univ-orleans.fr, now at: Université d'Orléans, CNRS-INSU, Institut des Sciences de la Terre d'Orléans, ISTO, UMR7327, Orléans, France

Short title: Pre-kinematic metamorphism in Pyrenees

ABSTRACT

Pre-kinematic greenschist-facies metamorphism is often observed in granites and basement units of mountains belts, but rarely dated and accounted for in orogenic cycle reconstructions. Studying pre-kinematic alteration is challenging because of its usual obliteration by subsequent syn-kinematic metamorphism often occurring at conditions typical of the brittle-ductile transition. It is however to be expected that pre-kinematic alteration has major implications for the rheology of the upper crust. In the 305 Ma-old Variscan basement of the Bielsa massif (located in the Axial Zone of the Pyrenees), successive fluid-rock interaction events are recorded in granites at temperatures below 350°C. Combined microstructural and petrographic analysis, low-temperature thermobarometry and *in situ* U-Th/Pb dating of anatase, titanite and monazite show extensive pre-orogenic (pre-Alpine) and pre-kinematic alteration related to feldspar sericitization and chloritization of biotite and amphibole at temperatures of 270-350°C at 230-300 Ma. This event is followed by a second fluid-rock interaction stage marked by new crystallisation of phyllosilicates at temperatures of 200-280°C and associated with the formation of mylonitic shear zones and fractures parallel to the shear planes. U-Pb anatase and monazite ages as well as the microtextural relationships of accessory minerals suggest an age for this event at 40-70 Ma, consistent with independent regional geology constraints. The Variscan basement was therefore softened at late- to post Variscan time, at least 150-200 Ma before the main Alpine shortening while Alpine-age compression lead to the formation of a dense net of mylonites. The associated deformation, both distributed at the scale of the Bielsa massif and localized at decametric scale in mylonitic corridors, precedes the strain localization along the major thrusts of the Axial zone. The Bielsa massif is a good example where, inherited,

pre-orogenic upper crustal softening controls the deformation patterns in granitic basement units through low-grade metamorphic reactions.

Key words**:** U-Th/Pb anatase-titanite-monazite dating, mylonites, chlorite-white mica thermobarometry, Bielsa, Axial zone

1. INTRODUCTION

Granites deformed at the brittle-ductile transition show mineral assemblages characteristic of low-grade metamorphism. Greenschist-facies metamorphic reactions often result in the growth of phyllosilicates (e.g. white mica, chlorite) whose presence strongly affect the rheological behaviour of the upper crust through softening, strain localization and fluid migration (Tullis, Yund, & Farver, 1996; Ingles, Lamouroux, Soula, Guerrero, & Debat, 1999; Jackson, Austrheim, McKenzie, & Priestley, 2004; Wintsch, Christoffersen, & Kronenberg, 2005; Goncalves, Oliot, Marquer, & Connolly, 2012). The breakdown of 80 % of feldspar into white mica, for example, reduces the depth of the brittle-ductile transition by two thirds (Gueydan, Leroy, Jolivet, & Agard, 2003). Reactions forming low-grade mineral assemblages responsible for crustal softening are generally observed to be syn-kinematic, occurring during the major deformation phases of an orogenic cycle (Wayne & McCaig, et al., 1998; Gueydan et al., 2003; Mansard, Raimbourg, Augier, Précigout, & Le Breton, 2018). Static or quasi-static hydrothermal alteration is also observed in granites and has been widely documented, especially in large igneous provinces (e.g. Parneix, Beaufort, Dudoignon, & Meunier, 1985; Cathelineau et al., 1986; Yuguchi, Sasao, Ishibashi, & Nishiyama, 2015). However static alteration is rarely characterised, and hardly ever dated and placed in a regional orogenic context. Indeed, low-grade metamorphic reactions often leave tenuous fingerprints only hinted at by equivocal

74 microtextural relationships, especially in granites (e.g. Airaghi et al., 2017b), which are
75 generally considered poorly reactive rocks at temperatures below 400°C.

76 At a microscopic scale, pre-kinematic and syn-kinematic transformations are difficult
77 to distinguish, particularly so if the rocks have been deformed through several orogenic cycles.
78 The timing and conditions of pre-kinematic metamorphic reactions and their effects on (i) the
79 syn-kinematic transformation and (ii) the rheological response of the upper crust to successive
80 compressive phases remain therefore poorly constrained. This study addresses these issues by
81 focussing on the Bielsa massif, a Variscan granite located in the Axial Zone of the central
82 Pyrenees (Figure 1a). This massif is an excellent natural laboratory to study how granitic rocks
83 record distinct low-grade metamorphic events. The massif is part of the central Pyrenean belt,
84 which experienced at least two well-known deformation phases (Late Variscan and
85 Alpine/Pyrenean, Cochelin et al. 2017), which are difficult to distinguish in the Axial zone
86 (Cochelin et al, 2017). The Bielsa massif is located in the most external basement domain of
87 the Pyrenees (implying it experienced the lowest peak metamorphic temperatures with respect
88 to Alpine tectonics), south of the zones of large-scale shear bands that have affected other
89 granitic basement units of Pyrenees (e.g. Maladeta, Néouvielle; Wayne & McCaig, 1988). In
90 addition, structural and microstructural studies show significant distributed shortening at the
91 scale of the massif (Román-Berdiel et al., 2004; Bellahsen et al., 2019), raising questions about
92 the link between low-grade metamorphism and strain accommodation mechanisms. Early
93 feldspar destabilisation has been proposed to have a major control on subsequent mechanical
94 softening in Bielsa (Bellahsen et al., 2019), but the conditions and the age of such reaction still
95 remains unconstrained.

96 In this contribution we estimate the conditions of crystallization of both pre-kinematic and syn-
97 kinematic greenschist-facies mineral assemblages in the Bielsa granite and its Triassic
98 sedimentary cover. Microstructural and petrographic analyses were combined with low-

temperature thermobarometry and *in situ* U-Th/Pb dating of zircon, titanite and monazite. Attempt to date anatase (polymorph of rutile) by the U/Pb method were also undertaken. The implications for the timing of crustal softening relative to the major shortening phases are discussed with respect to their associated mineral assemblages. Results suggest that pre-kinematic (pre-Alpine) alteration controls the deformation pattern and strain localisation in the Bielsa granite during Alpine shortening.

2. THE BIELSA MASSIF IN THE AXIAL ZONE (CENTRAL PYRENEES)

The Axial zone (central Pyrenees) is part of a S-verging thrust system made of imbricated thrust units stacked during the Late Cretaceous-Early Miocene collision of the Iberian and European plates (Figure 1a). The plutons of the Axial zone (i.e. Bielsa, Neuville, Maladetta massifs etc., Figure 1a) were emplaced into Paleozoic sediments during Late-Variscan (320-300 Ma, e.g. Paquette, Gleizes, Leblanc, & Bouchez, 1997; Vacherat et al., 2017). These plutons and their Paleozoic sedimentary cover constitute the basement to the Permian and Mesozoic sedimentary units (Fig. 1a). Several tectono-metamorphic stages are documented in the metasedimentary units Axial zone but are difficult to distinguish within the basement. Recent studies have proposed that the majority of the deformation in the Axial zone is of Variscan age (Cochelin et al., 2017). Cretaceous hydrothermal events have been identified in the eastern Axial zone (Fallourd et al., 2014; Boutin et al., 2015) and related to extensive tectonics centered on the SE Bay of Biscay. Basement thrusts in the central-western Pyrenees (named Gavarnie and Guarga thrusts) were (re)activated during the Eocene to Miocene (20-30 and 32-36 Ma respectively, Jolivet et al., 2007; Elmola et al., 2018 and references therein). In the hanging wall of the Gavarnie thrust, an older deformation event (*c.* 48 Ma) is recognised in the massifs of Néouvielle and Eaux Chaudes. It has been associated with the activation of mylonitic shear bands (e.g. Wayne & McCaig, 1998).

This study focusses on the Bielsa massif, mainly constituted by a pluton emplaced at *c.* 305 Ma (Vacherat et al., 2017), in the S-verging thrust system structurally located between the Gavarnie and Guarga thrusts (Figure 1b). Close to Lake Urdiceto (Figure 1c-d), granitic to granodioritic rocks (Román-Berdiel et al., 2004) are unconformably overlain by Triassic continental red sandstones and pelites. The basement and its sedimentary cover were deformed (folded) during the Alpine compressional phase (Figure 1d, Casas et al., 2003; Román-Berdiel et al., 2004, Bellashen et al., 2019) with a wavelength of ~1 km. Several sub-vertical S- or N-dipping normal or reverse steep faults bound the antiforms and synforms (Figure 1d). In the core of the synforms, Triassic sediments crop out. They exhibit a sub-vertical to N-dipping cleavage (e.g. Figure 2b and 3c), with nord side up sense of shear kinematic indicators above the sediment-cover interface (Bellahsen et al., 2019). The granitic basement is heterogeneously deformed. At the decametric scale, undeformed and weakly deformed granitic rocks alternate with zones of distributed ductile deformation, zones of fracturing and faulting and mylonites (Figures 1c-d and 2a-f). A pervasive N-dipping schistosity is widespread in the basement (Figure 2a-c and e). Mylonitic corridors, with 1-2 m wide, are observed within the basement and at its boundary with the Triassic sedimentary cover (Figure 2a-c). Mylonitic corridors alternate with less deformed rocks with a wave length of ~100 m (Figure 1c) and they are characterized by pervasive schistosity (S) and steep, N-dipping (45-70°) and S-dipping (55-70°) shear planes (C) associated either with a north or with a south-verging movement (Figure 2a-e). In some shear zone, the dips of mylonitic planes varies from S-dipping to N-dipping, with an apparent sense of shear from top-to-north to top-to-south (Figure 2b-d). Some of the shear bands at the boundary between the Triassic sediments and the late Variscan granite (regionally trending N110, Figure 1c) contain deformed fragments of the Triassic red sandstone (Román-Berdiel et al., 2004; Figure 2b), indicating that they are post-Triassic. The high density of mylonitic corridors and the pervasive schistosity development result in a distributed deformation pattern

149 (as observed in other crystalline units as the Aar massif, Wehrens et al., 2017). The
150 granitic/granodioritic basement (regardless of the intensity of the strain) is pervasively hydrated
151 and the original magmatic mineral assemblage is partly to totally replaced by greenschist-facies
152 minerals. The steep topography of the massif allows one to infer that the latter replacement
153 affects the pluton at least over a topographic vertical profile of 2 km from the lowest outcrop
154 of the massif (yellow stars in Figures 1b).

155 At the boundary between the Triassic sediments and the granite/granodiorite, sub-
156 horizontal quartz and chlorite-bearing veins which are 1-5 cm-wide are observed (yellow square
157 in Fig. 3b). Fifty meters from the contact, Triassic sediments show two generations of chlorite-
158 and quartz-bearing veins: (1) sub-horizontal veins parallel to the ones observed at the contact
159 between the basement and the sedimentary rocks produced by vertical extension, locally folded
160 and associated with a crenulation cleavage (N184S) and (2) sub-vertical veins (Figure 3c).

161

162 **3. SAMPLE DESCRIPTION AND CHRONOLOGY OF MINERAL ASSEMBLAGES**

163 Twenty-seven samples were collected along two transects east and west of Lake Urdiceto, from
164 the undeformed granite (e.g. ZA16-84 and B11-16, Figure 4a, b) up to the zone of intense
165 mylonitisation (e.g. ZA16-96, ZA16-98; Figures 1c, 4g). One sample (ZAL18-11) was
166 collected at the contact between the Triassic sandstones and a basement-hosted vein (Figures
167 3b). Two samples (ZA16-12 and ZA16-13) were collected in the Triassic sediments (Figures
168 3c).

169

170 3.1 Samples from the basement

171 In the basement unit, we distinguished the following rock fabrics: *Undeformed* samples (e.g.
172 ZA16-84, Figure 4a), where the magmatic, euhedral shape of grains is still preserved. *Weakly*
173 *deformed* rocks (e.g. Figure 2f and 4c) exhibiting a weak yet pervasive schistosity (at an outcrop
174 scale: S in Figure 2a). In some of those samples the schistosity is associated to mm-scale

fractures (e.g. ZA16-82, ZA16-78, ZA16-128, Figure 4e-f and h) that are parallel to the subvertical shear planes observed at an outcrop scale in mylonites (C in Figure 2a). *Mylonites* showing S and C planes (e.g. ZA16-133, Figure 4g), where the C planes are as pervasive as S. In the samples defined as mylonite, both brittle and ductile deformation features are identified, with the brittle ones underlined by fractures parallel to the shear planes C (Figure 4g).

All samples, regardless of the degree of the strain, exhibit extensive alteration of the magmatic mineral assemblage originally defined by quartz, K-feldspar and plagioclase, biotite ± amphibole, apatite, zircon (all in textural equilibrium, Figures 4a-b) and ilmenite preserved as inclusions in the less altered amphibole and biotite grains (Figure 5a-b). The alteration is comprised by the breakdown of plagioclase and K-feldspar into white mica (10-30 µm in size) + albite + calcite ± rare epidote (Figure 4a, c, e-f). Biotite and amphibole break down to chlorite flakes (ChlA, abbreviations are from Whitney & Evans, 2010) ± white mica (20-100 µm in size) ± prehnite (Figure 4a) and a Ti-bearing phase (anatase or titanite or both, Figure 4b, d, f and g). In the paragraph below, mineral assemblages are described in relation to their microstructural evolution from the undeformed granites and granodiorites to mylonites.

In the undeformed samples, relicts of feldspar, biotite and amphibole are still visible and their euhedral magmatic grain shapes are preserved (Figure 4a). Chlorite flakes (ChlA) grow at the grain boundaries of parent minerals and along biotite cleavages, and they are associated with a Ti-bearing phase (see below) ± prehnite ± K-feldspar (Figure 4a-b). Ilmenite grains are preserved in unaltered biotite and amphibole domains (Figure 5a). Quartz grains contain sparse, micrometric fluid inclusions and are cross-cut by microcracks. Allanite is locally observed in textural equilibrium with the magmatic minerals. Euhedral magmatic zircon grains are found within relicts of feldspar or at the boundaries between feldspar and amphibole. Cathodoluminescence imaging of zircon in samples ZA16-84 and ZA16-119 typically reveals primary oscillatory growth zoning without internal complexity. However, some zircon grains,

especially in sample ZA16-119, show metamictization with porous domains and lobate rims 5-20 µm thick, and very low cathodoluminescence emission (Figure 5d). In the weakly deformed samples, feldspar is pervasively sericitized (up to 80-90%). Original biotite grains are chloritized between 70-90% (Figure 4c). Chlorite flakes (ChlA) and secondary reaction phases (quartz, Ti-phase ± white mica) are oriented parallel to the main schistosity and tightly folded to form kinks (Figure 4d). Quartz grains partly preserve their magmatic texture, but are fractured, with fractures subparallel to the kink axes. Grains are cross-cut by fluid inclusion trails. Originally euhedral grains of ilmenite are first altered to aggregates of anatase + calcite then to titanite (Figure 5a-b), following the reaction proposed by Hansen, Reimink, & Harlov (2010) for low temperature conditions. Anatase is itself replaced by titanite, in textural equilibrium with chlorite flakes (Figures 5a-b). Anatase and titanite are systematically aligned with the chlorite flakes, within the S-planes. When they are folded to form kinks, anatase relicts are mainly preserved in the microfold hinges (Figure 5c). In some of the weakly deformed samples, titanite is the major Ti-bearing phase preserved (samples ZA16-119, B11-16, ZA16-77 and ZA16-84).

In weakly deformed samples showing millimetric fractures, biotite deformation and stretching along the main schistosity S is more pronounced (e.g. Figure 4e). Calcite is present in the matrix. Fractures 1-3 mm thick displace the folded chlorite flakes to form en-echelon microstructures (Figure 4e). These fractures are filled with secondary chlorite (ChlB) ± white mica (Figure 4f). Sheets of ChlB are oriented parallel to the fracture walls in contrast to ChlA grains which are mainly perpendicular (Figure 4f). Furthermore, ChlB is rarely associated with biotite breakdown products as prehnite and Ti-bearing phases (Figure 4f). Quartz grains are both fractured and stretched, they exhibit undulose extinction and abundant fluid inclusion trails. Titanite is observed in the same microstructural position as in undeformed samples (folded within ChlA flakes). The microstructural position of anatase is instead more variable. Anatase

is observed: (1) as ~70 µm sub-euhedral relicts in titanite cores at the rims of the ChlA flakes (as in the undeformed samples, type-1 Ant, Figure 4h, 5b-c, f-h and Figure S1) and (2) as grains 20-30 µm in size not associated with titanite within ChlA flakes along the ancient biotite cleavages (type-2 Ant, e.g. Figure 4h, 5f-h and Figure S1). Locally, type-2 anatase is observed within ChlB-bearing fractures (e.g. ZA16-73, Figure 5i). Type-2 anatase of type 2 is often observed close to type-1 anatase. Magmatic accessory minerals such as apatite and zircon are fragmented and stretched along the S planes.

In mylonitic samples, the schistosity is defined by folded chlorite + white mica flakes and interconnected layers of white mica (Figure 4g). Flakes are folded up to kinks. Shear planes (C) form at high angle with the main schistosity S (Figure 4g-h). The kink axes are kinematically compatible with shear movement on the C planes. Quartz grains are partially stretched and most of them are fractured, with cracks subparallel to the C planes (Figure 4g). Within the grains, evidences of ductile deformation are observed such as deformation lamellae. A larger amount of fluid inclusions in quartz are observed with these samples compared to weakly deformed samples. In mylonites (ZA16-96, ZA16-98), only one type of anatase is observed (small anatase grains of type 2 predominate). In these samples, monazite grains, 10-40 µm in size, were identified in mylonites (sample ZA16-98 and ZA16-88). These monazite grains are wrapped by secondary chlorite and white mica (suggesting post-magmatic origin). The largest grains of monazite (20-40 µm) (Mnz1) are lobate, and stretched along the C planes with fractures perpendicular to them and exhibit irregular grain boundaries, micrometric large fractures, patchy textures with bright and dark spots in BSE images and 'inclusion-like dissolution figures' (as described by Grand'Homme et al., 2018; Airaghi, Janots, Lanari, de Sigoyer, & Magnin, 2018, Figure 5c). Small monazite grains (~10 µm) with rounded shape share features with that of ZA16-88, aligned along the main foliation or within alteration halos marking the reaction front along secondary fractures subparallel to the C (Figure 5j). In sample

ZA16-98 monazite is locally Th and Si-enriched (tending towards a thorite composition, inset in Figure 5i).

In summary, the granitic rocks experienced a first transformation of the original magmatic mineral assemblage of Qz + Fs + Pl + Bt ± Amph (+ Ilm + Ap + Zr ± Aln) to Qz + ChlA + Ti-phase (Ttn or Ant then Ttn) ± Pr ± KFs. Zircon and titanite grains with anatase core (type-1 Ant) are stretched in the main schistosity and folded during shearing. They therefore predate any deformation stage. ChlB is rarely associated with secondary reaction products and helps to define the C-parallel fractures. It is considered to precipitate from a fluid during a second syn-kinematic (syn C planes) alteration event. The varying characteristics of anatase, only found in deformed samples, suggest that in these samples two generations of anatase may be preserved. That type-2 anatase is located within ChlA flakes along former biotite cleavage suggests that type-2 Ant grew after type-1 Ant on ChlA rims. The chloritization reaction front and replacement is indeed expected to progress from the grain boundaries to the core, along the biotite cleavages. The proximity of type-2 anatase to type-1 anatase grains indicates however transport scale of the anatase-forming elements limited to some dozen of µm. In sample ZA16-73 (discretely deformed). Type-2 Ant is observed in C-parallel fractures (Figure 5i). Type-2 Ant may have crystallized during the shearing. Mnz1 is affected by deformation and mainly observed within the main schistosity, while Mnz2 (and type-2 Ant, see below) are associated with C parallel fractures. Mnz2 is therefore syn C planes forming stage.

3.2 Samples from Triassic sediments and at the boundary between sediments and the granodiorite

At the brecciated contact between the Triassic sediments and the chlorite-quartz bearing vein in contact with the basement (Figure 6a), the Triassic sediments are composed of quartz, chlorite, white mica, Fe-oxides and clasts in a calcite matrix (sample ZAL18-11). The vein is

composed of mm-size quartz grains recrystallized by bulging and hosting a dense net of fluid inclusions, interlayered with elongate chlorite and white mica (± calcite) (Figure 6b). Along chlorite grain boundaries, abundant Fe-oxides, 20-40 µm large anatase grains, monazite, REE-bearing carbonates and tourmaline are occasionally observed (Figure 6b). The textural aspect of monazite in sediments is similar to that of monazite in the basement (inset in Figure 6b).

The red-coloured, foliated pelitic rocks are comprised of white mica, chlorite and quartz grains on the scale of tents of microns (± detrital monazite, apatite and anatase, samples ZAL18-12 and ZAL18-13). The veins are approximately 100 µm thick, they opened at high angle with the foliation and are filled by elongate grains of quartz rich in fluid inclusions (in the core of the vein). Chlorite developed along the vein-host rock interface with long axes parallel to the vein opening direction (Figure 6c). Veins are stretched and displaced by 30-50 µm secondary chlorite and quartz-bearing layers cross-cutting the foliation, forming 'en échelon' fractures (Figure 6c-d). Monazite in pelites forms euhedral grains 5-10 µm in diameter, sometimes in association with Fe-oxides and xenotime at the interface between the veins and host-rock.

4. ANALYTICAL AND COMPUTATIONAL METHODS

The chemical composition of metamorphic chlorite and white mica has been analysed with a CAMECA SX-FIVE electron probe micro-analyser (EPMA) at ISTeP (Sorbonne Université). Point measurements were made under a 15 kV acceleration voltage and 10 nA beam current with a ~1µm beam size, in wavelength-dispersive spectroscopy (WDS) mode, using diopside (Ca, Mg, Si), $MnTiO_3$ (Mn, Ti), orthoclase (K, Al), hematite (Fe), albite (Na) and Cr_2O_3 (Cr) as standards for measuring the elements written in parentheses. The compositional variability of chlorite and white mica in different microstructural sites was characterised by element mapping using both the EPMA and a Zeiss SUPRA-55VP scanning electron microscope (SEM) at ISTeP (Sorbonne Université). EPMA elemental maps were acquired in WDS mode at 100

nA beam current, 15 keV acceleration voltage with a 200 ms dwell time. SEM maps were acquired in energy-dispersive spectroscopy (EDS) mode at 15 keV acceleration voltage, 30 nA beam current with a dwell time of 256 µs. SEM and EPMA maps were quantified with the software XMapTools (Lanari et al., 2014). The U, Th, Pb and REE contents of monazite were analysed with the JEOL-JXA-8230 EPMA at ISTerre (University of Grenoble), at 15 keV acceleration voltage, 200 nA beam current with a spot beam size. For each monazite analysis, a chemical U-Th/Pb age was determined and the average age of different populations of monazite (identified on the base of compositional criteria) was calculated with the software NiLeDAM. The analytical protocol and data processing are detailed in Appendix 1.

Titanite, anatase and zircon were dated *in-situ* by the U-Pb LA-ICP-MS technique at Trinity College, Dublin (Ireland), on the same thin sections as used for the microstructural and petrological studies. U-Pb ages were determined using a Photon Machines Analyte Exite 193 nm ArF Excimer laser-ablation system with a Helex 2-volume ablation cell coupled to an Agilent 7900 ICPMS. For titanite, zircon and anatase, 300 shots were ablated per analysis with a laser spot size of 24 µm (Figure S1). The laser repetition rate and fluency were set at 15 Hz, 1.60 J/cm^2 and 11 Hz and 2.25 J/cm^2 for anatase/titanite and zircon respectively, and typically 50 analyses were obtained on each sample (usually 1-2 spots per grain) and plotted on a Tera-Wasserburg diagram (Tera and Wasserburg, 1972) with 2σ error ellipses, allowing determination of the initial Pb intercept on the $^{207}Pb/^{206}Pb$ axis.

The raw titanite and anatase isotope data were reduced using the "VizualAge UcomPbine" data reduction scheme (DRS) of Chew, Petrus, and Kamber, (2014). The "VizualAge" DRS was employed for zircon data reduction. Common Pb in the titanite and rutile standards was corrected using the ^{207}Pb-based correction method. For unknowns, the initial Pb in titanite and anatase was determined from the upper intercept (y-intercept on the $^{207}Pb/^{206}Pb$ axis) of the discordia line defined by the analyses on Tera-Wasserbutg Concordia.

The age for each population of grains was calculated from the lower intercept of the discordia line on Tera-Wasserburg Concordia. line with the Pb evolution model. Zircon ages were instead estimated by calculating the weighted average of $^{206}Pb/^{238}U$ corrected ages (Table S3). The primary standards employed, the secondary standard ages and further details on the analytical procedure are reported in Supplementary Material S1. Titanite and anatase included in ilmenite were not dated due to their small size. When anatase core relicts were preserved in titanite grains (type-1 Ant), it was rarely possible to ablate separately relicts of anatase and their titanite host due to the small grain size (e.g. Figure S1). In anatase-dominated samples, where the bulk of grain was anatase, these analyses were classified and processed as anatase, in titanite dominated samples with only minor relict anatase the analyses were classifies as titanite. The contribution of relicts of anatase to the calculated age was estimated by comparison with results from samples where the only anatase or titanite only were sampled. In sample where two types of anatase were observed, all anatase data were processed together. The existence of one or two population(s) of anatase based on the data interpretation was compared to microstructural observations.

Monazite ages were calculated from the EPMA U, Pb and Th contents. The associated detection limits were 90 ppm for Pb, 120 ppm for U and 115 ppm for Th. For each monazite analysis, a chemical U-Th-Pb age was determined (see Montel et al., 1996). When the Pb content was lower than the EPMA detection limit, a value of 90 ppm was used to estimate a maximum age.

The crystallization temperature and the minimum content of XFe^{3+} ($Fe^{3+}/(Fe^{2+} + Fe^{3+})$) of each generation of chlorite in 23 selected samples were estimated using the Chl-Qz-H_2O thermodynamic model of Vidal et al. (2006) from element abundances at a reference pressure of 3 kbar and H_2O activity at fixed unit value. The absolute uncertainty on the crystallization temperature estimates is around 50°C (Vidal et al., 2006; Dubacq, Soret, Jewison and Agard,

2019), although the relative uncertainty between samples is likely lower (10-20°C). The semi-empirical thermometer of Bourdelle, Parra, Beyssac, Chopin, and Vidal (2013) formulated for low-temperature chlorite was used for comparison.

5. RESULTS

5.1 Composition of pre-kinematic and syn-kinematic chlorite and white mica

Chlorite generally exhibits compositional variation at the µm-scale with high variability in Fe, Mg and Al contents (especially in discretely deformed granites), as shown in Figure 7 (and Table S1). In samples collected east of Lake Urdiceto, two groups of chlorite are recognized. The first, named Chl1, is ubiquitous from undeformed granites (pre-kinematic) to mylonites, and mainly observed in ChlA flakes (Figure 7a). It should be noted that Chl1 refers to a chemical composition while ChlA refers to the microtexture of chlorite (which do not necessarily correspond, e.g. Vidal et al., 2006; Airaghi et al., 2017). Chl1 is Al-poor (2.2-2.4 apfu) and Mg-rich (1.7-2.5 apfu). The second group of chlorites, Chl2, is mainly observed in syn-kinematic ChlB (Figure 7a, c-d) and exhibits higher Al content (Al= 2.5-2.86 apfu) and lower Mg content (Mg= 1.5-1.7 apfu). The Fe content increases slightly from Chl1 (2.15-2.3 apfu) to Chl2 (2.4-2.5 apfu). In undeformed samples, only homogeneous Chl1 in chlorite flakes is observed (e.g. sample ZA16-84). In the most deformed samples, chlorite flakes (ChlA) exhibit µm-scale Mg and Al zoning and portions of Chl1 are pseudomorphically replaced by Chl2. Chl1 is also found as relicts in ChlB in fractures, wrapped by Chl2 (Figure 7a). In samples collected west of Lake Urdiceto, Chl1 in flakes is Fe-rich (1.97-2.13 apfu) and Mg-poor (2.18-2.47 apfu) compared to Chl2 in veins and along fractures (Fe= 1.39-1.50 apfu, Mg= 2.83-2.95 apfu) (Figure 7b, c, e) while the Al content is typically constant (Table S1). A micron-scale zoning within Chl1 flakes is observed miming cleavage planes of the original magmatic crystal

375 (biotite or amphibole) in discretely deformed samples, while Chl2 within ChlB within fractures
376 is homogeneous (Figure 7b). In mylonites, chlorite shows intermediate compositions (e.g.
377 sample ZA16-96 in Figure 7c) difficult to relate to a specific microtextural sequence due to
378 extensive deformation. In the Triassic sediments, chlorite is Al-enriched compared to chlorite
379 in the basement, but exhibits similar compositional trends (Figure 7c-e). Two groups are
380 recognized in samples ZAL18-13 and ZAL18-12: one is Mg-depleted (1.7-1.97 apfu) and Al-
381 enriched (2.90-2.92 apfu) and is observed in veins, the other is Mg-enriched (2.18-2.40 apfu)
382 or Al-depleted (2.68-2.78 apfu) and is observed within the matrix (Figure 7c-e). Only the
383 second group of chlorite is observed in sample ZAL18-11 (Table S1).

384 White mica in the granitic basement shows 55-80 % muscovite (*Ms*), pyrophyllite (*Prl*)
385 content in the 0-20% range and up to ~30 % celadonite content (*Cel,* Figure 8a). White mica in
386 fractures, veins and in the deformed matrix (syn-kinematic) exhibits lower muscovite (55-70 %)
387 and higher (or similar) celadonite content (20-30 %) than white mica in chlorite flakes (pre-
388 kinematic, 70-80 % muscovite, 10-20 % celadonite, Figure 8a). The composition of white mica
389 in sedimentary samples is similar to that of white mica from feldspar in basement samples
390 (Figure 8b), but with lower variability. While in samples ZAL18-12 and ZAL18-11 one single
391 group of white mica is observed, in sample ZAL18-13 two groups are identified: white mica in
392 the veins have higher celadonite contents (18-28%) than in the matrix (10-18%).

393

394 **5.2 Thermobarometry of low-grade fluid-rock interaction events**

395 Thermodynamic modelling was combined to empirical thermobarometry to distinguish the
396 conditions of crystallisation of the different generations of chlorite and white mica possibly
397 recorded by the restricted range of compositional variations. Crystallisation temperature
398 calculated with the chlorite thermometers of Vidal et al. (2006) and Bourdelle et al. (2013) are
399 reported in Figure 9a, and range between 180 and 350°C. The minimum content of XFe^{3+} in

chlorite calculated with the method of Vidal et al. (2006) ranges between 0.1 and 0.55, which is realistic for low-T chlorite (Masci et al., 2019). The entire iron content was considered divalent for the thermometer of Bourdelle et al. (2013) as recommended in that study. Calculated temperatures for all groups of chlorites are in the same range, with small but systematic differences between Chl1 and Chl2. In samples recording two compositional groups of chlorites (that correspond to pre and syn-kinematic grains), where Fe variations prevail on other element variations (ZA16-82, B11-19, ZA16-78), Chl1 records higher temperatures (220-320°C) than Chl2 (180-250°C). In samples where dominant chemical variations involve Al and Mg (ZA16-126, ZA16-73, B10-32), Chl1 records lower temperatures (170-280°C) than Chl2 (230-350°C, Figure 8a). In other samples (ZA16-133, B10-31), where two compositional groups of chlorite were observed, calculated temperature cover the entire temperature range estimated for all samples. Undeformed granite samples preserving only Chl1 (e.g. ZA16-79, B11-16, ZA16-117) record the highest range of temperatures (280-350 °C). Crystallisation temperatures calculated for chlorite in mylonites (e.g. ZA16-96, ZA16-98, ZA16-128, ZA16-97) are intermediate between the Chl1 and Chl2 crystallisation temperatures. Two ranges of temperatures were also obtained for chlorite in sedimentary samples (ZAL18-12). The highest temperatures (240-350°C) are generally associated with chlorite in veins, while lowest temperatures (180-280°C) are mostly associated with chlorites in C planes (with variability, especially for samples collected Est and West of the Lake of Urdiceto, Fig. 1c). Only one range of chlorite temperatures (Chl2, 200-300°C) is observed within the vein of sample ZAL18-11. To test for the statistical validity of the two temperature intervals (240-350°C and 180-280°C), 3000 temperatures were randomly sampled from the dataset calculated with the thermometer of Vidal et al. (2006) assuming a Gaussian error of ± 30°C (Figure 9b). In the basement, two main peaks at 260 and 330°C persist. Scattered values at low-T conditions are attributed to

424 modelling artefacts due to Fe^{3+} overestimation and/or to departure of some chlorite
425 compositions from equilibrium with assumed unit activity for quartz and water.
426 The moderate celadonite contents of white mica (accounting for the Tschermark substitution
427 only) suggest crystallization pressures in the range 1-4.5 kbar following the calibration of
428 Massone and Schreyer (1988) (Figure 9c), as opposed to sub-surface hydrous alteration of
429 feldspar only, which would favour pyrophyllitic substitution (Dubacq, Vidal, & De Andrade,
430 2010). Following this calibration, the higher celadonite content (and Si apfu content) of white
431 mica in fractures, veins and shear bands indicates higher pressure conditions than in white mica
432 growing from feldspar or from biotite (white mica in flakes, Figure 9c).
433
434 **5.3 *In situ* U-Th/Pb dating of magmatic zircon and hydrothermal anatase, titanite and**
435 **monazite**
436 Results for titanite, anatase and monazite dating are shown in Figure 10a-c and summarized in
437 Table 1; the raw isotopic ratios and age data for zircon, titanite and anatase are provided in
438 Table S3. The entire geochronological dataset is combined with previous literature age
439 constraints of metamorphic events, derived from other localities of the Axial zone in Figure
440 10d. The composition of monazite together with all concordias for zircon, titanite and anatase
441 are provided in Figure S2. Zircon analyses yield weighted mean Concordia ages at 300-310 Ma
442 (Figure 10d and f). Some zircon analyses, especially in sample ZA16-119, exhibit Pb loss and
443 broadly define a discordia line intercepting the Concordia at c. 285-290 Ma (see Figure S1).
444 Titanite grains contain on average 16 ppm of U, 1.7 ppm of Th and 50 ppm of common
445 Pb, and exhibit a Th/U ratio of 0.1 with ages spanning from 336 ± 12 to 313 ± 11 (Figure 10a
446 and d). Titanite in ZA16-84 provides the age constraint with the lowest uncertainty (313 ± 11,
447 MSWD of 1.1, Figure 10a) and exhibits the lowest common Pb content (10 ppm) and the highest
448 Th/U ratio (0.20). Anatase contains on average lower amounts of U (8 ppm) and common Pb

(24 ppm), and higher Th contents (3.4 ppm) than titanite, with Th/U ratios of 0.4, with ages from 301 to 48 Ma (Figure 10b and d). The age of anatase is difficult to constrain because of high common Pb and low radiogenic Pb contents. When possible, two Tera-Wasserburg concordia lower intercepts for anatase U-Pb age data were defined for each sample, delimiting the possible youngest and oldest grain populations (e.g. Figure 10b). In this case, youngest ages cluster at *c.* 30-80 Ma while oldest ages cluster at *c.* 240-280 Ma (Figure 10b, d). The mylonitic granite ZA16-96 exhibits the young age population only (Tera-Wasserburg concordia lower intercept of 39 ± 8 Ma, Figures 10c and S1), despite the low variability of the radiogenic U/Pb ratio.

Patchy monazite in samples ZA16-98 and ZAL18-11 shows low and variable U and Th contents (Figure 10e and Table S2), typical of low-temperature secondary monazite (Rasmussen & Muhling, 2007; Janots, Berger, & Engi, 2011). The U-Th/Pb ages (with Pb > EPMA detection limits of ~100 ppm) range between 180 and 325 Ma (Figure 10c). In both samples, Pb-depleted domains (Pb < EPMA detection limits despite Th contents up to few wt%, Table S2) are observed within Th-depleted monazite grains, indicating late partial replacement of monazite grains by recrystallization and dissolution-reprecipitation (Figure 10e). The oldest ages generally correspond to monazite with relatively high Th content (ThO_2 > 2.4 wt %) and variable U content (0.04 wt% < UO_2 < 1.0 wt %). They cluster around 254 ± 6 Ma. A second group of monazite has a lower Th content (ThO_2 < 1.9 wt%), variable U content (0.01 wt% < UO_2 < 1.9 wt%) and provides an age of 196 ± 18 Ma. In both samples ZA16-98 and ZAL18-11 young ages are estimated from the Pb-depleted domains (Pb < detection limits). Assuming a Pb content equal to the EPMA detection limit (~90 ppm), a maximum age for this late stage crystallisation has been calculated at *c.* 100 Ma in sample ZA16-98 and at *c.* 20 Ma in sample ZAL18-11 for the domains with the highest Th (ThO_2=7.6 wt.%) and U contents (UO_2=0.9750 wt.%) (Figure 10c). Cenozoic ages of *c.* 50 Ma have also been estimated in sample ZA16-98

474 from thorite-monazite domains. No ages could be obtained for monazite from the sedimentary
475 samples due to their low U, Th and Pb contents.

476

477 **6. DISCUSSION**

478

479 **6.1 Evaluation of geochronological results**

480 Estimated crystallisation temperatures are far below the closure temperature of Pb diffusion in
481 rutile (580-630°C), titanite (575-700°C), monazite (~800 °C) and zircon (~900 °C, Rubatto,
482 2017; Engi, 2017 and references therein). Therefore, U-Th/Pb dates are interpreted as
483 crystallisation ages. Zircon is dominantly of magmatic origin as attested by its microtextures.
484 Concordant zircon ages, inferred to bracket the timing of the Bielsa pluton emplacement at 300-
485 310 Ma (Figure 10d and Table 1), are in agreement with previously published ages (Vacherat
486 et al., 2017). Zircon ages therefore constrain the upper limit of the first alteration event.
487 Discordant ages defining a chord with an intercept at *c.* 290 Ma in sample ZA16-119 (Figure
488 S1) derive from sampling of metamictic zircon domains, characterized by decreasing
489 crystallinity, Pb loss and variable incorporation of common Pb. Since metamict domains show
490 typical textures of dissolution-reprecipitation under low-T conditions (Geisler et al., 2003) and
491 are observed in undeformed samples, the c. 290 Ma age may indicate re-opening of the system
492 during the early pre-kinematic fluid-rock interaction, started shortly after the pluton
493 emplacement, in Late Variscan times.

494 Titanite ages are less accurate but cluster within uncertainty of the zircon ages, at *c.* 300
495 Ma (Late Variscan) (Figure 10d and Table 1). Some of the titanite ages are older than the
496 corresponding zircon ages from the same sample. The titanite Discordia line on Tera-
497 Wasserbourg Concordia diagram is well constrained due to the large variation in U:Pb ratio of
498 the titanite grains (Figure 10a and Figure S2). Therefore, the titanite ages marginally older than

their corresponding zircon ages may originate from local incorporation of radiogenic PB at the time of titanite crystallization (see also Essex and Gromet, 2000). The $^{207}Pb/^{206}Pb$ initial ratio of metamorphic titanite has been shown to vary up to 2% in the same sample (Kohn, 2017), and is often significantly lower (i.e. more radiogenic) than the crustal evolution model of Stacey and Kramers (1975). This signs the incorporation of radiogenic Pb from the breakdown of a U-rich mineral phase such as rutile or anatase, anatase being observed here as the most common titanite precursor.

The U/Pb ages obtained for anatase are less well constrained than the titanite due to higher common Pb, lower radiogenic Pb contents and the smaller spread in U-Pb ratio of the anatase grains. Calculated ages range between 40 Ma and 280 Ma. Anatase does not record the magmatic stage since it is observed to replace magmatic ilmenite. If type-1 Ant or titanite recrystallize into type-2 Ant, inter and intra-grain variations in the radiogenic Pb and U content could be inherited from the parent mineral given the small transport scales for anatase-forming elements deduced from microtextural evidence (see section 3.1). Such variations and possible incorporation of type-1 Ant in spot ablations of titanite (see section 4) contribute to the large spread of the anatase ages (e.g. samples ZA16-79, ZA16-73). However, a recurrently young signal of *c.* 40-80 Ma is exclusively observed only in samples with both types of anatase and in mylonites. As solid-state Pb diffusion can be excluded due to the low metamorphic grade, the youngest U-Pb anatase ages likely indicate partial (re-)crystallization of the smallest anatase grains (type-2 Ant), in agreement with microtextural observations. In addition, the upper limit of the range of anatase ages is the youngest in samples with both types of anatase: This suggests mixing at a smaller scale than laser beam size between older titanite-anatase and new anatase. The two age end-members are shown on Figure 10d for all anatase-bearing samples.

Monazite is unlikely to record the magmatic stage since (1) magmatic allanite and apatite incorporate the rare earth elements and phosphorous necessary for monazite crystallization, (2)

monazite is observed to replace magmatic allanite or apatite and (3) the oldest monazite ages are younger than the zircon ages. Monazite ages in both samples ZA16-98 and ZAL18-11 indicate a series of events at *c.* 250 Ma, 200 Ma, and possibly < 50 Ma. This range of ages suggests successive episodes of partial dissolution-reprecipitation, as also shown by the patchy textures and the dissolution figures of monazite grains (Figures 5c and 6b). The mineral assemblage corresponding to the monazite ages of *c.* 200 Ma remains difficult to identify as textural and chemical evidences is lacking. The ages of 190-250 Ma obtained in monazite of chlorite-bearing veins in sediments indicate that monazite grains were likely inherited from the underlying basement and partially re-crystallized during vein opening and fluid circulation soon after sediments deposition in Triassic times.

6.2 Timing and conditions of fluid-rock interactions and deformation

Detailed microstructural and petrological observations show a poly-phase alteration history in the Bielsa basement at temperatures below 350°C. Within this temperature range, a first fluid-rock interaction event is related to the breakdown of the original magmatic assemblage and the growth of Ttn, Chl1, anatase (type-1 Ant) at 270-350°C. This alteration event predates all deformation stages since the earliest deformation phase deforms this mineral assemblage and the alteration event is also observed in undeformed samples (e.g. Figure 4a-b). During the first alteration event, the source of Al and Ca for chlorite and titanite (± prehnite) growth is the contemporaneous breakdown of plagioclase and the albitization of alkali-feldspar (always largely consumed), irrespective of the strain intensity. Calcium may also derive from external fluids as attested by calcite growth within weakely deformed granite matrix. Titanite, zircon, anatase and oldest monazite ages allow bracketing the timing of the early alteration(s) to 230-300 Ma (late to post-Variscan). This age range is in agreement with $^{40}Ar/^{39}Ar$ ages of biotite of *c.* 280 and 250 Ma obtained in the Bielsa and Maladeta massifs respectively (Jolivet et al., 2007).

549 The second fluid-rock interaction event is related to the syn-kinematic growth of Chl2
550 during the formation of C-S structures (see section 3) at ~200-280°C. The pervasive schistosity,
551 kinking, shearing and fracturing are likely to have occurred at the same time since they are
552 kinematically compatible. The S planes are observed in both the basement and in the Triassic
553 sediments (see section 2). The S-forming stage is therefore post-late Triassic in age at least.

554 In such deformed samples, the youngest ages are yielded by anatase (in samples bearing
555 both types of anatase) and by monazite; this suggests that deformation triggered the partial re-
556 crystallization of anatase and monazite. The youngest anatase ages only (*c.*40 Ma) and the
557 youngest monazite ages (*c.* 50 Ma) are obtained in mylonites (ZA16-96 and ZA16-98). This
558 observation suggests that the mylonitization related to the deformation stage likely occurred
559 between 40 and 70 Ma. These ages are in agreement with Rb-Sr ages of *c.* 48 Ma obtained for
560 the (re)activation of mylonitic bands in the Néouvielle massif (~ 15 km to the northwest of
561 Bielsa, Wayne & McCaig, 1998). In sample ZA16-79 an age population at *c.* 120 Ma is
562 observed, but no clear textural relationships are identified, while the large uncertainties mean it
563 Eocene ages.

564 Chlorite temperatures calculated with the method of Vidal et al. (2006) and Bourdelle
565 et al. (2013) are consistent despite differences in how they employ the oxidation state of Fe.
566 The calculated range of temperatures (200-350°C) is also consistent with hydrothermal
567 conditions typically associated with the appearance of prehnite and titanite in the cleavages of
568 biotite (e.g. Eggleton & Banfield, 1985; Morad, Sirat, El-Ghali, & Mansurbeg, 2011; Yuguchi
569 et al., 2015) and with temperatures calculated for the overlying sediments, suggesting that fluids
570 were freely circulating between the basement and the overlying sediments. In details,
571 thermometric results indicate that the pre-kinematic greenschist-facies metamorphism occurred
572 at higher temperature (270-350°C) than later syn-kinematic fluid-rock interaction (200-280°C,
573 Figure 9b), with spatial variations (east and west of Lake Urdiceto, Figure 9a) due to local

574 variations in fluid composition. The systematic differences between temperatures estimated for
575 Chl1 and Chl2 support however the existence of two different fluid-rock interaction events.

576 The moderate celadonite content of white mica, especially in fractures, veins and shear
577 bands (Figure 8a and c) suggests crystallization at a pressure of 1-5 kbar (1 - 4.5 kbar, following
578 the formulation of Massone and Schreyer, 1988, Figure 9c and below 3 kbar according to
579 Cathelineau et al., 1986 for hydrothermal alteration in granites). No paragonite nor margarite
580 components are observed within our white mica dataset. Pyrophyllite substitution, which
581 increases the Si content of muscovite, is not predominant compared to the Tschermak
582 substitution (Figure 8a). Increasing pyrophyllite content in sample B11-31 implies
583 crystallization during continuous cooling (Dubacq et al., 2010). Fluid inclusion trapping
584 pressures in the range 2-5 kbar are reported by Henderson and McCaig (1996), consistent with
585 pressure estimates from white mica in mylonite veins (Wayne & McCaig, 1998). The lowest
586 pressure values of ~ 2 kbar are consistent with the maximum burial depth estimated for the
587 Bielsa (Jolivet et al., 2007; Bellahsen et al., 2019).

588 This low-grade petro-chronological dataset allows the timing of low-grade
589 metamorphism and deformation to be discussed in the light of the Variscan and Alpine orogenic
590 cycles, with major implications for the crustal rheology and the evolution of the deformation
591 style in granites.

592

593 **6.3 Pre-orogenic alteration and implications for crustal softening prior to shortening**

594 Petro-chronological results and microstructural analyses show that Late to post-Variscan lower
595 greenschist-facies metamorphism in the Bielsa massif transformed an initially strong
596 assemblage made of plagioclase, K-feldspar (forming together close to half of the primary
597 modal composition) and amphibole into weaker, hydrated minerals such as white mica and

598 chlorite, without associated deformation (as suggested by Bellashen et al., 2019). The
599 breakdown of feldspar to white mica decreases by up to two orders-of-magnitude the sustained
600 shear stress (at a constant strain rate) at 400°C, lowering the depth of the brittle-ductile
601 transition by at least a third (Wintsch et al., 1995; Gueydan et al., 2003). In the Bielsa massif,
602 pre-orogenic sub to lower greenschist-facies metamorphic reactions have two effects: they
603 enhance grain size reduction (e.g. from magmatic feldspars to minute white micas) and also
604 replace strong minerals such as feldspar and amphibole with mechanically weaker
605 phyllosilicates (e.g. Shea & Kronenberg, 1993). Both processes are known to result in enhanced
606 softening of the granitic rocks (e.g. Fitz Gerald & Stünitz, 1993; Wintsch et al., 1995; Oliot,
607 Goncalves, Marquer, 2010). Early pre-kinematic alteration therefore considerably softened the
608 granite at least 150 Ma before the major Alpine shortening phases. Furthermore, the massive
609 growth of pre-kinematic and pre-Alpine white mica and chlorite indicates high fluid-rock ratios
610 during Late-to post-Variscan times and may strongly influence the water availability in the
611 rocks at the grain boundaries during deformation. This has been shown to have major effects
612 on the mechanisms of strain accommodation in other major phases as quartz (e.g. Palazzin et
613 al., 2018) and hence impact the deformation style.

614 Sericitisation of feldspar and chloritisation of biotite is observed to increase with
615 deformation. This suggests that granite alteration continued during syn-kinematic Alpine
616 shortening. In mylonites, syn-kinematic chlorite and white mica partly replace the pre-
617 kinematic chlorite and mica grains, this time without needing huge supplementary amounts of
618 external fluid. Consequently, in the latter fluid-rock interaction event, there is no evidence for
619 additional large-scale reaction-driven softening outside mylonitic zones, consistent with
620 observations reported for the Néouvielle massif (~ 15 km to the northwest, Wayne & McCaig,
621 1998). The crystallisation of new phyllosilicates and the larger amount of fluid inclusions in
622 quartz in fractured and mylonitic samples as well as the partial age resetting up to ~40 Ma close

623 to shear zones also appear to indicate progressive localisation of metamorphism with strain
624 localisation.

625 Zones of fractures and faults indicate that granitic rocks were also deformed by frictional
626 behaviour, as commonly observed at temperatures of 200-350°C (e.g. Copley, 2017). The
627 crystallization of phyllosilicates during a pre-orogenic alteration event may weaken fault zones
628 by at least 30% as phyllosilicates have much lower coefficients of friction than undeformed and
629 unaltered crystalline rocks (e.g. Kaduri, Gratier, Renard, Çakir, & Lasserre, C., 2017; Copley,
630 2017). The pre-existence of phyllosilicate in the Bielsa basement therefore appears to have
631 generated a network of weak rocks with low friction coefficient resulting in their distributed
632 deformation.

633

634 **6.4 Effect of the early alteration on deformation patterns at field scale**

635 The pervasive schistosity (S) observed within the Bielsa massif along the studied transects
636 indicates that the deformation is distributed at the scale of the massif (Figure 1b). The existence
637 of mylonitic corridors shows a phase of strain localization with variations in the sense of shear
638 at the kilometric to decametric scale, but their high density also results in a distributed
639 deformation at the massif scale. At Bielsa, both S and C forming stages post-date the Late to
640 post-Variscan pervasive alteration that softened the basement. In the Maladeta massif, (50-60
641 km to the northeast), less pervasive pre-kinematic alteration is observed as well as localized
642 deformation and lower density of mylonitic corridors (Leblanc, Gleizes, Lespinasse, Olivier, &
643 Bouchez, 1994). This indicates that pre-orogenic crustal softening controlled the deformation
644 patterns observed on a outcrop scale, in particular the frequency of mylonitic bands the location
645 of faults and of fractures.

646 In the Bielsa massif, strain localization in mylonitic bands may have occurred during
647 the intense folding of the basement and the sedimentary cover in the Eocene as indicated by the

young ages from the mylonites. During this stage, the re-activation of steep faults may have served as fluid pathways and triggered alteration. Interfaces between differently-altered domains formed different phase strength contrasts. Consequently, ductile strain and reactions interacted positively to produce narrow ductile shear zones (as described by Holyoke & Tullis, 2006). Furthermore, deformation at this stage may strongly influence the breakdown on residual feldspar to muscovite (e.g. Knipe & Wintsch, 1985), as attested by the greater amount of white mica observed in mylonites compared to weakly and undeformed samples.

The youngest ages obtained in this study (*c.* 40 Ma) are older than the activation of the Gavarnie and Guarga thrusts (Figure 1b), in the hanging and footwall of the Bielsa unit, dated at 32-36 Ma et 20-30 Ma respectively (e.g. Bosch et al., 2016; Elmola et al., 2018) and similar to the age of mylonitization in the Néouvielle massif (Wayne & McCaig, 1998). This may indicate that the distributed shortening in Bielsa and at a larger scale predates the localization of the strain along some of the major thrust of the Axial zone. These findings are consistent with the distributed / localized modes of shortening documented in the external Western Alps (Bellahsen et al., 2014), in the central Alps (Wehrens, Baumberger, Berger & Herweg, 2017) and in the Longmen Shan where pre-kinematic and a syn-kinematic greenschist-facies metamorphic events were also recognized (Airaghi et al., 2017b), indicating that they might be typical of the evolution of basement massif in the external domains of the orogenic wedges.

6.5 Onset and preservation of early alteration in granitic basement

Late to post-Variscan fluid-rock interaction took place on the scale of the Axial zone as metamorphic reactions similar to those observed in the Bielsa massif are found in other crystalline massifs in the Pyrenees (e.g. Maladeta, Néouvielle, Col de Jau; Cathelineau, 1986; Boutin et al., 2016). The early alteration stages may be linked to protracted magmatic activity recorded in the Pyrenean domain throughout the entire Permian (Denèle, Paquette, Olivier, & Barbey, 2012). Late Variscan magmatic activity has also been invoked as the cause of

674 hydrothermal alteration in the French Massif Central (Cathelineau, 1986; Turpin, Leroy, &
675 Sheppard, 1990). Permian to Triassic ages similar to those obtained for fluid-rock interaction
676 events in the Bielsa massif have also been documented in the Variscan basement of the Eastern
677 Iberian Central System and in NE Spain by fluid inclusion and isotopic studies (Tornos,
678 Delgado, Casquet, & Galindo, 2000 and references therein). The associated hydrothermal
679 alteration in these cases is related to hydrothermal cells formed during extensional tectonic
680 events rather than to plutonism (Tornos et al., 2000; Cardellach, Canals, & Grandia, 2002). In
681 the Bielsa massif, high fluid-rock ratios have been proposed to result from ingress of seawater
682 and meteoric fluids during the extensional phase following the Variscan orogeny (McCaig,
683 Tritlla, & Banks, 2000). This is consistent with the fact that the Bielsa basement was exposed
684 at the surface before or during the Permian, as attested by the erosional unconformity between
685 the basement and its sedimentary cover. The preservation of early alteration features in granites
686 over two orogenic cycles (Variscan and Alpine) implies that the basement remained at low
687 grade conditions for over 200 Ma. In the Pyrenees, the main post-Variscan metamorphic phase
688 related to fluid circulation is dated at 110 Ma (e.g. Boutin, 2016). Although Cretaceous ages
689 were obtained for samples which contain both types of anatase, the large U/Pb age uncertainties
690 for this time period in our petro-chronological dataset mean that strong evidence for extensive
691 fluid circulation, mineral replacement and deformation during Cretaceous times is lacking. This
692 is in contrast to the eastern Pyrenees where a hydrothermal event characterized by newly formed
693 rutile and titanite associated with Cretaceous rifting overprints the 'post'-Variscan
694 hydrothermal alteration assemblages (Figure 10d; Boutin et al., 2016; Fallourd et al., 2014).
695 This may indicate that, within the Pyrenean belt, metamorphism related to rifting has only
696 weakly affected the southern part of the Axial zone.
697
698 **7. CONCLUSIONS**

699 The granitic basement rocks in the southern Axial zone of the Pyrenees (Bielsa massif) acted
700 as reactive rocks at low temperatures (T < 350 °C) over a long (*c.* 300 Ma) polyphase history.
701 At an outcrop scale, the Bielsa pluton and the Triassic sedimentary cover exhibit a pervasive
702 N-dipping schistosity, folded or associated to steep C planes localized within a dense network
703 of mylonitic bands. Within the granitic basement, partial mineral replacement and
704 compositional variations at the micron-scale record an extensive fluid-rock interaction event at
705 ~270-350°C in Late to post-Variscan times (230-300 Ma), as indicated by the titanite, anatase
706 and zircon U/Pb ages dataset. This event is ubiquitous and particularly well preserved in the
707 less deformed areas of the massif. It is responsible for pre-kinematic (pre-Alpine) plagioclase
708 and amphibole replacement with growth of phyllosilicates, some tens of million years after
709 pluton emplacement. A second syn-kinematic fluid-rock interaction event is marked by the
710 (re)crystallisation of phyllosilicates at ~200-280°C and is related to the formation of mylonitic
711 corridors and fractures parallel to the C shear planes. In the most deformed samples, despite the
712 low radiogenic Pb content, monazite and anatase U-Th/Pb ages systematically show a young
713 age component at 40-70 Ma, coeval with the Alpine/ Pyrenean deformation in the southern
714 Axial zone and related to the second alteration event. As the strength of phyllosilicate-rich
715 material is lower by up to an order-of-magnitude than that of the original granite, the granitic
716 massif was significantly softened (and hydrated) at least 150-200 Ma before the major Alpine
717 shortening phase. The dense network of mylonites in the Bielsa pluton resulted in distributed
718 deformation at the massif scale before the localization of the strain along the major thrusting
719 systems of the Axial zone. Pre-orogenic crustal softening controlled the deformation patterns
720 where strain and shortening localized during successive deformation events. Pre-orogenic
721 greenschist-facies metamorphism is often poorly characterized compared to higher-grade
722 metamorphic domains in mountain belts. The case of the Bielsa massif shows that moderate
723 analytical effort can provide valuable information allowing for a better constraints on the

724 rheological and thermobarometric evolution of basement rocks during the orogenic cycle, even
725 at low-grade conditions.
726
727 **ACKNOWLEDGEMENTS**
728 This study was founded by the CNRS-BRGM-TOTAL 'OROGEN' project. We acknowledge
729 Prof. S. Duchene and the anonymous review for their constructive comments and remarks.
730 We thank Michel Fialin, Nicolas Rividi and Omar Boudouma for their help with the electron
731 microscopy at ISTeP. DC acknowledges support from Science Foundation Ireland grants
732 12/IP/1663, 15/IA/3024 and 13/RC/2092 (iCRAG Research Centre). iCRAG is funded under
733 the SFI Research Centres Programme and is co-funded under the European Regional
734 Development Fund. We also thank Gary O'Sullivan (Trinity College) for his support with the
735 LA-ICP-MS analysis. Authors have no conflict of interest to declare.
736
737 **REFERENCES**
738 Airaghi, L., Janots, E., Lanari, P., de Sigoyer, J. & Magnin, V. (2018). Allanite
739 petrochronology in fresh and retrogressed garnet-biotite metapelites from the Longmen
740 Shan (eastern Tibet), Journal of Petrology, in press.
741 Airaghi, L., de Sigoyer, J., Lanari, P., Guillot, S., Vidal, O., Monié, P., … Tan, Xibin (2017).
742 Total exhumation across the Beichuan fault in the Longmen Shan (eastern Tibetan
743 plateau, China) : Constraints from petrology and thermobarometry. Journal of Asian
744 Earth Sciences, 140, 108-121.
745 Bellahsen, N., Mouthereau, F., Boutoux, A., Bellanger, M., Lacombe, O., Jolivet, L., …
746 Rolland, Y. (2014). Collision kinematics in the western external Alps, Tectonics, 33.

747 Bellahsen, N., Bayet, L., Denele, Y., Waldner, M., Airaghi, L., Rosenberg, C. … Vacherat, A.
748 (2019). Shortening of the axial zone, Pyrenees: Shortening sequence, upper crustal
749 mylonties and crustal strength. Tectonophysics, 766, 433-452.
750 Bosch, G. V., Teixell, A., Jolivet, M., Labaume, P., Stockli, D., Domènech, M., …Monié, P.
751 (2016). Timing of Eocene-Miocene thrust activity in the Western Axial Zone and
752 Chaînons Bérnais (west-central Pyrenees) revealed by multi-method thermochronology.
753 Comptes Rendus Geoscience, 348(3-4), 246-256.
754 Bourdelle, F., Parra, T., Beyssac, O., Chopin, C. & Vidal, O. (2013). Clay minerals as geo-
755 thermometer: A comparative study based on high spatial resolution analyses of illite
756 and chlorite in Gulf Coast sandstone (Texas, U. S.A.). American Mineralogist, 98, 914-
757 926.
758 Boutin, A., de Saint Blanquat, M., Poujol, M., Boulvais, P., de Parseval, P., Rouleau,
759 C., …Robert, J.-F. (2016). Succession of Permian and Mesozoic metasomatic events in
760 the eastern Pyrenees with emphasis on the Trimouns talc-chlorite deposit. International
761 Journal of Earth Science, 105, 747-770.
762 Cardellach, E., Canals, A. & Grandia, F. (2002). Recurrent hydrothermal activity induced by
763 successive extensional episodes: the case of the Berta F-(Pb-Zn) vein system (NE
764 Spain). Ore Geology Reviews, 22, 133-141.
765 Casas, A.M., Oliva, B., Román-Berdiel, T. and Pueyo, E. (2003). Basement deformation:
766 tertiary folding and fracturing of the Variscan Bielsa granite (Axial zone, central
767 Pyrenees). Geodinamica Acta, 16(2-6), 99-117.
768 Cathelineau, M. (1986). The Hydrothermal Alkali Metasomatism Effects on Granitic Rocks :
769 Quartz Dissolution and Related Subsolidus Changes. Journal of Petrology, 27, 945-965.
770 Chew, D. M ;, Petrus, J. A. & Kamber, B. S. (2014). U-Pb LA-ICPMS dating using accessory
771 mineral standards with variable common Pb. Chemical Geology, 363, 185-199.

772 Cochelin, B., Lemirre, B., Denèle, Y., de Saint Blanquant, M., Lahfid, A., & Duchene, S.
773 (2017). Structural inheritance in the Central Pyrenees : the Variscan to Alpine
774 tectonometamorphic evolution of the Axial Zone. Journal of the Geological Society,
775 175(2), 336.
776 Copley, A. (2017). The strength of earthquake-generating faults. Journal of the Geological
777 Society, 10.1144/jgs2017-037.
778 Denèle, Y., Paquette, J.-L., Olivier, P. & Barbey, P. (2012). Permian granites in the Pyrenees:
779 the Aya pluton (Basque Country). Terra Nova, 24, 105-113.
780 Dubacq, B., Soret, M., Jewison, E., Agard, P. (2019). Early subduction dynamics recorded by
781 the metamorphic sole of the Mt Albert ophiolitic complex (Gaspé, Quebec). Lithos, 334
782 – 335, 161 – 179, doi: 10.1016/j.lithos.2019.03.019.
783 Dubacq, B., Vidal, O., De Andrade, V., 2010. Dehydration of dioctahedral aluminous
784 phyllosilicates: thermodynamic modelling and implications for thermobarometric
785 estimates. Contributions to Mineralogy and Petrology 159, 159–174.
786 Eggleton, R. A. & Banfield, J., F. (1985). The alteration of granitic biotite to chlorite. American
787 Mineralogist, 70, 902-910.
788 Elmola, A. A., Buatier, M., Monié, P., Labaume, P., Trap, P., & Charpentier, D. (2018).
789 40Ar/39Ar muscovite dating of thrust activity: a case study from the Axial Zone of the
790 Pyrenees. Tectonophysics, in press.
791 Engi, M. (2017). Petrochronology Based on REE-Minerals: Monazite, Allanite, Xenotime,
792 Apatite. In: Petrochronology: Methods and Applications, Kohn, M. J., Engi, M. &
793 Lanari, P. Reviews in Mineralogy & Geochemistry.
794 Fallourd, S., Poujol, M., Boulvais, P., Paquette, J.-L., de Saint Blanquant, M., & Rémy, P.
795 (2014). In situ LA-ICP-MS U-Pb titanite dating of Na-Ca metasomatism in orogenic

796 belts: the North Pyrenean example. International Journal of Earth Science, 103, 667-
797 682.
798 Fitz Gerald, J. D. & Stünitz, H. (1993). Deformation of granitoids at low metamorphic grade.
799 I: Reaction and grain size reduction. Tectonophysics, 221 (3-4), 269-297.
800 Geisler, T., Rashwan, A. A., Rahn, M. K., Poller, U., Zwingmann, H., Pidgeon, R.
801 T., …Tomaschek, F. (2003). Low-temperature hydrothermal alteration of natural
802 metamict zircon from the Eastern Desert, Egypt. Mineralogical Megazine, 67(3), 485-
803 508.
804 Goncalves, P., Oliot, E., Marquer, D. & Connolly, J. A. D. (2012). Role of chemical processes
805 on shear zone formation: an example from the Grimsel metagranodiorite (Aar massif,
806 Central Alps). Journal of Metamorphic Geology, 30(7), 703-722.
807 Grand'Homme, A., Janots, E., Seydoux-Guillaume, A.M., Guillaume, D., Magnin, V.,
808 Hövelmann, J., …Boiron, M.C. (2018) Mass transport and fractionation during
809 monazite alteration by anisotropic replacement. Chemical Geology, 484, 51–68.
810 Gueydan, F., Leroy, Y.M., Jolivet, L., & Agard, P. (2003). Analysis of continental midcrustal
811 strain localization induced by microfracturing and reaction-softening. Journal of
812 Geophysical Research, 108(B2), 2064.
813 Henderson, I. H. C. & McCaig, A.M. (1996). Fluid pressure and salinity variations in shear
814 zone-related veins, central Pyrenees, France: Implications for the fault-valve model.
815 Tectonophysics, 262, 321-348.
816 Hansen, E., Reimink, J. & Harlov, D. (2010). Titaniferous accessory minerals in very low-grade
817 metamorphic rocks, Keweenaw Peninsula Michigan, USA. Lithos, 116, 167-174.
818 Ingles, J., Lamouroux, C., Soula, J.-C., Guerrero, N. & Debat, P. (1999). Nucleation of ductile
819 shear zone in a granodiorite under greenschist facies conditions, Néouvielle massif,
820 Pyrenees, France. Journal of Structural Geology, 21, 555-576.

821 Jackson, J. A., Austrheim, H., McKenzie, D. & Priestley, K. (2004). Metastability, mechanical
822 strength, and support of mountain belts. Geology, 32(7), 625-628.
823 Janots, E., Berger, A. & Engi, M. (2011). Physico-chemical control on the REE minerals in
824 chloritoid-grade metasediments from a single outcrop (Central Alps, Switzerland).
825 Lithos, 121, 1-11.
826 Jolivet, M., Labaume, P., Monié, P., Brunel, M., Arnaud, N., & Campani, M. (2007).
827 Thermochronology constraints for the propagation sequence of the south Pyrenean
828 basement thrust system (France-Spain). Tectonics, 26, TC5007.
829 Kaduri, M., Gratier, J.-P., Renard, F., Çakir, Z., & Lasserre, C. (2017). The implications of
830 fault zone transformation on aseismic creep: Example of the North Anatolian Fault,
831 Turkey, Journal of Geophysical Research : Solid Earth, 122, 4208-4236.
832 Knipe, R. J. & Wintsch, R. P. (1985). Heterogeneous, deformation, foliation development, and
833 metamorphic processes in a polyphaser mylonite. In: Thompson, A. B., Rubie, D. C.
834 (Eds.), Advances in Physical Chemistry, 4, Springer-Verlag, New York, 180-210.
835 Kohn, M. J. (2017). Titanite petrochronology, In: Petrochronology: Methods and Applications,
836 Kohn, M. J., Engi, M. & Lanari, P. Reviews in Mineralogy & Geochemistry.
837 Lanari, P., Vidal, O., De Andrade, V., Dubacq, B., Lewin, E., Grosch, E., …Schwartz, S.
838 (2014). XMapTools: a MATLAB-based program for electron microprobe X-ray image
839 processing and geothermobarometry. Computers & Geosciences 62, 227–240.
840 Leblanc, D., Gleizes, G., Lespinasse, P., Olivier, Ph. & Bouchez, J.-L. (1994). The Maladeta
841 granite polydiapir, Spanish Pyrenees : a detailed magneto-structural study. Journal of
842 Structural Geology, 16(2), 223-235.
843 Mansard, N., Raimbourg, H., Augier, R., Précigout, J. & Le Breton, N. (2018). Large-scale
844 strain localization induced by phase nucleation in mid-crustal granitoids of the south
845 Armorican massif. Tectonophysics, 745, 46-65.

Masci, L., Dubacq, B., Verlaguet, A., Chopin, C., De Andrade, V., & Herviou, C. (2019). A XANES and EPMA study of Fe^{3+} in chlorite: importance of oxychlorite and implications for cation site distribution and thermobarometry. American Mineralogist. 104(3), 403-417.

Massonne, H-J. & Schreyer, W. (1987). Phengite geobarometry based on the limiting assemblage with K-feldspar, phlogopite, and quartz. Contributions to Mineralogy and Petrology, 96, 2, 212-224, doi: 10.1007/BF00375235.

McCaig, A. M., Tritlla, J. & Banks, D.A. (2000). Fluid mixing and recycling during Pyrenean thrusting: evidence from fluid inclusion halogen ratios. Geochimica et Cosmochimica Acta, 64,(19), 3395-3412.

Morad, S., Sirat, M., El-Ghali, M. A., K. & Mansurbeg, H. (2011). Chloritization in Proterozoic granite from the Äspö Laboratory, southeastern Sweden: record of hydrothermal alterations and implications for nuclear waste storage.Clay Minerals, 46, 495-513.

Oliot, E., Goncalves, P. & Marquer, D. (2010). Role of plagioclase and reaction softening in metagranite shear zone at mid-crustal conditions (Gotthard Massif, Swiss Central Alps). Journal of Metamorphic Geology, 28, 849-871.

Palazzin, G., Raimbourg, H., Stünitz, H., Heilbronner, R., Neufald, K., & Précigout, J. Evolution in H_2O contents during deformation of polycrystalline quartz : An experimental study. Journal of Structural geology, 114, 95-110.

Parneix, J. C., Beaufort, D., Dudoignon, P. & Meunier, A. (1985). Biotite chloritization process in hydrothermally altered granites. Chemical Geology, 51, 89-101.

Paquette, J.-L., Gleizes, G., Leblanc, D. & Bouchez, J.-L. (1997). Le granite de Bassiès (pyrénées) : un pluton syntectonique d'âge Westphalien. Géochronologie U-Pb sur zircons. Compte Rendus de l'Académie des Sciences de Paris 324, 387-392.

870 Rasmussen, B. & Muhlig, J. R. (2007). Monazite begets monazite: evidence for dissolution of
871 detrital monazite and reprecipitation of syntectonic monazite during low-grade regional
872 metamorphism. Contribution t Mineralogy and Petrology, 154, 675-689.
873 Román-Berdiel, T., Casas, A. M., Oliva-Urcia, B., Pueyo, E. L. & Rillo, C. (2004). The main
874 Variscan deformation event in the Pyrenees: new data from the structural study of the
875 Bielsa granite. Journal of Structural Geology, 26, 659-677.
876 Rubatto, D. (2017). Zircon: The Metamorphic Mienral, In: Petrochronology: Methods and
877 Applications, Kohn, M. J., Engi, M. & Lanari, P. Reviews in Mineralogy &
878 Geochemistry.
879 Shea, W. T.J., Kronenberg, A.K. (1993). Strength and anisotropy of foliated rocks with varied
880 mica contents. Journal of Structural Geology, 15, 1097-1121.
881 Stacey, J. S. & Kramers, J. D. (1975). Approximation of terrestrial lead isotope evolution by
882 two-stage model. Earth and Planetary Science Letters, 26, 207-221.
883 Tera, F. & Wasserburg, G. J. (1972). U-Th-Pb systematics in lunar highland samples from the
884 Luna 20 and Apollo 16 missions. Earth and Planetary Science Letters, 17, 36-51.
885 Tornos, F., Delgado, A. Casquet, C. & Galindo, C. (2000). 300 Million years of episodic
886 hydrothermal activity: stable isotope evidence from hydrothermal rocks of the Eastern
887 Iberian Central System. Mineralium Deposita, 35, 551-569.
888 Tullis, J., Yund, R. & Farver, J. (1996). Deformation-enhanced fluid distribution in feldspar
889 aggregates and implications for ductile shear zones. Geology, 24(1), 63-66.
890 Turpin, L., Leroy, J. L. & Sheppard, S. M. F. (1990). Isotopic systematics (O, H, C, Sr, Nd) of
891 superimposed barren and U-bearing hydrothermal system in a Hercynian granite,
892 Massif Central, France. Chemical Geology, 88, 85-98.
893 Vacherat, A., Mouthereau, F., Pik, R., Huyghe, D., Paquette, J-L., Christophoul, F., …Tibari,
894 B. (2017). Rift-to-collision sediment routing in the Pyrenees: A synthesis from

sedimentological, geochronological and kinematic constraints. Earth-Sciences Reviews, 172, 43-74.

Vidal, O., De Andrade, V., Lewin, E., Munoz, M., Parra, T., & Pascarelli, S. (2006). P-T deformation-Fe3+/Fe2+ mapping at the thin section scale and comparison with XANES mapping. Application to a garnet-bearing metapelite from Sambagawa metamorphic belt (Japan). Journal of Metamorphic Geology 24, 669–683.

Wayne, D. M. & McCaig, A. M. (1998). Dating fluid flow in shear zones: Rb-Sr and U-Pb studies of syntectonic veins in the Néouvielle Massif, Pyrenees. Geological Society, London, Special Publications, 144, 129-135.

Wehrens, P., Baumberger, R. Berger, A. & Herweg, M. (2017). Journal of Structural Geology, 94, 47-67.

Wintsch, R.P., Christoffersen, R. & Kronenberg, A.K. (1995). Fluid-rock reaction weakening of fault zones. Journal of Geophysical Research, 100(B7), 13021-13032.

Withney, D., & Evans, B. (2010). Abbreviations for names of rock-forming minerals. American Mineralogist, 95, 185-187.

Yuguchi, T., Sasao, E., Ishibashi, M. & Nishiyama, T. (2015). Hydrothermal chloritization processes from biotite in the Toki granite, Central Japan: Temporal vairations of the composition of hydrothermal fluids associated with chloritization. American Mineralogist, 100, 1134-1152.

SUPPORTING INFORMATION

Additional Supporting Information may be found online in the supporting information tab for this article.

Description Supinfo.doc/x

Appendix S1. Analytical methods for geochronology and monazite analysis

920 **Figure S1.** Example of location of laser spot for zircon, anatase and titanite dating.

921 **Figure S2.** Tera-Wasserburg diagrams for all analysed anatase, titanite and zircon. Concordia-

922 discordia diagrams for zircon.

923 Dataset.xls/x

924 **Table S1.** Rapresentative chemical composition of chlorite and white mica.

925 **Table S2.** Representative chemical composition of monazite in samples ZA16-98 and ZAL18-

926 11.

927 **Table S3.** Original istopic data for zircon, titanite and anatase. Graphs represents weighted

928 mean zircon ages.

929

930 **FIGURE CAPTION**

931 **Figure 1** Geological maps and cross section. (a) Schematic structural map of the Pyrenees,

932 modified from Román-Berdiel, Casas, Oliva-Urcia, Pueyo, and Rillo, 2004. Red square: Bielsa,

933 N: Néouvielle, M: Maladeta, J: Jau. (b) Schematic structural cross section of the Axial Zone

934 (modified from Jolivet et al., 2007). Yellow stars indicate limits of the area where pervasive

935 alteration of the original granite has been documented. Black rectangle denotes the studied area.

936 (c) Geological map of the studied area. (d) Cross sections along transects AA' and BB'.

937

938 **Figure 2** Field structures around Lake Urdiceto. (a) Mylonitic corridor along the transect BB'

939 of Figure 1c. White: schistosity (S), yellow: shear planes (C). (b) Second example of mylonitic

940 corridor a few hundred meters eastward of transect BB', at the contact with the Triassic

941 sediments. Schistosity (S, filled white lines) is subparallel to S-dipping shear planes (C, marked

942 in yellow) due to high strain. (c) Mylonitic bands within the basement with C planes varying

943 from S-dipping to N-dipping. (d) N-dipping shear planes in a mylonite at the contact between

the basement and the sedimentary cover. (e) Enlarged view of mylonitic granite (see panel a for location). (f) Enlarged view of weakly deformed (but altered) granite (see panel a for location).

Figure 3 Field structures in the Triassic sediments. (a) Unconformity between the basement and the Triassic sediments. (b) Chlorite-quartz bearing veins at the contact between the basement and the basal breccia in the Triassic sediments. (c) Two generations of chlorite-quartz bearing veins within Triassic sandstones and pelites.

Figure 4 Photomicrographs (a, c, e and g) and backscattered electron images (BSE) (panels b, d, f and h) of granitic basement with increasing deformation. Abbreviations are from Whitney & Evans (2010), except Wm: white mica; (a) Undeformed but altered granite; (b) BSE image of a Chl + Wm + Ttn pseudomorph after Bt; (c) weakly deformed and altered granite with dark Chl-Wm pseudomorphs after Bt folded to form kink bands; (d) BSE images of a kinked Chl flake; (e) weakly deformed sample with opening fractures. Chlorite flakes are cross cut by secondary mm-size fractures. (f) BSE image of a Chl + Ttn flake after Bt (Bt relicts still visible), cross cut by a fracture filled with secondary chlorite; (g) mylonite; (h) folded Chl + Wm + Ant flake cross cut by a secondary fracture in a highly deformed sample. Two types of anatase grains are recognized.

Figure 5 Backscattered images of accessory minerals in the granitic basement. (a) and (b) magmatic Ilm breaking down to Ant + Cal, then to Ttn. (c) Anatase 1 folded within a Chl flake and replaced by Ttn. (d) Magmatic zircon (core) with metamict rims (low CL intensity) in sample ZA16-119. (e) Chlorite flakes (ChlA) with type-1 Ant cross cut by ChlB-bearing fractures with type-2 Ant (sample ZA16-73). (f) Type-2 Ant rimming titanite after anatase

(type-1 Ant, preserved in the core of titanite). (g) Chlorite flake (ChlA) in sample ZA16-79 with both types of anatase. (h) Relationships between titanite and anatase in sample ZA16-128. (i) Monazite in sample ZA16-98. The inset image shows the patchy and porous aspect of the monazite grains. (j) Monazite in reaction halos around fractures in sample ZA16-88.

Figure 6 Macro- and micro-scale petrography of the Triassic sediments. (a) Hand sample collected at the boundary between sediments and the granitic basement (ZAL18-11). (b) Backscattered electron image of panel a, showing the occurrence of anatase, Fe-oxides and Mnz within neocrystallized Chl and Wm. The inset show the patchy texture of monazite grains. (c) Chlorite-bearing veins and shear planes forming 'en-echelon' microstructures in sample ZA16-12. (d) Two generations of chlorite (in veins and shear planes) in samples ZA16-12 (zoom of panel c). ChlA and ChlB refer to chlorite flakes and chlorite in fractures/veins respectively but may be different in origin to ChlA and ChlB observed in the basement.

Figure 7 Chemical composition of chlorite. (a) Quantified SEM map of Al_2O_3 content in chlorite in sample B10-31 (mylonite). (b) Quantified SEM map of FeO content in chlorite of sample ZA16-82 (fractured sample). (c) Elementary Al vs Mg (%) content of all analysed chlorites; (d) Trends and compositional groups identified in chlorite in samples collected east of Lake Urdiceto; (e) Trends and compositional groups identified in chlorite in samples collected west of Lake Urdiceto.

Figure 8 Chemical composition of white mica. (a) Compositional triangular plot and trends for white mica in the basement. (b) Compositional ternary diagram of white mica in the sedimentary samples. Mus: muscovite, Cel: celadonite, Pyr: pyrophillite.

Figure 9 Thermobarometric results. (a) Chlorite temperatures calculated with the method of Vidal et al. (2006) (circles) and Bourdelle et al. (2013) (rectangles). (b) Monte Carlo simulation for the temperature dataset calculated for basement chlorite (3000 iterations, see the text for details). (c) Pressure range estimated from the celadonite content in white mica, following the calibration of Massonne and Schreyer (1988). This calibration does not consider the pyrophillite content in white mica, as it is the case in the Bielsa granite. Pressure values should therefore be considered as minimum values.

Figure 10 Geochronology results. (a) Representative Tera-Wasserburg concordia lower intercept age defined by titanite analyses in an undeformed sample (ZA16-84). (b) Tera-Wasserburg Concordia lower intercept ages defined by various anatase populations (red: old, blue: young) in a deformed sample (ZA16-128). (c) Frequency distribution of monazite ages. Note that youngest monazite ages are estimated from Pb depleted domains (Pb < EPMA detection limits of ~100 ppm) and monazite-thorite domains (see the text for details). Note the ages calculated for domains where Pb is below the EPMA detection limit are maximum ages. (d) Summary of geochronological results (this study) integrated with previously published data for metamorphic events in the Axial zone. U-Pb Ant-Ttn indicate the ages obtained for analysis where a titanite locally preserved anatase cores (type-1 Ant, see the text for details). (e) U and Th content of monazite in sample ZAL18-11. (f) Probability density plot of all zircon ages for samples ZA16-84 and ZA16-119 (2σ error).

Table 1 Summary of sample descriptions and ages.

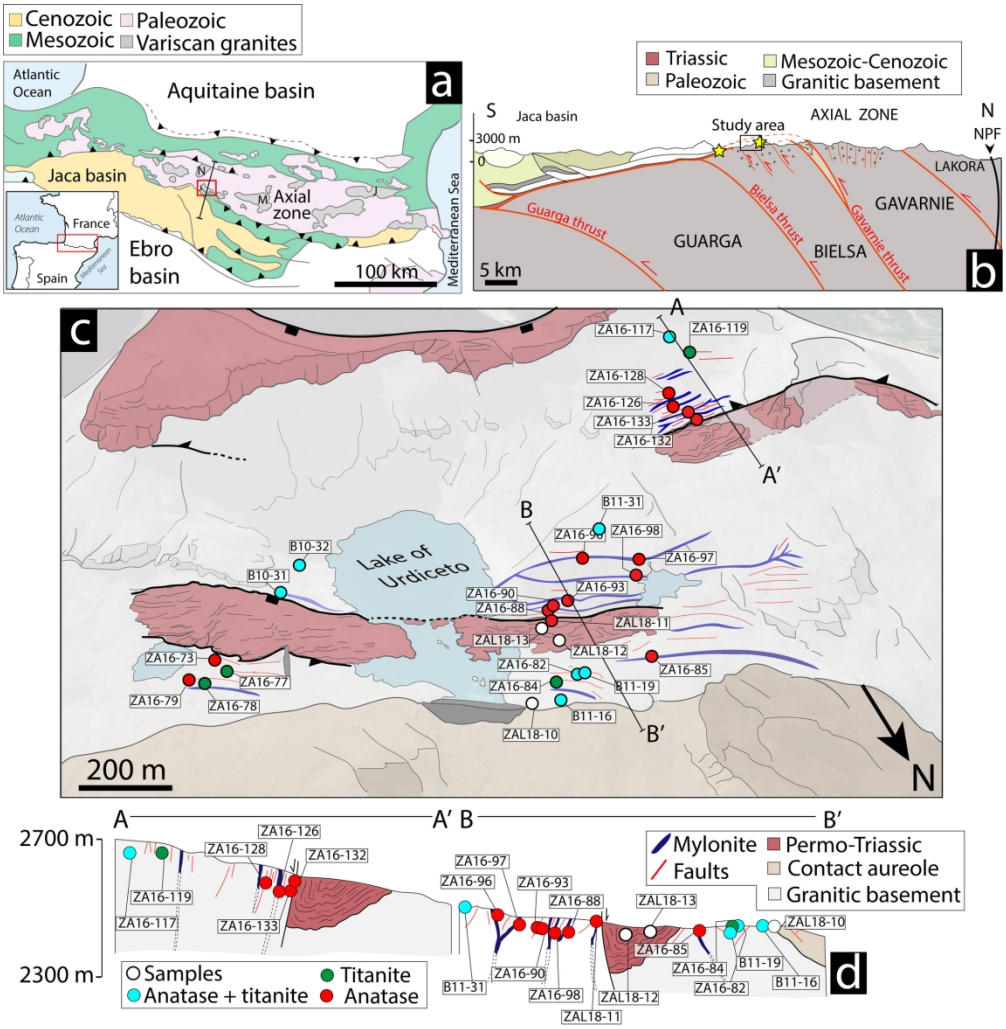

Figure 1. Geological maps and cross section of the studied area

185x189mm (300 x 300 DPI)

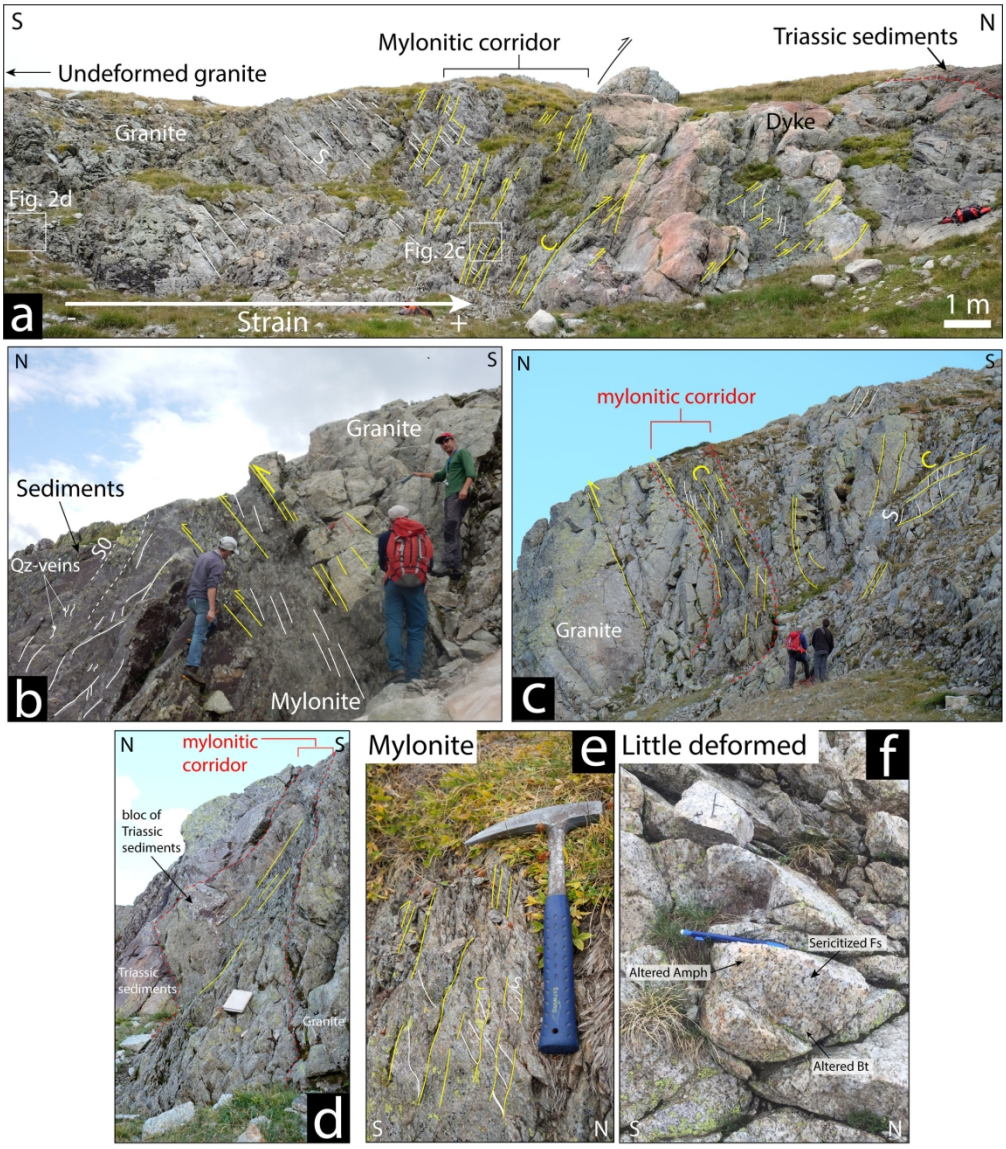

Figure 2. Field relationships within the cristalline basement

180x207mm (300 x 300 DPI)

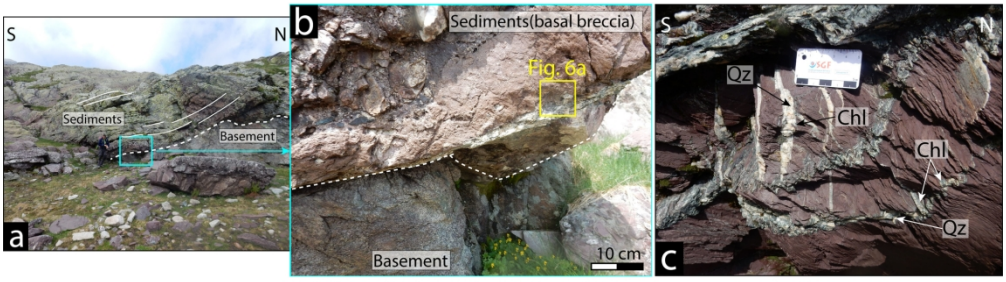

Figure 3. Field relationships within the Triassic sediments

190x53mm (300 x 300 DPI)

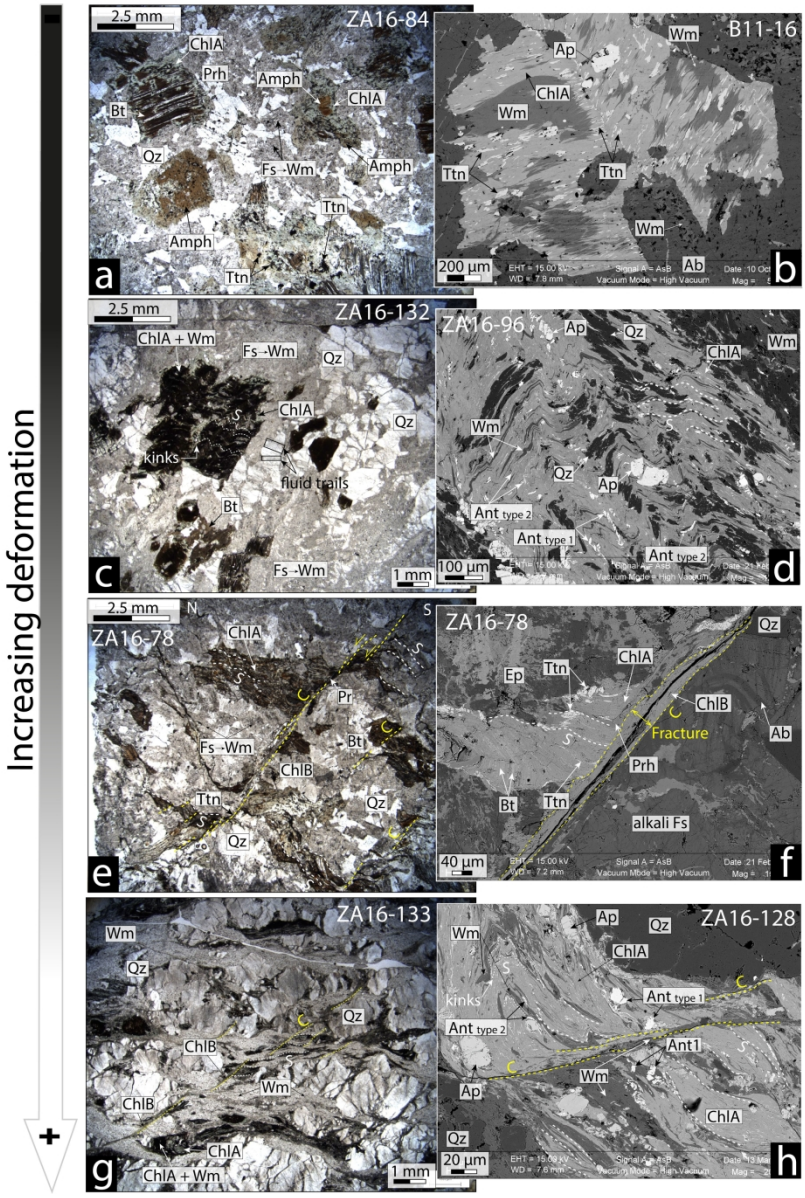

Figure 4. Microphotographs (optical microscope and SEM) of differently deformed granodioritic samples

204x305mm (300 x 300 DPI)

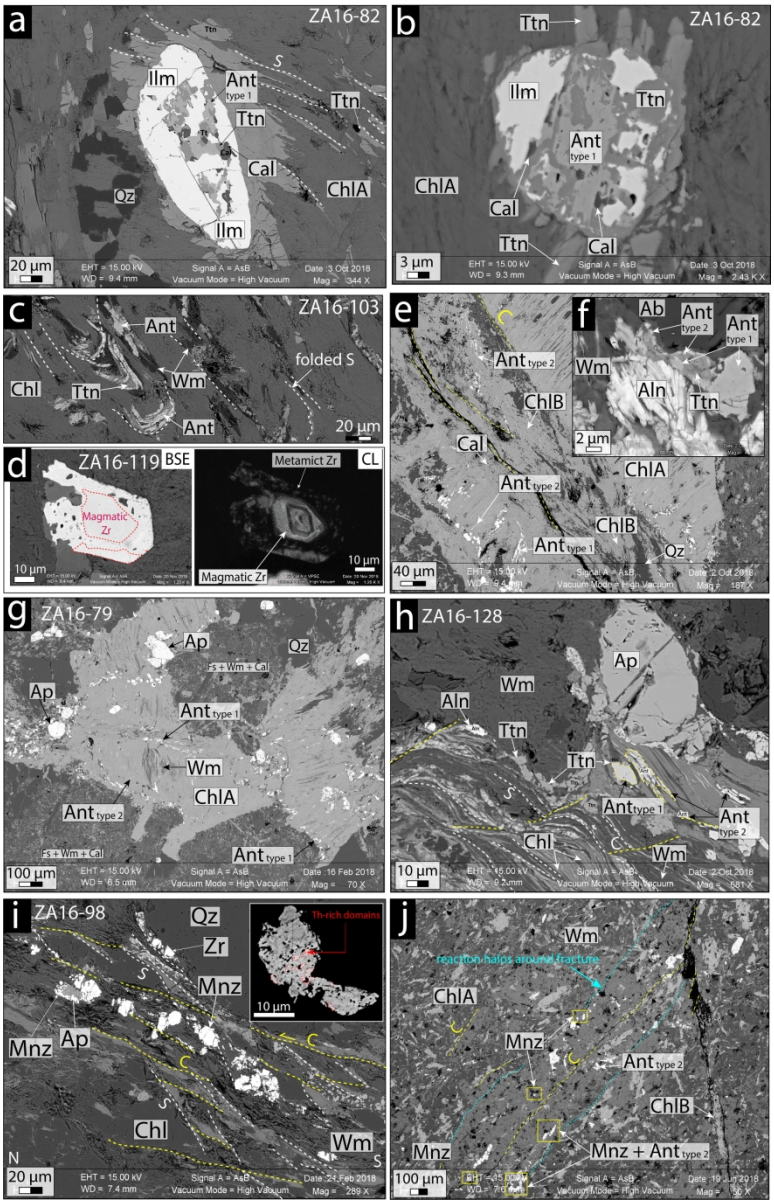

Figure 5. SEM images of accessory minerals in the granodiorite

187x292mm (300 x 300 DPI)

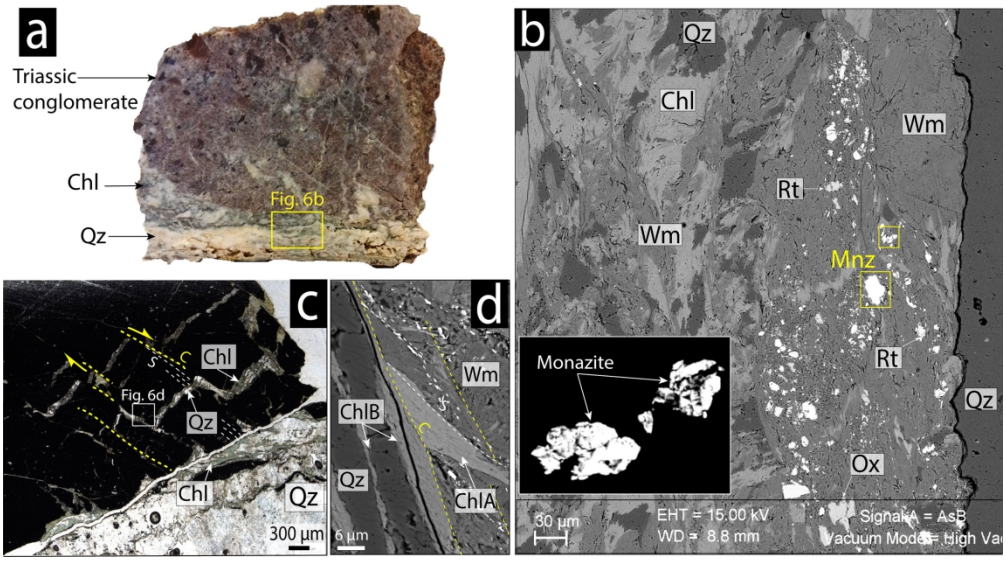

Figure 6. Microviews of Triassic sediments

197x110mm (300 x 300 DPI)

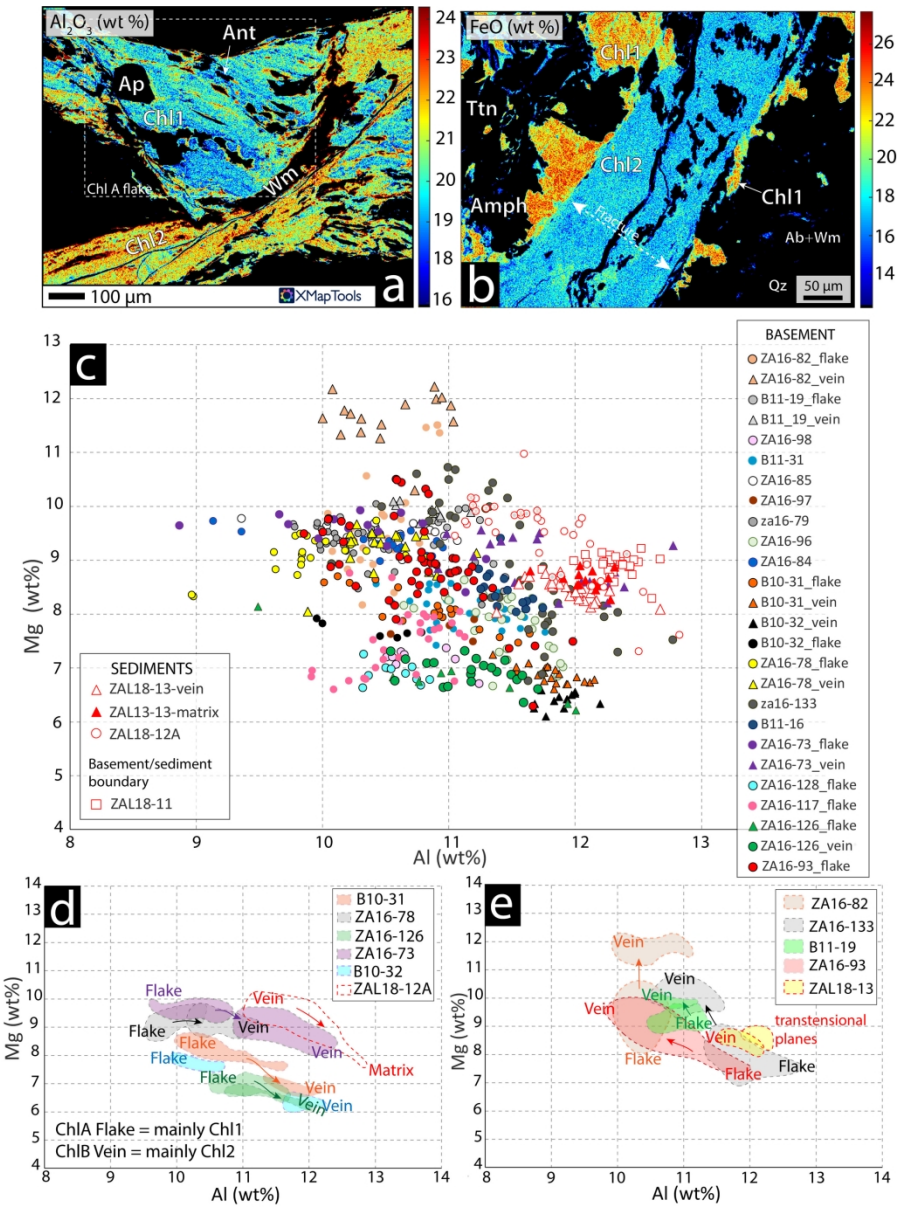

Figure 7. Chlorite chemical composition

189x254mm (300 x 300 DPI)

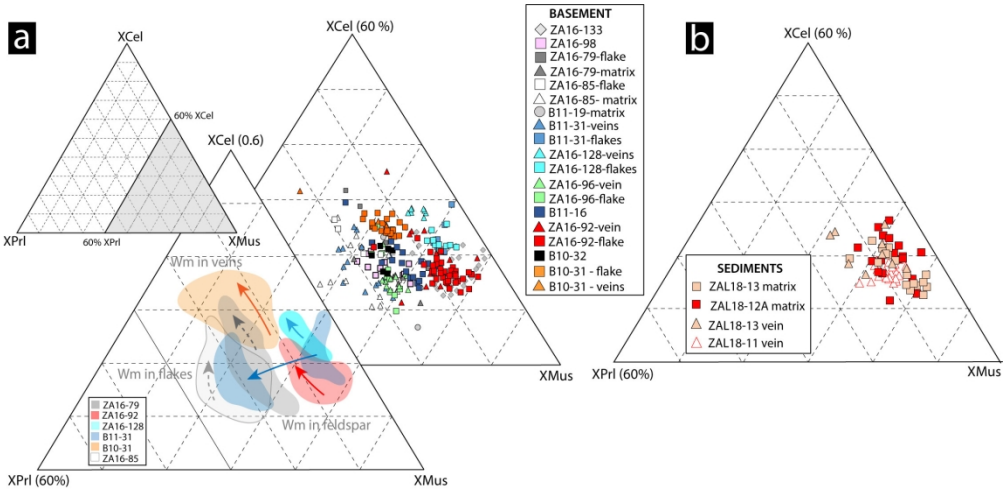

Figure 8. White mica chemical composition

190x92mm (300 x 300 DPI)

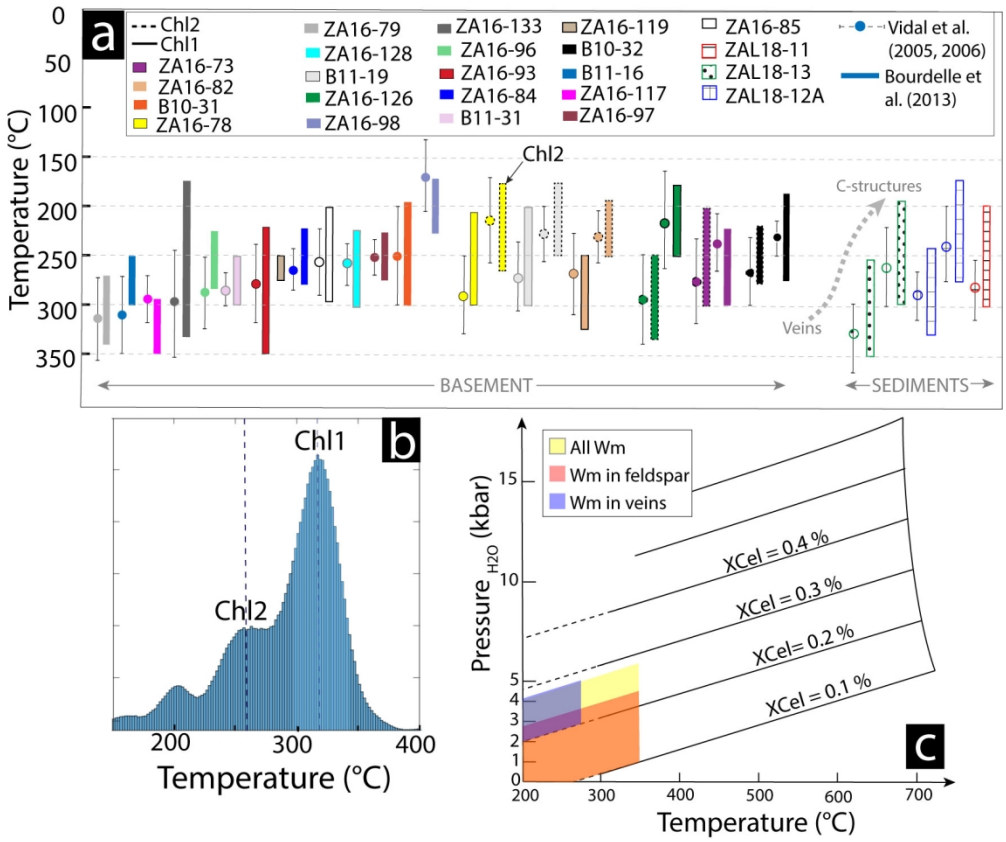

Figure 9. Thermobarometry

149x125mm (300 x 300 DPI)

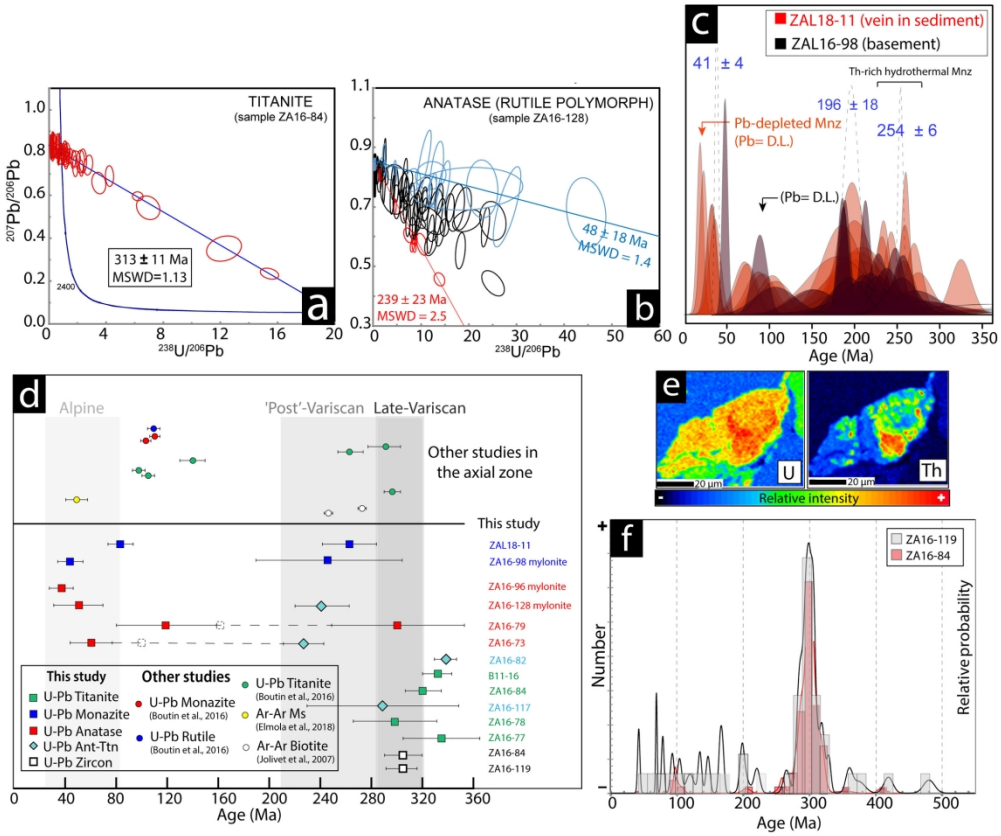

Figure 10. Geochronological results

189x166mm (300 x 300 DPI)

Sample	Deformation	Ttn age (Ma)	Ant age (Ma)	Mnz age (Ma)	Zr age (Ma)	Comments
B11-16	undeformed	336 ± 12				
ZA16-119	undeformed				310 ± 20 285-291 (?)	Metamict zircon domains
ZA16-117	undeformed	337 ± 20 293 ± 59				Relicts of anatase in titanite
ZA16-84	undeformed	313 ± 11			300 ± 10	
ZA16-77	little deformed	337 ± 34				
ZA16-79	distributed to discretely deformed		301 ± 56 120 ± 39			Difficult distinction between two anatase age populations
ZA16-82	discretely deformed	339 ± 7				Relicts of anatase in titanite
ZA16-78	discretely deformed	303 ± 36				Titanite only
ZA16-73	discretely deformed		221 ± 19 60 ± 18			
ZA16-128	discretely deformed to mylonite		239 ± 23 48 ± 18			
ZA16-96	mylonite		39 ± 8			Low variability of initial Pb
ZA16-98	(proto-)mylonite			254 ± 6 < 50		Ages < 100 Ma for Pb < D.L. Ages < 50 Ma for Mnz-Thr
ZA16-11	Triassic sediment			196 ± 18 < 20		Ages < 20 Ma for Pb < D.L.

Table 1 Summary of sample characteristic and ages.

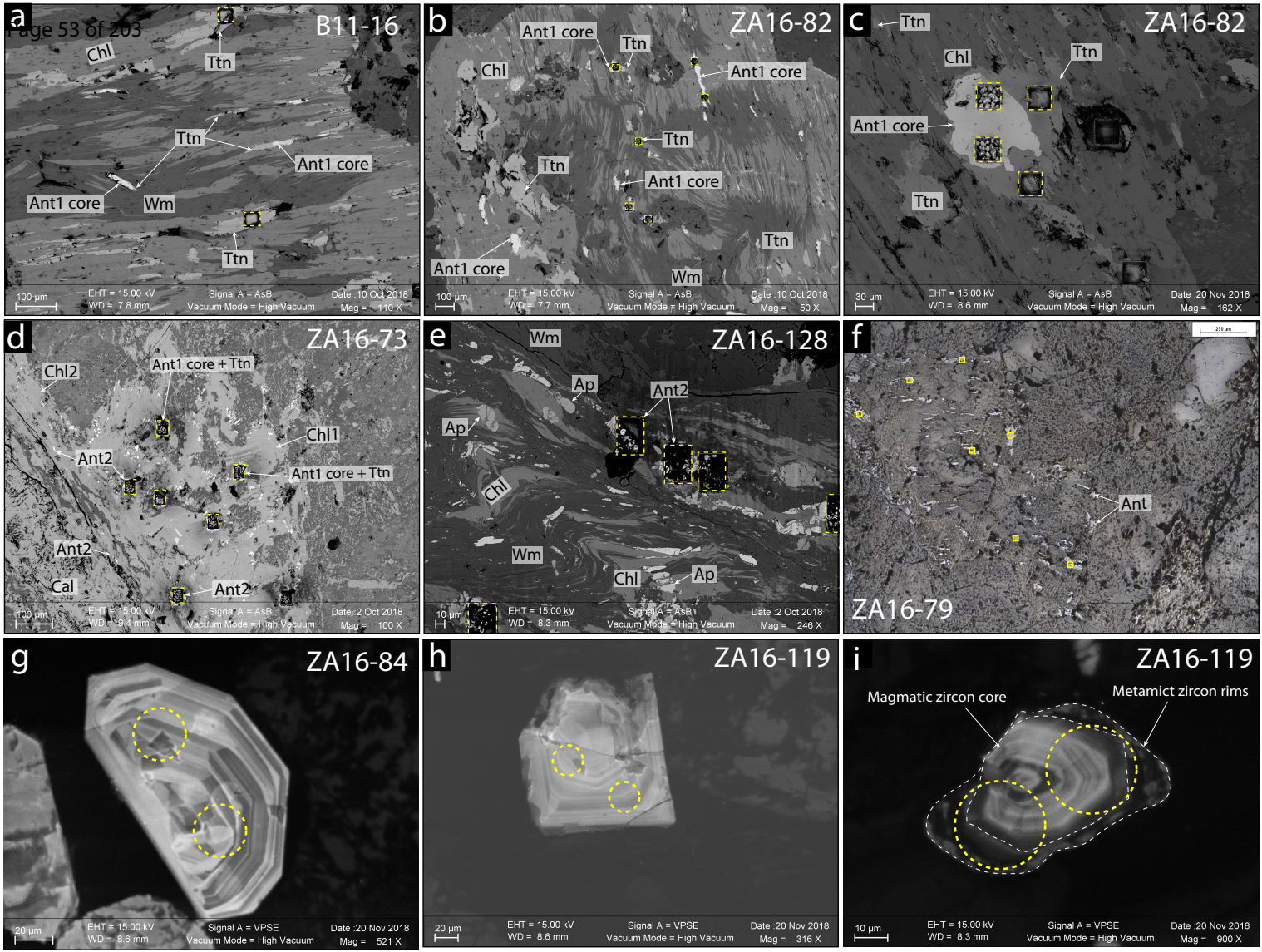

Figure S1. Examples of the location of the laser spots for dating on BSE images (a-e, g-i) and under reflected light (f). Laser spot location is indicated by the yellow dashed square (anatase and titanite) or circle (zircon).

TITANITE

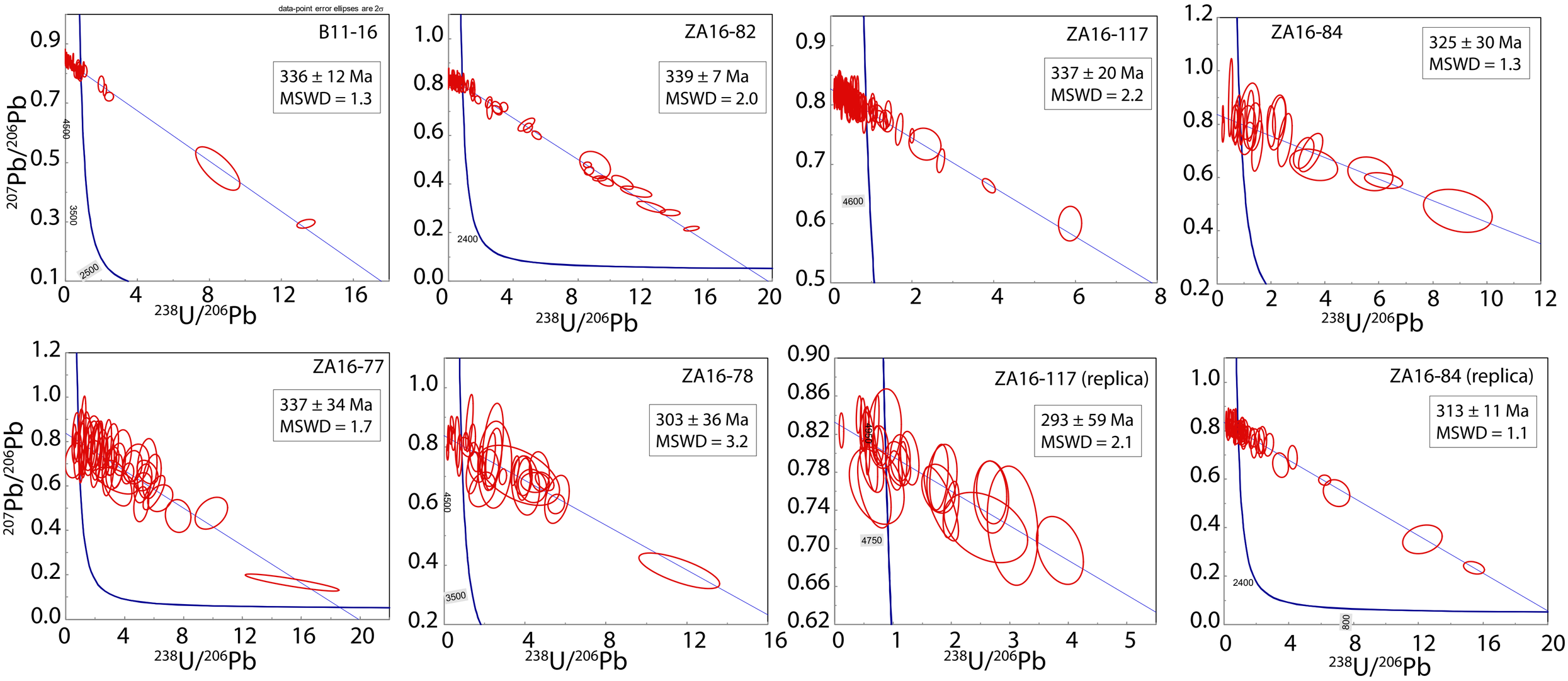

ANATASE

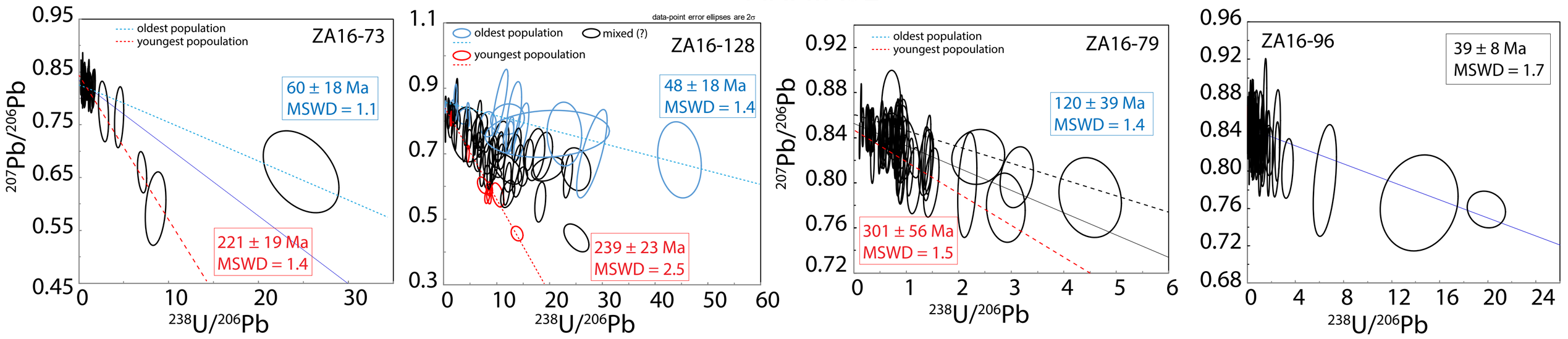

ZIRCON

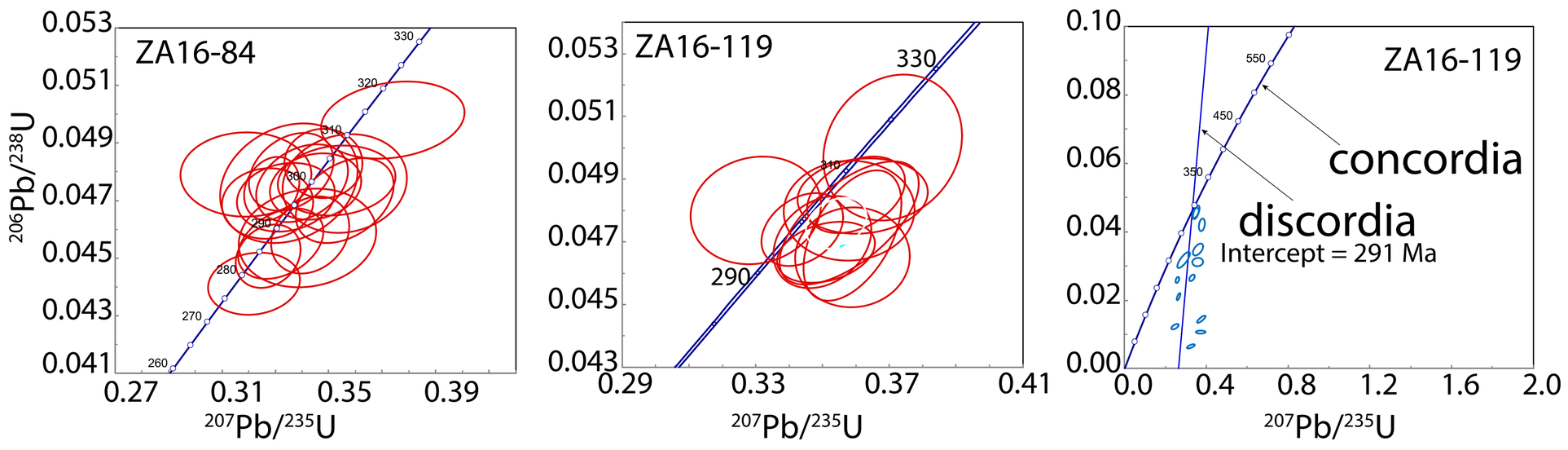

Fig. S1. Tera-Wasserburg diagrams for dated titanite and anatase, concordia diagrams for zircon.

Appendix S1. Analytical methods for geochronology and monazite analysis

1. Protocol used for monazite EPMA compositional analysis

Monazite was analyzed by electron probe micro-analysis (EPMA) with a JEOL JXA-8230 instrument at the Institute des Sciences de la Terre (ISTerre, Grenoble) on thin sections coated with a 55-60 nm thick layer of carbon to avoid material degradation during analysis at high beam current (Montel et al., 2011). Standards were coated in the same way. For the point analyses, the acceleration voltage was set at 15 keV with a spot beam size and a beam current of 200 nA. The duration of each analysis was ~9 minutes. During this exposure time, the evolution of the absorbed current was negligible (< 5 nA).

Quantitative analyses were carried out using the X-ray lines: SiKα, UMβ, ThMα, CaKα, PKα, YLα, DyLβ, GdLβ, SmLβ, PrLβ, NdLα, CeLα, LaLα, PbMβ. Background positions were carefully selected with high sensitivity wavelength scans before and after the element signal. The background value for each line was estimated by linear interpolation. A calibrated overlap correction of 0.0079 was applied for peak interference of ThMα on UMβ. A standard monazite (Madagascar, Paquette et al., 2007) was analyzed before and after the unknown analyses of the target (5 points each time) to track possible instrumental drift and to verify the consistency of the age calculated for the monazite grains. Other standards used were ThO_2 for thorium, UO_2 for uranium and crocoite ($PbCrO_4$) for lead. ZAF correction procedure was applied using the JEOL software for quantitative analysis. EPMA X-rays maps of monazite grains was done for Si, U, Th, Ca using an acceleration voltage of 15kV, a beam current of 100 nA with a focused beam and a counting time per pixel of 500 ms.

U, Th and Pb contents were measured with counting time (peak plus background) of 480s for Pb, 300s for U and 160s for Th. The detection limit associated were 90 ppm for Pb, 120 ppm for U and 115 ppm for Th. For each monazite analysis, a chemical U-Th-Pb age was determined (Montel et al., 1996). Ages obtained for the standard monazite Madagascar cluster around 552

± 4 Ma. Monazite analyses in studied samples were divided into populations on the base of their composition (e.g. ThO_2 content, see the main text for details). The average age of each population was calculated using the software NiLeDAM (Seydoux-Guillaume et al., 2012).

2. U/Pb geochronology: titanite, rutile and zircon standards

Titanite and anatase (rutile polymorph) were dated *in-situ* by the U-Pb LA-ICP-MS technique at Trinity College, Dublin (Ireland). U-Pb ages were determined using a Photon Machines Analyte Exite 193 nm ArF Excimer laser-ablation system with a Helex 2-volume ablation cell coupled to an Agilent 7900 ICPMS. The ICPMS was tuned using NIST 612 standard glass to yield Th/U ratios of unity and low oxide production rates (ThO^+/Th^+ typically <0.15%). 0.15 l/min He carrier gas was fed into the cell body and 0.25 l/min He was fed into the cup. The aerosol was subsequently mixed with 0.6 l/min Ar make-up gas and a small volume of N_2 (ca. 10 ml/min) in a c. 1 cm^3 signal smoothing device to enhance signal sensitivity and reduce oxide formation. NIST612 was used as the trace element primary standard for titanite, rutile and zircon. For titanite analysis, OLT-1 (Kennedy et al., 2010) was used as the primary standard for titanite geochronology (published TIMS ages of 1014.8 ± 2 Ma, obtained age of 1018 ± 5 ma) while MKED (Spandler et al., 2016) was used as a secondary age standard (TIMS age of 1517.3 ± 0.3, obtained age of 1541 ± 8 Ma). The trace elements analysed were: ^{90}Zr, ^{139}La, ^{51}V, ^{93}Nb, ^{43}Ca, ^{153}Eu, ^{157}Gd, ^{202}Hg, ^{204}Pb, ^{206}Pb, ^{207}Pb, ^{208}Pb, ^{232}Th, ^{238}U, ^{172}Yb, ^{147}Sm, ^{181}Ta. For analysis of rutile polymorphs, rutile R10 (Luvizotto et al., 2009) was used as the primary standard (U-Ob TIMS age of 1090 Ma, obtained age of 1089 ± 5 Ma). Rutile R19 (TIMS age of 489.5 ± 0.9 Ma, obtained age of 491 ± 11) and PCA-S207 rutile (age of 1865.0 ± 7.5 Ma, obtained age of 1921 ± 36) was used as secondary standards (Zack et al., 2011; Bracciali et al., 2013). The trace elements analyzed were Al, ^{43}Ca, ^{49}Ti, ^{24}Mg, ^{51}V, ^{52}Cr, ^{57}Fe, ^{89}Y, ^{90}Zr, ^{93}Nb, ^{118}Sn, ^{121}Sb, ^{181}Ta, ^{182}W, ^{202}Hg, ^{204}Pb, ^{206}Pb, ^{207}Pb, ^{208}Pb, ^{232}Th and ^{238}U. For zircon analysis

the primary standard employed was zircon 91500. The zircon age standards WRS1348 (TIMS age of 526.26 ± 0.70, obtained age of 523.4 ± 2.1 Ma), Plesovice and Temora-2 (TIMS age of 416.8 ± 1.3, obtained age of 416.5 ± 2.6 Ma) were used as secondary age standards (Chew et al, 2019 and references therein). The trace elements analysed were: ^{49}Ti, ^{90}Zr, ^{202}Hg, ^{204}Pb, ^{206}Pb, ^{207}Pb, ^{208}Pb, ^{232}Th and ^{238}U. Three of each standard were analysed under the same conditions as the unknowns, with each block of unknowns comprising 20-30 analyses.

The raw titanite and rutile isotope data were reduced using the "VizualAge UcomPbine" data reduction scheme (DRS) of Chew et al. (2014), a modification of the U-Pb geochronology "VizualAge" DRS of Petrus & Kamber (2012) that can account for the presence of variable common Pb in the primary standard materials. The "VizualAge" DRS was employed for zircon data reduction. Both DRSs runs within the freeware IOLITE package of Paton et al. (2011). In IOLITE, user-defined time intervals are established for the baseline correction procedure to calculate session-wide baseline-corrected values for each isotope. The time-resolved fractionation response of individual standard analyses is then characterised using a user-specified down-hole correction model (such as an exponential curve, a linear fit or a smoothed cubic spline). The VizualAge data reduction scheme then fits this appropriate session-wide "model" U-Th-Pb fractionation curve to the time-resolved standard data and the unknowns. Sample-standard bracketing is applied after the correction of down-hole fractionation to account for long-term drift in isotopic or elemental ratios by normalizing all ratios to those of the U-Pb reference standards. Common Pb in the titanite and rutile standards was corrected using the ^{207}Pb-based correction method.

3. References

Black, L. P., Kamo, S. L., Allen, C. M., Aleinikoff, J. N., Davis, D. W., Korsch, R. J. & Foudoulis, C. (2003). TEMORA 1: A new zircon standard for Phanerozoic U-Pb geochronology. Chemical Geology, 200, 155-170.

Bracciali, L., Parrish, R. R., Horstwood, M. S. A., Condon, D. J., & Najman, Y. (2013). U-Pb LA-(MC)-ICP-MS dating of rutile: New reference materials and applications to sedimentary provenance. Chemical Geology, 347, 82-101.

Chew, D., Drost, K. & Petrus, J. A. (2019). Ultrafast, > 50 Hz LA-ICP-MS Spot Analysis Applied to U-Pb Dating of Zircon and other U-Bearing Minerals. Geostandards and Geoanalytical Research, 43(1), 39-60.

Chew, D., Petrus, J.A. & Kamber, B.S. (2014). U–Pb LA–ICPMS dating using accessory mineral standards with variable common Pb. Chemical Geology, 363 185–199

Kennedy, A.K., Kamo, S.L., Nasdala, L., Timms,N.E., 2010. Grenville Skarn Titanite: potential reference material for SIMS U–Th–Pb analysis. Can. Mineral. 48 (6), 1423–1443.

Luvizotto, G.L., Zack, T., Meyer, H.P., Ludwig, T., Triebold, S., Kronz, A., Münker, C., Stockli, D.F., Prowatke, S., Klemme, S., Jacob, D.E., von Eynatten, H., 2009. Rutile crystals as potential trace element and isotope mineral standards for microanalysis. Chem. Geol. 261 (3-4), 346–369.

Montel, J.-M., Foret, S., Veschambre, M., Nicollet, C. & Provost, A. (1996). Electron microprobe dating of monazite. Chemical Geology, 131, 37-53.

Montel, J.M., Razafimahatratra, D., Ralison, B., De Parseval, P., Thibault, M. & Randranja, R. (2011). Monazite from mountain to ocean: a case study from Trolognaro (Fort-Dauphin), Madagascar. *European Journal of Mineralogy* **23**(5), 745-757.

Paquette, J. L. & tiepolo, M. (2007). High resolution (5 µm) U-Th-Pb isotope dating of monazite with excimer laser ablation (ELA)-ICPMS, Chemical Geology, 240(3-4), 222-237.

Pointon, M. A., Cliff, R. A. & Chew, D. M. (2012). The provenance of Western Irish Namurian Basin sedimentary strata inferred using detrital zircon U-Pb LA-ICP-MS geochronology. Geological Jounral, 47, 77-98.

Seydoux-Guillaume, A.-M., Montel, J.-M., Bingen, B., Bosse, V., de Parseval, P., Paquette, J.-L., Janots, E. & Wirth, R. (2012). Low-temperature alteration of monazite : Fluid mediated coupled dissolution-preciputation, irradiation damage and disturbance of the U-Pb geochronology. Chemical Geology, 330-331, 140-158.

Spandler, C., Hammerli, J., Sha, P., Hilbert-Wolf, H., Hu, Y., Roberts, E. & Schmitz, M. (2016). MKED1: A new titanite standard for in situ analysis of Sm-Nd isotopes and U-Pb geochronology. Chemical Geology, 425, 110-126.

Zack, T., Stockli, D. F., Luvizotto, G. L., Barth, M. G., Belousova, E., Wolfe, M. R. & Hinton, R. W. (2011). In situ U-Pb rutile dating by LA-ICP-MS: Pb-208 correction and prospects for geological applications. Contributions to Mineralogy and Petrology, 162, 515-530.

Sample	ZA16-82		B11-19			ZA16-98			B11-31			ZA16-85			ZA16-97
Lat/Long	42°40'7.3"N/0°16'43.3"E		42°40'6.9"N/0°16'42.9"E			42°40'2.3"N/0°16'31.3"E			42°39'51.7"N/0°16'9.3"E			42°40'6.1"N/0°16'40.6"E			42°40'0.9"N/0°16'32.4"E
Deformation	Discretely deformed		Discretely deformed			Mylonite			Mylonite			Distributed deformation			Mylonite
Mineral	Chl1	Chl2	Chl1	Chl2	Wm1	Chl	Wm2	Wm1	Chl	Wm2	Wm1	Chl	Wm2	Wm1	Chl
Oxides															
SiO2	27,60	28,37	26,80	27,74	47,62	25,65	48,08	47,50	28,28	48,70	47,43	27,41	48,66	47,39	27,09
TiO2	0,07	0,05	0,09	0,02	0,02	0,11	0,17	0,02	0,17	0,16	0,15	0,12	0,06	0,20	0,02
Al2O3	19,81	20,57	19,82	20,76	35,97	20,07	32,35	32,42	21,25	33,60	32,27	18,96	34,52	32,82	20,80
FeO	23,85	17,85	24,46	22,58	1,01	29,04	2,27	0,93	22,08	1,39	2,60	24,49	1,30	2,46	27,96
MnO	0,52	0,43	0,32	0,30	0,04	0,45	0,06	0,01	0,33	0,05	<D.L.	0,51	<D.L.	0,04	0,34
MgO	16,28	20,26	15,27	15,92	0,78	12,10	1,58	1,11	13,70	1,28	1,40	15,98	1,15	1,92	12,90
CaO	0,09	0,10	0,09	0,11	0,06	0,07	0,09	0,07	0,13	0,04	0,05	0,05	0,08	0,08	0,04
Na2O	0,07	0,02	0,05	<D.L.	0,19	0,01	0,16	0,32	0,04	0,16	0,24	0,02	0,41	0,42	0,03
K2O	0,08	0,02	0,03	0,01	9,31	0,06	8,75	9,30	1,03	9,17	10,32	0,03	8,35	8,96	0,02
Total	*88,38*	*87,67*	*86,93*	*87,44*	*95,02*	*87,56*	*93,52*	*91,68*	87,03	94,55	94,47	87,64	94,52	94,30	89,21
Cations															
Si	2,81	2,82	2,83	2,87	3,13	2,72	3,23	3,24	2,89	3,22	3,20	2,83	3,20	3,17	2,79
Ti	0,01	0,03	0,01	0,00	<D.L.	0,01	0,01	0,00	0,01	0,01	0,01	0,01	0,00	0,01	0,00
Al	2,38	2,33	2,47	2,53	2,79	2,51	2,56	2,61	2,56	2,62	2,56	2,31	2,68	2,59	2,52
FeTOT	1,97	1,52	2,16	1,96	0,06	2,51	0,13	0,05	1,81	0,08	0,15	2,05	0,07	0,14	2,35
Mn	0,05	0,03	0,03	0,03	0,00	0,04	0,00	0,00	0,03	0,00	0,00	0,04	0,00	0,00	0,03
Mg	2,47	2,85	2,41	2,46	0,08	1,91	0,16	0,11	2,09	0,13	0,14	2,46	0,11	0,19	1,98
Ca	0,01	0,04	0,01	0,01	0,00	0,01	0,01	0,00	0,01	0,00	0,00	0,01	0,01	0,01	0,00
Na	0,01	0,01	0,01	0,00	0,02	0,00	0,02	0,04	0,01	0,02	0,03	0,00	0,05	0,06	0,01
K	0,01	0,00	0,00	0,00	0,78	0,01	0,75	0,81	0,13	0,77	0,89	0,00	0,70	0,77	0,00
Oxygens	*14*	*14*	*14*	*14*	*11*	*14*	*11*	*11*	14	11	11	14	11	11	14
XMg	*0,63*	*0,78*	*0,62*	*0,65*	*0,58*	*0,50*	*0,55*	*0,68*	*0,65*	*0,62*	*0,49*	*0,62*	*0,61*	*0,58*	*0,52*
AlVI	*1,20*	*1,18*	*1,31*	*1,41*	-	*1,24*	-	-	*1,46*	-	-	*1,15*	-	-	*1,31*
Octahedral sum	*5,69*	*5,58*	*5,81*	*5,76*	-	*5,71*	-	-	*5,39*	-	-	*5,71*	-	-	*5,67*
Xceladonite	-	-	-	-	*0,07*	-	*0,17*	*0,14*	-	*0,14*	*0,21*	-	*0,10*	*0,19*	-
Xmuscovite	-	-	-	-	*0,74*	-	*0,62*	*0,68*	-	*0,67*	*0,69*	-	*0,64*	*0,62*	-
Xpyrophyllite	-	-	-	-	*0,17*	-	*0,18*	*0,14*	-	*0,18*	*0,07*	-	*0,21*	*0,14*	-

Chl1 flake

Chl2 veins

Wm1: in flakes or feldspar

Wm2: in the matrix/shear planes

Discretely deformed = fractures

Sample	**ZA16-84**	**ZA16-96**			**ZA16-79**			**B10-31**			**B10-32**			**ZA16-78**	
Lat/Long	42°40'7.3"N/0°16'43.3"E	42°39'59.1"N/0°16'35.1"E			42°39'58.9"N/0°17'8.95"E			42°39'49.2"N/0°17'4.4"E			42°39'46.3"N/0°17'2.0"E			42°39'59.4"N/0°17'8.5"E	
Deformation	Undeformed	Mylonite			Distributed deformation			Mylonite			Mylonite			Discretely deformed	
Mineral	Chl	Chl	Wm1	Wm2	Chl1	Wm1	Wm2	Chl1	Chl2	Wm	Chl1	Chl2	Wm	Chl1	Chl2
Oxides															
SiO2	29,59	27,14	48,35	49,23	26,72	44,97	47,78	27,37	26,78	49,30	27,64	26,72	49,67	28,60	27,42
TiO2	1,56	<D.L.	0,10	0,22	0,21	0,11	0,14	0,24	0,01	0,06	0,02	0,02	0,04	0,69	0,03
Al2O3	17,68	21,02	33,96	32,92	18,81	34,68	33,46	19,12	22,67	31,82	18,81	22,51	32,45	18,58	20,61
FeO	22,98	24,78	1,78	1,04	23,93	2,79	1,34	26,67	28,07	3,43	29,36	29,05	2,19	23,99	24,34
MnO	0,32	0,90	0,03	0,04	0,31	0,04	0,00	0,42	0,53	0,02	0,21	0,18	<D.L.	0,35	0,51
MgO	15,79	14,30	1,20	1,37	15,97	1,76	1,43	14,42	10,86	2,64	13,12	10,36	1,63	14,93	14,44
CaO	0,53	0,04	0,03	<D.L.	0,04	0,07	0,10	0,03	0,05	0,03	0,03	0,05	0,07	0,15	0,11
Na2O	<D.L.	0,02	0,09	0,11	0,04	0,68	0,26	<D.L.	0,02	0,05	0,01	0,02	0,15	0,05	0,04
K2O	0,33	0,03	9,25	9,35	0,02	9,37	9,16	0,02	0,10	9,66	0,06	0,03	9,85	1,12	0,06
Total	88,86	88,23	94,78	94,32	86,09	94,48	93,67	88,30	89,10	97,01	89,28	88,92	96,04	88,46	87,55
Cations															
Si	2,98	2,80	3,20	3,26	2,81	3,03	3,20	2,83	2,77	3,23	2,88	2,75	3,26	2,91	2,83
Ti	0,12	0,00	0,00	0,01	0,02	0,01	0,01	0,02	0,00	0,00	0,00	0,00	0,00	0,05	0,00
Al	2,10	2,55	2,65	2,57	2,33	2,76	2,64	2,33	2,77	2,46	2,31	2,73	2,51	2,23	2,42
FeTOT	1,87	2,09	0,10	0,06	2,04	0,16	0,08	2,24	2,40	0,19	2,52	2,41	0,12	1,96	1,92
Mn	0,03	0,08	0,00	0,00	0,03	0,00	0,00	0,04	0,05	0,00	0,02	0,02	0,00	0,03	0,04
Mg	2,37	2,20	0,12	0,14	2,50	0,18	0,14	2,22	1,68	0,26	2,04	1,59	0,16	2,27	2,39
Ca	0,06	0,00	0,00	0,00	0,00	0,00	0,01	0,00	0,01	0,00	0,00	0,01	0,00	0,02	0,01
Na	0,00	0,00	0,01	0,01	0,01	0,09	0,03	-0,01	0,00	0,01	0,00	0,00	0,02	0,01	0,00
K	0,04	0,00	0,78	0,79	0,00	0,81	0,78	0,00	0,01	0,81	0,01	0,00	0,82	0,15	0,00
Oxygens	14	14	11	11	14	11	11	14	14	11	14	14	11	14	14
XMg	*0,65*	*0,56*	*0,55*	*0,70*	*0,63*	*0,53*	*0,66*	*0,58*	*0,45*	*0,58*	*0,48*	*0,49*	*0,57*	*0,65*	*0,67*
AlVI	*1,20*	*1,35*	-	-	*1,15*	-	-	*1,18*	*1,54*	-	*1,20*	*1,47*	-	*1,20*	*1,24*
Octahedral sum	*5,47*	*5,72*	-	-	*5,72*	-	-	*5,67*	*5,66*	-	*5,78*	*5,49*	-	*5,46*	*5,59*
Xceladonite	-	-	*0,13*	*0,15*	-	*0,16*	*0,14*	-	-	*0,25*	-	-	*0,20*	-	-
Xmuscovite	-	-	*0,68*	*0,66*	-	*0,69*	*0,67*	-	-	*0,60*	-	-	*0,64*	-	-
Xpyrophyllite	-	-	*0,18*	*0,18*	-	*0,08*	*0,16*	-	-	*0,14*	-	-	*0,14*	-	-

Sample	ZA16-133			B11-16		ZA16-73		ZA16-128			ZA16-117	ZA16-126	
Lat/Long	42°39'49.5"N/0°16'17.8"E			42°40'7.9"N/0°16'47.9"E		42°39'56.2"N/0°17'6.9"E		42°39'49.2"N/0°16'16.6"E			42°39'45.0"N/0°16'5.7"E	42°39'48.9"N/0°16'17.5"E	
Deformation	Mylonite			Undeformed		Discretely deformed		Mylonite			Undeformed	Mylonite	
Mineral	Chl1	Chl2	Wm	Chl	Wm	Chl1	Chl2	Chl	Wm1	Wm2	Chl	Chl1	Chl2
Oxides													
SiO2	26,33	27,03	48,67	26,45	49,43	28,33	26,92	26,51	48,97	48,58	26,33	26,02	28,67
TiO2	0,05	0,19	0,35	0,06	0,20	1,47	0,01	0,29	0,12	0,20	0,01	<D.L.	0,04
Al2O3	23,11	21,38	34,85	21,56	34,30	18,38	22,10	19,84	32,57	31,07	19,80	21,20	23,86
FeO	26,22	22,15	2,41	23,85	0,84	23,74	22,90	29,63	2,04	2,93	30,71	29,50	25,93
MnO	0,15	0,12	<D.L.	0,38	0,03	0,24	0,24	0,43	0,05	0,02	0,70	0,42	0,31
MgO	13,17	17,05	1,07	15,59	1,13	16,03	15,58	11,60	1,61	2,04	11,87	11,88	8,86
CaO	0,04	0,10	0,03	0,08	0,07	0,18	0,09	0,06	0,08	0,11	0,06	0,07	0,11
Na2O	0,05	0,07	0,22	<D.L.	0,14	0,01	0,01	<D.L.	0,13	0,12	0,03	0,02	0,03
K2O	0,02	0,04	10,55	<D.L.	10,07	0,23	<D.L.	0,11	10,73	10,75	0,04	<D.L.	1,80
Total	89,15	88,13	98,18	88,00	96,22	88,66	87,85	88,50	96,29	95,85	89,54	89,12	89,63
Cations													
Si	2,68	2,58	3,15	2,75	3,22	2,92	2,78	2,83	3,23	3,24	2,80	2,75	2,95
Ti	0,00	0,03	0,02	0,00	0,01	0,11	0,00	0,02	0,01	0,01	0,00	0,00	0,00
Al	2,63	2,51	2,66	2,64	2,63	2,24	2,69	2,50	2,53	2,44	2,48	2,64	2,90
FeTOT	1,93	2,06	0,13	2,07	0,05	2,05	1,98	2,65	0,11	0,16	2,73	2,61	2,23
Mn	0,01	0,01	0,00	0,03	0,00	0,02	0,02	0,04	0,00	0,00	0,06	0,04	0,03
Mg	2,57	2,53	0,10	2,42	0,11	2,47	2,40	1,85	0,16	0,20	1,88	1,87	1,36
Ca	0,01	0,01	0,00	0,01	0,01	0,02	0,01	0,01	0,01	0,01	0,01	0,01	0,01
Na	0,00	0,00	0,03	0,00	0,02	0,00	0,00	0,00	0,02	0,01	0,01	0,00	0,01
K	0,00	0,01	0,87	0,00	0,84	0,03	0,00	0,01	0,90	0,91	0,01	0,00	0,24
Oxygens	14	14	11	14	11	14	14	14	11	11	14	14	14
XMg	*0,62*	*0,66*	*0,44*	*0,54*	*0,70*	*0,55*	*0,55*	*0,41*	*0,58*	*0,55*	*0,41*	*0,42*	*0,38*
AlVI	*1,31*	*1,13*	-	*1,40*	-	*1,27*	*1,47*	*1,35*	-	-	*1,28*	*1,40*	*1,85*
Octahedral sum	*5,82*	*5,73*	-	*5,92*	-	*5,80*	*5,87*	*5,88*	-	-	*5,95*	*5,92*	*5,47*
Xceladonite	-	-	*0,17*	-	*0,14*	-	-	-	*0,22*	*0,28*	-	-	-
Xmuscovite	-	-	*0,72*	-	*0,72*	-	-	-	*0,69*	*0,65*	-	-	-
Xpyrophyllite	-	-	*0,09*	-	*0,13*	-	-	-	*0,07*	*0,05*	-	-	-

Sample	**ZA16-119**	**ZA16-93**				**ZAL18-11**		**ZAL18-12**			**ZAL18-13**			
Lat/Long	42°39'46.4"N/0°16'14.3"E	42°40'1.1"N/0°16'38.4"E				42°40'4.6"N/0°16'41.9"E		42°40'1.3"N/0°16'43.4"E			42°40'4.3"N/0°16'43.1"E			
Deformation	Undeformed	Distributed deformation				Vein in sediments		Triassic sediments			Triassic sediments			
Mineral	Chl	Chl1	Chl2	Wm1	Wm2	Chl2	Wm	Chl1	Chl2	Wm	Chl1	Chl2	Wm1	Wm2
Oxides														
SiO2	27,68	27,84	25,18	48,72	48,62	27,83	48,68	27,27	28,82	47,37	26,17	27,49	47,23	49,25
TiO2	0,18	0,06	0,23	0,09	0,03	<D.L.	0,05	0,09	0,01	0,32	<D.L.	0,04	0,24	0,15
Al2O3	17,45	20,01	21,47	33,14	33,70	23,82	34,68	23,62	22,73	35,03	23,94	22,82	35,16	32,41
FeO	27,88	22,63	28,73	1,17	1,36	21,27	2,59	23,23	20,77	1,09	25,03	22,89	1,73	2,55
MnO	0,39	0,35	0,21	<D.L.	<D.L.	0,30	<D.L.	0,30	0,21	0,04	0,27	0,19	<D.L.	0,00
MgO	13,91	17,38	11,77	1,22	1,64	13,74	0,71	12,11	16,03	0,93	13,41	14,29	0,85	0,92
CaO	0,22	0,03	<D.L.	<D.L.	<D.L.	0,04	0,03	0,05	0,12	0,13	0,01	0,05	0,04	0,08
Na2O	0,02	<D.L.	0,02	0,11	0,21	0,03	0,40	0,04	0,02	1,17	<D.L.	0,03	0,31	0,28
K2O	0,17	<D.L.	<D.L.	10,42	10,82	0,74	10,12	0,54	0,11	9,13	0,02	0,39	10,61	10,46
Total	87,90	88,32	87,61	94,88	96,38	87,79	97,26	87,29	88,83	95,25	88,87	88,21	96,20	96,12
Cations														
Si	2,95	2,86	2,70	3,23	3,19	2,85	3,17	2,84	2,89	3,13	2,70	2,82	3,11	3,25
Ti	0,01	0,00	0,02	0,00	0,00	0,00	0,00	0,01	0,00	0,02	0,00	0,00	0,01	0,01
Al	2,20	2,42	2,72	2,59	2,61	2,87	2,66	2,90	2,69	2,73	2,91	2,76	2,73	2,52
FeTOT	2,49	1,94	2,58	0,06	0,07	1,82	0,14	2,02	1,74	0,06	2,16	1,97	0,10	0,14
Mn	0,04	0,03	0,02	0,00	0,00	0,03	0,00	0,03	0,02	0,00	0,02	0,02	0,00	0,00
Mg	2,21	2,66	1,88	0,12	0,16	2,10	0,07	1,88	2,40	0,09	2,06	2,19	0,08	0,09
Ca	0,03	0,00	0,00	0,00	0,00	0,00	0,00	0,01	0,01	0,01	0,00	0,01	0,00	0,01
Na	0,00	0,00	0,00	0,01	0,03	0,01	0,05	0,01	0,00	0,15	-0,01	0,01	0,04	0,04
K	0,02	0,00	0,00	0,88	0,91	0,10	0,84	0,07	0,01	0,77	0,00	0,05	0,89	0,88
Oxygens	14	14	14	11	11	14	11	14	14	11	14	14	11	11
XMg	*0,47*	*0,52*	*0,42*	*0,65*	*0,68*	*0,54*	*0,33*	*0,48*	*0,58*	*0,60*	*0,49*	*0,53*	*0,47*	*0,39*
AlVI	*1,16*	*1,29*	*1,44*	-	-	*1,74*	-	*1,74*	*1,58*	-	*1,61*	*1,59*	-	-
Octahedral sum	*5,90*	*5,92*	*5,92*	-	-	*5,69*	-	*5,66*	*5,74*	-	*5,85*	*5,76*	-	-
Xceladonite	-	-	-	*0,17*	*0,19*	-	*0,15*	-	-	*0,13*	-	-	*0,14*	*0,21*
Xmuscovite	-	-	-	*0,72*	*0,73*	-	*0,71*	-	-	*0,66*	-	-	*0,77*	*0,68*
Xpyrophyllite	-	-	-	*0,10*	*0,06*	-	*0,10*	-	-	*0,07*	-	-	*0,06*	*0,07*

Table S2. Representative chemical composition of dated monazite for samples ZA16-98 and ZAL18-11.

SESSION 1

ZA16-98	Wt%																
No.	CaO	SiO2	P2O5	Y2O3	Dy2O3	Gd2O3	Sm2O3	Pr2O3	Nd2O3	Ce2O3	La2O3	ThO2	UO2	PbO	TOTAL	Age (Ma)	std
D.L. (ppm)	99	58	244	217	723	626	559	520	341	391	415	130	136	93			
za16-98_Mz33	1,19	0,86	27,83	0,45	0,20	0,59	1,14	3,29	10,12	34,62	15,59	7,65	0,15	0,06	103,75	188	6
za16-98_Mz34	1,15	0,70	28,49	0,43	0,15	0,63	1,23	3,30	10,36	33,83	16,06	7,38	0,16	0,07	103,96	212	6
za16-98_Mz35	0,64	1,49	28,30	0,32	0,20	0,54	1,09	3,31	10,19	35,68	16,89	2,39	0,06	0,02	101,12	227	18
za16-98_Mz36	0,70	1,54	27,82	0,47	0,23	0,71	1,29	3,20	9,98	33,86	16,37	2,36	0,10	0,02	98,67	210	17
za16-98_Mz38	1,08	1,11	27,85	0,46	0,18	0,52	0,92	3,13	9,18	35,18	18,04	3,69	0,18	0,04	101,56	227	11
za16-98_Mz39	0,59	0,50	29,18	0,44	0,27	0,78	1,27	3,20	10,24	35,00	17,89	1,59	0,06	0,01	101,00	150	26
za16-98_Mz40	0,84	0,26	27,53	0,59	0,23	0,54	0,96	3,29	9,84	37,36	18,52	1,13	0,08	0,01	101,20	253	33
za16-98_Mz41	0,70	0,54	29,32	0,76	0,30	0,72	1,09	3,12	9,66	34,40	17,78	1,88	0,11	0,02	100,40	190	20
za16-98_Mz42	0,55	0,36	28,10	1,13	0,43	0,95	1,30	3,27	10,39	35,40	18,35	0,29	0,13	0,01	100,67	353	62
za16-98_Mnz1	1,23	1,23	26,94	0,42	0,25	0,51	1,07	3,15	9,74	33,57	15,02	7,77	0,16	0,06	101,11	185	6
za16-98_Mnz1-2	1,13	1,02	27,34	0,43	0,18	0,62	1,19	3,14	9,89	32,85	15,38	7,17	0,14	0,06	100,54	186	6
za16-98_Mnz2-2	0,73	0,36	28,35	0,61	0,27	0,72	1,26	3,39	10,45	36,07	16,39	1,45	0,07	0,02	100,13	225	28
za16-98_Mz3	0,43	0,27	29,82	1,05	0,52	1,51	2,21	3,36	11,57	33,35	18,45	0,00	0,05	<D.L.	102,61	88	9
za16-98_Mz7	0,79	0,17	29,61	1,16	0,51	1,62	2,23	3,39	11,94	33,09	17,39	0,01	0,05	<D.L.	101,93	275	47
za16-98_Mz9	0,72	0,14	28,58	0,76	0,36	0,85	1,40	3,41	10,74	36,89	16,51	0,82	0,10	0,01	101,30	204	40
za16-98_Mz10	0,90	1,38	27,41	0,44	0,28	0,70	1,30	3,27	10,23	34,14	15,76	4,29	0,09	0,05	100,24	247	10
za16-98_Mz15	0,79	2,58	27,73	0,40	0,18	0,58	1,01	3,16	9,50	34,18	17,62	2,50	0,15	0,03	100,39	218	16
za16-98_Mz16	0,73	0,61	28,18	0,32	0,12	0,43	0,90	3,26	9,49	36,36	17,94	1,95	0,10	0,02	100,40	205	20
za16-98_Mz17	1,13	0,58	21,80	0,39	0,13	0,51	0,91	3,33	9,94	38,70	19,34	3,63	0,16	0,04	100,58	256	11
za16-98_Mz18	0,85	0,72	28,43	0,45	0,21	0,58	1,00	3,29	9,79	35,67	18,10	2,75	0,15	0,03	102,02	237	14
za16-98_Mz23	0,93	0,22	28,06	0,58	0,26	0,55	1,01	3,20	9,49	36,10	18,21	2,15	0,11	0,02	100,90	193	19
za16-98_Mz24	0,74	0,31	28,83	0,66	0,23	0,63	1,07	3,19	9,57	35,67	18,63	1,75	0,08	0,01	101,39	106	23
za16-98_Mz25	0,58	0,12	28,74	0,70	0,29	0,79	1,24	3,30	10,26	35,85	18,75	1,29	0,11	0,02	102,04	271	29
za16-98_Mz26	0,60	0,02	29,52	1,68	0,50	1,14	1,38	3,14	9,99	34,48	20,04	0,65	0,12	0,02	103,27	438	42
za16-98_Mz27	0,53	0,02	30,28	1,44	0,58	1,13	1,39	3,06	10,07	33,16	19,17	0,58	0,09	0,00	101,51	47	3
za16-98_Mz28	0,75	0,42	28,55	0,50	0,16	0,53	1,00	3,17	9,44	35,41	17,91	2,28	0,08	0,03	100,22	255	19

SESSION 2

Sample	ZAL18-11																
No.	**CaO**	**SiO2**	**P2O5**	**Y2O3**	**Dy2O3**	**Gd2O3**	**Sm2O3**	**Pr2O3**	**Nd2O3**	**Ce2O3**	**La2O3**	**ThO2**	**UO2 Corr**	**PbO**	**TOTAL**	**Age (Ma)**	**Std**
D.L. (ppm)	101	41	288	228	729	649	563	527	341	385	414	141	142	101			
ZAL18-11-Mnz3	1,07	0,22	30,13	2,01	0,59	1,43	1,83	3,23	12,30	29,29	14,75	4,45	0,72	0,07	102,10	259	8
ZAL18-11-Mnz1-5	0,28	0,52	29,28	0,25	0,20	1,40	2,09	3,39	13,40	33,52	14,58	2,95	0,04	0,04	101,93	275	16
ZAL18-11-Mnz2	0,60	0,20	30,49	1,45	0,59	1,45	1,95	3,32	12,73	30,60	15,50	2,75	0,37	0,05	102,04	325	12
ZAL18-11-Mnz3-2	0,30	0,22	29,53	0,25	0,20	0,97	1,76	3,30	12,29	34,37	16,19	1,50	0,01	0,01	100,92	203	32
ZAL18-11-Mnz3-3	0,55	0,35	29,28	0,29	0,16	1,09	2,18	3,49	14,69	32,33	13,79	2,96	0,06	0,03	101,24	212	16
ZAL18-11-Mnz3-4	0,55	0,14	29,75	0,40	0,19	1,11	1,81	3,22	12,20	33,16	17,35	1,18	0,03	0,01	101,10	204	39
ZAL18-11-Mnz3-6	0,64	0,25	30,02	1,19	0,49	1,47	1,78	3,11	11,65	33,03	15,21	3,08	0,30	0,04	102,28	258	12
ZAL18-11-Mnz3-7	0,33	0,38	29,14	0,24	0,20	0,96	1,83	3,39	12,83	33,68	15,52	2,56	0,04	0,03	101,13	229	18
ZAL18-11-Mnz3-8	0,38	0,29	29,72	1,06	0,39	1,15	1,51	3,05	11,37	33,73	16,17	2,39	0,13	0,03	101,39	235	17
ZAL18-11-Mnz3-9	0,99	0,31	29,62	0,72	0,37	1,45	1,96	3,17	12,83	31,96	13,25	4,99	0,26	0,06	101,91	232	9
ZAL18-11-Mnz3-10	0,53	0,19	29,83	0,75	0,26	1,07	1,71	3,22	11,99	33,62	16,63	1,44	0,05	0,01	101,30	209	31
ZAL18-11-Mnz3-11	0,39	0,20	29,93	1,07	0,35	0,98	1,42	3,06	11,39	33,85	17,16	1,85	0,14	0,02	101,80	200	22
ZAL18-11-Mnz3-12	1,04	0,28	29,88	0,39	0,23	1,20	1,90	3,23	12,62	32,06	14,17	4,74	0,18	0,06	101,97	270	10
ZAL18-11-Mnz5-3	0,59	2,85	27,91	0,31	0,13	0,95	1,24	2,86	10,55	30,48	17,04	0,63	0,01	0,01	95,59	403	72
ZAL18-11-Mnz6-1	2,54	0,34	28,50	1,71	0,52	1,37	1,99	3,08	11,34	27,18	12,89	8,53	2,14	0,06	102,18	90	3
ZAL18-11-Mnz8-1	0,66	0,69	29,83	1,32	0,47	1,35	2,15	3,36	13,36	30,23	14,43	1,85	0,43	0,03	100,15	197	16
ZAL18-11-Mnz8-2	1,18	1,31	29,93	0,84	0,32	1,31	2,24	3,35	13,19	29,16	13,50	3,51	0,84	0,06	100,75	243	8
ZAL18-11-Mnz9-1	0,96	0,18	29,78	0,65	0,32	1,44	2,58	3,54	14,75	30,17	13,18	1,60	0,18	0,02	99,34	185	23
ZAL18-11-Mnz9-6	0,95	1,41	29,85	0,40	0,24	1,21	2,16	3,40	13,48	31,40	14,61	1,09	0,08	0,01	100,30	180	37
ZAL18-11-Mnz6	2,84	0,34	29,14	1,76	0,56	1,49	2,03	3,08	11,54	26,68	12,22	7,61	0,98	0,12	100,37	90	3
ZAL18-11-Mnz6-3	2,84	0,32	29,87	1,76	0,55	1,51	2,14	3,27	11,99	27,93	12,84	7,40	0,57	0,06	103,03	160	6
ZAL18-11-Mnz6-4	2,93	0,16	29,84	1,15	0,41	1,43	2,16	3,20	12,19	29,25	15,04	4,69	0,70	0,07	103,21	234	7

Sample	$^{207}Pb/^{235}U$	Error 2σ	$^{206}Pb/^{238}U$	Error 2σ	orrelation_6_38\	$^{238}U/^{206}Pb$
T_MKED1_1	3.830	0.200	0.271	0.006	0.185	3.685
T_MKED1_2	3.469	0.067	0.262	0.005	0.295	3.824
T_MKED1_3	3.830	0.550	0.270	0.006	-0.010	3.708
T_MKED1_4	3.480	0.074	0.263	0.005	0.795	3.797
T_MKED1_5	3.452	0.068	0.269	0.006	0.266	3.723
T_MKED1_6	3.387	0.068	0.258	0.005	0.630	3.880
T_MKED1_7	3.497	0.080	0.263	0.005	0.276	3.804
T_MKED1_8	3.534	0.091	0.267	0.006	0.859	3.751
T_MKED1_9	3.400	0.110	0.261	0.004	0.227	3.837
T_MKED1_10	3.580	0.110	0.265	0.006	0.505	3.771
T_MKED1_11	3.389	0.094	0.260	0.005	0.346	3.849
T_MKED1_12	3.605	0.089	0.272	0.006	0.262	3.679
T_MKED1_13	3.620	0.082	0.273	0.005	0.664	3.662
T_MKED1_14	3.740	0.110	0.272	0.005	0.078	3.674
T_MKED1_15	3.680	0.110	0.281	0.007	0.475	3.557
T_MKED1_16	3.570	0.130	0.269	0.005	0.673	3.720
T_MKED1_17	3.650	0.110	0.274	0.006	0.596	3.650
T_MKED1_18	3.491	0.076	0.265	0.007	0.648	3.774
T_MKED1_19	3.570	0.160	0.265	0.006	0.810	3.774
T_MKED1_20	3.570	0.150	0.268	0.006	0.010	3.727
T_MKED1_21	3.370	0.140	0.257	0.006	0.381	3.894
T_MKED1_22	3.641	0.092	0.279	0.006	0.672	3.583
T_MKED1_23	3.650	0.120	0.274	0.007	0.963	3.652
T_MKED1_24	3.880	0.270	0.269	0.007	0.013	3.717
T_MKED1_25	3.650	0.240	0.264	0.007	0.842	3.782
T_MKED1_26	4.800	1.200	0.272	0.007	0.446	3.682
T_MKED1_27	3.700	0.260	0.259	0.005	0.876	3.867
T_MKED1_28	3.590	0.100	0.268	0.006	0.406	3.736
T_MKED1_29	3.682	0.089	0.277	0.006	0.148	3.614
T_MKED1_30	3.360	0.110	0.259	0.007	0.426	3.864
T_MKED1_31	4.040	0.290	0.285	0.008	0.462	3.506
T_MKED1_32	3.680	0.100	0.278	0.008	0.439	3.604
T_MKED1_33	3.448	0.095	0.262	0.005	0.351	3.811
T_MKED1_34	4.080	0.330	0.282	0.012	0.567	3.546
T_MKED1_35	3.990	0.330	0.274	0.007	0.317	3.647
T_MKED1_36	3.590	0.150	0.272	0.006	0.272	3.681
X16_ttn_1	429.000	36.000	3.720	0.300	0.963	0.269
X16_ttn_2	329.000	28.000	2.880	0.250	0.989	0.347
X16_ttn_3	154.000	25.000	1.320	0.180	0.715	0.758
X16_ttn_4	601.000	38.000	5.270	0.320	0.966	0.190
X16_ttn_5	104.000	11.000	0.938	0.098	0.975	1.066
X16_ttn_6	237.000	28.000	2.120	0.250	0.983	0.472
X16_ttn_7	40.900	3.500	0.410	0.033	0.564	2.439
X16_ttn_8	1360.000	120.000	11.900	1.100	0.985	0.084
X16_ttn_9	758.000	51.000	6.630	0.450	0.817	0.151
X16_ttn_10	268.000	14.000	2.330	0.130	0.348	0.429
X16_ttn_11	181.000	13.000	1.595	0.092	0.940	0.627
X16_ttn_12	1700.000	210.000	14.300	1.700	0.990	0.070

X16_ttn_13	181.000	29.000	1.630	0.270	0.992	0.613
X16_ttn_14	288.000	12.000	2.550	0.120	0.910	0.392
X16_ttn_15	1359.000	47.000	11.680	0.410	0.915	0.086
X16_ttn_16	1497.000	54.000	12.960	0.500	0.943	0.077
X16_ttn_17	1660.000	130.000	14.500	1.300	0.249	0.069
X16_ttn_18	2120.000	250.000	18.500	2.200	0.993	0.054
X16_ttn_19	1519.000	59.000	12.970	0.640	0.015	0.077
X16_ttn_20	9010.000	510.000	77.800	4.400	0.983	0.013
X16_ttn_21	349.000	20.000	3.070	0.180	0.990	0.326
X16_ttn_22	142.000	13.000	1.290	0.110	0.978	0.775
X16_ttn_23	174.000	24.000	1.430	0.180	0.848	0.699
X16_ttn_24	52.200	3.700	0.501	0.034	0.857	1.996
X16_ttn_25	46.500	1.500	0.454	0.014	0.791	2.203
X16_ttn_26	113.600	3.400	1.024	0.033	0.926	0.977
X16_ttn_27	111.200	3.900	0.989	0.037	0.904	1.011
X16_ttn_28	4350.000	900.000	41.400	9.500	0.607	0.024
X16_ttn_29	1757.000	72.000	14.900	0.650	0.946	0.067
X16_ttn_30	1850.000	150.000	16.000	1.200	0.987	0.063
X16_ttn_31	5390.000	510.000	46.400	4.500	0.987	0.022
X16_ttn_32	138.000	19.000	1.220	0.170	0.973	0.820
X16_ttn_33	1159.000	76.000	9.960	0.680	0.951	0.100
X16_ttn_34	-25000000.000	########	-180000.000	130000.000	0.997	0.000
X16_ttn_35	1051.000	96.000	8.500	0.670	0.844	0.118
X16_ttn_36	4080.000	670.000	33.800	5.400	0.998	0.030
X16_ttn_37	8.000	1.700	0.118	0.014	0.956	8.475
X16_ttn_38	143.900	9.400	1.285	0.078	0.922	0.778
X16_ttn_39	3.050	0.160	0.075	0.002	0.139	13.369
X16_ttn_40	151.000	10.000	1.341	0.082	0.882	0.746
X16_ttn_41	294.000	29.000	2.580	0.260	0.987	0.388
X16_ttn_42	220.000	11.000	1.930	0.086	0.978	0.518
X82_ttn_1	1020.000	190.000	8.900	1.600	0.997	0.112
X82_ttn_2	256.000	20.000	2.260	0.180	0.980	0.442
X82_ttn_3	71.100	4.300	0.685	0.045	0.986	1.460
X82_ttn_4	274.000	36.000	2.450	0.300	0.990	0.408
X82_ttn_5	12800.000	2500.000	110.000	23.000	0.993	0.009
X82_ttn_6	8200.000	1000.000	73.600	9.700	0.900	0.014
X82_ttn_7	356.000	76.000	3.100	0.660	0.986	0.323
X82_ttn_8	258.000	22.000	2.240	0.170	0.859	0.446
X82_ttn_9	187.000	19.000	1.700	0.170	0.987	0.588
X82_ttn_10	459.000	18.000	3.970	0.150	0.941	0.252
X82_ttn_11	627.000	54.000	5.560	0.490	0.046	0.180
X82_ttn_12	47000.000	########	384.000	75.000	0.983	0.003
X82_ttn_13	3.420	0.350	0.080	0.005	0.913	12.516
X82_ttn_14	1.996	0.043	0.067	0.002	0.289	15.015
X82_ttn_15	7.690	0.240	0.116	0.003	0.826	8.591
X82_ttn_16	33.000	3.000	0.337	0.027	0.934	2.967
X82_ttn_17	5.860	0.350	0.103	0.004	0.908	9.709
X82_ttn_18	5.180	0.490	0.093	0.005	0.884	10.753
X82_ttn_19	8.000	1.300	0.111	0.009	0.601	9.050

X82_ttn_20	15.600	0.980	0.184	0.008	0.927	5.441
X82_ttn_21	137.000	13.000	1.200	0.110	0.899	0.833
X82_ttn_22	6.260	0.240	0.107	0.004	0.852	9.346
X82_ttn_23	2.890	0.130	0.073	0.003	0.762	13.680
X82_ttn_24	7.290	0.300	0.115	0.003	0.514	8.688
X82_ttn_25	4.400	0.430	0.086	0.006	0.916	11.601
X82_ttn_26	77.100	4.700	0.712	0.040	0.985	1.404
X82_ttn_27	107.900	7.200	0.997	0.064	0.886	1.003
X82_ttn_28	144.000	12.000	1.340	0.120	0.599	0.746
X82_ttn_29	18.200	1.300	0.208	0.018	0.535	4.808
X82_ttn_30	17.820	0.780	0.204	0.009	0.887	4.912
X82_ttn_31	57.500	5.100	0.553	0.046	0.973	1.808
X82_ttn_32	175.100	6.000	1.564	0.052	0.941	0.639
X82_ttn_33	432.000	19.000	3.760	0.160	0.882	0.266
X82_ttn_34	223.900	5.700	2.006	0.051	0.882	0.499
X82_ttn_35	169.500	9.800	1.507	0.083	0.770	0.664
X82_ttn_36	205.900	7.000	1.801	0.048	0.373	0.555
X82_ttn_37	319.000	29.000	2.990	0.320	0.610	0.334
X82_ttn_38	236.000	12.000	2.010	0.093	0.523	0.498
X82_ttn_39	355.000	13.000	3.050	0.110	0.931	0.328
X82_ttn_40	200.000	11.000	1.743	0.082	0.961	0.574
X82_ttn_41	243.000	11.000	2.180	0.100	0.913	0.459
X82_ttn_42	131.500	9.800	1.330	0.220	0.203	0.752
X82_ttn_43	75.100	6.200	0.670	0.049	0.147	1.493
X82_ttn_44	207.200	8.400	1.805	0.074	0.921	0.554
X82_ttn_45	1019.000	83.000	8.990	0.720	0.980	0.111
X82_ttn_46	75.700	3.100	0.678	0.021	0.052	1.475
X82_ttn_47	452.000	16.000	3.880	0.140	0.655	0.258
X82_ttn_48	122.800	6.400	1.084	0.040	0.343	0.923
X82_ttn_49	226.000	36.000	1.940	0.290	0.982	0.515
X82_ttn_50	95.600	3.500	0.857	0.030	0.859	1.167
X82_ttn_51	330.000	26.000	2.890	0.220	0.961	0.346
X82_ttn_52	166.500	9.800	1.540	0.110	0.911	0.649
X82_ttn_53	530.000	84.000	4.420	0.680	0.768	0.226
X82_ttn_54	771.000	51.000	6.740	0.400	0.959	0.148
X82_ttn_55	360.000	13.000	3.190	0.140	0.317	0.313
X82_ttn_56	29.600	2.100	0.293	0.017	0.870	3.413
X82_ttn_57	190.000	36.000	1.590	0.300	0.988	0.629
X82_ttn_58	33.500	3.200	0.333	0.028	0.961	3.003
X82_ttn_59	39.100	2.700	0.402	0.028	0.739	2.488
X82_ttn_60	144.000	27.000	1.200	0.190	0.998	0.833
X82_ttn_61	168.000	14.000	1.500	0.100	0.901	0.667
X82_ttn_62	38.700	2.100	0.393	0.022	0.165	2.545
X84_ttn_1	164.000	35.000	1.590	0.360	0.994	0.629
X84_ttn_2	48.900	6.200	0.455	0.047	-0.059	2.198
X84_ttn_3	55.600	4.800	0.542	0.044	0.296	1.845
X84_ttn_4	63.400	5.700	0.583	0.044	0.695	1.715
X84_ttn_5	125.000	13.000	1.110	0.120	0.931	0.901
X84_ttn_6	111.000	23.000	0.980	0.200	0.978	1.020

X84_ttn_7	92.600	4.600	0.862	0.045	0.703	1.160
X84_ttn_8	524.000	66.000	4.550	0.570	0.982	0.220
X84_ttn_9	4.140	0.890	0.082	0.007	0.038	12.255
X84_ttn_10	44.400	4.500	0.420	0.036	0.061	2.381
X84_ttn_11	37.000	3.300	0.362	0.033	0.852	2.762
X84_ttn_12	58.000	9.000	0.537	0.078	0.965	1.862
X84_ttn_13	83.300	7.200	0.755	0.057	0.712	1.325
X84_ttn_14	101.000	14.000	0.880	0.110	0.306	1.136
X84_ttn_15	44.700	2.800	0.442	0.023	0.255	2.262
X84_ttn_16	154.600	8.500	1.420	0.170	0.884	0.704
X84_ttn_17	163.000	10.000	1.482	0.095	0.189	0.675
X84_ttn_18	610.000	140.000	5.600	1.300	0.982	0.179
X84_ttn_19	26.200	3.900	0.286	0.033	0.556	3.497
X84_ttn_20	280.000	49.000	2.550	0.400	0.768	0.392
X84_ttn_21	296.000	35.000	2.510	0.290	0.658	0.398
X84_ttn_22	169.000	27.000	1.367	0.078	0.243	0.732
X84_ttn_23	106.700	5.900	0.995	0.094	0.917	1.005
X84_ttn_24	772.000	82.000	7.500	1.200	0.360	0.133
X84_ttn_25	21.400	1.500	0.236	0.013	0.338	4.237
X84_ttn_26	401.000	40.000	3.570	0.360	0.346	0.280
X84_ttn_27	87.900	7.100	0.800	0.100	0.536	1.250
X84_ttn_28	117.000	17.000	1.240	0.240	0.455	0.806
X84_ttn_29	880.000	150.000	8.000	1.500	0.954	0.125
X84_ttn_30	166.000	15.000	1.405	0.063	0.037	0.712
X84_ttn_31	13.140	0.850	0.161	0.008	0.885	6.219
X84_ttn_32	90.100	9.800	0.823	0.082	0.653	1.215
X84_ttn_33	72.000	14.000	0.750	0.150	0.640	1.333
X84_ttn_34	83.400	9.900	0.776	0.095	0.458	1.289
X84_ttn_35	2.110	0.190	0.065	0.002	0.422	15.432
X84_ttn_36	11.300	1.500	0.144	0.014	0.257	6.944
X84_ttn_37	207.000	12.000	1.810	0.110	-0.128	0.552
X84_ttn_38	102.000	14.000	0.940	0.120	0.104	1.064
X84_ttn_39	120.000	20.000	1.340	0.740	0.899	0.746
X84_ttn_40	158.800	8.800	1.423	0.067	0.627	0.703
X84_ttn_41	176.000	27.000	1.460	0.200	0.707	0.685
X84_ttn_42	128.200	9.100	1.196	0.073	0.876	0.836
X84_ttn_43	201.000	40.000	1.640	0.290	0.376	0.610
X84_ttn_44	346.000	38.000	3.800	1.100	0.445	0.263
X117_ttn_1	173.000	18.000	1.680	0.190	0.272	0.595
X117_ttn_2	87.000	10.000	0.796	0.081	0.994	1.256
X117_ttn_3	235.100	7.500	2.127	0.066	0.901	0.470
X117_ttn_4	470.000	26.000	4.070	0.230	0.984	0.246
X117_ttn_5	317.500	9.100	2.850	0.100	0.321	0.351
X117_ttn_6	512.000	51.000	4.290	0.390	0.776	0.233
X117_ttn_7	640.000	35.000	5.640	0.300	0.979	0.177
X117_ttn_8	722.000	33.000	6.400	0.300	0.972	0.156
X117_ttn_9	134.600	5.400	1.234	0.040	0.464	0.810
X117_ttn_10	257.600	7.700	2.335	0.068	0.206	0.428
X117_ttn_11	378.900	8.900	3.416	0.091	0.789	0.293

X117_ttn_12	281.000	16.000	2.570	0.140	0.952	0.389
X117_ttn_13	931.000	85.000	8.430	0.790	0.995	0.119
X117_ttn_14	201.000	11.000	1.820	0.092	0.585	0.549
X117_ttn_15	378.000	36.000	3.370	0.310	0.864	0.297
X117_ttn_16	727.000	39.000	6.430	0.330	0.894	0.156
X117_ttn_17	630.000	110.000	6.000	1.100	0.407	0.167
X117_ttn_18	274.000	16.000	2.450	0.140	0.983	0.408
X117_ttn_19	263.000	13.000	2.350	0.120	0.553	0.426
X117_ttn_20	520.000	34.000	4.560	0.240	0.908	0.219
X117_ttn_21	298.000	11.000	2.720	0.110	0.901	0.368
X117_ttn_22	1164.000	47.000	10.570	0.420	0.961	0.095
X117_ttn_23	414.000	29.000	3.560	0.240	0.981	0.281
X117_ttn_24	224.000	10.000	2.052	0.094	0.911	0.487
X117_ttn_25	262.000	14.000	2.380	0.120	0.600	0.420
X117_ttn_26	261.000	20.000	2.330	0.170	0.988	0.429
X117_ttn_27	283.000	31.000	2.500	0.260	0.851	0.400
X117_ttn_28	132.200	7.200	1.202	0.060	0.657	0.832
X117_ttn_29	753.000	26.000	6.650	0.240	0.968	0.150
X117_ttn_30	1170.000	100.000	10.480	0.950	0.986	0.095
X117_ttn_31	401.000	35.000	3.460	0.280	0.945	0.289
X117_ttn_32	63.300	2.700	0.594	0.026	0.733	1.684
X117_ttn_33	291.000	14.000	2.600	0.130	0.337	0.385
X117_ttn_34	224.800	8.300	2.023	0.079	0.911	0.494
X117_ttn_35	322.000	15.000	2.840	0.130	0.978	0.352
X117_ttn_36	890.000	120.000	7.900	1.000	0.992	0.127
X117_ttn_37	305.000	15.000	2.680	0.140	0.440	0.373
X117_ttn_38	329.000	35.000	2.920	0.300	0.991	0.342
X117_ttn_39	609.000	72.000	5.120	0.590	0.969	0.195
X117_ttn_40	323.000	19.000	2.860	0.150	0.966	0.350
X117_ttn_41	248.000	29.000	2.240	0.260	0.969	0.446
X117_ttn_42	428.000	46.000	3.710	0.390	0.987	0.270
X117_ttn_43	725.000	42.000	6.720	0.400	0.908	0.149
X117_ttn_44	569.000	63.000	4.830	0.460	0.949	0.207
X117_ttn_45	347.000	46.000	3.100	0.390	0.969	0.323
X117_ttn_46	247.000	19.000	2.210	0.170	0.878	0.452
X117_ttn_47	421.000	29.000	3.710	0.260	0.981	0.270
X117_ttn_48	289.000	23.000	2.640	0.220	0.975	0.379
X117_ttn_49	142.600	9.100	1.317	0.080	0.847	0.759
X117_ttn_50	134.900	4.400	1.241	0.040	0.961	0.806
X117_ttn_51	259.000	16.000	2.300	0.140	0.959	0.435
X117_ttn_52	89.700	7.800	0.853	0.075	0.985	1.172
X117_ttn_53	329.000	17.000	2.840	0.120	0.550	0.352
X117_ttn_54	132.500	3.200	1.207	0.041	0.587	0.829
X117_ttn_55	79.400	2.900	0.748	0.019	-0.023	1.337
X117_ttn_56	208.800	8.600	1.879	0.076	0.722	0.532
X117_ttn_57	332.000	23.000	2.970	0.200	0.988	0.337
X117_ttn_58	144.000	14.000	1.310	0.130	0.778	0.763
X117_ttn_59	97.700	3.800	0.911	0.037	0.688	1.098
X117_ttn_60	108.000	6.600	0.963	0.046	0.499	1.038
X117_ttn_61	103.000	4.200	0.941	0.037	0.772	1.063

X117_ttn_62	224.800	5.600	2.063	0.054	-0.010	0.485
X117_ttn_63	13.690	0.810	0.170	0.007	0.826	5.869
X117_ttn_64	35.900	1.200	0.370	0.011	0.833	2.703
X117_ttn_65	80.800	8.600	0.731	0.072	0.486	1.368
X117_ttn_66	193.200	6.800	1.750	0.089	0.705	0.571
X117_ttn_67	46.200	7.400	0.433	0.060	0.813	2.309
X117_ttn_68	219.000	14.000	1.940	0.120	0.898	0.515
X117_ttn_69	597.000	48.000	5.440	0.460	0.993	0.184
X117_ttn_70	271.500	6.300	2.408	0.065	0.807	0.415
X117_ttn_71	241.000	14.000	2.180	0.130	0.955	0.459
X117_ttn_72	375.000	13.000	3.320	0.120	0.969	0.301
X117_ttn_73	422.000	16.000	3.770	0.150	0.933	0.265
X117_ttn_74	1200.000	130.000	10.960	0.750	0.344	0.091
X117_ttn_75	284.000	14.000	2.570	0.180	0.877	0.389
X117_ttn_76	192.000	11.000	1.770	0.140	0.376	0.565
X117_ttn_77	404.000	19.000	3.660	0.160	0.952	0.273
X117_ttn_78	156.300	6.500	1.420	0.065	0.933	0.704
X117_ttn_79	615.000	29.000	5.380	0.260	0.935	0.186
X117_ttn_80	1350.000	140.000	11.900	1.200	0.966	0.084
X117_ttn_81	709.000	34.000	6.220	0.260	0.501	0.161
X117_ttn_82	452.000	15.000	4.000	0.130	0.968	0.250
X117_ttn_83	1103.000	62.000	9.830	0.580	0.993	0.102
X117_ttn_84	196.000	7.600	1.757	0.078	0.985	0.569
X117_ttn_85	421.000	16.000	3.800	0.140	0.812	0.263
X117_ttn_86	101.600	5.100	0.928	0.048	0.632	1.078
X117_ttn_87	118.800	6.700	1.097	0.061	0.861	0.912
X117_ttn_88	206.000	11.000	1.870	0.110	0.499	0.535
X117_ttn_89	218.000	16.000	1.920	0.130	0.947	0.521
X117_ttn_90	111.500	4.500	1.021	0.037	0.858	0.979
X117_ttn_91	581.000	43.000	4.980	0.400	0.976	0.201
X117_ttn_92	311.000	13.000	2.710	0.110	0.876	0.369
X117_ttn_93	226.600	6.300	2.043	0.061	0.861	0.489
X117_ttn_94	23.570	0.820	0.258	0.009	0.990	3.880
X117_ttn_95	103.200	8.100	0.951	0.071	0.987	1.052
X117_ttn_96	163.000	12.000	1.510	0.110	0.979	0.662
X117_ttn_97	198.600	7.800	1.816	0.073	0.978	0.551
X117_ttn_98	135.100	7.000	1.238	0.061	0.966	0.808
X117_ttn_99	192.500	6.000	1.729	0.050	0.789	0.578
X117_ttn_100	52.200	1.400	0.501	0.011	0.805	1.996
X117_ttn_101	661.000	17.000	5.830	0.180	0.205	0.172
X117_ttn_102	182.600	5.100	1.618	0.055	0.505	0.618
X117_ttn_103	689.000	30.000	6.010	0.260	0.965	0.166
X117_ttn_104	163.500	9.900	1.484	0.092	0.708	0.674
X117_ttn_105	155.000	13.000	1.390	0.110	0.605	0.719
X117_ttn_106	222.400	7.500	2.044	0.088	0.655	0.489
X117_ttn_107	279.000	19.000	2.480	0.170	0.977	0.403
X117_ttn_108	176.700	9.100	1.509	0.064	0.139	0.663
X117_ttn_109	529.000	52.000	4.520	0.400	0.965	0.221
X117_ttn_110	396.000	15.000	3.530	0.150	0.986	0.283
X117_ttn_111	161.900	5.900	1.466	0.058	0.160	0.682

X117_ttn_112	391.000	14.000	3.440	0.110	0.717	0.291
X117_ttn_113	256.000	11.000	2.248	0.085	0.964	0.445
X117_ttn_114	313.000	13.000	2.760	0.110	0.715	0.362
X117_ttn_115	192.100	8.400	1.732	0.096	0.909	0.577
X117_ttn_116	78.000	4.300	0.710	0.033	0.081	1.408

Error 2σ	$^{207}Pb/^{206}Pb$	Error 2σ	rCorrelation_38_6v	FinalAge $^{206}Pb/^{238}U$	Error 2σ
0.081	0.100	0.004	0.061	1547.904	34.220
0.072	0.096	0.002	0.030	1497.512	28.060
0.084	0.101	0.013	0.001	1539.279	34.815
0.076	0.095	0.001	0.195	1507.214	30.327
0.080	0.094	0.002	0.666	1533.692	33.118
0.072	0.096	0.002	0.430	1478.064	27.531
0.071	0.096	0.002	0.134	1504.662	28.044
0.089	0.096	0.002	-0.290	1523.521	36.002
0.065	0.095	0.002	0.000	1492.911	25.206
0.078	0.098	0.003	-0.198	1516.391	31.449
0.070	0.095	0.002	0.009	1488.819	26.934
0.084	0.096	0.003	-0.012	1549.932	35.355
0.071	0.096	0.001	0.096	1556.518	30.207
0.073	0.097	0.003	0.201	1551.959	30.788
0.082	0.095	0.002	-0.254	1596.900	36.926
0.075	0.095	0.002	0.094	1534.708	30.831
0.083	0.096	0.002	-0.201	1561.074	35.324
0.097	0.095	0.002	0.454	1515.372	38.885
0.088	0.098	0.003	-0.579	1515.372	35.454
0.086	0.099	0.004	0.011	1532.167	35.406
0.085	0.095	0.003	-0.246	1473.449	32.131
0.071	0.094	0.002	0.128	1586.828	31.270
0.091	0.096	0.002	0.650	1560.062	38.745
0.100	0.104	0.009	0.147	1535.724	41.105
0.097	0.097	0.004	-0.249	1512.314	38.895
0.095	0.123	0.028	-0.302	1548.918	39.921
0.081	0.101	0.004	-0.350	1482.675	30.961
0.080	0.098	0.003	0.196	1529.117	32.559
0.077	0.095	0.002	0.550	1574.721	33.577
0.099	0.095	0.002	-0.059	1483.700	37.838
0.098	0.102	0.005	-0.192	1617.498	45.372
0.100	0.096	0.002	0.358	1578.759	43.807
0.074	0.096	0.002	0.198	1502.109	29.195
0.151	0.100	0.007	0.248	1601.427	68.146
0.096	0.101	0.006	-0.073	1562.086	41.018
0.076	0.096	0.004	-0.102	1549.425	31.935
0.022	0.840	0.017	0.008	10003.602	806.742
0.030	0.829	0.010	0.007	8740.275	758.704
0.103	0.811	0.023	-0.116	5425.091	739.785
0.012	0.846	0.014	-0.294	11834.175	718.584
0.111	0.809	0.017	-0.051	4265.312	445.630
0.056	0.820	0.010	-0.131	7334.943	864.970
0.196	0.722	0.012	0.020	2214.922	178.274
0.008	0.846	0.011	0.142	16484.946	1523.819
0.010	0.836	0.017	0.167	13099.680	889.119
0.024	0.849	0.016	0.484	7754.858	432.674
0.036	0.807	0.019	-0.111	6147.214	354.573
0.008	0.846	0.012	-0.153	17584.869	2090.509

0.102	0.806	0.016	0.171	6233.578	1032.556
0.018	0.829	0.012	0.329	8167.269	384.342
0.003	0.836	0.013	0.277	16374.059	574.774
0.003	0.841	0.011	0.219	16994.012	655.633
0.006	0.842	0.011	0.340	17668.590	1584.080
0.006	0.850	0.011	-0.149	19148.522	2277.122
0.004	0.851	0.017	0.353	16998.628	838.791
0.001	0.843	0.009	0.027	28150.930	1592.083
0.019	0.833	0.009	0.052	9048.464	530.529
0.066	0.804	0.015	-0.001	5341.188	455.450
0.088	0.826	0.017	0.285	5723.715	720.468
0.135	0.765	0.022	0.073	2618.092	177.675
0.068	0.744	0.016	0.302	2413.011	74.410
0.031	0.808	0.010	0.450	4545.210	146.477
0.038	0.820	0.017	0.300	4432.761	165.836
0.006	0.848	0.018	0.070	24155.670	5542.968
0.003	0.848	0.011	0.107	17832.839	777.943
0.005	0.833	0.010	-0.256	18264.067	1369.805
0.002	0.842	0.011	0.033	24874.277	2412.376
0.114	0.803	0.023	-0.078	5141.062	716.377
0.007	0.844	0.010	0.306	15434.342	1053.750
0.000	0.859	0.019	0.341	#VALUE!	#VALUE!
0.009	0.844	0.017	-0.148	14512.759	1143.947
0.005	0.847	0.007	-0.253	22882.304	3655.753
1.005	0.480	0.060	-0.706	719.042	85.310
0.047	0.805	0.017	-0.027	5327.098	323.357
0.411	0.294	0.012	0.400	465.009	14.298
0.046	0.798	0.014	0.343	5483.179	335.288
0.039	0.826	0.012	0.182	8221.517	828.525
0.023	0.821	0.010	-0.117	6929.911	308.794
0.020	0.834	0.012	0.092	14778.629	2656.832
0.035	0.822	0.011	0.085	7617.903	606.736
0.096	0.771	0.008	-0.245	3363.517	220.961
0.050	0.807	0.016	-0.193	7983.073	977.519
0.002	0.844	0.019	0.104	30359.582	6347.913
0.002	0.839	0.032	0.419	27797.844	3663.575
0.069	0.832	0.032	-0.025	9095.806	1936.527
0.034	0.826	0.017	-0.054	7578.233	575.134
0.059	0.812	0.011	0.120	6402.912	640.291
0.010	0.840	0.011	0.032	10336.308	390.541
0.016	0.822	0.022	0.066	12125.644	1068.627
0.001	0.834	0.034	-0.180	38377.072	7495.522
0.721	0.306	0.018	-0.694	495.526	28.528
0.383	0.217	0.007	0.407	415.639	10.609
0.199	0.479	0.009	0.001	709.810	16.465
0.238	0.708	0.013	-0.387	1872.221	150.000
0.386	0.410	0.015	-0.474	631.966	25.156
0.543	0.407	0.023	-0.636	573.255	28.971
0.770	0.479	0.046	-0.309	675.651	57.476

0.240	0.602	0.014	-0.463	1087.701	47.935
0.076	0.808	0.024	0.070	5082.723	465.916
0.349	0.423	0.008	0.126	655.302	24.497
0.505	0.282	0.010	-0.149	454.805	16.799
0.234	0.455	0.014	0.201	702.299	18.915
0.781	0.369	0.018	-0.599	533.024	35.865
0.079	0.783	0.016	-0.216	3465.994	194.719
0.064	0.798	0.017	-0.107	4458.637	286.211
0.067	0.823	0.016	0.351	5480.425	490.784
0.416	0.645	0.022	0.680	1218.154	105.417
0.222	0.632	0.015	0.240	1194.631	53.981
0.150	0.748	0.013	-0.237	2837.638	236.042
0.021	0.819	0.010	-0.010	6069.741	201.807
0.011	0.838	0.012	0.052	10058.003	428.000
0.013	0.829	0.011	0.315	7094.990	180.381
0.037	0.819	0.014	0.246	5924.814	326.317
0.015	0.833	0.014	-0.048	6639.655	176.959
0.036	0.828	0.012	0.341	8920.491	954.701
0.023	0.828	0.011	-0.004	7103.562	328.672
0.012	0.839	0.011	0.121	9016.708	325.193
0.027	0.832	0.030	-0.682	6504.768	306.019
0.021	0.833	0.013	0.274	7457.735	342.098
0.124	0.812	0.019	0.457	5452.817	901.970
0.109	0.788	0.037	0.002	3305.873	241.773
0.023	0.835	0.013	0.108	6648.854	272.585
0.009	0.828	0.018	0.126	14836.968	1188.278
0.046	0.797	0.020	0.021	3336.681	103.349
0.009	0.843	0.014	0.075	10218.503	368.709
0.034	0.825	0.027	-0.014	4733.532	174.669
0.077	0.800	0.015	-0.222	6951.875	1039.198
0.041	0.808	0.017	0.294	3990.087	139.676
0.026	0.829	0.015	0.043	8756.868	666.613
0.046	0.816	0.016	0.367	6009.116	429.223
0.035	0.829	0.034	0.199	10895.058	1676.163
0.009	0.821	0.012	-0.221	13191.953	782.905
0.014	0.829	0.017	0.673	9235.782	405.332
0.198	0.718	0.016	-0.060	1656.503	96.111
0.119	0.828	0.025	-0.094	6134.781	1157.506
0.253	0.713	0.022	-0.402	1852.906	155.800
0.173	0.737	0.019	0.377	2178.242	151.718
0.132	0.817	0.015	-0.024	5082.723	804.764
0.044	0.811	0.029	0.094	5906.790	393.786
0.142	0.708	0.033	0.101	2136.726	119.613
0.142	0.794	0.019	0.232	6134.781	1389.007
0.227	0.758	0.043	0.065	2417.443	249.714
0.150	0.736	0.039	-0.049	2791.815	226.642
0.129	0.768	0.035	0.207	2960.978	223.470
0.097	0.812	0.024	0.210	4813.460	520.374
0.208	0.776	0.027	-0.419	4403.525	898.679

0.061	0.792	0.022	0.271	4007.421	209.204
0.028	0.828	0.016	0.192	11047.851	1384.017
1.006	0.352	0.048	0.220	505.666	41.519
0.204	0.761	0.046	-0.002	2260.479	193.755
0.252	0.741	0.038	0.215	1991.647	181.559
0.270	0.771	0.030	0.044	2770.878	402.474
0.100	0.783	0.029	-0.010	3625.907	273.744
0.142	0.805	0.041	-0.069	4069.439	508.680
0.118	0.728	0.031	-0.078	2359.588	122.784
0.084	0.795	0.038	0.791	5697.132	682.051
0.043	0.784	0.035	0.090	5860.207	375.654
0.041	0.811	0.033	-0.064	12164.833	2823.979
0.403	0.658	0.041	-0.164	1621.509	187.097
0.062	0.808	0.032	0.367	8167.269	1281.140
0.046	0.850	0.030	0.108	8094.221	935.189
0.042	0.842	0.040	-0.074	5554.381	316.929
0.095	0.817	0.022	0.321	4452.178	420.608
0.021	0.839	0.034	0.282	13795.753	2207.320
0.233	0.690	0.040	-0.064	1365.869	75.239
0.028	0.837	0.046	-0.215	9795.411	987.773
0.156	0.786	0.017	-0.011	3789.116	473.640
0.156	0.777	0.027	0.323	5198.877	1006.234
0.023	0.822	0.021	-0.049	14164.220	2655.791
0.032	0.820	0.033	0.011	5657.050	253.661
0.313	0.596	0.017	-0.058	961.221	48.420
0.121	0.767	0.036	0.090	3870.965	385.685
0.267	0.777	0.034	0.464	3607.515	721.503
0.158	0.806	0.033	-0.114	3702.586	453.280
0.524	0.235	0.021	-0.324	404.751	13.742
0.675	0.543	0.045	-0.185	867.242	84.315
0.034	0.842	0.028	0.502	6660.335	404.772
0.136	0.798	0.045	0.380	4271.961	545.357
0.412	0.805	0.027	0.037	5480.425	3026.503
0.033	0.790	0.030	-0.011	5705.118	268.618
0.094	0.798	0.019	0.022	5802.813	794.906
0.051	0.797	0.024	-0.171	5070.991	309.517
0.108	0.827	0.049	-0.137	6258.043	1106.605
0.076	0.805	0.037	0.061	10111.948	2927.143
0.067	0.801	0.019	0.023	6354.983	718.718
0.128	0.775	0.013	-0.486	3774.775	384.117
0.015	0.801	0.011	-0.154	7349.390	228.049
0.014	0.820	0.010	0.087	10464.727	591.373
0.012	0.814	0.013	0.620	8690.238	304.921
0.021	0.837	0.017	-0.013	10738.554	976.232
0.009	0.828	0.011	-0.006	12203.784	649.137
0.007	0.824	0.008	0.224	12902.369	604.799
0.026	0.799	0.017	-0.239	5181.587	167.961
0.012	0.796	0.008	0.661	7764.530	226.119
0.008	0.810	0.012	0.566	9574.436	255.057

0.021	0.805	0.012	-0.107	8203.485	446.882
0.011	0.814	0.009	0.203	14465.084	1355.565
0.028	0.791	0.013	-0.172	6683.235	337.834
0.027	0.815	0.013	0.025	9506.933	874.525
0.008	0.813	0.009	0.709	12928.450	663.513
0.031	0.823	0.013	0.227	12544.143	2299.760
0.023	0.813	0.012	0.152	7983.073	456.176
0.022	0.811	0.009	0.445	7793.459	397.964
0.012	0.839	0.016	-0.295	11059.456	582.077
0.015	0.800	0.011	0.311	8468.807	342.489
0.004	0.813	0.009	0.133	15783.501	627.159
0.019	0.831	0.010	0.058	9781.290	659.413
0.022	0.795	0.011	-0.244	7192.890	329.499
0.021	0.805	0.013	-0.206	7850.931	395.845
0.031	0.806	0.009	-0.157	7754.858	565.805
0.042	0.808	0.010	-0.099	8075.829	839.886
0.042	0.782	0.024	0.314	5088.580	254.006
0.005	0.827	0.006	0.157	13116.555	473.379
0.009	0.825	0.012	0.148	15733.160	1426.193
0.023	0.828	0.013	0.156	9638.348	779.982
0.074	0.759	0.022	0.460	3005.619	131.559
0.019	0.814	0.014	0.541	8257.430	412.872
0.019	0.802	0.011	0.309	7131.344	278.485
0.016	0.822	0.008	0.080	8673.472	397.025
0.016	0.835	0.011	0.097	14092.192	1783.822
0.019	0.825	0.017	0.672	8399.115	438.760
0.035	0.818	0.012	-0.030	8806.393	904.766
0.023	0.834	0.013	-0.012	11678.080	1345.716
0.018	0.813	0.012	-0.167	8706.960	456.659
0.052	0.798	0.021	0.125	7578.233	879.616
0.028	0.834	0.012	-0.082	9989.930	1050.154
0.009	0.816	0.017	0.299	13175.274	784.242
0.020	0.809	0.010	0.079	11365.138	1082.394
0.041	0.819	0.015	-0.009	9095.806	1144.311
0.035	0.795	0.020	-0.100	7518.266	578.328
0.019	0.823	0.010	0.051	9989.930	700.103
0.032	0.807	0.011	0.224	8328.662	694.055
0.046	0.786	0.010	0.224	5416.749	329.036
0.026	0.786	0.010	-0.186	5201.755	167.663
0.026	0.822	0.012	0.219	7696.519	468.484
0.103	0.785	0.012	-0.209	3976.187	349.606
0.015	0.827	0.014	-0.038	8673.472	366.485
0.028	0.799	0.013	0.821	5103.201	173.348
0.034	0.773	0.013	0.136	3600.144	91.447
0.022	0.805	0.011	0.050	6816.716	275.716
0.023	0.811	0.006	0.195	8888.097	598.525
0.076	0.794	0.018	0.170	5397.244	535.604
0.045	0.789	0.014	0.397	4174.870	169.561
0.050	0.791	0.023	-0.119	4347.938	207.690
0.042	0.795	0.014	-0.411	4275.283	168.104

0.013	0.793	0.010	0.318	7216.083	188.884
0.231	0.600	0.024	0.026	1014.315	39.882
0.080	0.706	0.016	0.393	2029.400	60.334
0.135	0.773	0.015	-0.161	3537.143	348.392
0.029	0.797	0.013	0.597	6521.198	331.650
0.320	0.734	0.022	-0.106	2319.227	321.371
0.032	0.821	0.023	0.091	6951.875	430.013
0.016	0.809	0.011	-0.463	12006.630	1015.267
0.011	0.818	0.011	0.438	7904.114	213.359
0.027	0.805	0.014	0.408	7457.735	444.727
0.011	0.815	0.009	0.425	9432.750	340.943
0.011	0.811	0.013	0.413	10071.531	400.724
0.006	0.819	0.021	-0.075	15997.214	1094.700
0.027	0.823	0.013	0.741	8203.485	574.563
0.045	0.801	0.019	-0.310	6567.912	519.496
0.012	0.789	0.011	0.089	9921.131	433.711
0.032	0.803	0.015	0.472	5697.132	260.784
0.009	0.827	0.013	0.275	11946.289	577.330
0.008	0.816	0.010	-0.042	16484.946	1662.348
0.007	0.812	0.016	0.048	12743.626	532.692
0.008	0.816	0.009	0.292	10375.103	337.191
0.006	0.815	0.008	0.125	15357.422	906.135
0.025	0.810	0.011	0.431	6537.587	290.229
0.010	0.812	0.015	0.155	10111.948	372.545
0.056	0.779	0.018	0.670	4231.963	218.895
0.051	0.786	0.013	-0.327	4773.620	265.443
0.031	0.805	0.010	0.542	6796.532	399.796
0.035	0.814	0.014	-0.168	6907.872	467.720
0.035	0.797	0.011	0.153	4535.648	164.367
0.016	0.840	0.014	0.495	11528.900	926.016
0.015	0.829	0.013	0.035	8451.454	343.048
0.015	0.811	0.012	0.305	7173.853	214.197
0.130	0.664	0.010	-0.559	1478.064	49.326
0.079	0.786	0.010	-0.163	4308.410	321.658
0.048	0.783	0.010	-0.029	5932.524	432.171
0.022	0.799	0.012	0.052	6674.085	268.286
0.040	0.790	0.010	-0.022	5193.119	255.881
0.017	0.811	0.013	0.205	6471.782	187.154
0.044	0.748	0.010	0.116	2618.092	57.483
0.005	0.835	0.013	0.632	12385.655	382.404
0.021	0.818	0.018	0.638	6204.098	210.893
0.007	0.831	0.011	0.203	12553.345	543.073
0.042	0.790	0.010	-0.045	5865.400	363.623
0.057	0.798	0.019	0.020	5616.718	444.488
0.021	0.811	0.024	0.614	7175.971	308.946
0.028	0.815	0.012	0.110	8038.887	551.053
0.028	0.811	0.031	0.115	5929.955	251.502
0.020	0.813	0.017	0.000	11012.911	974.594
0.012	0.817	0.013	0.575	9738.739	413.827
0.027	0.799	0.021	-0.134	5818.517	230.201

0.009	0.820	0.013	0.045	9609.376	307.277
0.017	0.820	0.014	0.030	7594.130	287.145
0.014	0.819	0.022	0.198	8537.753	340.273
0.032	0.817	0.026	0.338	6478.865	359.106
0.065	0.785	0.018	0.130	3458.458	160.745

FinalAge $^{207}Pb/^{235}U$	Error 2σ	alAge $^{207}Pb/^{20}$	Error 2σ	FinalAge ^{207}Pb corr	Error 2σ
1599.072	83.502	1624.083	60.091	1540.952	33.594
1520.196	29.361	1543.853	30.619	1493.591	27.240
1599.072	229.632	1642.570	211.420	1529.869	40.345
1522.692	32.379	1522.114	17.680	1505.951	29.357
1516.326	29.870	1516.130	30.515	1535.215	32.245
1501.392	30.143	1541.890	24.168	1472.768	26.619
1526.538	34.922	1553.632	35.493	1500.476	27.291
1534.858	39.522	1537.955	30.598	1522.270	34.950
1504.396	48.672	1522.114	36.968	1490.477	24.619
1545.107	47.475	1582.592	43.691	1510.617	30.640
1501.855	41.657	1535.984	32.201	1484.887	26.165
1550.635	38.282	1555.580	43.569	1549.426	34.550
1553.937	35.200	1539.924	22.551	1558.009	29.394
1579.974	46.470	1565.283	51.691	1550.758	30.316
1567.039	46.841	1530.055	30.569	1603.150	36.149
1542.888	56.184	1528.074	32.170	1535.288	30.050
1560.509	47.029	1549.728	29.027	1562.101	34.394
1525.182	33.204	1526.090	28.946	1514.456	37.706
1542.888	69.149	1584.503	50.173	1509.345	34.549
1542.888	64.827	1607.248	58.386	1525.450	34.665
1497.449	62.209	1534.010	41.851	1468.489	31.216
1558.542	39.381	1510.122	27.282	1593.877	30.629
1560.509	51.304	1547.772	33.858	1561.173	37.747
1609.530	112.003	1693.150	140.280	1521.170	42.099
1560.509	102.609	1571.075	63.037	1507.230	38.059
1784.899	446.225	2000.193	455.328	1501.864	61.561
1571.369	110.421	1640.731	56.913	1469.121	30.187
1547.322	43.101	1580.679	51.772	1524.559	31.884
1567.473	37.888	1534.010	25.755	1578.443	32.758
1495.123	48.947	1524.103	25.723	1480.364	36.563
1642.287	117.887	1660.831	83.042	1613.173	44.936
1567.039	42.583	1545.814	33.850	1581.796	42.728
1515.413	41.753	1541.890	32.223	1498.738	28.355
1650.314	133.481	1625.942	113.702	1599.049	67.252
1632.163	134.991	1649.901	92.746	1553.855	40.778
1547.322	64.651	1545.814	59.640	1549.748	31.601
6157.065	516.677	4991.118	101.011	-401.040	610.286
5888.300	501.132	4972.394	59.981	154.398	300.827
5121.008	831.333	4941.178	140.132	748.550	250.532
6498.713	410.900	5001.222	82.763	-9194.813	3356.044
4725.552	499.818	4937.664	103.758	384.788	139.866
5556.451	656.458	4957.224	59.835	2392.282	349.571
3792.746	324.563	4775.137	79.365	454.768	55.969
7326.979	646.498	5001.222	65.028	-1074.208	1543.692
6734.022	453.081	4984.340	101.356	-343.904	1074.347
5680.775	296.757	5006.245	94.346	-141.388	347.474
5284.060	379.518	4934.141	116.169	1385.289	229.824
7553.406	933.068	5001.222	70.939	0.000	2202.335

5284.060	846.617	4932.376	97.913	1511.353	307.697
5753.594	239.733	4972.394	71.977	0.000	317.777
7326.232	253.372	4984.340	77.508	0.000	1650.374
7424.365	267.813	4992.807	65.304	-588.624	1570.171
7529.243	589.640	4994.495	65.249	-790.532	1805.057
7777.472	917.155	5007.915	64.808	0.000	3649.522
7439.169	288.947	5009.583	100.074	-1819.880	2556.074
9246.283	523.374	4996.011	53.345	0.000	14678.327
5948.046	340.862	4979.404	55.586	62.943	310.882
5039.188	461.334	4928.839	91.956	869.468	169.742
5244.236	723.343	4967.242	102.231	464.039	210.263
4035.192	286.019	4857.929	139.705	371.889	92.303
3920.120	126.455	4818.134	103.616	420.276	61.774
4814.386	144.093	4935.904	61.088	470.880	99.522
4792.895	168.096	4956.877	102.765	264.286	145.243
8507.043	1760.078	5004.573	106.229	#VALUE!	#VALUE!
7586.873	310.902	5004.573	64.918	0.000	1908.918
7639.215	619.396	4978.380	58.006	0.000	1664.220
8724.665	825.525	4994.495	65.249	0.000	8419.178
5010.381	689.835	4927.067	141.124	785.949	236.327
7164.721	469.818	4997.526	56.857	0.000	1993.199
#VALUE!	#VALUE!	5022.854	111.099	0.000	##########
7065.491	645.373	4997.862	100.668	#VALUE!	#VALUE!
8441.994	1386.308	5002.898	40.756	0.000	10115.893
2231.025	474.093	4180.933	522.617	348.264	67.881
5052.591	330.051	4930.609	104.125	839.021	177.243
1420.233	74.504	3438.894	140.363	329.210	12.206
5101.163	337.825	4918.171	86.284	1098.240	160.127
5774.458	569.589	4967.242	72.163	#NUM!	#VALUE!
5481.203	274.060	4958.610	60.397	1627.507	176.120
7035.120	1310.464	4980.938	71.668	3385.691	4883.850
5634.438	440.190	4960.341	66.379	2969.523	401.525
4343.864	262.709	4868.901	48.632	524.547	64.606
5703.174	749.322	4934.141	97.827	#VALUE!	#VALUE!
9602.760	1875.539	4997.862	112.511	0.000	18707.297
9150.644	1115.932	4989.427	190.300	0.000	25304.139
5968.153	1274.100	4977.527	191.443	#VALUE!	#VALUE!
5642.309	481.127	4967.242	102.231	2371.912	341.172
5316.994	540.229	4942.932	66.961	1452.917	206.668
6225.543	244.139	4991.118	65.360	-448.218	478.129
6541.646	563.395	4960.341	132.759	0.000	1106.807
10923.414	2324.131	4980.938	203.060	0.000	109771.265
1509.001	154.430	3500.863	205.933	344.120	22.446
1114.158	24.002	2954.841	96.902	333.391	9.170
2195.434	68.518	4177.848	80.243	344.383	12.061
3580.607	325.510	4747.041	87.163	403.295	49.259
1955.331	116.786	3946.162	144.372	360.241	18.627
1849.336	174.937	3935.141	222.379	327.230	23.293
2231.025	362.541	4177.848	401.213	326.647	47.855

2852.620	179.203	4512.833	104.950	368.837	26.604
5003.050	474.742	4935.904	146.611	657.971	228.086
2012.875	77.171	3993.978	77.370	363.191	15.274
1379.306	62.045	3374.039	119.647	328.581	13.270
2147.586	88.378	4101.635	126.204	362.310	16.052
1712.341	167.342	3787.319	184.747	328.895	24.929
4425.029	269.749	4891.124	99.946	457.887	98.393
4762.583	317.800	4918.171	104.773	589.581	142.139
5053.291	421.108	4962.070	96.468	462.836	185.064
3000.366	214.312	4612.796	157.336	346.440	46.896
2980.068	130.441	4583.348	108.782	360.615	29.887
4131.621	366.457	4825.806	83.871	518.098	74.497
5250.599	179.918	4955.142	60.502	883.739	144.238
6164.124	271.107	4987.733	71.423	#VALUE!	#VALUE!
5498.965	139.992	4972.394	65.979	1293.145	187.114
5217.785	301.677	4955.142	84.703	791.461	178.586
5414.262	184.069	4979.233	83.685	619.729	214.629
5857.055	532.460	4970.679	72.039	184.230	349.723
5552.176	282.314	4970.679	66.036	1377.853	193.198
5965.305	218.448	4989.427	65.416	-84.562	347.716
5384.886	296.169	4977.527	179.478	591.252	398.830
5581.731	252.671	4979.233	77.707	1435.972	231.504
4961.753	369.773	4942.932	115.660	737.620	229.594
4398.688	363.141	4900.201	230.086	381.037	194.833
5420.622	219.755	4982.640	77.574	508.575	208.014
7034.125	572.946	4970.679	108.058	544.492	1382.989
4406.663	180.458	4916.385	123.372	318.017	112.720
6209.973	219.822	4996.180	82.973	-741.349	576.880
4892.793	254.999	4965.520	162.508	233.166	239.043
5508.402	877.445	4921.737	92.283	3077.205	701.221
4640.888	169.907	4935.904	103.849	338.205	124.154
5891.373	464.169	4972.394	89.971	154.930	398.089
5199.760	306.052	4949.923	97.057	949.728	202.766
6371.287	1009.789	4972.394	203.934	#VALUE!	#VALUE!
6751.266	446.582	4958.610	72.477	#VALUE!	#VALUE!
5979.467	215.925	4972.394	101.967	#VALUE!	#VALUE!
3473.625	246.440	4767.170	106.232	318.086	43.464
5333.069	1010.476	4970.679	150.081	573.257	325.480
3595.430	343.444	4757.143	146.784	382.988	66.532
3748.161	258.824	4804.602	123.864	388.497	67.636
5053.291	947.492	4951.665	90.912	472.564	169.855
5208.812	434.068	4941.178	176.688	1043.501	316.779
3737.982	202.836	4747.041	221.260	482.341	102.594
5184.491	1106.446	4911.012	117.518	1826.333	456.493
3970.169	503.375	4844.795	274.837	360.070	156.127
4098.095	353.792	4802.658	254.489	568.703	164.696
4229.186	380.226	4863.519	221.645	436.065	160.713
4910.679	510.711	4942.932	146.096	484.710	216.178
4791.084	992.747	4878.312	169.735	860.835	257.278

4608.855	228.950	4907.418	136.317	520.849	151.930
6359.748	801.037	4970.679	96.052	2370.845	715.484
1662.236	357.341	3715.676	506.683	322.173	39.880
3874.206	392.656	4850.440	293.193	314.020	153.177
3693.543	329.424	4812.351	246.787	329.655	111.643
4140.262	642.455	4869.086	189.459	374.217	137.519
4502.596	389.180	4891.124	181.153	500.483	172.963
4696.119	650.947	4930.609	251.124	389.706	283.413
3880.894	243.098	4787.001	203.842	473.245	108.082
5124.931	281.772	4912.805	234.826	1340.170	395.381
5178.318	317.688	4892.944	218.435	1802.651	356.221
6513.781	1494.966	4941.178	201.059	1074.127	1455.540
3354.031	499.264	4641.615	289.219	458.049	103.077
5725.090	1001.891	4935.904	195.481	1243.817	629.212
5781.319	683.602	5007.915	176.750	-78.036	636.027
5214.803	833.134	4994.495	237.268	-79.174	460.571
4751.332	262.726	4951.665	133.337	312.718	182.080
6752.581	717.243	4989.427	202.194	-6296.547	6039.846
3156.888	221.277	4710.033	273.045	306.919	75.734
6088.696	607.351	4986.038	274.024	#VALUE!	#VALUE!
4556.544	368.048	4896.577	105.906	519.000	127.968
4844.072	703.840	4880.150	169.581	1332.373	338.274
6885.371	1173.643	4960.341	126.724	#VALUE!	#VALUE!
5196.724	469.584	4956.877	199.484	618.875	349.911
2689.757	173.995	4498.277	128.307	328.440	27.526
4581.365	498.306	4861.659	228.187	729.881	228.332
4356.460	847.089	4880.150	213.546	547.493	220.887
4503.800	534.624	4932.376	201.946	305.360	206.632
1152.077	103.742	3086.418	275.808	315.161	14.895
2548.205	338.257	4362.409	361.526	354.526	60.321
5419.646	314.182	4994.495	166.088	83.010	421.849
4706.025	645.925	4918.171	277.340	529.096	325.320
4869.564	811.594	4930.609	165.374	926.873	559.754
5151.975	285.500	4903.814	186.221	1478.449	294.783
5255.775	806.284	4918.171	117.099	1350.722	266.628
4936.144	350.382	4916.385	148.047	868.544	218.268
5389.925	1072.622	4968.962	294.412	683.405	600.820
5939.305	652.294	4930.609	226.624	#NUM!	#VALUE!
5238.417	545.038	4923.516	116.788	1852.082	301.933
4546.212	522.553	4876.472	81.799	618.905	107.063
5548.312	176.998	4923.516	67.614	0.000	240.115
6249.539	345.719	4956.877	60.450	0.000	455.124
5852.285	167.735	4946.432	78.997	#VALUE!	#VALUE!
6336.270	631.152	4986.038	101.270	-157.902	678.122
6562.451	358.884	4970.679	66.036	#NUM!	#VALUE!
6684.682	305.533	4964.486	49.380	0.000	693.909
4985.236	200.002	4919.955	104.680	888.694	164.368
5640.740	168.609	4915.133	51.849	1521.573	193.744
6031.282	141.669	4939.422	73.177	0.000	380.204

5728.697	326.189	4930.609	73.500	1387.576	272.470
6942.512	633.849	4946.257	54.695	#VALUE!	#VALUE!
5389.925	294.971	4905.617	80.623	2922.426	278.614
6028.874	574.178	4948.178	78.928	#VALUE!	#VALUE!
6691.680	358.976	4944.683	55.346	0.000	666.599
6546.485	1143.037	4962.070	78.380	#VALUE!	#VALUE!
5703.174	333.032	4944.683	72.984	442.544	278.819
5661.724	279.857	4940.652	53.630	#VALUE!	#VALUE!
6351.983	415.322	4989.427	95.150	-1227.326	813.690
5788.134	213.656	4921.737	67.674	1747.613	270.125
7169.088	289.473	4944.858	53.517	#VALUE!	#VALUE!
6121.012	428.767	4975.818	59.877	374.538	360.980
5499.417	245.510	4912.805	67.976	0.000	276.127
5657.871	302.329	4930.609	79.625	578.401	282.946
5654.003	433.257	4932.729	55.678	544.860	222.998
5735.873	628.311	4935.904	61.088	1207.253	259.149
4967.103	270.523	4889.301	150.055	1159.129	211.552
6727.311	232.284	4969.133	33.043	0.000	581.774
7174.304	613.188	4965.520	72.226	0.000	1299.774
6088.696	531.432	4970.679	78.042	582.401	407.668
4227.608	180.325	4846.679	140.483	502.842	105.131
5764.080	277.310	4946.432	85.074	448.747	329.889
5503.020	203.181	4925.292	67.554	0.000	238.677
5866.530	273.286	4960.514	47.065	#VALUE!	#VALUE!
6896.831	929.910	4982.640	65.640	845.538	822.089
5811.631	285.818	4965.520	102.320	229.619	404.045
5888.300	626.415	4953.404	72.666	#VALUE!	#VALUE!
6512.118	769.906	4980.938	77.641	702.973	599.135
5869.669	345.275	4944.683	72.984	1225.974	302.952
5602.328	655.111	4918.171	129.426	666.328	394.236
6154.701	661.487	4980.938	71.668	142.573	434.619
6688.887	387.494	4949.923	103.123	#VALUE!	#VALUE!
6443.252	713.400	4937.664	61.034	1003.917	478.158
5942.227	787.730	4955.142	90.754	1035.941	405.027
5598.242	430.634	4912.805	123.593	#VALUE!	#VALUE!
6137.996	422.807	4962.760	59.669	2273.580	392.191
5757.101	458.178	4934.141	67.256	1355.796	277.558
5043.440	321.846	4896.577	62.297	1322.297	134.454
4987.480	162.675	4896.577	62.297	1161.279	111.680
5646.222	348.801	4960.341	72.414	3299.381	520.199
4576.897	397.991	4894.762	74.824	586.516	102.741
5888.300	304.259	4968.962	84.118	197.817	369.502
4969.388	120.015	4919.955	80.049	846.700	132.374
4454.500	162.696	4872.784	81.949	579.496	84.224
5428.395	223.583	4930.609	67.375	2405.458	195.936
5897.489	408.561	4941.529	37.159	1397.566	232.257
5053.291	491.292	4911.012	111.333	1130.417	204.871
4662.725	181.355	4902.008	86.981	608.115	109.602
4763.515	291.104	4905.617	142.641	644.651	172.839
4715.836	192.296	4912.805	86.515	568.263	113.533

5503.020	137.086	4908.857	59.441	697.601	197.661
2728.504	161.438	4507.998	180.320	343.417	34.886
3663.717	122.464	4742.979	107.490	456.016	50.279
4472.028	475.983	4872.784	94.556	559.815	105.564
5349.940	188.300	4916.385	80.192	2274.218	208.190
3913.686	626.867	4798.761	143.832	437.262	96.126
5476.598	350.102	4958.610	138.914	1658.009	323.135
6491.944	521.965	4937.664	67.138	#VALUE!	#VALUE!
5693.901	132.124	4953.404	66.611	0.000	257.261
5573.374	323.764	4930.609	85.750	0.000	351.792
6020.804	208.721	4947.654	54.657	3106.476	495.533
6140.399	232.811	4941.178	79.205	#VALUE!	#VALUE!
7199.990	779.999	4955.142	127.055	#VALUE!	#VALUE!
5739.442	282.930	4962.070	78.380	261.252	314.885
5343.646	306.146	4923.516	116.788	2167.342	291.227
6096.245	286.705	4902.008	68.342	1320.782	376.248
5135.965	213.588	4927.067	92.037	1124.928	170.721
6522.056	307.544	4968.962	78.109	0.000	657.380
7319.491	759.058	4950.097	57.623	#VALUE!	#VALUE!
6666.259	319.680	4942.932	97.398	0.000	871.509
6209.973	206.083	4950.445	56.400	#NUM!	#VALUE!
7114.480	399.907	4947.480	47.373	0.000	1046.334
5364.476	208.010	4939.422	67.079	1702.488	170.393
6137.996	233.273	4942.932	91.310	0.000	495.774
4702.074	236.029	4883.818	112.848	747.834	135.259
4859.444	274.060	4896.577	80.987	903.376	125.732
5414.752	289.137	4930.609	61.250	2366.063	213.322
5471.972	401.613	4946.432	85.074	2031.171	241.937
4795.607	193.545	4916.385	67.855	631.295	103.269
6464.406	478.433	4991.118	83.185	#VALUE!	#VALUE!
5831.348	243.754	4972.394	77.975	#VALUE!	#VALUE!
5511.083	153.221	4941.178	73.112	2805.842	237.815
3250.775	113.094	4654.711	70.101	395.354	26.699
4717.787	370.291	4896.577	62.297	693.415	100.448
5178.318	381.226	4891.124	62.466	1918.645	183.106
5377.789	211.212	4919.955	73.892	2457.337	201.044
4988.973	258.496	4903.814	62.074	1076.689	118.529
5346.274	166.637	4941.178	79.205	1575.284	176.862
4035.192	108.224	4825.806	64.516	456.029	47.839
6595.183	169.619	4982.640	77.574	382.865	701.468
5292.948	147.832	4953.404	108.999	1019.942	222.521
6637.246	288.995	4975.818	65.865	3177.747	1285.040
5181.409	313.737	4903.814	62.074	1639.353	155.770
5127.538	430.052	4918.171	117.099	1196.352	212.540
5492.170	185.213	4941.178	146.225	2811.695	409.860
5721.470	389.634	4948.178	72.857	408.994	283.488
5259.782	270.877	4941.178	188.874	1060.752	333.538
6369.373	626.101	4944.683	103.394	#NUM!	#VALUE!
6075.987	230.151	4951.665	78.790	3303.166	944.639
5171.485	188.461	4919.955	129.310	1336.083	223.248

6063.118	217.094	4956.877	78.585	1149.739	383.777
5634.438	242.105	4956.877	84.630	3177.038	395.950
5837.836	242.466	4955.142	133.105	865.667	477.770
5344.172	233.686	4951.665	157.581	1309.415	321.703
4436.663	244.585	4894.762	112.237	439.738	106.820

Sample	$^{207}Pb/^{235}U$	Error 2σ	$^{206}Pb/^{238}U$	Error 2σ	orrelation_6_38\	$^{238}U/^{206}Pb$
BLR_1	2.263	0.056	0.178	0.003	0.351	5.618
BLR_2	2.130	0.055	0.176	0.003	0.319	5.688
BLR_3	2.108	0.056	0.178	0.003	0.156	5.624
BLR_4	2.091	0.077	0.176	0.003	0.366	5.698
BLR_5	2.242	0.059	0.178	0.004	0.559	5.609
BLR_6	2.124	0.061	0.175	0.003	0.516	5.727
BLR_7	2.210	0.058	0.178	0.003	0.199	5.615
BLR_8	2.181	0.067	0.182	0.003	0.298	5.501
BLR_9	2.209	0.045	0.178	0.002	0.245	5.624
BLR_10	2.223	0.050	0.179	0.002	0.218	5.583
BLR_11	2.062	0.051	0.174	0.003	0.128	5.741
BLR_12	2.158	0.057	0.178	0.003	0.182	5.618
BLR_13	2.256	0.061	0.182	0.003	0.362	5.488
BLR_14	2.217	0.064	0.176	0.003	0.422	5.672
BLR_15	2.103	0.058	0.172	0.002	0.418	5.804
BLR_16	2.182	0.063	0.175	0.003	0.344	5.718
BLR_17	2.228	0.053	0.176	0.003	0.115	5.688
BLR_18	2.290	0.077	0.181	0.002	0.203	5.522
BLR_19	2.165	0.088	0.180	0.003	-0.008	5.546
BLR_20	2.203	0.057	0.183	0.003	0.344	5.476
T_MKED1_1	3.442	0.083	0.266	0.006	0.094	3.759
T_MKED1_2	3.520	0.110	0.264	0.005	0.641	3.788
T_MKED1_3	3.360	0.120	0.269	0.006	0.359	3.713
T_MKED1_4	3.520	0.120	0.273	0.005	0.572	3.660
T_MKED1_5	3.610	0.140	0.270	0.006	0.408	3.698
T_MKED1_6	3.500	0.120	0.266	0.007	0.662	3.759
T_MKED1_7	3.620	0.160	0.269	0.006	0.602	3.723
T_MKED1_8	3.499	0.093	0.272	0.005	0.253	3.671
T_MKED1_9	3.610	0.140	0.274	0.005	0.488	3.647
T_MKED1_10	3.569	0.097	0.273	0.006	0.561	3.667
T_MKED1_11	3.550	0.120	0.273	0.004	0.318	3.660
T_MKED1_12	3.596	0.093	0.273	0.004	0.089	3.668
T_MKED1_13	3.600	0.110	0.273	0.004	0.077	3.670
T_MKED1_14	3.550	0.110	0.270	0.006	0.343	3.705
T_MKED1_15	3.630	0.120	0.271	0.008	0.505	3.686
T_MKED1_16	3.480	0.140	0.272	0.005	0.311	3.676
T_MKED1_17	3.610	0.130	0.274	0.007	0.556	3.644
T_MKED1_18	3.514	0.084	0.270	0.004	0.277	3.702
T_MKED1_19	3.350	0.150	0.263	0.004	0.298	3.804
T_MKED1_20	3.470	0.130	0.266	0.005	0.476	3.766
ZA16_77_1	31.500	5.400	0.295	0.046	0.818	3.390
ZA16_77_2	16.000	2.600	0.181	0.018	0.752	5.525
ZA16_77_3	48.100	8.300	0.477	0.078	0.737	2.096
ZA16_77_4	105.000	18.000	0.880	0.150	0.527	1.136
ZA16_77_5	187.000	29.000	1.680	0.240	0.934	0.595
ZA16_77_6	164.000	45.000	1.480	0.430	0.893	0.676
ZA16_77_7	135.000	27.000	1.330	0.280	0.923	0.752

ZA16_77_8	87.000	18.000	0.675	0.095	0.818	1.481
ZA16_77_9	35.200	5.000	0.318	0.037	0.728	3.145
ZA16_77_10	30.300	3.100	0.316	0.036	0.799	3.165
ZA16_77_11	27.100	4.400	0.264	0.038	0.591	3.788
ZA16_77_12	26.300	2.400	0.289	0.027	0.572	3.460
ZA16_77_13	51.300	9.100	0.496	0.065	0.685	2.016
ZA16_77_14	32.000	4.000	0.326	0.034	0.845	3.067
ZA16_77_15	32.300	4.800	0.346	0.039	0.390	2.890
ZA16_77_16	21.300	3.700	0.210	0.032	0.832	4.762
ZA16_77_17	86.000	74.000	1.700	1.500	0.964	0.588
ZA16_77_18	11.800	1.500	0.156	0.017	0.834	6.410
ZA16_77_19	10.300	6.000	0.164	0.074	0.974	~~6.098~~
ZA16_77_20	21.500	2.200	0.238	0.019	0.765	4.202
ZA16_77_21	17.000	2.000	0.191	0.017	0.877	5.236
ZA16_77_22	14.500	2.000	0.195	0.016	0.459	5.128
ZA16_77_23	13.300	1.000	0.167	0.017	0.094	5.988
ZA16_77_24	43.000	13.000	0.460	0.130	0.937	2.174
ZA16_77_25	7.520	0.970	0.131	0.012	0.610	7.634
ZA16_77_26	6.680	0.860	0.101	0.009	0.693	9.891
ZA16_77_27	40.900	5.300	0.403	0.049	0.670	2.481
ZA16_77_28	15.000	2.000	0.171	0.015	0.293	5.848
ZA16_77_29	30.000	12.000	0.291	0.098	0.974	3.436
ZA16_77_30	15.100	1.600	0.191	0.018	0.435	5.236
ZA16_77_31	67.000	4.100	0.626	0.037	0.187	1.597
ZA16_77_32	86.000	15.000	0.870	0.130	0.768	1.149
ZA16_77_33	49.300	6.600	0.471	0.067	0.676	2.123
ZA16_77_34	1.750	0.750	0.065	0.011	0.987	15.385
ZA16_77_35	39.300	5.100	0.412	0.054	0.587	2.427
ZA16_77_36	116.000	31.000	1.220	0.330	0.860	0.820
ZA16_77_37	19.700	2.500	0.221	0.026	0.766	4.525
ZA16_77_38	83.000	25.000	0.690	0.200	0.802	1.449
ZA16_77_39	104.000	21.000	0.950	0.170	0.498	1.053
ZA16_77_40	80.000	12.000	0.770	0.120	0.733	1.299
ZA16_77_41	65.000	15.000	0.520	0.120	0.867	1.923
ZA16_77_42	61.000	14.000	0.580	0.140	0.797	1.724
ZA16_77_43	17.300	2.800	0.180	0.019	0.900	5.556
ZA16_77_44	30.700	9.600	0.287	0.068	0.953	3.484
ZA16_77_45	38.800	4.500	0.353	0.027	0.455	2.833
ZA16_77_46	55.200	4.000	0.491	0.043	0.482	2.037
ZA16_78_1	59.200	3.300	0.549	0.030	0.715	1.821
ZA16_78_2	249.000	42.000	2.230	0.370	0.965	0.448
ZA16_78_3	283.000	45.000	2.470	0.390	0.981	0.405
ZA16_78_4	106.000	26.000	0.900	0.220	0.987	1.111
ZA16_78_5	104.600	9.300	0.927	0.081	0.905	1.079
ZA16_78_6	48.600	9.700	0.445	0.075	0.935	2.247
ZA16_78_7	175.000	40.000	1.510	0.220	0.856	0.662
ZA16_78_8	3.750	0.420	0.037	0.004	0.012	~~27.322~~
ZA16_78_9	68.000	12.000	0.710	0.130	0.964	1.408
ZA16_78_10	25.100	2.700	0.256	0.024	0.737	3.906

ZA16_78_11	29.000	14.000	0.270	0.120	0.982	3.704
ZA16_78_12	22.300	3.400	0.212	0.018	0.890	4.717
ZA16_78_13	67.000	15.000	0.620	0.130	0.952	1.613
ZA16_78_14	45.600	3.800	0.434	0.036	0.531	2.304
ZA16_78_15	55.000	17.000	0.530	0.150	0.967	1.887
ZA16_78_16	153.000	28.000	1.300	0.170	0.780	0.769
ZA16_78_17	536.000	50.000	4.660	0.460	0.918	0.215
ZA16_78_18	14.730	0.960	0.180	0.011	0.819	5.556
ZA16_78_19	20.100	2.400	0.222	0.028	0.919	4.505
ZA16_78_20	33.400	1.700	0.343	0.018	0.814	2.915
ZA16_78_21	610.000	110.000	5.600	1.000	0.976	0.179
ZA16_78_22	4.900	1.200	0.086	0.012	0.966	11.628
ZA16_78_23	18.700	1.700	0.201	0.015	0.932	4.975
ZA16_78_24	349.000	53.000	2.980	0.440	0.984	0.336
ZA16_78_25	42.000	15.000	0.400	0.110	0.898	2.500
ZA16_78_26	21.100	3.100	0.229	0.030	0.843	4.367
ZA16_78_27	81.000	8.600	0.718	0.069	0.936	1.393
ZA16_78_28	24.000	4.300	0.248	0.035	0.779	4.032
ZA16_78_29	28.900	1.800	0.285	0.014	0.607	3.509
ZA16_78_30	92.000	10.000	0.794	0.097	0.821	1.259
ZA16_78_31	14.000	1.400	0.179	0.016	0.472	5.587
ZA16_78_32	44.500	8.300	0.415	0.075	0.825	2.410
ZA16_78_33	23.800	2.200	0.254	0.018	0.625	3.937
ZA16_78_34	43.700	6.300	0.410	0.058	0.681	2.439
ZA16_78_35	66.000	7.900	0.655	0.089	0.971	1.527
ZA16_117_1	101.000	18.000	0.920	0.150	0.991	1.087
ZA16_117_2	142.000	21.000	1.280	0.190	0.985	0.781
ZA16_117_3	135.000	37.000	1.170	0.320	0.993	0.855
ZA16_117_4	51.900	2.500	0.502	0.028	0.837	1.992
ZA16_117_5	162.000	57.000	1.470	0.510	0.996	0.680
ZA16_117_6	191.200	9.000	1.750	0.084	0.914	0.571
ZA16_117_7	182.000	33.000	1.630	0.260	0.982	0.613
ZA16_117_8	880.000	240.000	8.500	2.400	0.995	0.118
ZA16_117_9	38.200	3.900	0.373	0.034	0.928	2.681
ZA16_117_10	33.600	5.200	0.328	0.038	0.933	3.049
ZA16_117_11	275.000	27.000	2.410	0.220	0.979	0.415
ZA16_117_12	100.000	14.000	0.890	0.110	0.985	1.124
ZA16_117_13	156.000	87.000	1.390	0.740	0.998	0.719
ZA16_117_14	205.000	11.000	1.820	0.100	0.941	0.549
ZA16_117_15	37.000	8.900	0.386	0.087	0.976	2.591
ZA16_117_16	56.400	6.400	0.544	0.062	0.896	1.838
ZA16_117_17	170.000	46.000	1.570	0.410	0.995	0.637
ZA16_117_18	24.600	2.400	0.259	0.022	0.897	3.861
ZA16_117_19	57.300	7.700	0.562	0.074	0.953	1.779
ZA16_117_20	39.800	3.900	0.372	0.029	0.934	2.688
ZA16_117_21	57.800	9.200	0.547	0.072	0.982	1.828
ZA16_117_22	104.000	11.000	0.960	0.089	0.985	1.042
ZA16_117_23	88.000	9.800	0.778	0.080	0.960	1.285
ZA16_117_24	218.000	26.000	1.950	0.240	0.985	0.513

ZA16_117_25	59.800	4.600	0.560	0.041	0.895	1.786
ZA16_117_26	151.000	15.000	1.350	0.130	0.974	0.741
ZA16_117_27	227.000	20.000	2.040	0.170	0.967	0.490
ZA16_117_28	156.700	8.000	1.400	0.078	0.858	0.714
ZA16_117_29	93.300	5.000	0.856	0.042	0.826	1.168
ZA184_1	157.000	16.000	1.440	0.130	0.760	0.694
ZA184_2	124.000	11.000	1.052	0.091	0.822	0.951
ZA184_3	494.000	73.000	4.390	0.640	0.939	0.228
ZA184_4	105.000	31.000	0.860	0.250	0.895	1.163
ZA184_5	255.000	27.000	1.960	0.240	0.588	0.510
ZA184_6	27.100	6.700	0.279	0.056	0.930	3.584
ZA184_7	161.000	14.000	1.390	0.120	0.814	0.719
ZA184_8	27.900	2.600	0.288	0.030	0.681	3.472
ZA184_9	29.400	2.700	0.311	0.030	0.746	3.215
ZA184_10	99.000	21.000	0.890	0.200	0.901	1.124
ZA184_11	173.000	35.000	1.460	0.280	0.937	0.685
ZA184_12	119.000	10.000	1.095	0.066	0.485	0.913
ZA184_13	505.000	29.000	4.400	0.270	0.862	0.227
ZA184_14	51.800	5.200	0.434	0.038	0.687	2.304
ZA184_15	82.000	14.000	0.730	0.120	0.855	1.370
ZA184_16	65.200	6.800	0.669	0.078	0.567	1.495
ZA184_17	41.900	4.900	0.397	0.035	0.540	2.519
ZA184_18	91.600	9.800	0.815	0.074	0.593	1.227
ZA184_19	55.900	4.200	0.498	0.032	0.610	2.008
ZA184_20	7.800	1.600	0.112	0.013	0.746	8.929
ZA184_21	13.100	1.500	0.162	0.015	0.950	6.173
ZA184_22	48.600	7.100	0.451	0.056	0.768	2.217
ZA184_23	14.700	2.300	0.176	0.021	0.825	5.682
ZA184_24	153.000	16.000	1.360	0.200	0.860	0.735
ZA184_25	87.000	13.000	0.820	0.120	0.942	1.220

Error 2σ	$^{207}Pb/^{206}Pb$	Error 2σ	orrelation_38_	alAge $^{206}Pb/^{23}$	Error 2σ	FinalAge ^{207}Pb
0.092	0.092	0.003	0.240	1056.039	17.205	1200.840
0.097	0.089	0.002	0.407	1043.989	17.816	1158.586
0.095	0.086	0.002	0.409	1054.945	17.800	1151.423
0.097	0.086	0.003	0.110	1042.344	17.818	1145.854
0.120	0.090	0.002	0.243	1057.681	22.542	1194.284
0.085	0.088	0.002	0.039	1037.406	15.448	1156.637
0.079	0.089	0.002	0.339	1056.586	14.831	1184.212
0.088	0.087	0.003	0.215	1076.801	17.177	1174.997
0.076	0.091	0.002	0.359	1054.945	14.240	1183.895
0.065	0.090	0.002	0.372	1062.056	12.453	1188.316
0.092	0.086	0.002	0.401	1035.211	16.639	1136.283
0.088	0.088	0.002	0.376	1056.039	16.612	1167.628
0.090	0.090	0.003	0.114	1078.982	17.766	1198.659
0.084	0.091	0.002	0.314	1046.730	15.437	1186.424
0.081	0.088	0.002	0.150	1024.771	14.274	1149.789
0.101	0.089	0.003	0.221	1039.053	18.417	1175.316
0.084	0.092	0.003	0.435	1043.989	15.440	1189.890
0.073	0.092	0.003	0.198	1072.981	14.220	1209.207
0.086	0.088	0.004	0.352	1068.613	16.595	1169.877
0.075	0.088	0.002	0.129	1081.163	14.802	1181.995
0.078	0.093	0.003	0.554	1520.466	31.438	1514.042
0.070	0.097	0.003	-0.266	1510.274	28.032	1531.718
0.076	0.092	0.003	0.217	1537.248	31.396	1495.123
0.064	0.094	0.003	-0.005	1557.024	27.356	1531.718
0.078	0.096	0.003	0.283	1542.832	32.523	1551.737
0.095	0.096	0.002	0.037	1520.466	38.297	1527.215
0.078	0.097	0.004	0.052	1533.692	31.976	1553.937
0.067	0.093	0.002	0.498	1552.973	28.505	1526.989
0.068	0.095	0.003	0.115	1562.086	29.054	1551.737
0.074	0.094	0.002	0.219	1554.492	31.352	1542.666
0.054	0.094	0.003	0.151	1557.024	22.797	1538.435
0.052	0.096	0.003	0.345	1553.986	22.232	1548.648
0.057	0.097	0.003	0.353	1553.479	23.944	1549.532
0.085	0.096	0.003	0.344	1540.294	35.383	1538.435
0.109	0.098	0.003	0.322	1547.397	45.629	1556.132
0.065	0.094	0.003	0.100	1550.946	27.370	1522.692
0.086	0.097	0.003	0.089	1563.097	37.027	1551.737
0.055	0.093	0.002	0.330	1541.310	22.826	1530.369
0.064	0.095	0.003	0.202	1504.662	25.183	1492.792
0.077	0.095	0.003	0.064	1517.920	30.873	1520.423
0.529	0.690	0.085	0.398	1666.467	259.856	3534.792
0.549	0.680	0.110	0.193	1072.435	106.651	2876.797
0.343	0.740	0.120	0.521	2514.185	411.125	3953.758
0.194	0.810	0.160	0.593	4069.439	693.654	4735.177
0.085	0.825	0.043	-0.039	6354.983	907.855	5316.994
0.196	0.816	0.093	0.321	5855.011	1701.118	5184.491
0.158	0.776	0.054	-0.113	5452.817	1147.962	4988.227

0.209	0.828	0.087	-0.272	3325.145	467.983	4546.212
0.366	0.783	0.079	0.289	1779.954	207.102	3644.270
0.361	0.712	0.051	0.370	1770.165	201.664	3496.591
0.545	0.750	0.084	0.162	1510.274	217.388	3387.084
0.323	0.668	0.062	0.356	1636.530	152.894	3357.757
0.264	0.750	0.100	0.070	2596.583	340.278	4017.867
0.320	0.708	0.049	0.179	1818.965	189.708	3550.295
0.326	0.690	0.110	0.332	1915.470	215.906	3559.484
0.726	0.699	0.073	0.185	1228.818	187.248	3152.345
0.519	0.715	0.064	0.199	6402.912	5649.629	4534.607
0.699	0.545	0.049	0.252	934.509	101.838	2588.663
~~2.751~~	~~0.444~~	~~0.080~~	~~-0.805~~	978.968	441.729	2462.104
0.335	0.657	0.038	0.208	1376.291	109.872	3161.411
0.466	0.619	0.033	0.104	1126.790	100.290	2934.835
0.421	0.518	0.064	0.234	1148.404	94.228	2783.003
0.610	0.571	0.063	0.726	995.561	101.345	2701.182
0.614	0.722	0.069	-0.370	2439.558	689.440	3842.402
0.699	0.465	0.060	-0.074	793.568	72.693	2175.373
0.910	0.478	0.058	0.348	620.852	57.111	2069.980
0.302	0.763	0.074	0.136	2182.838	265.407	3792.746
0.513	0.643	0.082	0.365	1017.619	89.265	2815.240
1.157	0.625	0.049	-0.579	1646.524	554.500	3486.812
0.493	0.612	0.071	0.355	1126.790	106.190	2821.566
0.094	0.767	0.052	0.651	3133.750	185.222	4284.417
0.172	0.760	0.100	-0.023	4035.058	602.940	4534.607
0.302	0.781	0.092	0.661	2487.945	353.911	3978.276
2.604	0.165	0.031	-0.891	405.962	68.701	1027.162
0.318	0.722	0.083	0.336	2224.059	291.503	3753.213
0.222	0.737	0.086	0.137	5141.062	1390.615	4835.431
0.532	0.689	0.057	0.184	1287.157	151.430	3076.746
0.420	0.789	0.097	-0.099	3382.617	980.469	4498.976
0.188	0.800	0.120	0.046	4305.105	770.387	4725.552
0.202	0.758	0.086	0.558	3680.771	573.627	4462.049
0.444	0.801	0.094	-0.017	2699.180	622.888	4254.104
0.416	0.770	0.100	0.410	2948.750	711.767	4190.622
0.586	0.663	0.044	-0.355	1066.975	112.625	2951.618
0.826	0.614	0.084	-0.446	1626.520	385.378	3509.485
0.217	0.798	0.082	0.340	1948.908	149.067	3740.536
0.178	0.818	0.061	0.575	2575.001	225.509	4090.894
0.100	0.759	0.035	0.304	2821.012	154.154	4160.707
0.074	0.828	0.032	-0.140	7558.305	1254.069	5606.398
0.064	0.874	0.025	-0.301	8020.336	1266.369	5735.873
0.272	0.800	0.027	-0.372	4137.656	1011.427	4744.711
0.094	0.819	0.025	0.051	4228.618	369.491	4731.338
0.379	0.729	0.051	0.003	2372.985	399.941	3964.046
0.096	0.816	0.071	-0.122	5932.524	864.341	5250.022
~~3.210~~	~~0.750~~	~~0.120~~	~~0.670~~	231.724	27.224	1582.114
0.258	0.713	0.058	0.343	3458.458	633.239	4299.240
0.366	0.703	0.055	0.005	1469.345	137.751	3312.114

1.646	0.704	0.083	-0.493	1540.802	684.801	3453.518
0.400	0.718	0.054	-0.112	1239.464	105.238	3196.886
0.338	0.732	0.042	-0.270	3109.919	652.080	4284.417
0.191	0.771	0.063	0.519	2323.724	192.751	3900.696
0.534	0.657	0.048	0.281	2741.452	775.883	4087.274
0.101	0.771	0.057	0.185	5369.277	702.136	5114.436
0.021	0.830	0.035	0.238	11174.368	1103.049	6382.696
0.340	0.607	0.027	0.100	1066.975	65.204	2797.959
0.568	0.680	0.027	-0.024	1292.434	163.010	3096.180
0.153	0.700	0.022	0.143	1901.086	99.765	3592.483
0.032	0.783	0.022	-0.020	12164.833	2172.292	6513.781
1.622	0.382	0.049	-0.732	531.837	74.210	1802.257
0.371	0.684	0.026	-0.448	1180.690	88.111	3026.470
0.050	0.840	0.025	0.033	8904.315	1314.731	5948.046
0.688	0.740	0.120	0.079	2169.039	596.486	3819.059
0.572	0.669	0.046	-0.102	1329.256	174.138	3143.197
0.134	0.825	0.043	0.198	3488.547	335.250	4474.508
0.569	0.670	0.081	-0.117	1428.153	201.554	3268.392
0.172	0.720	0.041	0.520	1616.495	79.407	3450.128
0.154	0.881	0.079	0.577	3767.592	460.273	4602.325
0.499	0.623	0.066	0.341	1061.509	94.884	2749.708
0.435	0.800	0.120	0.422	2237.741	404.411	3876.440
0.279	0.691	0.058	0.246	1459.071	103.399	3260.236
0.345	0.759	0.085	0.415	2214.922	313.330	3858.429
0.207	0.766	0.040	-0.267	3247.710	441.292	4269.374
0.177	0.789	0.019	-0.328	4205.158	685.624	4696.119
0.116	0.808	0.017	-0.133	5312.976	788.645	5039.188
0.234	0.826	0.034	0.104	4994.212	1365.938	4988.227
0.111	0.741	0.024	0.432	2622.386	146.269	4029.449
0.236	0.763	0.034	-0.468	5828.965	2022.294	5172.108
0.027	0.797	0.016	0.226	6521.198	313.018	5339.429
0.098	0.804	0.036	-0.600	6233.578	994.313	5289.624
0.033	0.824	0.015	-0.048	14512.759	4097.720	6885.371
0.244	0.754	0.031	-0.075	2043.501	186.271	3725.112
0.353	0.724	0.051	-0.159	1828.680	211.859	3598.369
0.038	0.841	0.016	0.280	7907.896	721.883	5706.860
0.139	0.795	0.020	-0.034	4103.638	507.191	4686.115
0.383	0.766	0.033	-0.300	5616.718	2990.195	5134.026
0.030	0.827	0.018	0.222	6683.235	367.211	5409.835
0.584	0.722	0.030	-0.357	2104.251	474.274	3693.543
0.210	0.774	0.029	0.192	2800.171	319.137	4112.346
0.166	0.787	0.023	-0.468	6084.808	1589.026	5220.758
0.328	0.698	0.029	-0.337	1484.724	126.116	3292.473
0.234	0.763	0.021	-0.214	2874.888	378.544	4128.143
0.210	0.759	0.027	-0.132	2038.804	158.939	3765.733
0.241	0.747	0.032	-0.726	2812.684	370.225	4136.815
0.097	0.782	0.017	-0.230	4338.079	402.176	4725.552
0.132	0.795	0.023	-0.269	3709.841	381.475	4557.685
0.063	0.823	0.017	0.201	6973.764	858.309	5471.972

0.131	0.775	0.028	0.279	2866.629	209.878	4170.777
0.071	0.809	0.016	-0.194	5507.915	530.392	5101.163
0.041	0.831	0.022	-0.203	7167.494	597.291	5512.866
0.040	0.831	0.025	0.455	5643.634	314.431	5138.543
0.057	0.789	0.019	0.085	3986.615	195.605	4616.420
0.063	0.790	0.055	0.182	5750.189	519.114	5140.473
0.082	0.810	0.066	0.561	4633.779	400.831	4902.588
0.033	0.781	0.040	0.293	10859.277	1583.129	6300.003
0.338	0.820	0.110	0.362	4000.493	1162.934	4735.177
0.062	0.900	0.120	0.418	6995.579	856.602	5630.479
0.719	0.647	0.048	-0.274	1586.324	318.402	3387.084
0.062	0.837	0.044	0.463	5616.718	484.897	5165.859
0.362	0.694	0.059	0.614	1631.527	169.951	3415.588
0.310	0.692	0.047	0.429	1745.626	168.388	3466.967
0.252	0.806	0.052	0.129	4103.638	922.166	4676.012
0.131	0.802	0.058	0.082	5802.813	1112.868	5238.417
0.055	0.781	0.048	0.301	4767.469	287.354	4861.138
0.014	0.838	0.026	0.160	10871.226	667.098	6322.320
0.202	0.823	0.064	0.295	2323.724	203.460	4027.528
0.225	0.791	0.073	0.223	3533.418	580.836	4486.816
0.174	0.718	0.077	0.478	3302.012	384.988	4257.177
0.222	0.740	0.081	0.490	2155.211	190.006	3816.695
0.111	0.832	0.078	0.243	3842.614	348.900	4597.948
0.129	0.793	0.063	-0.031	2605.195	167.402	4103.463
1.036	0.475	0.066	-0.275	684.353	79.434	2208.206
0.572	0.589	0.024	-0.360	967.882	89.619	2686.881
0.275	0.807	0.084	0.339	2399.697	297.967	3964.046
0.678	0.614	0.052	-0.194	1045.085	124.698	2796.020
0.108	0.828	0.067	0.681	5535.288	814.013	5114.436
0.178	0.757	0.041	0.010	3860.348	564.929	4546.212

Error 2σ	FinalAge ^{207}Pb	Error 2σ	FinalAge 207Pb corr	Error 2σ
29.716	1473.566	39.912	1034.455	16.528
29.917	1399.849	34.681	1026.331	17.090
30.588	1335.933	34.215	1041.105	17.142
42.195	1340.429	43.591	1027.880	17.268
31.429	1431.882	31.714	1038.571	21.475
33.218	1382.484	34.562	1020.531	14.884
31.079	1412.744	36.346	1038.543	14.328
36.096	1360.495	39.095	1062.308	16.624
24.117	1442.411	31.771	1035.156	13.687
26.728	1433.994	30.139	1042.940	12.014
28.104	1333.681	37.306	1020.896	16.076
30.841	1382.484	37.704	1039.682	16.032
32.411	1423.406	42.750	1060.956	17.168
34.249	1448.694	36.575	1026.375	14.853
31.711	1373.727	31.364	1008.038	13.742
33.934	1408.458	42.633	1020.787	17.739
28.305	1463.252	39.849	1022.728	14.888
40.659	1461.181	50.990	1052.557	14.014
47.552	1384.666	64.440	1052.505	16.543
30.583	1378.112	34.531	1065.817	14.329
36.509	1487.888	43.197	1523.232	30.815
47.866	1573.001	54.966	1504.857	27.610
53.397	1465.320	47.834	1543.420	30.956
52.218	1512.128	41.736	1561.021	26.962
60.178	1539.924	53.156	1543.089	32.009
52.362	1539.924	38.659	1518.786	37.227
68.682	1557.526	62.947	1531.591	31.625
40.586	1483.809	36.775	1559.046	28.014
60.178	1530.055	45.049	1564.970	28.635
41.927	1510.122	38.515	1558.429	30.738
52.003	1514.130	48.170	1560.846	22.759
40.051	1547.772	45.143	1554.544	22.094
47.347	1559.469	48.431	1552.940	23.770
47.670	1555.580	53.251	1538.939	34.695
51.442	1594.022	48.598	1543.176	44.363
61.258	1498.035	54.474	1555.604	27.247
55.880	1574.924	53.360	1562.015	36.320
36.583	1481.766	31.969	1546.469	22.445
66.841	1522.114	54.648	1503.189	24.988
56.961	1534.010	51.509	1516.537	30.326
605.964	4710.033	580.221	392.959	200.363
467.479	4689.023	758.518	245.631	157.484
682.249	4810.418	780.068	465.316	436.577
811.745	4939.422	975.688	330.614	1083.929
824.561	4965.520	258.809	835.558	532.600
1422.574	4949.923	564.146	848.010	1002.931
997.645	4878.312	339.470	1570.974	566.641

940.596	4970.679	522.281	67.214	475.481
517.652	4891.124	493.485	160.279	200.902
357.737	4755.129	340.606	363.478	130.747
549.932	4829.625	540.918	208.059	177.380
306.411	4663.371	432.828	438.751	141.606
712.721	4829.625	643.950	440.561	378.961
443.787	4747.041	328.538	388.232	128.974
528.964	4710.033	750.875	470.812	290.457
547.590	4728.664	493.838	254.143	125.898
3901.872	4761.163	426.174	2816.309	3305.071
329.067	4367.791	392.701	382.578	71.414
1434.235	4065.230	732.474	533.375	254.291
323.493	4639.420	268.338	376.535	75.876
345.275	4553.243	242.742	357.428	58.120
383.862	4293.266	530.442	524.253	101.988
203.096	4435.883	489.423	375.609	88.821
1161.656	4775.137	456.350	522.825	277.438
280.600	4133.909	533.408	402.866	69.883
266.494	4174.756	506.560	299.260	52.925
491.481	4854.190	470.786	290.856	234.574
375.365	4608.308	587.685	284.107	111.695
1394.725	4567.221	358.070	547.612	208.941
298.974	4536.749	526.322	368.427	109.309
262.181	4861.659	329.604	487.491	247.424
790.920	4848.561	637.969	869.667	624.755
532.589	4887.476	575.733	268.635	339.939
440.212	2507.554	471.116	351.289	60.450
487.058	4775.137	548.942	457.427	264.417
1292.227	4804.602	560.646	1979.795	847.913
390.450	4707.946	389.482	287.583	103.734
1355.113	4902.008	602.655	390.045	522.286
954.198	4921.737	738.260	513.290	854.391
669.307	4844.795	549.673	736.457	489.066
981.716	4923.516	577.791	196.824	388.720
961.782	4867.233	632.108	420.946	450.886
477.719	4652.537	308.766	269.914	68.248
1097.429	4541.482	621.310	565.516	220.936
433.825	4918.171	505.376	130.615	231.936
296.442	4953.404	369.386	94.254	242.520
231.931	4846.679	223.496	452.590	149.723
945.657	4970.679	192.104	2113.084	599.165
912.065	5047.387	144.376	-7773.769	3123.516
1163.797	4921.737	166.109	465.880	220.223
420.664	4955.142	151.256	245.230	191.232
791.178	4788.968	335.031	473.007	188.582
1200.005	4949.923	430.692	897.541	765.974
177.197	4829.625	772.740	25.991	35.883
758.689	4757.143	386.977	985.294	334.588
356.283	4736.863	370.594	306.856	113.107

1667.216	4738.905	558.706	323.205	223.438
487.418	4767.170	358.534	222.103	92.374
959.198	4794.852	275.114	703.929	238.191
325.058	4869.086	397.863	284.823	214.628
1263.339	4639.420	338.953	939.459	312.357
935.975	4869.086	359.971	1596.406	521.135
595.401	4974.107	209.752	1850.412	1221.136
182.352	4524.844	201.270	353.447	43.587
369.693	4689.023	186.182	306.030	60.963
182.851	4730.719	148.680	435.922	63.696
1174.616	4891.124	137.426	0.000	1858.966
441.369	3839.697	492.527	319.368	54.613
275.134	4697.466	178.559	268.039	46.358
903.285	4991.118	148.545	0.000	850.375
1363.950	4810.418	780.068	375.003	380.281
461.797	4665.528	320.799	337.926	92.534
475.071	4965.520	258.809	101.911	251.876
585.587	4667.681	564.302	366.477	162.029
214.887	4771.159	271.691	303.261	92.735
500.253	5058.683	453.616	-518.623	571.843
274.971	4562.578	483.355	327.836	95.648
723.021	4921.737	738.260	151.053	397.099
301.366	4712.115	395.518	330.543	116.271
556.249	4846.679	542.777	312.718	273.158
511.031	4859.795	253.775	526.503	209.876
836.932	4902.008	118.046	618.570	169.432
745.232	4935.904	103.849	763.448	203.842
1367.144	4967.242	204.463	261.000	325.582
194.097	4812.351	155.866	491.381	97.800
1819.816	4854.190	216.307	2329.268	902.691
251.333	4916.385	98.698	2274.218	229.987
959.108	4928.839	220.694	1586.692	460.118
1877.828	4963.796	90.360	#VALUE!	#VALUE!
380.313	4837.232	198.878	296.440	95.726
556.890	4779.104	336.650	344.135	135.272
560.310	4992.807	94.988	1167.503	314.074
656.056	4912.805	123.593	515.254	155.283
2863.207	4859.795	209.365	1968.621	1082.343
290.284	4968.962	108.152	994.687	254.744
888.447	4775.137	198.413	423.259	129.745
466.649	4874.629	182.641	363.894	131.128
1412.676	4898.390	143.155	1994.055	572.291
321.217	4726.607	196.378	322.072	65.218
554.742	4854.190	133.602	443.899	110.438
369.004	4846.679	172.412	278.055	83.652
658.455	4823.892	206.646	516.189	149.140
499.818	4889.301	106.289	755.601	144.969
507.560	4912.805	142.131	412.261	149.142
652.621	4962.070	102.497	1557.591	303.804

320.829	4876.472	176.182	372.455	126.852
506.738	4937.664	97.655	842.833	187.630
485.715	4975.818	131.730	1227.460	338.128
262.338	4975.818	149.694	281.068	285.428
247.397	4902.008	118.046	547.157	132.688
523.870	4903.814	341.405	1521.680	535.476
434.907	4939.422	402.471	465.050	525.907
930.972	4887.476	250.319	#VALUE!	#VALUE!
1398.005	4956.877	664.947	200.911	747.813
596.168	5088.870	678.516	-9576.750	10702.179
837.397	4617.270	342.549	471.613	137.189
449.205	4986.038	262.110	86.062	498.014
318.298	4718.345	401.127	372.530	135.895
318.395	4714.195	320.184	411.601	118.431
991.881	4932.376	318.218	385.601	366.103
1059.795	4925.292	356.193	1236.119	615.626
408.499	4887.476	300.383	978.164	371.950
363.064	4987.733	154.751	-286.523	1020.538
404.308	4962.070	385.872	57.655	226.222
766.042	4905.617	452.731	407.501	411.383
444.000	4767.170	511.242	874.842	375.637
446.344	4810.418	526.546	371.627	248.348
491.920	4977.527	466.643	49.873	516.650
308.310	4909.216	390.013	227.287	247.916
452.965	4165.438	578.777	334.706	68.532
307.658	4481.095	182.591	340.244	43.587
579.110	4934.141	513.591	135.552	303.410
437.473	4541.482	384.621	335.078	80.925
534.843	4970.679	402.217	340.959	704.188
679.319	4842.908	262.298	820.106	268.033

Sample	$^{207}Pb/^{235}U$	Error 2σ	$^{206}Pb/^{238}U$	Error 2σ	rrelation_6_38	$^{238}U/^{206}Pb$
R_R19_1	0.680	0.120	0.088	0.005	0.244	11.429
R_R19_2	0.970	0.150	0.094	0.005	-0.098	10.616
R_R19_3	0.760	0.120	0.087	0.005	0.216	11.494
R_R19_4	0.880	0.100	0.079	0.003	0.261	12.674
R_R19_5	1.300	1.000	0.084	0.005	0.005	11.862
R_R19_6	0.680	0.130	0.080	0.004	0.937	12.563
R_R19_7	1.050	0.580	0.087	0.006	-0.036	11.547
R_R19_8	1.200	1.100	0.087	0.013	0.428	11.494
R_R19_9	0.600	0.110	0.086	0.004	0.672	11.574
R_R19_10	0.672	0.094	0.077	0.004	0.247	13.072
R_R19_11	6.900	6.300	0.084	0.011	0.889	11.905
R_R19_12	0.649	0.089	0.076	0.003	-0.043	13.245
R_R19_13	1.230	0.680	0.079	0.003	0.219	12.723
R_R19_14	0.940	0.360	0.085	0.004	0.661	11.792
R_R19_16	0.614	0.085	0.084	0.002	0.030	11.976
R_R19_18	1.310	0.950	0.084	0.009	0.067	11.905
X73__1	100.000	17.000	0.850	0.140	0.968	1.176
X73__2	168.000	10.000	1.480	0.100	0.949	0.676
X73__3	121.500	5.800	1.090	0.049	0.646	0.917
X73__4	112.000	5.300	0.974	0.045	0.908	1.027
X73__5	224.900	9.700	1.946	0.098	0.893	0.514
X73__6	253.000	22.000	2.320	0.200	0.073	0.431
X73__7	3.720	0.700	0.040	0.006	0.916	24.752
X73__8	64.500	3.800	0.575	0.029	0.889	1.739
X73__9	204.000	30.000	1.860	0.280	0.979	0.538
X73__10	110.900	4.000	0.959	0.030	0.740	1.043
X73__11	291.000	13.000	2.520	0.110	0.861	0.397
X73__12	117.300	5.200	1.041	0.042	0.943	0.961
X73__13	249.000	14.000	2.210	0.130	0.971	0.452
X73__14	136.500	5.500	1.196	0.047	0.950	0.836
X73__15	336.000	11.000	2.937	0.096	0.869	0.340
X73__16	300.000	17.000	2.600	0.130	0.919	0.385
X73__17	176.000	14.000	1.560	0.120	0.972	0.641
X73__18	167.000	8.900	1.418	0.084	0.916	0.705
X73__19	192.500	9.500	1.648	0.081	0.866	0.607
X73__20	209.000	12.000	1.828	0.095	0.151	0.547
X73__21	219.000	12.000	1.902	0.094	0.951	0.526
X73__22	271.000	11.000	2.390	0.110	0.546	0.418
X73__23	478.000	42.000	4.220	0.370	0.975	0.237
X73__24	271.000	11.000	2.260	0.200	0.761	0.442
X73__25	244.000	24.000	2.140	0.220	1.000	0.467
X73__26	190.000	11.000	1.720	0.120	0.767	0.581
X73__27	188.000	16.000	1.620	0.110	0.495	0.617
X73__28	170.400	6.200	1.485	0.060	0.862	0.673
X73__29	154.600	9.000	1.387	0.053	0.625	0.721
X73__30	73.700	7.000	0.627	0.056	0.920	1.595
X73__31	250.000	17.000	2.220	0.150	0.926	0.450
X73__32	155.000	12.000	1.810	0.670	0.583	0.552

X73__33	289.000	19.000	2.510	0.160	0.935	0.398
X73__34	180.000	10.000	1.571	0.087	0.856	0.637
X73__35	183.000	16.000	1.550	0.140	0.953	0.645
X73__36	374.000	16.000	3.240	0.150	0.909	0.309
X73__37	296.000	15.000	2.560	0.130	0.857	0.391
X73__38	207.500	8.800	1.858	0.079	0.432	0.538
X73__39	76.200	5.300	0.701	0.053	0.882	1.427
X73__40	9.500	1.300	0.117	0.013	0.757	8.547
X73__41	37.400	7.600	0.364	0.061	0.961	2.747
X73__42	23.600	2.900	0.223	0.021	0.782	4.484
X73__43	13.400	1.100	0.142	0.008	0.828	7.057
X73__44	95.800	3.300	0.877	0.030	0.672	1.140
X73__45	99.000	9.000	0.863	0.075	0.963	1.159
X73__46	167.000	16.000	1.520	0.150	0.965	0.658
X73__47	104.300	4.600	0.894	0.038	0.901	1.119
X73__48	103.500	4.700	0.924	0.051	0.637	1.082
X73__49	456.000	32.000	3.910	0.260	0.909	0.256
X73__50	354.000	15.000	3.030	0.150	0.931	0.330
X79__1	35.400	2.900	0.322	0.027	0.973	3.106
X79__2	272.000	22.000	2.320	0.190	0.987	0.431
X79__3	37.100	3.900	0.345	0.036	0.950	2.899
X79__4	23.900	2.900	0.222	0.024	0.963	4.505
X79__5	51.500	3.700	0.463	0.032	0.761	2.160
X79__6	82.300	4.600	0.726	0.038	0.152	1.377
X79__7	72.900	4.600	0.678	0.055	0.349	1.475
X79__8	125.800	6.100	1.116	0.052	0.769	0.896
X79__9	98.300	9.100	0.872	0.080	0.938	1.147
X79__10	183.000	6.100	1.589	0.052	0.934	0.629
X79__11	303.000	19.000	2.570	0.150	0.987	0.389
X79__12	123.800	9.500	1.079	0.083	0.930	0.927
X79__13	193.000	11.000	1.703	0.092	0.956	0.587
X79__14	140.000	8.000	1.217	0.070	0.913	0.822
X79__15	132.900	5.600	1.172	0.047	0.855	0.853
X79__16	135.300	6.800	1.177	0.066	0.872	0.850
X79__17	192.000	11.000	1.685	0.098	0.145	0.593
X79__18	130.300	8.100	1.113	0.070	0.896	0.898
X79__19	81.700	3.300	0.701	0.030	0.755	1.427
X79__20	142.400	7.600	1.227	0.069	0.904	0.815
X79__21	124.500	8.400	1.108	0.072	0.899	0.903
X79__22	152.700	8.600	1.328	0.065	0.930	0.753
X79__23	236.200	8.400	2.038	0.081	0.807	0.491
X79__24	45.900	7.500	0.422	0.073	0.982	2.370
X79__25	143.600	5.300	1.226	0.052	0.652	0.816
X79__26	148.100	5.800	1.295	0.055	0.885	0.772
X79__27	199.000	14.000	1.740	0.120	0.932	0.575
X79__28	461.000	47.000	3.840	0.370	0.986	0.260
X79__29	676.000	56.000	5.730	0.480	0.992	0.175
X79__30	117.000	13.000	1.090	0.130	0.293	0.917
X79__31	143.000	15.000	1.210	0.120	0.925	0.826

X79__32	161.300	8.100	1.490	0.120	0.240	0.671
X79__33	180.000	40.000	1.400	0.290	0.993	0.714
X79__34	325.000	15.000	2.770	0.140	0.922	0.361
X79__35	170.000	12.000	1.450	0.100	0.984	0.690
X79__36	174.700	7.500	1.482	0.063	-0.097	0.675
X79__37	152.000	31.000	1.320	0.280	0.994	0.758
X79__38	170.600	9.300	1.497	0.049	0.987	0.668
X79__39	130.800	9.400	1.088	0.092	0.439	0.919
X79__40	180.000	14.000	1.540	0.120	0.991	0.649
X79__41	685.000	47.000	5.900	0.420	0.990	0.169
X79__42	448.000	50.000	3.700	0.380	0.982	0.270
X79__43	134.100	6.200	1.172	0.081	0.307	0.853
X79__44	337.000	26.000	2.820	0.200	0.964	0.355
X79__45	119.000	15.000	1.050	0.130	0.995	0.952
X79__46	81.300	3.100	0.719	0.031	0.653	1.391
X79__47	133.700	6.300	1.143	0.062	0.866	0.875
X79__48	315.000	24.000	2.810	0.210	0.961	0.356
X79__49	105.000	14.000	0.920	0.110	0.978	1.087
X79__50	182.000	8.100	1.547	0.077	0.925	0.646
X79__51	104.300	4.600	0.933	0.045	0.863	1.072
X79__52	81.600	6.700	0.727	0.061	0.963	1.376
X79__53	364.000	25.000	3.110	0.200	0.943	0.322
X79__54	994.000	59.000	8.730	0.560	0.951	0.115
X79__55	880.000	54.000	7.360	0.460	0.949	0.136
X79__56	417.000	21.000	3.660	0.190	0.935	0.273
X79__57	484.000	36.000	4.060	0.280	0.965	0.246
X79__58	215.000	15.000	1.850	0.120	0.931	0.541
X79__59	215.000	11.000	1.880	0.100	0.780	0.532
X128__1	65.000	14.000	0.570	0.110	0.983	1.754
X128__2	29.700	6.600	0.263	0.057	0.994	3.802
X128__3	131.000	34.000	1.180	0.300	0.994	0.847
X128__4	88.800	6.700	0.778	0.056	0.932	1.285
X128__5	405.000	58.000	3.720	0.530	0.066	0.269
X128__6	7.550	0.950	0.098	0.009	0.985	10.194
X128__7	5.600	0.570	0.058	0.005	0.443	17.271
X128__8	16.500	1.200	0.152	0.011	0.544	6.579
X128__9	9.400	2.000	0.083	0.018	0.763	12.048
X128__10	2.580	0.390	0.040	0.003	0.912	25.126
X128__11	6.490	0.640	0.083	0.008	-0.079	12.107
X128__12	17.100	1.400	0.220	0.120	-0.016	4.545
X128__13	14.900	1.800	0.157	0.016	0.920	6.369
X128__14	14.700	2.000	0.148	0.027	0.406	6.757
X128__15	104.000	36.000	0.800	0.260	0.990	1.250
X128__16	9.300	1.100	0.093	0.011	0.919	10.753
X128__17	11.000	1.200	0.094	0.011	0.421	10.638
X128__18	46.400	5.400	0.432	0.056	0.622	2.315
X128__19	5.730	0.340	0.067	0.003	0.701	14.925
X128__20	3.770	0.280	0.043	0.001	-0.116	23.529
X128__21	8.320	0.860	0.075	0.007	0.471	13.263

X128__22	10.210	0.920	0.106	0.007	0.346	9.425
X128__23	9.390	0.440	0.092	0.004	0.768	10.881
X128__24	12.560	0.720	0.124	0.007	0.800	8.045
X128__25	15.200	1.100	0.151	0.009	0.913	6.636
X128__26	38.900	3.600	0.360	0.034	0.923	2.778
X128__27	17.220	0.680	0.171	0.005	-0.030	5.851
X128__28	14.170	0.840	0.150	0.007	0.476	6.662
X128__29	5.220	0.440	0.053	0.004	0.589	18.727
X128__30	106.000	24.000	0.950	0.210	0.992	1.053
X128__31	3.670	0.370	0.040	0.004	0.795	25.063
X128__32	9.470	0.590	0.095	0.005	0.770	10.549
X128__33	22.400	2.500	0.211	0.019	0.791	4.739
X128__34	13.000	1.800	0.119	0.017	0.968	8.403
X128__35	7.500	1.700	0.083	0.015	0.981	12.048
X128__36	7.040	0.530	0.083	0.004	0.099	12.019
X128__37	11.500	1.100	0.119	0.011	0.761	8.403
X128__38	52.700	5.000	0.456	0.050	0.360	2.193
X128__39	6.090	0.390	0.062	0.003	0.476	16.026
X128__40	336.000	43.000	2.840	0.370	0.993	0.352
X128__41	52.500	5.700	0.455	0.044	0.965	2.198
X128__42	76.100	6.800	0.667	0.062	0.948	1.499
X128__43	48.600	4.800	0.428	0.042	-0.013	2.336
X128__44	7.250	0.610	0.077	0.008	0.571	12.920
X128__45	8.320	0.500	0.080	0.004	0.139	12.484
X128__46	8.600	0.590	0.081	0.005	0.591	12.285
X128__47	95.300	5.800	0.841	0.052	0.956	1.189
X128__48	21.580	0.790	0.220	0.009	0.115	4.554
X128__49	12.100	0.860	0.137	0.008	0.502	7.321
X128__50	78.500	5.400	0.703	0.046	0.931	1.422
X128__51	19.800	1.100	0.205	0.025	0.004	4.878
X128__52	11.100	1.500	0.135	0.015	0.968	7.407
X128__53	9.350	0.580	0.108	0.005	-0.435	9.268
X128__54	9.250	0.330	0.116	0.004	0.841	8.621
X128__55	4.890	0.690	0.051	0.006	0.024	19.646
X128__56	10.450	0.570	0.109	0.005	0.387	9.158
X128__57	9.220	0.440	0.118	0.005	0.689	8.503
X128__58	59.800	4.700	0.534	0.049	0.178	1.873
X128__59	131.000	12.000	1.102	0.093	0.140	0.907
X128__60	25.100	3.300	0.246	0.027	0.769	4.065
X128__61	7.140	0.500	0.068	0.005	0.383	14.706
X128__62	8.740	0.540	0.092	0.005	0.839	10.881
X128__63	4.600	0.350	0.044	0.005	-0.025	22.831
X128__64	16.800	1.300	0.158	0.013	0.879	6.329
X128__65	3.300	2.500	0.022	0.002	0.292	44.643
X128__66	3.350	0.350	0.036	0.003	-0.036	28.011
X128__67	7.290	0.410	0.073	0.004	0.277	13.793
X128__68	3.750	0.490	0.051	0.025	0.034	19.608
X128__69	24.500	1.600	0.218	0.012	0.801	4.587
X128__70	362.000	16.000	3.190	0.160	0.305	0.313
X128__71	4.550	0.440	0.072	0.005	0.907	13.870

X128__72	10.790	0.860	0.122	0.007	0.807	8.183
X128__73	9.270	0.640	0.116	0.006	0.867	8.621
X128__74	9.550	0.490	0.122	0.006	0.353	8.197
X128__75	9.000	0.790	0.101	0.008	0.975	9.940
X128__76	10.230	0.900	0.115	0.006	0.609	8.688
X128__77	6.220	0.500	0.071	0.005	0.385	14.104
X128__78	4.000	0.290	0.055	0.003	0.161	18.282
X128__79	25.400	1.400	0.239	0.013	0.333	4.184
X128__80	15.000	1.000	0.145	0.009	0.604	6.878

Error 2σ	$^{207}Pb/^{206}Pb$	Error 2σ	orrelation_38_	alAge $^{206}Pb/^{23}$	Error 2σ	FinalAge ^{207}Pb
0.679	0.058	0.010	0.037	540.735	32.135	526.774
0.507	0.079	0.015	0.081	580.329	27.723	688.464
0.674	0.062	0.011	0.154	537.770	31.524	574.010
0.466	0.077	0.008	0.072	489.554	17.994	640.983
0.746	0.106	0.092	0.095	521.738	32.802	845.722
0.616	0.058	0.010	0.210	493.735	24.191	526.774
0.760	0.090	0.052	0.039	535.398	35.240	728.882
1.718	0.130	0.110	0.002	537.770	80.356	800.586
0.509	0.052	0.010	-0.424	534.211	23.495	477.234
0.701	0.064	0.009	-0.210	475.198	25.468	521.928
1.559	0.180	0.150	-0.168	519.954	68.089	2098.657
0.579	0.062	0.009	0.217	469.207	20.508	507.863
0.534	0.089	0.041	0.095	487.761	20.479	814.339
0.612	0.083	0.035	-0.362	524.710	27.226	672.882
0.301	0.052	0.007	-0.032	516.980	13.002	486.080
1.219	0.074	0.026	-0.024	519.954	53.233	850.127
0.194	0.822	0.023	0.002	3965.741	653.181	4686.115
0.046	0.828	0.015	0.333	5855.011	395.609	5208.812
0.041	0.822	0.021	0.306	4752.065	213.625	4882.074
0.047	0.836	0.017	0.096	4383.961	202.544	4800.109
0.026	0.828	0.018	0.412	6965.017	350.756	5503.470
0.037	0.834	0.043	0.366	7735.470	666.851	5622.515
3.431	0.661	0.063	-0.390	255.312	35.390	1575.680
0.088	0.828	0.022	0.168	2928.318	147.689	4246.383
0.081	0.821	0.025	-0.017	6774.031	1019.747	5404.894
0.033	0.835	0.021	0.176	4334.789	135.603	4790.177
0.017	0.842	0.017	0.328	8112.561	354.120	5764.080
0.039	0.820	0.017	0.063	4599.129	185.556	4846.651
0.027	0.819	0.012	0.255	7518.266	442.251	5606.398
0.033	0.825	0.014	-0.199	5070.991	199.278	4999.364
0.011	0.832	0.011	0.320	8834.289	288.761	5909.614
0.019	0.821	0.015	0.120	8257.430	412.872	5794.903
0.049	0.832	0.015	0.103	6059.676	466.129	5255.775
0.042	0.835	0.019	0.393	5691.802	337.173	5202.786
0.030	0.817	0.021	0.120	6277.548	308.545	5346.274
0.028	0.816	0.024	0.045	6701.497	348.273	5429.362
0.026	0.826	0.014	0.105	6868.011	339.428	5476.598
0.019	0.839	0.022	0.503	7869.975	362.216	5692.036
0.021	0.821	0.012	0.072	10652.683	934.003	6266.640
0.039	0.830	0.016	0.028	7617.903	674.151	5692.036
0.048	0.841	0.020	0.245	7376.134	758.294	5585.884
0.041	0.820	0.022	0.535	6450.488	450.034	5333.069
0.042	0.815	0.027	-0.292	6209.021	421.600	5322.381
0.027	0.828	0.019	0.432	5867.995	237.091	5223.130
0.028	0.830	0.025	-0.040	5608.621	214.316	5124.931
0.142	0.818	0.030	0.329	3137.714	280.242	4379.835
0.030	0.838	0.023	0.295	7538.317	509.346	5610.451
0.205	0.820	0.025	0.700	6660.335	2465.428	5127.538

0.025	0.833	0.020	0.054	8094.221	515.966	5757.101
0.035	0.829	0.025	0.310	6087.316	337.108	5278.466
0.058	0.844	0.020	0.201	6034.446	545.047	5295.157
0.014	0.843	0.016	0.234	9312.253	431.123	6018.100
0.020	0.831	0.022	0.196	8185.402	415.665	5781.319
0.023	0.817	0.025	0.573	6769.522	287.832	5422.084
0.108	0.803	0.025	0.266	3424.440	258.909	4413.260
0.950	0.591	0.057	0.237	713.273	79.253	2387.547
0.460	0.775	0.047	-0.285	2001.106	335.350	3704.176
0.422	0.764	0.047	0.235	1297.707	122.206	3252.014
0.418	0.660	0.032	-0.286	854.268	50.641	2708.258
0.039	0.803	0.023	0.249	4059.144	138.853	4642.988
0.101	0.824	0.018	0.074	4010.882	348.570	4676.012
0.065	0.805	0.017	0.104	5958.156	587.976	5202.786
0.048	0.835	0.015	0.136	4117.267	175.007	4728.449
0.060	0.836	0.031	0.526	4218.574	232.843	4720.706
0.017	0.842	0.025	0.061	10258.011	682.118	6218.900
0.016	0.832	0.018	0.454	8984.795	444.792	5962.449
0.260	0.805	0.022	0.215	1799.489	150.889	3649.864
0.035	0.848	0.009	0.217	7735.470	633.508	5695.763
0.302	0.778	0.025	-0.078	1910.679	199.375	3696.212
0.487	0.787	0.029	-0.142	1292.434	139.723	3264.322
0.149	0.798	0.038	0.305	2452.790	169.523	4021.743
0.072	0.817	0.027	0.084	3518.495	184.164	4490.479
0.120	0.800	0.025	0.425	3336.681	270.675	4368.902
0.042	0.811	0.024	0.308	4831.765	225.136	4917.105
0.105	0.802	0.024	0.277	4041.949	370.821	4668.879
0.021	0.839	0.009	0.267	6132.291	200.679	5295.157
0.023	0.844	0.008	-0.273	8203.485	478.803	5804.973
0.071	0.836	0.019	0.189	4718.047	362.927	4900.962
0.032	0.838	0.015	-0.071	6410.071	346.287	5348.894
0.047	0.829	0.019	0.295	5132.344	295.205	5024.887
0.034	0.809	0.017	0.312	5000.151	200.518	4972.425
0.048	0.832	0.024	0.333	5014.974	281.213	4990.464
0.035	0.841	0.021	0.332	6366.999	370.306	5343.646
0.057	0.828	0.023	0.329	4822.619	303.309	4952.515
0.061	0.817	0.022	0.327	3424.440	146.552	4483.139
0.046	0.850	0.018	0.333	5161.356	290.247	5042.025
0.059	0.808	0.022	0.248	4807.347	312.391	4906.641
0.037	0.837	0.018	-0.098	5447.281	266.621	5112.456
0.020	0.831	0.019	0.315	7163.252	284.702	5553.032
0.410	0.823	0.020	0.085	2269.552	392.600	3907.212
0.035	0.839	0.029	0.610	5158.461	218.793	5050.486
0.033	0.835	0.018	0.423	5355.248	227.443	5081.604
0.040	0.837	0.020	0.293	6497.714	448.118	5379.822
0.025	0.847	0.016	-0.081	10165.445	979.483	6229.949
0.015	0.856	0.008	0.004	12290.573	1029.577	6617.933
0.109	0.834	0.028	0.195	4752.065	566.760	4844.072
0.082	0.846	0.019	0.281	5111.958	506.971	5046.264

0.054	0.838	0.024	0.580	5880.952	473.634	5167.738
0.148	0.868	0.026	0.057	5643.634	1169.038	5278.466
0.018	0.847	0.016	0.361	8554.875	432.376	5875.918
0.048	0.849	0.012	-0.068	5776.555	398.383	5220.758
0.029	0.850	0.013	0.455	5860.207	249.118	5248.290
0.161	0.841	0.017	-0.154	5425.091	1150.777	5107.821
0.022	0.842	0.014	-0.271	5899.049	193.088	5224.315
0.078	0.852	0.018	0.226	4745.893	401.307	4956.375
0.051	0.848	0.008	0.150	6009.116	468.243	5278.466
0.012	0.843	0.009	-0.062	12451.387	886.370	6631.342
0.028	0.851	0.015	-0.142	9976.229	1024.586	6200.968
0.059	0.845	0.027	0.709	5000.151	345.574	4981.485
0.025	0.847	0.016	-0.160	8639.809	612.752	5912.622
0.118	0.823	0.016	-0.029	4627.493	572.928	4861.138
0.060	0.827	0.027	0.688	3492.298	150.572	4478.216
0.047	0.841	0.023	0.419	4913.500	266.524	4978.474
0.027	0.824	0.020	0.097	8622.912	644.417	5844.283
0.130	0.830	0.021	-0.583	4205.158	502.791	4735.177
0.032	0.836	0.021	0.407	6026.857	299.979	5289.624
0.052	0.814	0.021	0.422	4248.659	204.919	4728.449
0.115	0.818	0.024	0.386	3522.229	295.538	4481.911
0.021	0.844	0.017	-0.013	9111.510	585.949	5990.656
0.007	0.837	0.013	0.475	14666.971	940.837	7008.928
0.008	0.871	0.014	0.526	13688.693	855.543	6885.371
0.014	0.848	0.015	0.387	9921.131	515.031	6128.326
0.017	0.848	0.016	0.000	10452.000	720.828	6279.280
0.035	0.835	0.018	0.079	6751.452	437.932	5457.967
0.028	0.845	0.023	0.297	6818.954	362.710	5457.967
0.339	0.834	0.025	-0.082	2907.820	561.158	4254.104
0.824	0.814	0.019	0.090	1505.172	326.216	3476.938
0.215	0.804	0.023	0.159	5023.851	1277.250	4957.914
0.093	0.812	0.022	0.181	3709.841	267.032	4566.772
0.038	0.795	0.049	0.145	10003.602	1425.244	6098.749
0.966	0.574	0.030	-0.432	603.265	57.190	2178.942
1.491	0.698	0.065	0.331	362.842	31.333	1916.099
0.476	0.790	0.060	0.563	912.165	66.012	2906.230
2.613	0.806	0.038	0.086	514.005	111.471	2377.830
1.957	0.443	0.035	-0.499	251.593	19.596	1294.982
1.099	0.578	0.034	0.420	511.623	46.455	2044.544
2.479	0.759	0.068	-0.062	1281.875	699.205	2940.460
0.649	0.687	0.034	-0.049	940.083	95.805	2808.874
1.233	0.777	0.038	0.428	889.742	162.318	2796.020
0.406	0.793	0.036	-0.013	3789.116	1231.463	4725.552
1.272	0.740	0.048	0.340	573.255	67.804	2368.019
1.245	0.855	0.084	0.801	579.150	67.773	2523.132
0.300	0.820	0.090	0.576	2314.727	300.057	3917.980
0.735	0.630	0.024	0.159	418.056	20.591	1935.904
0.720	0.632	0.054	0.534	268.311	8.207	1586.380
1.214	0.814	0.087	0.556	468.607	42.883	2266.500

0.657	0.687	0.055	0.175	650.058	45.339	2453.984
0.414	0.730	0.021	0.095	566.764	21.585	2376.853
0.440	0.743	0.031	0.193	755.266	41.318	2647.230
0.383	0.738	0.023	-0.151	904.886	52.240	2827.853
0.262	0.802	0.023	-0.077	1982.174	187.205	3743.084
0.164	0.727	0.025	0.173	1017.068	28.566	2947.170
0.302	0.686	0.028	0.066	901.524	40.842	2761.151
1.508	0.694	0.058	0.386	335.362	27.005	1855.887
0.233	0.841	0.018	-0.056	4305.105	951.655	4744.711
2.261	0.653	0.053	-0.159	252.213	22.756	1564.867
0.601	0.720	0.038	0.488	583.863	33.258	2384.641
0.427	0.775	0.049	-0.042	1234.143	111.131	3201.235
1.200	0.790	0.031	0.076	724.805	103.544	2679.654
2.177	0.654	0.038	-0.490	514.005	92.892	2172.987
0.592	0.608	0.053	0.555	515.195	25.388	2116.494
0.777	0.687	0.040	0.212	724.805	66.999	2564.582
0.240	0.870	0.035	0.387	2421.872	265.556	4044.690
0.770	0.697	0.039	0.239	390.205	18.760	1988.816
0.046	0.859	0.014	0.040	8673.472	1129.995	5909.614
0.213	0.815	0.019	-0.133	2417.443	233.775	4040.901
0.139	0.825	0.026	0.064	3294.283	306.215	4411.944
0.229	0.831	0.022	0.371	2296.695	225.377	3964.046
1.319	0.671	0.072	0.449	480.585	49.052	2142.675
0.655	0.756	0.046	0.577	496.720	26.045	2266.500
0.800	0.751	0.039	0.418	504.474	32.847	2296.556
0.074	0.830	0.014	0.200	3934.304	243.263	4637.730
0.191	0.700	0.021	0.381	1279.761	53.615	3165.015
0.402	0.655	0.045	0.342	825.408	45.319	2612.187
0.093	0.808	0.018	0.177	3432.015	224.570	4443.070
0.595	0.717	0.047	0.018	1202.125	146.601	3081.640
0.823	0.604	0.020	-0.357	816.327	90.703	2531.559
0.438	0.640	0.040	0.879	660.540	31.221	2372.937
0.312	0.588	0.010	0.745	707.500	25.616	2363.078
2.432	0.654	0.030	0.329	320.045	39.613	1800.534
0.453	0.708	0.032	0.143	668.100	33.038	2475.493
0.347	0.570	0.019	-0.307	716.735	29.254	2360.102
0.172	0.819	0.027	0.069	2758.283	253.101	4170.777
0.077	0.845	0.021	-0.084	4788.972	404.151	4957.914
0.446	0.757	0.067	0.513	1417.814	155.614	3312.114
1.146	0.768	0.071	0.683	424.095	33.054	2129.045
0.533	0.691	0.031	0.225	566.764	27.752	2311.257
2.658	0.760	0.080	-0.041	276.344	32.177	1749.268
0.521	0.765	0.039	0.426	945.653	77.807	2923.489
3.388	0.682	0.095	-0.156	142.806	10.838	1481.053
2.354	0.700	0.110	0.753	226.124	19.002	1492.792
0.685	0.726	0.043	0.444	451.200	22.404	2147.586
9.612	0.761	0.059	0.121	320.658	157.185	1582.114
0.253	0.820	0.030	-0.110	1271.298	69.980	3288.499
0.016	0.843	0.015	0.607	9235.782	463.237	5985.077
0.943	0.456	0.018	-0.237	448.795	30.501	1740.161

0.469	0.630	0.029	0.105	743.214	42.574	2505.206
0.461	0.592	0.018	-0.188	707.500	37.815	2365.058
0.383	0.571	0.019	0.372	742.065	34.670	2392.370
0.790	0.644	0.013	-0.370	617.924	49.139	2338.006
0.438	0.654	0.051	0.300	702.299	35.390	2455.794
0.935	0.648	0.065	0.406	441.576	29.272	2007.265
0.836	0.553	0.050	0.313	343.313	15.691	1634.196
0.228	0.765	0.032	0.541	1381.496	75.144	3323.718
0.416	0.746	0.046	0.302	875.126	52.965	2815.240

Error 2σ	FinalAge ^{207}Pb	Error 2σ	FinalAge ^{207}Pb corr	Error 2σ
92.960	529.762	91.338	540.924	32.029
106.463	1172.135	222.557	566.699	28.373
90.633	674.109	119.600	535.329	31.437
72.839	1131.515	122.800	477.481	17.868
650.555	1731.725	1503.007	491.426	65.318
100.707	518.389	88.944	493.353	24.349
402.621	1425.530	823.639	514.901	47.089
733.871	2097.963	1775.199	491.219	101.274
87.493	294.181	55.793	537.999	23.945
73.008	744.932	101.106	470.887	25.189
1916.165	2652.870	2210.725	442.861	110.598
69.645	687.846	98.106	465.824	20.551
450.204	1404.160	646.860	468.862	30.898
257.700	1269.216	535.211	508.853	33.964
67.291	298.548	39.388	520.308	13.476
616.504	1041.468	365.921	509.792	53.515
796.640	4960.341	138.793	173.354	166.386
310.048	4970.679	90.049	448.415	192.587
233.054	4960.341	126.724	290.458	190.335
227.148	4984.340	101.356	16.214	149.925
237.366	4970.679	108.058	1213.151	266.439
488.914	4980.938	256.811	1787.042	681.328
296.499	4648.179	443.019	58.375	22.183
250.174	4970.679	132.071	52.099	109.274
794.837	4958.610	150.993	1428.435	383.614
172.775	4982.640	125.312	29.716	175.671
257.502	4994.495	100.839	1349.044	325.782
214.856	4956.877	102.765	294.640	152.131
315.219	4955.142	72.603	3025.584	362.410
201.440	4965.520	84.263	298.413	150.266
193.469	4977.527	65.809	#VALUE!	#VALUE!
328.378	4958.610	90.596	305.523	352.334
418.073	4977.527	89.739	377.927	205.139
277.274	4982.640	113.377	163.983	232.276
263.842	4951.665	127.277	1120.597	257.702
311.734	4949.923	145.586	1614.651	311.359
300.088	4967.242	84.191	1236.386	215.693
231.042	4989.427	130.831	1385.310	380.925
550.625	4958.610	72.477	0.000	575.783
231.042	4974.107	95.886	2019.055	319.781
549.431	4992.807	118.735	555.995	346.578
308.757	4956.877	132.989	1142.588	284.318
452.969	4948.178	163.927	1142.035	318.379
190.043	4970.679	114.061	453.505	231.514
298.347	4974.107	149.823	302.436	281.536
415.995	4953.404	181.665	133.295	155.659
381.511	4987.733	136.895	1034.133	381.328
396.971	4956.877	151.124	1353.427	577.371

378.495	4979.233	119.549	2833.533	480.231
293.248	4972.394	149.952	509.851	308.671
462.965	4997.862	118.433	-130.682	279.598
257.459	4996.180	94.827	-197.347	489.098
292.972	4975.818	131.730	0.000	440.307
229.949	4951.665	151.520	1649.011	323.759
306.959	4927.067	153.396	284.903	144.066
326.717	4486.026	432.662	240.881	58.641
752.720	4876.472	295.734	215.986	140.621
399.612	4856.061	298.737	144.690	85.455
222.320	4645.995	225.260	213.151	38.401
159.936	4927.067	141.124	410.642	162.251
425.092	4963.796	108.432	154.381	136.028
498.471	4930.609	104.125	1277.305	225.483
208.541	4982.640	89.509	22.592	124.609
214.370	4984.340	184.826	11.632	241.326
436.414	4994.495	148.293	#VALUE!	#VALUE!
252.646	4977.527	107.687	89.122	485.991
299.000	4930.609	134.750	95.542	61.001
460.687	5004.405	53.709	6.502	231.721
388.551	4881.985	156.876	192.831	73.859
396.089	4898.390	180.500	98.343	54.494
288.941	4918.171	234.199	183.128	142.392
250.987	4951.665	163.641	176.617	161.963
275.678	4921.737	153.804	294.494	139.534
238.429	4941.178	146.225	508.316	211.543
432.216	4925.292	147.390	418.053	170.942
176.505	4990.104	50.531	85.941	151.551
364.008	4998.535	45.581	1089.098	210.791
376.084	4984.340	113.280	29.707	181.428
304.859	4987.733	89.279	231.221	227.895
287.136	4972.394	113.963	221.634	197.581
209.523	4937.664	103.758	604.962	163.090
250.814	4977.527	143.583	136.361	237.469
306.146	4992.807	124.672	60.937	305.385
307.869	4970.679	138.074	191.508	214.264
181.082	4951.665	133.337	166.951	130.314
269.097	5007.915	106.050	-292.111	210.425
331.051	4935.904	134.393	553.192	194.834
287.931	4986.038	107.227	63.931	211.814
197.483	4975.818	113.767	1222.400	288.797
638.433	4962.070	120.585	55.597	74.346
186.404	4989.427	172.459	-12.717	301.791
199.009	4982.640	107.410	108.172	204.905
378.480	4986.038	119.141	318.962	289.842
635.157	5002.898	94.506	-364.081	592.728
548.231	5018.556	49.225	-5689.769	1570.951
538.230	4980.938	167.226	69.460	256.182
529.328	5001.222	112.321	-185.542	212.711

259.508	4987.733	142.847	94.260	302.335
1172.992	5037.628	150.897	-1044.046	443.883
271.196	5002.898	94.506	1184.548	347.330
368.524	5006.245	70.760	-330.343	185.316
225.313	5007.915	76.592	-379.474	200.948
1041.727	4992.807	100.925	-53.996	205.832
284.796	4994.495	83.044	-57.780	200.528
356.192	5011.250	105.871	-284.534	187.699
410.547	5004.573	47.803	-307.365	156.854
454.997	4995.843	52.756	-7802.717	2332.840
692.072	5009.583	88.301	#NUM!	#VALUE!
230.315	4999.543	159.749	-155.763	277.938
456.167	5002.898	94.506	1362.315	356.185
612.748	4962.070	96.468	250.041	150.150
170.756	4968.962	162.227	84.012	163.119
234.588	4992.807	136.545	-64.932	230.631
445.279	4963.796	120.480	262.991	483.616
631.357	4974.107	125.851	94.115	166.802
235.417	4984.340	125.205	205.445	273.680
208.541	4946.432	127.611	315.205	162.390
368.000	4953.404	145.332	167.972	146.441
411.446	4997.862	100.668	0.000	481.163
416.023	4986.038	77.441	-3155.743	1795.990
422.511	5042.516	81.051	-2481.884	1398.378
308.621	5004.573	88.524	-377.805	538.007
467.054	5004.573	94.426	#VALUE!	#VALUE!
380.788	4982.640	107.410	571.313	272.291
279.245	4999.543	136.082	-78.477	377.323
916.269	4980.938	149.309	12.180	122.352
772.653	4946.432	115.457	53.430	45.422
1286.787	4928.839	140.999	711.352	271.171
344.565	4942.932	133.922	247.811	143.251
873.401	4912.805	302.802	#VALUE!	#VALUE!
274.172	4443.524	232.240	214.528	30.925
195.031	4726.607	440.157	66.482	31.049
211.362	4903.814	372.442	60.980	74.376
505.921	4932.376	232.544	20.920	26.607
195.753	4061.872	320.915	128.055	14.942
201.619	4453.645	261.979	177.261	27.569
240.739	4846.679	434.222	152.282	145.128
339.327	4703.764	232.792	201.899	47.403
380.411	4880.150	238.669	75.969	48.216
1635.768	4909.216	222.865	450.846	264.043
280.088	4810.418	312.027	75.528	37.426
275.251	5016.235	492.823	-15.672	65.017
455.972	4956.877	544.048	70.717	314.665
114.870	4578.760	174.429	114.759	14.409
117.821	4583.348	391.615	71.561	18.737
234.278	4946.432	528.673	13.827	53.666

221.123	4703.764	376.575	133.839	47.731
111.375	4790.932	137.821	82.315	16.705
151.752	4816.209	200.945	99.169	32.200
204.647	4806.544	149.797	128.112	29.912
346.404	4925.292	141.249	119.771	70.884
116.381	4785.031	164.547	162.759	35.508
163.682	4701.668	191.905	193.780	35.145
156.435	4718.345	394.329	62.974	25.667
1074.274	4992.807	106.862	-60.601	156.173
157.766	4630.604	375.838	60.263	18.031
148.568	4771.159	251.811	92.966	29.878
357.281	4876.472	308.319	115.518	84.267
371.029	4903.814	192.428	46.954	31.521
492.544	4632.813	269.185	126.464	34.150
159.338	4527.234	394.644	158.215	36.017
245.308	4703.764	273.873	150.840	40.746
383.747	5040.889	202.794	-170.967	139.963
127.363	4724.546	264.358	72.288	20.204
756.290	5022.854	81.863	-2386.617	675.423
438.726	4948.178	115.356	99.417	75.963
394.234	4965.520	156.489	90.243	146.224
391.511	4975.818	131.730	21.055	81.868
180.280	4669.830	501.085	106.850	46.083
136.208	4841.019	294.559	53.943	30.307
157.554	4831.531	250.905	58.268	26.375
282.254	4974.107	83.901	77.135	110.125
115.865	4730.719	141.922	264.918	39.298
185.660	4635.019	318.436	210.793	50.081
305.638	4935.904	109.958	244.266	109.290
171.202	4765.170	312.361	215.893	80.750
342.103	4517.650	149.591	264.956	36.371
147.198	4601.546	287.597	178.259	35.503
84.304	4478.622	76.167	241.593	13.545
254.063	4632.813	212.514	76.735	15.731
135.027	4747.041	214.556	118.729	29.155
112.630	4433.327	147.778	262.229	20.956
327.804	4955.142	163.356	99.869	121.045
454.160	4999.543	124.249	-145.643	209.060
435.457	4842.908	428.633	176.853	132.439
149.093	4863.519	449.622	38.718	39.474
142.801	4712.115	211.397	112.256	23.954
133.096	4848.561	510.375	27.571	28.767
226.222	4857.929	247.659	97.968	50.963
1122.010	4693.251	653.752	28.318	17.458
155.963	4730.719	743.399	40.062	32.062
120.783	4783.058	283.294	66.829	25.700
206.730	4850.440	376.052	31.782	29.122
214.759	4956.877	181.349	31.240	55.053
264.534	4996.180	88.900	0.000	450.088
168.279	4104.897	162.035	225.241	18.392

199.673	4578.760	210.768	212.892	30.889
163.283	4488.485	136.474	237.812	21.239
122.750	4435.883	147.604	271.344	22.537
205.225	4610.554	93.070	162.493	17.230
216.052	4632.813	361.274	177.273	47.571
161.356	4619.502	463.376	111.097	37.748
118.479	4389.109	396.845	127.704	22.683
183.197	4857.929	203.208	154.166	62.917
187.683	4821.975	297.334	113.363	54.581

Sample	$^{207}Pb/^{235}U$	Error 2σ	$^{206}Pb/^{238}U$	Error 2σ	rrelation_6_38	$^{238}U/^{206}Pb$
PCA_1	5.420	0.290	0.349	0.014	0.462	2.865
PCA_2	5.910	0.270	0.351	0.012	0.349	2.849
PCA_3	5.570	0.300	0.336	0.014	0.390	2.976
PCA_4	5.570	0.290	0.351	0.012	0.424	2.849
PCA_5	5.980	0.280	0.356	0.016	0.451	2.809
PCA_6	6.170	0.370	0.362	0.011	0.372	2.762
PCA_7	5.690	0.320	0.335	0.011	0.365	2.985
PCA_8	5.470	0.300	0.356	0.012	0.233	2.809
PCA_9	6.050	0.310	0.361	0.014	0.493	2.770
PCA_10	5.480	0.290	0.344	0.012	0.516	2.907
PCA_11	5.520	0.290	0.362	0.014	0.390	2.762
PCA_12	7.900	0.680	0.372	0.014	0.566	2.688
PCA_13	5.340	0.290	0.356	0.014	0.431	2.809
PCA_14	5.070	0.310	0.306	0.010	0.381	3.268
PCA_15	4.950	0.310	0.305	0.011	0.313	3.279
PCA_16	5.470	0.240	0.344	0.010	0.253	2.905
PCA_17	5.420	0.310	0.349	0.012	0.391	2.865
PCA_18	5.720	0.310	0.357	0.014	0.344	2.801
PCA_19	5.690	0.280	0.355	0.011	0.271	2.817
PCA_20	5.320	0.280	0.329	0.011	0.211	3.040
PCA_21	5.200	0.310	0.342	0.013	0.505	2.924
PCA_22	5.320	0.270	0.345	0.011	0.186	2.899
PCA_23	5.470	0.260	0.345	0.012	0.375	2.899
PCA_24	5.670	0.340	0.365	0.014	0.565	2.740
PCA_25	5.590	0.260	0.342	0.010	0.340	2.924
PCA_26	6.480	0.440	0.363	0.016	0.705	2.755
PCA_27	5.620	0.260	0.368	0.013	0.309	2.717
PCA_28	5.700	0.300	0.356	0.015	0.489	2.809
PCA_29	5.210	0.240	0.332	0.012	0.478	3.012
R_R19_1	0.620	0.110	0.076	0.004	0.290	13.141
R_R19_2	0.720	0.110	0.084	0.005	0.010	11.933
R_R19_3	0.561	0.094	0.078	0.005	0.221	12.837
R_R19_4	0.645	0.098	0.082	0.005	0.188	12.255
R_R19_5	0.710	0.100	0.082	0.004	0.164	12.136
R_R19_6	0.760	0.110	0.084	0.004	0.290	11.848
R_R19_7	0.723	0.093	0.081	0.005	0.076	12.285
R_R19_8	0.620	0.100	0.082	0.005	0.010	12.136
R_R19_9	0.557	0.076	0.080	0.005	0.010	12.563
R_R19_10	0.715	0.088	0.086	0.005	0.261	11.682
R_R19_11	0.608	0.098	0.077	0.005	0.122	13.004
R_R19_12	0.595	0.091	0.073	0.003	0.363	13.717
R_R19_13	0.670	0.110	0.081	0.005	0.027	12.346
R_R19_14	0.670	0.096	0.083	0.004	0.218	11.990
R_R19_15	0.631	0.078	0.079	0.005	0.125	12.594
R_R19_16	0.761	0.096	0.080	0.005	0.143	12.453
R_R19_17	0.474	0.079	0.075	0.004	0.188	13.263
R_R19_18	0.557	0.076	0.077	0.004	0.091	12.953
R_R19_19	0.690	0.110	0.091	0.004	0.265	10.989

R_R19_20	0.650	0.110	0.079	0.004	0.117	12.723
R_R19_21	0.643	0.092	0.079	0.004	0.105	12.626
R_R19_22	0.569	0.076	0.070	0.004	0.212	14.306
R_R19_23	0.546	0.090	0.076	0.004	0.222	13.123
R_R19_24	0.682	0.084	0.083	0.004	0.216	12.077
R_R19_25	0.578	0.083	0.084	0.005	0.270	11.933
R_R19_26	~~0.493~~	~~0.080~~	~~0.062~~	~~0.004~~	~~0.198~~	~~16.181~~
R_R19_27	0.462	0.075	0.070	0.005	0.145	14.306
R_R19_28	0.590	0.100	0.076	0.005	0.430	13.245
R_R19_29	0.462	0.074	0.073	0.005	0.158	13.624
R632_1	0.645	0.022	0.081	0.002	0.345	12.407
R632_2	0.653	0.022	0.083	0.001	0.384	12.077
R632_3	0.658	0.022	0.080	0.001	0.270	12.563
R632_4	0.634	0.023	0.081	0.002	0.614	12.346
R632_5	0.620	0.019	0.079	0.001	0.416	12.594
R632_6	0.671	0.016	0.084	0.002	0.353	11.862
R632_7	0.636	0.019	0.080	0.002	0.489	12.531
R632_8	0.631	0.023	0.081	0.002	0.398	12.285
R632_9	0.669	0.027	0.083	0.002	0.381	11.990
R632_10	0.646	0.029	0.080	0.002	0.499	12.500
R632_11	0.611	0.021	0.077	0.002	0.209	12.970
R632_12	0.631	0.022	0.080	0.002	0.484	12.547
R632_13	0.670	0.020	0.085	0.002	0.306	11.751
R632_14	0.668	0.020	0.083	0.002	0.545	12.063
R632_15	0.596	0.018	0.076	0.002	0.140	13.141
R632_16	0.678	0.023	0.084	0.002	0.270	11.905
R632_17	0.628	0.022	0.083	0.002	0.442	12.092
R632_18	0.658	0.024	0.082	0.002	0.354	12.195
R632_19	0.639	0.023	0.082	0.002	0.558	12.255
R632_20	0.632	0.023	0.080	0.002	0.385	12.484
R632_21	0.638	0.023	0.080	0.002	0.202	12.531
R632_22	0.653	0.022	0.083	0.002	0.215	11.990
~~R632_23~~	~~0.573~~	~~0.022~~	~~0.072~~	~~0.002~~	~~0.531~~	~~13.850~~
R632_24	0.700	0.019	0.089	0.002	0.624	11.249
R632_25	0.630	0.018	0.078	0.002	0.329	12.870
~~R632_26~~	~~0.578~~	~~0.020~~	~~0.070~~	~~0.002~~	~~0.475~~	~~14.265~~
~~R632_27~~	~~0.575~~	~~0.022~~	~~0.074~~	~~0.002~~	~~0.614~~	~~13.605~~
R632_28	0.680	0.020	0.083	0.002	0.552	12.019
R632_29	0.685	0.019	0.086	0.002	0.365	11.641
X11B_1	55.100	3.000	0.476	0.025	0.758	2.101
X11B_2	84.100	6.400	0.725	0.064	0.954	1.379
X11B_3	15.600	2.700	0.153	0.026	0.870	6.536
X11B_4	19.700	2.700	0.188	0.022	0.937	5.319
X11B_5	18.580	0.990	0.189	0.009	0.752	5.291
X11B_6	20.780	0.790	0.215	0.008	0.472	4.647
X11B_7	5.270	0.560	0.057	0.005	0.764	17.422
X11B_8	18.100	1.200	0.165	0.010	0.686	6.075
X11B_9	13.200	1.300	0.124	0.012	0.866	8.065

X11B_10	41.400	1.700	0.368	0.016	0.881	2.717
X11B_11	49.800	3.700	0.452	0.031	0.885	2.212
X11B_12	11.750	0.600	0.145	0.007	0.870	6.916
X11B_13	13.840	0.440	0.164	0.005	0.454	6.098
X11B_14	30.650	0.900	0.277	0.008	0.571	3.613
X11B_15	52.100	1.900	0.463	0.023	0.827	2.160
X11B_16	22.300	1.700	0.217	0.016	0.828	4.608
X93_1	108.600	7.500	0.910	0.058	0.966	1.099
X93_2	138.800	6.800	1.204	0.065	0.912	0.831
X93_3	273.000	10.000	2.381	0.092	0.882	0.420
X93_4	360.000	18.000	3.060	0.140	0.907	0.327
X93_5	790.000	130.000	6.900	1.100	0.980	0.145
X93_6	1620.000	470.000	13.900	4.000	0.995	0.072
X93_7	272.000	26.000	2.310	0.210	0.911	0.433
X93_8	1200.000	340.000	10.900	3.300	0.911	0.092
X93_9	650.000	120.000	5.500	1.000	0.985	0.182
X93_10	1170.000	200.000	10.000	1.700	0.986	0.100
X93_11	245.000	24.000	2.270	0.220	0.952	0.441
X93_12	312.000	23.000	2.700	0.190	0.915	0.370
X93_13	236.000	17.000	2.070	0.160	0.927	0.483
X93_14	255.000	18.000	2.200	0.150	0.914	0.455
X93_15	214.000	18.000	1.840	0.150	0.936	0.543
X93_16	287.000	17.000	2.560	0.170	0.913	0.391
X93_17	82.000	13.000	0.760	0.120	0.961	1.316
X93_18	800.000	210.000	7.000	1.800	0.991	0.143
X93_19	437.000	40.000	3.840	0.350	0.934	0.260
X93_20	440.000	65.000	4.040	0.650	0.950	0.248
X93_21	226.000	20.000	1.910	0.170	0.962	0.524
X93_22	560.000	87.000	4.660	0.680	0.979	0.215
X93_23	1410.000	380.000	12.500	3.400	0.993	0.080
X93_24	192.000	15.000	1.700	0.140	0.872	0.588
X93_25	225.000	15.000	1.870	0.130	0.856	0.535
X93_26	920.000	110.000	7.900	1.000	0.981	0.127
X93_27	316.000	32.000	2.690	0.290	0.934	0.372
X93_28	78.400	5.600	0.686	0.040	0.479	1.458
X93_29	238.000	28.000	2.120	0.270	0.950	0.472
X93_30	69.400	6.500	0.623	0.050	0.876	1.605
X93_31	74.100	8.300	0.656	0.071	0.934	1.524
X93_32	173.000	15.000	1.550	0.140	0.961	0.645
X93_33	89.000	16.000	0.790	0.140	0.947	1.266
X93_34	148.000	15.000	1.300	0.120	0.952	0.769
X93_35	131.000	11.000	1.160	0.110	0.953	0.862
X93_36	384.000	28.000	3.330	0.280	0.878	0.300
X93_37	532.000	39.000	4.710	0.360	0.900	0.212
X93_38	970.000	130.000	8.200	1.100	0.974	0.122
X93_39	3230.000	630.000	28.200	5.300	0.989	0.035
X93_40	970.000	190.000	8.500	1.700	0.989	0.118
X93_41	183.000	14.000	1.650	0.130	0.807	0.606
X93_42	156.000	16.000	1.370	0.120	0.879	0.730

X93_43	55.700	5.400	0.488	0.040	0.841	2.049
X93_44	279.000	31.000	2.410	0.300	0.927	0.415
X93_45	2710.000	410.000	22.700	3.300	0.993	0.044
X93_46	399.000	39.000	3.430	0.340	0.920	0.292
X93_47	161.000	18.000	1.360	0.150	0.876	0.735
X93_48	151.000	44.000	1.200	0.240	0.978	0.833
X93_49	111.200	7.900	0.979	0.064	0.885	1.021
X93_50	273.000	23.000	2.290	0.170	0.850	0.437
X93_51	2500.000	780.000	19.300	5.700	0.989	0.052
X93_52	262.000	56.000	2.160	0.470	0.981	0.463
X93_53	212.000	22.000	1.910	0.200	0.902	0.524
X93_54	1620.000	220.000	14.200	1.900	0.991	0.070
X93_55	130.000	11.000	1.104	0.088	0.890	0.906
X93_56	320.000	32.000	2.710	0.280	0.890	0.369
X93_57	66.700	5.300	0.600	0.045	0.851	1.667
X96_1	590.000	120.000	5.100	1.100	0.989	0.196
X96_2	316.000	35.000	2.620	0.280	0.985	0.382
X96_3	415.000	23.000	3.610	0.220	0.955	0.277
X96_4	165.000	6.800	1.407	0.061	0.889	0.711
X96_5	2380.000	280.000	21.200	2.700	0.984	0.047
X96_6	304.000	31.000	2.570	0.260	0.985	0.389
X96_7	323.000	18.000	2.780	0.160	0.936	0.360
X96_8	1278.000	72.000	10.770	0.600	0.973	0.093
X96_9	136.000	13.000	1.150	0.100	0.946	0.870
X96_10	5.240	0.360	0.050	0.003	0.955	19.881
X96_11	197.000	13.000	1.670	0.110	0.939	0.599
X96_12	262.000	35.000	2.320	0.320	0.982	0.431
X96_13	45.700	4.900	0.412	0.047	0.917	2.427
X96_14	157.900	8.500	1.356	0.078	0.925	0.737
X96_15	1405.000	77.000	12.050	0.740	0.926	0.083
X96_16	314.000	20.000	2.690	0.180	0.961	0.372
X96_17	147.000	5.700	1.299	0.053	0.918	0.770
X96_18	602.000	24.000	5.140	0.190	0.952	0.195
X96_19	5750.000	740.000	50.200	6.400	0.991	0.020
X96_20	439.000	38.000	3.790	0.320	0.965	0.264
X96_21	234.000	40.000	2.030	0.330	0.985	0.493
X96_22	1470.000	320.000	12.400	2.700	0.995	0.081
X96_23	461.000	33.000	3.960	0.280	0.975	0.253
X96_24	299.000	17.000	2.660	0.150	0.943	0.376
X96_25	185.000	43.000	1.620	0.390	0.991	0.617
X96_26	107.500	9.500	0.962	0.092	0.940	1.040
X96_27	339.000	30.000	3.020	0.290	0.947	0.331
X96_30	920.000	320.000	6.900	1.900	0.998	0.145
X96_31	451.000	25.000	3.780	0.210	0.916	0.265
X96_32	153.000	22.000	1.300	0.180	0.981	0.769
X96_33	326.000	17.000	2.890	0.160	0.918	0.346
X96_34	337.000	24.000	2.890	0.200	0.967	0.346
X96_35	1520.000	130.000	13.000	1.100	0.978	0.077
X96_36	1620.000	120.000	13.740	0.960	0.980	0.073

X96_37	700.000	46.000	6.020	0.390	0.977	0.166
X96_38	1750.000	250.000	14.600	2.100	0.995	0.068
X96_39	3060.000	450.000	26.100	3.700	0.984	0.038
X96_40	81.800	6.700	0.682	0.060	0.763	1.466
X96_41	32.300	3.100	0.301	0.035	0.888	3.322
X96_42	3600.000	1400.000	30.000	12.000	0.999	0.033
X96_43	565.000	30.000	4.900	0.270	0.926	0.204
X96_44	495.000	42.000	4.040	0.340	0.929	0.248
X96_45	630.000	59.000	5.450	0.510	0.979	0.183
X96_46	222.000	31.000	1.950	0.260	0.990	0.513
X96_47	108.000	18.000	0.980	0.170	0.994	1.020
X96_48	505.000	52.000	4.360	0.450	0.985	0.229
X96_49	2450.000	280.000	20.900	2.400	0.987	0.048
X96_50	150.000	22.000	1.320	0.200	0.980	0.758
X96_51	275.000	19.000	2.280	0.170	0.955	0.439
X96_52	92.000	8.100	0.799	0.071	0.917	1.252
X96_53	940.000	190.000	8.500	1.800	0.994	0.118
X96_54	112.000	17.000	0.880	0.130	0.966	1.136
X96_55	1510.000	110.000	12.610	0.900	0.962	0.079
X96_56	200.000	11.000	1.725	0.091	0.964	0.580
X96_57	172.400	5.800	1.482	0.053	0.854	0.675
X96_58	1019.000	97.000	8.650	0.790	0.983	0.116
X96_59	144.000	11.000	1.268	0.096	0.932	0.789
X96_60	46.500	3.100	0.401	0.026	0.845	2.494
X96_61	73.300	3.300	0.636	0.028	0.852	1.572
X96_62	16.700	2.000	0.155	0.019	0.885	6.452
X96_63	66.100	4.500	0.571	0.039	0.915	1.751
X96_64	292.000	16.000	2.430	0.150	0.950	0.412
X96_65	217.000	21.000	1.850	0.180	0.931	0.541
X96_66	2220.000	310.000	18.900	2.600	0.993	0.053
X96_67	86.000	6.600	0.759	0.056	0.907	1.318
X96_68	124.000	26.000	1.070	0.210	0.996	0.935
X96_69	247.000	22.000	2.150	0.180	0.827	0.465
X96_70	730.000	120.000	6.300	1.100	0.964	0.159
X96_71	154.000	12.000	1.350	0.110	0.960	0.741
X96_72	63.100	3.500	0.565	0.028	0.764	1.770
X96_73	862.000	79.000	7.260	0.640	0.974	0.138
X96_74	318.000	42.000	2.750	0.340	0.979	0.364
X96_75	1007.000	84.000	8.440	0.680	0.966	0.118
X96_76	203.000	24.000	1.710	0.180	0.973	0.585
X96_77	361.000	58.000	3.200	0.510	0.985	0.313
X96_78	87.000	12.000	0.780	0.110	0.972	1.282
X96_79	173.000	16.000	1.480	0.140	0.962	0.676
X96_80	116.000	11.000	0.990	0.081	0.964	1.010
X96_81	540.000	100.000	4.390	0.830	0.995	0.228
X96_82	1062.000	80.000	9.320	0.700	0.970	0.107
X96_83	64.000	11.000	0.554	0.095	0.991	1.805
X96_84	7.400	1.300	0.070	0.013	0.990	14.286
X96_85	95.600	4.600	0.836	0.037	0.856	1.196
X96_86	480.000	51.000	4.220	0.440	0.937	0.237

X96_87	360.000	200.000	3.000	1.700	0.987	0.333
X96_88	171.000	14.000	1.460	0.120	0.958	0.685
X96_89	319.000	17.000	2.800	0.150	0.930	0.357
X96_90	151.000	23.000	1.260	0.190	0.975	0.794
X96_91	100.000	15.000	0.840	0.120	0.991	1.190
X96_92	194.000	12.000	1.650	0.110	0.961	0.606
X96_93	273.000	16.000	2.330	0.140	0.932	0.429
X96_94	204.000	11.000	1.752	0.086	0.948	0.571
X96_95	178.900	8.300	1.527	0.074	0.956	0.655
X96_96	254.000	17.000	2.220	0.140	0.951	0.450

Error 2σ	$^{207}Pb/^{206}Pb$	Error 2σ	orrelation_38_	alAge $^{206}Pb/^{23}$	Error 2σ	alAge $^{207}Pb/^{23}$
0.115	0.112	0.005	0.329	1929.822	77.414	1888.022
0.097	0.121	0.007	0.321	1939.372	66.303	1962.705
0.124	0.118	0.007	0.383	1867.398	77.808	1911.473
0.097	0.117	0.006	0.307	1939.372	66.303	1911.473
0.126	0.123	0.006	0.290	1963.186	88.233	1972.939
0.084	0.118	0.007	0.188	1991.647	60.520	2000.209
0.098	0.123	0.007	0.325	1862.571	61.159	1929.851
0.095	0.112	0.007	0.357	1963.186	66.175	1895.899
0.107	0.122	0.006	0.251	1986.912	77.055	1983.071
0.101	0.118	0.006	0.255	1905.884	66.484	1897.467
0.107	0.113	0.006	0.331	1991.647	77.025	1903.716
0.101	0.153	0.012	-0.133	2038.804	76.729	2219.679
0.110	0.113	0.006	0.333	1963.186	77.204	1875.289
0.107	0.116	0.007	0.260	1720.993	56.242	1831.100
0.118	0.116	0.007	0.327	1716.055	61.891	1810.825
0.081	0.114	0.005	0.311	1906.843	53.183	1895.899
0.099	0.115	0.006	0.262	1929.822	66.355	1888.022
0.110	0.117	0.006	0.398	1967.938	77.174	1934.394
0.087	0.120	0.006	0.280	1958.430	60.684	1929.851
0.102	0.118	0.007	0.400	1833.533	61.304	1872.081
0.111	0.111	0.006	0.194	1896.284	72.081	1852.616
0.092	0.112	0.006	0.375	1910.679	60.920	1872.081
0.101	0.117	0.006	0.404	1910.679	66.458	1895.899
0.105	0.113	0.006	0.015	2005.830	76.936	1926.811
0.085	0.118	0.006	0.356	1896.284	55.447	1914.559
0.121	0.129	0.006	-0.165	1996.378	87.995	2043.187
0.096	0.109	0.005	0.342	2019.983	71.358	1919.171
0.118	0.115	0.005	0.433	1963.186	82.719	1931.368
0.109	0.118	0.005	0.285	1848.068	66.798	1854.253
0.691	0.053	0.009	-0.009	472.802	24.852	489.847
0.712	0.064	0.010	0.264	518.765	30.953	550.667
0.791	0.055	0.009	0.207	483.576	29.797	452.177
0.781	0.057	0.009	0.403	505.666	32.224	505.397
0.604	0.062	0.009	0.238	510.432	25.398	544.746
0.547	0.068	0.010	-0.064	522.333	24.136	574.010
0.679	0.064	0.009	0.378	504.474	27.889	552.436
0.766	0.057	0.009	0.256	510.432	32.212	489.847
0.726	0.053	0.008	0.231	493.735	28.532	449.572
0.641	0.061	0.007	0.201	529.462	29.071	547.711
0.795	0.062	0.011	0.227	477.593	29.190	482.298
0.640	0.058	0.008	-0.023	453.604	21.156	474.056
0.716	0.062	0.010	0.375	502.089	29.134	520.712
0.532	0.055	0.008	0.047	516.385	22.909	520.712
0.746	0.061	0.009	0.175	492.540	29.155	496.719
0.775	0.072	0.010	0.352	497.913	31.003	574.587
0.721	0.048	0.009	0.243	468.607	25.481	393.948
0.654	0.053	0.007	0.187	479.388	24.218	449.572
0.531	0.055	0.009	0.076	561.449	27.147	532.800

0.696	0.059	0.009	0.353	487.761	26.684	508.479
0.686	0.060	0.009	0.325	491.346	26.677	504.162
0.737	0.059	0.008	0.010	435.553	22.432	457.368
0.672	0.056	0.009	0.179	473.401	24.229	442.373
0.627	0.061	0.008	0.306	512.814	26.632	527.982
0.669	0.053	0.008	0.130	518.765	29.095	463.175
~~1.021~~	~~0.056~~	0.009	0.223	386.563	24.395	406.953
1.023	0.044	0.008	0.171	435.553	31.155	385.648
0.789	0.054	0.009	-0.183	469.207	27.966	470.868
0.928	0.043	0.007	0.160	456.607	31.104	385.648
0.262	0.058	0.002	0.300	499.703	10.540	505.397
0.204	0.057	0.002	0.134	512.814	8.671	510.323
0.221	0.060	0.002	0.218	493.735	8.684	513.390
0.274	0.056	0.002	0.081	502.089	11.158	498.585
0.206	0.057	0.002	0.074	492.540	8.064	489.847
0.211	0.058	0.002	0.309	521.738	9.284	521.320
0.283	0.057	0.002	0.354	494.929	11.164	499.827
0.241	0.057	0.002	0.128	504.474	9.916	496.719
0.259	0.060	0.002	0.163	516.385	11.145	520.104
0.250	0.059	0.002	0.029	496.123	9.922	506.014
0.252	0.056	0.002	0.301	478.790	9.315	484.191
0.252	0.058	0.002	0.041	494.332	9.924	496.719
0.235	0.059	0.002	0.314	526.492	10.517	520.712
0.306	0.059	0.002	0.283	513.409	13.006	519.496
0.259	0.057	0.002	0.442	472.802	9.319	474.692
0.227	0.059	0.002	0.331	519.954	9.904	525.565
0.234	0.055	0.002	0.221	512.219	9.910	494.849
0.238	0.058	0.002	0.197	508.050	9.913	513.390
0.285	0.057	0.002	-0.009	505.666	11.774	501.687
0.265	0.058	0.002	0.121	496.720	10.542	497.341
0.283	0.057	0.002	0.455	494.929	11.164	501.067
0.244	0.057	0.002	0.422	516.385	10.526	510.323
~~0.345~~	~~0.058~~	0.002	0.170	449.396	11.204	459.953
0.202	0.057	0.001	0.005	549.028	9.881	538.791
0.282	0.059	0.002	0.398	482.380	10.554	496.096
~~0.387~~	~~0.060~~	0.002	0.373	436.758	11.838	463.175
~~0.370~~	~~0.059~~	0.002	0.165	457.208	12.441	461.243
0.246	0.059	0.002	0.119	515.195	10.527	526.774
0.217	0.058	0.002	0.362	531.243	9.895	529.792
0.110	0.837	0.030	0.318	2509.819	131.818	4089.085
0.122	0.817	0.020	0.026	3514.759	310.268	4512.187
1.111	0.720	0.046	0.010	917.758	155.959	2852.620
0.622	0.749	0.035	-0.040	1110.532	129.956	3076.746
0.260	0.715	0.026	0.340	1115.956	54.912	3020.266
0.175	0.716	0.027	0.468	1256.462	47.292	3128.387
1.427	0.622	0.041	0.001	359.794	29.460	1864.016
0.351	0.814	0.040	0.165	982.290	56.694	2995.064
0.780	0.776	0.040	0.432	753.546	72.924	2694.057

0.118	0.809	0.017	0.136	2019.983	87.825	3804.791
0.152	0.808	0.028	-0.119	2404.138	164.886	3988.319
0.349	0.596	0.016	0.258	870.622	43.953	2584.689
0.193	0.613	0.021	0.567	978.968	31.040	2738.819
0.110	0.802	0.022	0.474	1575.226	47.803	3507.883
0.107	0.824	0.022	0.693	2452.790	121.845	4033.281
0.340	0.751	0.034	0.140	1266.004	93.346	3196.886
0.070	0.852	0.023	0.406	4171.496	265.876	4769.089
0.045	0.830	0.017	0.462	5094.433	275.032	5016.208
0.016	0.842	0.017	0.481	7852.838	303.428	5699.475
0.015	0.855	0.018	0.179	9032.606	413.256	5979.467
0.023	0.840	0.035	0.064	13323.853	2124.093	6775.954
0.021	0.843	0.029	-0.153	17414.093	5011.250	7504.492
0.039	0.820	0.030	0.195	7716.024	701.457	5695.763
0.028	0.822	0.026	0.165	15964.792	4833.377	7199.990
0.033	0.842	0.024	0.169	12066.412	2193.893	6578.169
0.017	0.861	0.029	0.244	15457.826	2627.830	7174.304
0.043	0.792	0.027	0.142	7637.647	740.212	5590.020
0.026	0.830	0.026	0.288	8434.055	593.508	5834.597
0.037	0.821	0.025	0.358	7230.798	558.902	5552.176
0.031	0.835	0.022	0.236	7498.152	511.238	5630.479
0.044	0.844	0.024	0.200	6728.793	548.543	5453.255
0.026	0.825	0.025	0.337	8185.402	543.562	5750.074
0.208	0.836	0.032	-0.348	3644.247	575.407	4486.816
0.037	0.841	0.025	0.298	13404.941	3446.985	6788.710
0.024	0.843	0.026	0.232	10165.445	926.538	6175.782
0.040	0.839	0.035	0.334	10426.470	1677.526	6182.713
0.047	0.855	0.020	0.126	6885.757	612.868	5508.402
0.031	0.845	0.026	0.175	11174.368	1630.595	6427.091
0.022	0.823	0.032	0.534	16778.016	4563.620	7363.613
0.048	0.818	0.031	0.171	6402.912	527.299	5343.646
0.037	0.868	0.032	0.230	6796.532	472.486	5503.919
0.016	0.846	0.026	0.131	14092.192	1783.822	6930.456
0.040	0.868	0.041	0.185	8416.609	907.367	5847.491
0.085	0.808	0.051	0.385	3367.342	196.346	4441.792
0.060	0.838	0.034	0.116	7334.943	934.167	5560.708
0.129	0.824	0.034	-0.015	3121.846	250.549	4319.636
0.165	0.814	0.032	0.216	3251.604	351.927	4385.257
0.058	0.829	0.026	0.177	6034.446	545.047	5238.417
0.224	0.842	0.061	0.340	3753.203	665.125	4569.030
0.071	0.813	0.022	-0.024	5369.277	495.626	5080.922
0.082	0.837	0.027	0.388	4964.437	470.766	4957.914
0.025	0.833	0.033	0.546	9447.655	794.397	6044.822
0.016	0.812	0.025	0.395	11231.065	858.425	6375.104
0.016	0.847	0.025	0.314	14305.905	1919.085	6984.136
0.007	0.833	0.025	0.325	21751.289	4088.008	8204.850
0.024	0.857	0.033	0.116	14512.759	2902.552	6984.136
0.048	0.812	0.041	0.195	6282.415	494.978	5295.157
0.064	0.857	0.041	-0.145	5562.546	487.230	5134.026

0.168	0.812	0.039	0.132	2562.017	210.001	4099.888
0.052	0.847	0.033	0.079	7907.896	984.385	5721.470
0.006	0.833	0.018	0.238	20405.963	2966.506	8026.677
0.029	0.816	0.035	0.426	9594.840	951.092	6083.632
0.081	0.841	0.036	0.376	5535.288	610.510	5165.859
0.167	0.805	0.063	-0.001	5082.723	1016.545	5101.163
0.067	0.834	0.028	0.129	4400.269	287.658	4792.895
0.032	0.847	0.036	-0.076	7676.954	569.905	5699.475
0.015	0.850	0.032	-0.105	19407.709	5731.810	7944.810
0.101	0.856	0.036	0.052	7417.064	1613.898	5657.871
0.055	0.811	0.028	0.041	6885.757	721.022	5443.765
0.009	0.831	0.017	-0.269	17542.597	2347.249	7504.492
0.072	0.864	0.041	0.462	4795.103	382.218	4950.193
0.038	0.848	0.027	0.228	8451.454	873.213	5860.224
0.125	0.800	0.034	0.299	3029.838	227.238	4279.927
0.042	0.846	0.025	0.209	11656.978	2514.250	6479.988
0.041	0.856	0.016	0.055	8293.144	886.290	5847.491
0.017	0.833	0.015	0.281	9851.590	600.374	6123.456
0.031	0.844	0.017	0.470	5662.409	245.492	5190.626
0.006	0.836	0.019	-0.029	19984.479	2545.193	7894.883
0.039	0.858	0.015	0.043	8203.485	829.925	5808.308
0.021	0.839	0.017	0.303	8571.952	493.350	5869.669
0.005	0.858	0.011	0.087	15893.982	885.459	7263.882
0.076	0.834	0.028	0.118	4934.523	429.089	4995.665
1.304	0.759	0.016	-0.129	316.363	20.755	1859.146
0.039	0.855	0.019	0.373	6330.885	417.004	5369.617
0.059	0.824	0.018	-0.069	7735.470	1066.961	5657.871
0.277	0.830	0.047	0.413	2224.059	253.715	3902.873
0.042	0.844	0.020	0.380	5524.353	317.773	5146.241
0.005	0.852	0.017	0.247	16559.472	1016.930	7360.008
0.025	0.860	0.018	0.210	8416.609	563.193	5841.065
0.031	0.823	0.020	0.132	5366.474	218.955	5074.085
0.007	0.852	0.012	0.079	11699.112	432.457	6500.398
0.003	0.837	0.015	0.221	25371.407	3234.602	8790.302
0.022	0.841	0.018	0.034	10098.504	852.644	6180.408
0.080	0.817	0.021	-0.179	7146.254	1161.706	5543.571
0.018	0.857	0.017	-0.028	16730.087	3642.841	7405.897
0.018	0.849	0.013	0.106	10323.325	729.932	6229.949
0.021	0.813	0.016	0.283	8363.985	471.653	5791.524
0.149	0.846	0.032	0.158	6209.021	1494.764	5306.135
0.099	0.806	0.027	0.279	4344.653	415.497	4758.847
0.032	0.829	0.025	0.345	8968.779	861.240	5918.613
0.040	0.848	0.016	-0.092	13323.853	3668.887	6930.456
0.015	0.856	0.018	0.223	10085.032	560.280	6207.729
0.107	0.847	0.021	-0.024	5369.277	743.438	5114.436
0.019	0.837	0.019	0.294	8756.868	484.809	5879.027
0.024	0.837	0.016	0.119	8756.868	606.012	5912.622
0.007	0.848	0.014	0.025	17012.457	1439.516	7439.837
0.005	0.855	0.015	-0.028	17344.496	1211.842	7504.492

0.011	0.847	0.014	0.061	12562.535	813.852	6653.305
0.010	0.848	0.014	0.064	17710.046	2547.335	7582.822
0.005	0.854	0.021	0.026	21270.161	3015.310	8149.969
0.129	0.862	0.048	0.409	3352.029	294.900	4484.366
0.386	0.803	0.026	0.259	1696.266	197.240	3559.484
0.013	0.854	0.013	-0.121	22136.904	8854.762	8314.938
0.011	0.838	0.017	0.144	11442.078	630.482	6436.101
0.021	0.866	0.026	0.386	10426.470	877.475	6302.052
0.017	0.843	0.018	-0.001	12016.633	1124.492	6546.485
0.068	0.828	0.017	-0.217	6973.764	929.835	5490.351
0.177	0.829	0.019	0.087	4403.525	763.877	4763.515
0.024	0.847	0.014	0.008	10823.297	1117.083	6322.320
0.005	0.848	0.019	0.208	19896.771	2284.797	7924.305
0.115	0.820	0.024	0.030	5425.091	821.983	5094.461
0.033	0.860	0.017	0.190	7657.331	570.941	5706.860
0.111	0.835	0.038	0.382	3785.534	336.387	4602.325
0.025	0.839	0.019	0.172	14512.759	3073.290	6952.270
0.168	0.848	0.031	-0.229	4069.439	601.167	4800.109
0.006	0.855	0.016	0.355	16830.329	1201.213	7433.139
0.031	0.851	0.013	0.180	6462.327	340.911	5384.886
0.024	0.857	0.016	0.453	5860.207	209.576	5234.910
0.011	0.859	0.017	0.071	14613.750	1334.666	7034.125
0.060	0.828	0.023	0.318	5278.958	399.669	5053.291
0.162	0.821	0.026	0.127	2173.642	140.934	3920.120
0.069	0.842	0.019	0.204	3173.275	139.704	4374.383
0.791	0.790	0.049	0.420	928.931	113.869	2917.769
0.120	0.837	0.023	0.204	2911.925	198.888	4270.888
0.025	0.874	0.020	0.429	7945.594	490.469	5767.551
0.053	0.847	0.022	0.064	6751.452	656.898	5467.325
0.007	0.853	0.013	0.197	19279.418	2652.195	7824.250
0.097	0.830	0.027	0.206	3640.583	268.607	4534.607
0.183	0.827	0.021	0.167	4690.080	920.483	4902.588
0.039	0.844	0.044	0.334	7396.631	619.253	5598.242
0.028	0.828	0.035	0.191	12814.661	2237.481	6695.856
0.060	0.842	0.024	0.048	5507.915	448.793	5121.008
0.088	0.810	0.030	0.227	2887.258	143.085	4224.445
0.012	0.864	0.017	0.000	13611.117	1199.878	6864.411
0.045	0.851	0.026	-0.226	8520.586	1053.454	5853.877
0.010	0.840	0.017	0.217	14471.916	1165.984	7022.108
0.062	0.846	0.025	-0.113	6426.744	676.499	5399.929
0.050	0.839	0.019	0.103	9251.149	1474.402	5982.276
0.181	0.819	0.029	0.043	3717.089	524.205	4546.212
0.064	0.833	0.020	-0.126	5855.011	553.852	5238.417
0.083	0.826	0.024	-0.150	4436.001	362.946	4835.431
0.043	0.858	0.014	-0.321	10859.277	2053.121	6390.231
0.008	0.838	0.018	-0.088	15046.471	1130.100	7076.053
0.310	0.822	0.022	-0.066	2841.787	487.310	4238.602
2.653	0.766	0.042	0.139	436.156	81.000	2160.970
0.053	0.840	0.024	0.212	3916.772	173.350	4640.888
0.025	0.834	0.016	0.070	10652.683	1110.706	6270.871

0.189	0.834	0.025	0.047	8936.628	5064.089	5979.467
0.056	0.859	0.018	0.288	5802.813	476.944	5226.679
0.019	0.831	0.016	0.159	8605.970	461.034	5857.055
0.120	0.855	0.026	-0.126	5256.179	792.598	5101.163
0.170	0.836	0.017	-0.043	3930.801	561.543	4686.115
0.040	0.849	0.020	0.444	6282.415	418.828	5354.114
0.026	0.841	0.018	0.348	7754.858	465.957	5699.475
0.028	0.855	0.014	-0.145	6525.885	320.335	5404.894
0.032	0.845	0.015	0.399	5976.038	289.605	5272.276
0.028	0.838	0.018	-0.063	7538.317	475.389	5626.505

Error 2σ	alAge $^{207}Pb/^{206}$	Error 2σ	alAge 207Pb c	Error 2σ
101.020	1835.353	86.697	1943.094	78.102
89.667	1966.596	105.906	1935.338	67.059
102.952	1927.673	109.360	1859.215	77.441
99.520	1910.892	94.728	1943.515	67.073
92.378	2000.193	95.944	1957.502	88.297
119.948	1923.116	111.012	2002.218	62.645
108.533	1998.748	107.337	1843.730	61.018
103.980	1832.121	109.600	1982.234	68.169
101.612	1979.834	91.177	1988.019	77.816
100.413	1929.190	96.296	1902.590	66.723
100.014	1843.404	99.776	2013.927	79.029
191.061	2379.728	186.645	1974.421	79.069
101.842	1846.612	98.137	1980.208	78.631
111.961	1890.811	106.225	1701.423	55.434
113.405	1901.658	120.896	1694.696	61.011
83.184	1870.454	88.291	1911.893	53.947
107.986	1881.450	101.347	1936.721	67.328
104.836	1906.282	102.910	1977.164	78.400
94.966	1957.705	92.914	1958.539	61.563
98.531	1930.704	110.979	1820.782	61.265
110.444	1819.120	98.154	1906.697	72.701
95.012	1836.967	101.418	1920.835	62.019
90.116	1917.017	97.974	1909.782	66.873
115.541	1843.404	89.962	2030.610	78.972
89.049	1930.704	89.762	1891.464	55.783
138.735	2087.113	103.386	1981.528	88.125
88.787	1784.441	83.416	2055.776	73.874
101.651	1878.317	88.276	1975.708	83.652
85.417	1926.156	88.146	1837.682	66.131
86.908	328.797	58.315	474.807	24.993
84.130	741.630	115.880	514.845	30.643
75.766	408.153	68.397	484.679	29.689
76.789	495.398	74.613	505.828	31.924
76.725	670.656	98.594	507.727	25.305
83.080	856.315	120.340	516.186	24.046
71.060	751.514	102.851	500.248	27.548
79.008	475.982	79.050	510.979	32.022
61.342	345.831	51.810	495.907	28.410
67.411	635.704	76.201	527.615	28.659
77.739	674.109	119.600	474.507	29.067
72.503	529.762	76.724	452.525	21.169
85.490	674.109	108.727	499.234	28.947
74.610	424.372	60.625	517.840	22.964
61.401	632.166	88.378	490.303	28.817
72.484	977.437	130.870	489.197	30.331
65.658	94.333	17.134	473.416	25.657
61.342	320.212	44.272	481.633	24.165
84.939	424.372	70.601	563.829	27.287

86.050	555.987	89.034	486.705	26.613
72.135	585.440	84.618	489.864	26.494
61.090	559.699	72.342	433.854	22.256
72.919	464.219	77.507	473.534	24.308
65.030	646.271	81.312	510.567	26.332
66.511	333.072	47.044	521.635	28.946
66.037	448.399	73.797	385.845	24.292
62.605	-88.460	-14.942	441.441	31.179
79.808	383.513	64.272	470.410	27.910
61.770	-150.333	-23.956	463.663	31.142
17.238	533.535	17.448	499.169	10.352
17.193	499.252	14.838	513.032	8.537
17.165	599.964	19.031	492.045	8.535
18.087	448.399	12.834	502.918	10.963
15.011	479.884	13.542	492.734	7.943
12.431	522.189	14.455	521.731	9.120
14.932	506.935	13.247	494.743	10.944
18.105	475.982	16.819	504.920	9.773
20.991	599.964	22.035	514.988	10.941
22.716	552.267	20.734	495.238	9.770
16.642	460.278	16.380	479.062	9.188
17.318	533.535	17.448	493.720	9.754
15.544	548.538	15.003	526.122	10.311
15.554	548.538	15.940	512.835	12.732
14.336	495.398	15.617	472.470	9.168
17.829	578.128	17.549	518.981	9.719
17.335	424.372	13.813	513.596	9.768
18.725	525.980	16.352	507.762	9.741
18.058	506.935	16.780	505.646	11.561
18.099	518.389	17.968	496.382	10.366
18.064	479.884	18.620	495.160	10.995
17.193	487.660	17.998	516.849	10.371
17.660	537.299	19.387	448.161	11.000
14.624	503.098	10.536	549.826	9.685
14.174	567.096	17.301	481.080	10.346
16.027	585.440	19.679	434.701	11.592
17.648	548.538	15.003	455.895	12.176
15.493	570.782	15.453	514.277	10.311
14.695	518.389	14.375	531.460	9.716
222.636	4986.038	178.711	-6.510	121.171
343.377	4951.665	121.216	176.223	124.623
493.723	4771.159	304.824	153.718	62.167
421.686	4827.717	225.594	144.546	56.037
160.929	4761.163	173.133	200.933	41.233
118.933	4763.168	179.617	229.490	47.770
198.074	4560.250	300.595	101.792	20.785
198.568	4946.432	243.068	31.646	54.559
265.324	4878.312	251.459	63.973	41.217

156.235	4937.664	103.758	97.770	55.676
296.321	4935.904	171.046	131.288	105.298
131.984	4498.277	120.759	294.026	24.003
87.072	4539.118	155.500	312.456	29.273
103.005	4925.292	135.108	87.761	52.108
147.087	4963.796	132.529	57.886	87.873
243.709	4831.531	218.738	165.305	61.010
329.357	5011.250	135.280	-214.530	189.955
245.751	4974.107	101.879	192.279	179.259
208.772	4994.495	100.839	949.020	317.425
298.973	5016.235	105.605	-484.607	526.826
1115.030	4991.118	207.963	-6698.243	6170.266
2177.229	4996.180	171.873	0.000	4155.742
544.448	4956.877	181.349	0.000	569.772
2039.997	4960.341	156.896	0.000	3281.484
1214.431	4994.495	142.361	-4742.728	2748.354
1226.377	5026.151	169.290	-2406.996	3450.406
547.594	4907.418	167.298	1609.095	472.860
430.115	4974.107	155.815	0.000	572.979
399.945	4958.610	150.993	2111.130	389.962
397.446	4982.640	131.279	1294.628	357.764
458.685	4997.862	142.119	-30.103	380.375
340.597	4965.520	150.470	0.000	523.338
711.324	4984.340	190.788	2.541	204.962
1782.036	4992.807	148.419	-11193.841	11797.549
565.289	4996.180	154.093	-728.047	954.297
913.355	4989.427	208.141	-353.954	1248.184
487.469	5016.235	117.339	-890.326	402.674
998.495	4999.543	153.832	-1334.809	1283.412
1984.520	4962.070	192.936	0.000	4007.151
417.472	4953.404	187.721	1189.794	379.418
366.928	5037.628	185.719	-2082.530	754.107
828.642	5001.222	153.702	0.000	2939.200
592.151	5037.628	237.952	-6614.516	3134.434
317.271	4935.904	311.548	235.227	277.108
654.201	4987.733	202.366	809.326	536.915
404.577	4963.796	204.817	88.365	175.106
491.196	4946.432	194.454	173.780	172.160
454.198	4972.394	155.950	486.031	318.436
821.399	4994.495	361.834	-61.574	401.548
514.958	4944.683	133.804	673.073	228.725
416.313	4986.038	160.840	22.991	265.778
440.768	4979.233	197.257	192.377	902.121
467.348	4942.932	152.184	#NUM!	#VALUE!
936.018	5002.898	147.665	0.000	3391.160
1600.327	4979.233	149.437	0.000	6066.830
1368.027	5019.549	193.285	-1638.437	2947.108
405.094	4942.932	249.582	1328.142	468.519
526.567	5019.549	240.142	-585.610	522.277

397.476	4942.932	237.407	124.561	155.375
635.719	5002.898	194.918	276.740	631.691
1214.368	4979.233	107.594	#VALUE!	#VALUE!
594.641	4949.923	212.313	3187.661	1727.165
577.549	4992.807	213.723	-48.540	412.158
1486.432	4930.609	385.874	718.123	565.258
340.502	4980.938	167.226	47.785	231.064
480.176	5002.898	212.638	92.096	670.812
2478.781	5007.915	188.533	#VALUE!	#VALUE!
1209.316	5017.893	211.033	-1172.322	839.330
564.919	4941.178	170.596	2176.854	428.209
1019.128	4975.818	101.792	#VALUE!	#VALUE!
418.862	5031.082	238.743	-552.576	420.327
586.022	5004.573	159.344	764.786	554.463
340.084	4921.737	209.174	246.466	164.433
1317.964	5001.222	147.790	-1776.273	1495.844
647.665	5017.893	93.792	-1331.355	504.329
339.372	4979.233	89.662	219.362	491.529
213.917	4997.862	100.668	-142.844	222.684
928.810	4984.340	113.280	-66.077	3618.676
592.295	5021.203	87.783	-1859.514	538.210
327.102	4989.427	101.097	3438.879	1001.142
409.233	5021.203	64.374	-2264.366	1667.933
477.527	4980.938	167.226	84.741	269.386
127.728	4846.679	102.170	32.173	7.522
354.340	5016.235	111.472	-722.033	325.290
755.822	4963.796	108.432	3106.419	756.651
418.470	4974.107	281.666	24.267	159.822
277.030	4997.862	118.433	-143.222	245.657
403.360	5011.250	99.990	-1798.165	2369.308
372.042	5024.504	105.164	-2622.357	714.560
196.750	4962.070	120.585	424.705	212.524
259.152	5011.250	70.581	-3121.563	1012.100
1131.274	4986.038	89.356	#VALUE!	#VALUE!
534.978	4992.807	106.862	-511.807	662.611
947.619	4951.665	127.277	2259.699	483.485
1612.168	5019.549	99.571	#VALUE!	#VALUE!
445.962	5006.245	76.656	-443.475	529.363
329.284	4944.683	97.312	1097.356	349.049
1233.318	5001.222	189.172	-216.036	454.700
420.549	4932.376	165.228	444.503	208.108
523.771	4972.394	149.952	161.842	638.826
2410.594	5004.573	94.426	#VALUE!	#VALUE!
344.109	5017.893	105.516	1890.887	520.857
735.409	5002.898	124.039	-228.930	251.663
306.575	4986.038	113.184	0.000	468.653
421.077	4986.038	95.313	0.000	478.158
636.302	5004.573	82.623	0.000	2066.125
555.888	5016.235	88.004	-2549.439	2744.870

437.217	5002.898	82.693	0.000	1055.176
1083.260	5004.573	82.623	0.000	2818.139
1198.525	5014.575	123.309	0.000	10412.026
367.301	5027.797	279.970	-228.966	284.118
341.622	4927.067	159.531	93.914	66.586
3233.587	5014.575	76.334	#VALUE!	#VALUE!
341.740	4987.733	101.183	-1021.769	884.809
534.720	5034.359	151.147	0.000	1339.931
613.084	4996.180	106.680	#VALUE!	#VALUE!
766.671	4970.679	102.055	1222.915	293.775
793.919	4972.394	113.963	124.703	163.208
651.011	5002.898	82.693	-1459.899	742.932
905.635	5004.573	112.131	0.000	5013.396
747.188	4956.877	145.079	521.873	260.080
394.292	5024.504	99.322	-1946.945	522.533
405.205	4982.640	226.755	15.002	252.858
1405.246	4989.427	112.991	#VALUE!	#VALUE!
728.588	5004.573	182.950	-149.583	238.202
541.487	5016.235	93.871	-2301.500	2550.459
296.169	5009.583	76.527	-505.171	239.257
176.116	5019.549	93.714	-676.530	248.669
669.588	5022.854	99.405	-1848.490	1724.495
386.015	4970.679	138.074	275.461	240.799
261.341	4958.610	157.033	60.226	88.335
196.937	4994.495	112.702	-46.916	108.848
349.433	4903.814	304.161	62.278	62.541
290.756	4986.038	137.012	-7.602	114.234
316.030	5047.387	115.501	-7166.158	1711.174
529.096	5002.898	129.945	-237.187	368.255
1092.575	5012.914	76.398	0.000	4955.393
348.005	4974.107	161.808	62.705	172.930
1027.962	4968.962	126.177	190.786	193.534
498.629	4997.862	260.552	261.931	743.369
1100.689	4970.679	210.113	0.000	1909.128
399.040	4994.495	142.361	-80.861	283.222
234.319	4939.422	182.942	164.704	139.205
629.105	5031.082	98.991	#VALUE!	#VALUE!
773.154	5009.583	153.054	139.261	589.268
585.757	4991.118	101.011	0.000	1570.644
638.415	5001.222	147.790	-204.650	379.508
961.141	4989.427	112.991	#VALUE!	#VALUE!
627.064	4955.142	175.457	178.818	187.171
484.478	4979.233	119.549	272.266	249.315
458.532	4967.242	144.327	173.975	198.828
1183.376	5021.203	81.931	#NUM!	#VALUE!
533.036	4987.733	107.135	-10115.085	7631.405
728.510	4960.341	132.759	86.631	105.524
379.630	4859.795	266.464	41.066	25.376
223.306	4991.118	142.603	-41.827	174.735
666.280	4980.938	95.558	#VALUE!	#VALUE!

3321.926	4980.938	149.309	39.586	643.188
427.915	5022.854	105.252	-743.060	278.708
312.131	4975.818	95.804	105.023	407.670
776.998	5016.235	152.540	-445.224	312.337
702.917	4984.340	101.356	6.008	129.634
331.182	5006.245	117.933	-372.809	311.637
334.035	4992.807	106.862	954.149	327.702
291.440	5016.235	82.137	-780.551	271.038
244.605	4999.543	88.749	-176.235	220.322
376.577	4987.733	107.135	1034.133	310.733

Sample	$^{207}Pb/^{235}U$	Error 2σ	$^{206}Pb/^{238}U$	Error 2σ	rrelation_6_38	$^{238}U/^{206}Pb$
WRS_1	0.662	0.030	0.085	0.002	0.088	11.779
WRS_2	0.660	0.031	0.085	0.002	0.028	11.806
WRS_3	0.674	0.033	0.084	0.002	0.261	11.905
WRS_4	0.644	0.036	0.084	0.002	0.206	11.933
WRS_5	0.654	0.028	0.084	0.002	0.011	11.862
WRS_6	0.669	0.032	0.084	0.002	0.010	11.947
WRS_7	0.661	0.030	0.084	0.002	0.127	11.919
WRS_8	0.661	0.031	0.083	0.002	0.010	12.077
WRS_9	0.670	0.030	0.084	0.002	0.010	11.933
WRS_10	0.674	0.034	0.083	0.002	0.230	11.990
WRS_11	0.682	0.031	0.084	0.002	0.010	11.962
WRS_12	0.684	0.032	0.086	0.002	0.010	11.696
WRS_13	0.710	0.034	0.087	0.002	0.010	11.547
WRS_14	0.672	0.029	0.085	0.002	0.058	11.737
WRS_15	0.667	0.032	0.085	0.002	0.087	11.806
WRS_16	0.711	0.040	0.086	0.002	0.010	11.669
WRS_17	0.684	0.037	0.087	0.002	0.241	11.455
WRS_18	0.679	0.040	0.086	0.002	0.171	11.614
WRS_19	0.682	0.045	0.084	0.002	0.192	11.919
WRS_20	0.675	0.035	0.086	0.002	0.076	11.628
ZA16_84_1	0.769	0.048	0.049	0.002	0.332	20.408
ZA16_84_2	0.345	0.014	0.047	0.001	0.163	21.057
ZA16_84_3	0.332	0.013	0.046	0.001	0.349	21.978
ZA16_84_5	0.395	0.023	0.048	0.001	0.144	20.964
ZA16_84_6	0.484	0.034	0.048	0.001	0.335	21.008
ZA16_84_7	0.149	0.010	0.015	0.001	0.862	64.935
ZA16_84_8	0.334	0.015	0.047	0.001	0.150	21.227
ZA16_84_9	0.319	0.020	0.048	0.001	0.010	20.877
ZA16_84_10	0.340	0.014	0.048	0.001	0.318	21.008
ZA16_84_11	0.327	0.014	0.047	0.001	0.044	21.322
ZA16_84_13	0.353	0.018	0.048	0.001	0.116	20.964
ZA16_84_14	0.356	0.019	0.048	0.001	0.107	21.008
ZA16_84_15	0.514	0.044	0.050	0.002	0.725	19.960
ZA16_84_16	0.342	0.021	0.046	0.001	0.129	21.882
ZA16_84_17	0.391	0.016	0.048	0.001	0.641	20.790
ZA16_84_18	0.625	0.034	0.048	0.002	0.575	20.747
ZA16_84_19	0.204	0.010	0.017	0.002	0.148	60.241
ZA16_84_20	0.466	0.020	0.045	0.001	0.037	22.026
ZA16_84_21	0.665	0.044	0.051	0.002	0.220	19.763
ZA16_84_22	0.658	0.057	0.051	0.002	0.508	19.763
ZA16_84_23	0.380	0.021	0.048	0.001	0.194	20.964
ZA16_84_24	0.348	0.012	0.048	0.001	0.010	20.708
ZA16_84_25	0.652	0.052	0.049	0.001	0.735	20.450
ZA16_84_26	0.402	0.010	0.048	0.001	0.376	20.799
ZA16_84_27	0.445	0.018	0.047	0.001	0.034	21.277
ZA16_84_29	2.510	0.150	0.065	0.002	0.725	15.291
ZA16_84_30	0.162	0.006	0.015	0.001	0.310	65.833
ZA16_84_31	0.344	0.021	0.041	0.002	0.347	24.691

ZA16_84_32	0.335	0.021	0.048	0.002	0.213	21.008
ZA16_84_33	0.659	0.079	0.048	0.002	0.284	20.747
ZA16_84_34	0.274	0.014	0.032	0.002	0.776	30.960
ZA16_84_35	0.329	0.008	0.047	0.001	0.214	21.093
ZA16_84_36	0.310	0.010	0.041	0.001	0.442	24.396
ZA16_84_37	0.393	0.018	0.044	0.001	0.308	22.779
ZA16_84_38	0.336	0.013	0.048	0.001	0.299	20.833
ZA16_84_39	0.343	0.012	0.046	0.001	0.227	21.834
ZA16_84_40	0.475	0.031	0.048	0.002	0.250	20.704
ZA16_84_41	0.530	0.042	0.048	0.002	0.649	20.661
ZA16_84_42	0.479	0.026	0.046	0.001	0.225	21.882
ZA16_84_43	0.650	0.055	0.047	0.002	0.449	21.231
ZA16_84_44	1.340	0.300	0.056	0.005	0.913	17.762
ZA16_84_45	0.400	0.022	0.047	0.002	0.274	21.459
ZA16_84_46	0.356	0.015	0.047	0.001	0.368	21.277
ZA16_84_47	0.398	0.026	0.047	0.002	0.230	21.413
ZA16_84_48	0.569	0.055	0.049	0.002	0.550	20.576
ZA16_84_49	0.336	0.014	0.046	0.002	0.502	21.978
ZA16_84_50	0.338	0.014	0.046	0.002	0.334	21.786
ZA16_84_51	0.346	0.018	0.046	0.002	0.784	21.739
ZA16_84_53	0.328	0.016	0.045	0.002	0.520	22.371
ZA16_84_54	0.347	0.015	0.048	0.002	0.403	21.008
ZA16_84_55	0.374	0.029	0.049	0.002	0.234	20.450
ZA16_84_56	0.333	0.017	0.047	0.002	0.291	21.277
ZA16_84_57	0.335	0.026	0.046	0.002	0.191	21.834
ZA16_84_58	0.368	0.022	0.049	0.001	0.066	20.243
ZA16_84_59	0.345	0.019	0.048	0.001	0.062	20.704
ZA16_84_60	0.341	0.016	0.047	0.001	0.007	21.186
ZA16_84_61	0.350	0.016	0.048	0.001	0.113	20.661
ZA16_84_62	0.577	0.060	0.050	0.002	0.402	19.960
ZA16_84_63	0.341	0.018	0.047	0.001	0.177	21.186
ZA16_84_64	0.455	0.024	0.048	0.001	0.252	20.964
ZA16_84_65	0.330	0.014	0.046	0.001	0.134	21.678
ZA16_84_66	0.392	0.017	0.048	0.001	0.004	20.704
ZA16_84_67	0.349	0.015	0.047	0.001	0.225	21.169
ZA16_84_68	0.623	0.061	0.051	0.001	0.436	19.763
ZA16_84_69	0.368	0.023	0.047	0.001	0.323	21.277
ZA16_84_70	0.351	0.026	0.047	0.001	0.510	21.209
ZA16_84_71	0.367	0.013	0.049	0.001	0.030	20.462
ZA16_84_72	0.355	0.014	0.048	0.001	0.250	20.921
ZA16_84_73	0.509	0.035	0.051	0.002	0.287	19.646
ZA16_84_74	0.699	0.048	0.051	0.001	0.010	19.724
ZA16_119_1	0.687	0.016	0.023	0.001	0.562	43.459
ZA16_119_2	0.330	0.011	0.027	0.001	0.504	37.736
ZA16_119_3	3.080	0.300	0.060	0.003	0.868	16.722
ZA16_119_4	0.344	0.010	0.047	0.001	0.333	21.102
ZA16_119_5	0.774	0.073	0.051	0.002	0.444	19.763
ZA16_119_6	0.351	0.012	0.047	0.001	0.296	21.427
ZA16_119_7	0.330	0.016	0.048	0.001	0.107	20.833

ZA16_119_8	0.514	0.020	0.057	0.002	0.120	17.422
ZA16_119_9	0.552	0.026	0.052	0.001	0.291	19.084
ZA16_119_10	0.362	0.016	0.048	0.001	0.103	20.636
ZA16_119_11	0.388	0.023	0.048	0.001	0.452	20.921
ZA16_119_12	0.408	0.016	0.049	0.001	0.010	20.325
ZA16_119_13	3.650	0.230	0.077	0.003	0.918	12.920
ZA16_119_14	0.358	0.021	0.031	0.001	0.070	32.031
ZA16_119_15	0.289	0.026	0.032	0.002	0.788	31.447
ZA16_119_16	0.360	0.021	0.035	0.001	0.537	28.736
ZA16_119_17	0.541	0.018	0.047	0.002	0.348	21.459
ZA16_119_18	0.378	0.012	0.042	0.002	0.265	23.810
ZA16_119_19	0.350	0.012	0.047	0.001	0.268	21.277
ZA16_119_20	0.358	0.016	0.048	0.001	0.024	20.833
ZA16_119_21	0.259	0.007	0.026	0.001	0.462	38.580
ZA16_119_22	0.579	0.060	0.048	0.003	0.463	21.008
ZA16_119_24	0.843	0.075	0.051	0.001	0.512	19.685
ZA16_119_25	2.760	0.190	0.067	0.002	0.766	14.881
ZA16_119_26	0.347	0.013	0.046	0.001	0.501	21.978
ZA16_119_27	0.351	0.014	0.046	0.002	0.606	21.882
ZA16_119_28	0.400	0.011	0.049	0.001	0.142	20.547
ZA16_119_29	0.358	0.017	0.048	0.002	0.637	21.008
ZA16_119_30	0.467	0.022	0.045	0.001	0.424	22.075
ZA16_119_31	0.938	0.036	0.046	0.002	0.267	21.978
ZA16_119_32	0.372	0.019	0.011	0.000	0.010	93.371
ZA16_119_33	0.631	0.034	0.016	0.001	0.551	61.728
ZA16_119_34	0.836	0.050	0.019	0.002	0.742	53.476
ZA16_119_35	0.324	0.016	0.007	0.001	0.673	152.905
ZA16_119_36	0.247	0.014	0.012	0.001	0.607	81.833
ZA16_119_37	0.371	0.017	0.050	0.002	0.161	20.000
ZA16_119_39	0.360	0.012	0.049	0.001	0.363	20.619
ZA16_119_40	0.264	0.007	0.021	0.001	0.701	47.461
ZA16_119_41	0.375	0.016	0.014	0.001	0.817	69.061
ZA16_119_42	0.648	0.023	0.045	0.001	0.361	22.371
ZA16_119_43	0.386	0.020	0.047	0.001	0.674	21.097
Z_Plesovice_1	0.398	0.014	0.055	0.001	0.410	18.215
Z_Plesovice_2	0.411	0.013	0.055	0.001	0.257	18.315
Z_Plesovice_3	0.392	0.009	0.054	0.001	0.401	18.460
Z_Plesovice_4	0.399	0.009	0.053	0.001	0.293	18.847
Z_Plesovice_5	0.410	0.014	0.057	0.002	0.584	17.699
Z_Plesovice_6	0.396	0.009	0.053	0.001	0.412	18.720
Z_Plesovice_7	0.409	0.011	0.056	0.002	0.357	17.953
Z_Plesovice_8	0.405	0.013	0.057	0.001	0.323	17.575
Z_Plesovice_9	0.399	0.010	0.054	0.001	0.371	18.352
Z_Plesovice_10	0.404	0.011	0.056	0.002	0.261	17.825
Z_Plesovice_11	0.406	0.013	0.056	0.001	0.418	17.953
Z_Plesovice_12	0.392	0.010	0.054	0.001	0.387	18.362
Z_Plesovice_13	0.412	0.011	0.056	0.002	0.518	17.825
Z_Plesovice_14	0.400	0.012	0.055	0.001	0.296	18.282
Z_Plesovice_15	0.408	0.016	0.055	0.001	0.571	18.051

Z_Plesovice_16	0.404	0.010	0.056	0.002	0.410	17.762
Z_Plesovice_17	0.412	0.014	0.055	0.001	0.330	18.116
Z_Plesovice_18	0.401	0.009	0.054	0.001	0.454	18.522
Z_Plesovice_19	0.407	0.012	0.056	0.001	0.434	17.762
Z_Plesovice_20	0.412	0.012	0.055	0.001	0.476	18.083
Z_Temora2_1	0.509	0.026	0.067	0.002	0.075	14.881
Z_Temora2_2	0.488	0.030	0.066	0.002	0.010	15.198
Z_Temora2_3	0.507	0.025	0.067	0.002	0.224	15.038
Z_Temora2_4	0.499	0.025	0.065	0.001	0.102	15.337
Z_Temora2_5	0.507	0.026	0.067	0.001	0.169	14.903
Z_Temora2_6	0.515	0.027	0.068	0.002	0.127	14.663
Z_Temora2_7	0.521	0.021	0.068	0.001	0.095	14.620
Z_Temora2_9	0.511	0.018	0.066	0.001	0.157	15.221
Z_Temora2_10	0.512	0.020	0.068	0.001	0.281	14.620
Z_Temora2_11	0.518	0.023	0.067	0.001	0.259	14.948
Z_Temora2_12	0.503	0.028	0.068	0.001	0.158	14.641
Z_Temora2_13	0.493	0.023	0.065	0.002	0.119	15.361
Z_Temora2_14	0.488	0.028	0.067	0.002	0.260	14.925
Z_Temora2_15	0.500	0.029	0.066	0.001	0.010	15.106
Z_Temora2_16	0.506	0.032	0.068	0.002	0.134	14.815
Z_Temora2_17	0.510	0.025	0.065	0.001	0.348	15.337
Z_Temora2_18	0.513	0.022	0.068	0.002	0.090	14.706
Z_Temora2_20	0.516	0.026	0.065	0.002	0.010	15.385

Error 2σ	$^{207}Pb/^{206}Pb$	Error 2σ	orrelation_38_	alAge $^{206}Pb/^{23}$	Error 2σ	FinalAge ^{207}Pb
0.222	0.056	0.003	0.297	525.304	9.900	515.837
0.209	0.056	0.003	0.335	524.116	9.282	514.614
0.269	0.058	0.003	0.119	519.954	11.761	523.142
0.271	0.055	0.003	0.217	518.765	11.762	504.780
0.253	0.057	0.003	0.454	521.738	11.140	510.937
0.243	0.057	0.003	0.481	518.170	10.524	520.104
0.227	0.057	0.003	0.193	519.360	9.904	515.225
0.233	0.058	0.003	0.645	512.814	9.909	515.225
0.228	0.058	0.003	0.469	518.765	9.905	520.712
0.259	0.057	0.003	0.196	516.385	11.145	523.142
0.215	0.059	0.003	0.458	517.575	9.287	527.982
0.233	0.057	0.003	0.424	528.868	10.516	529.189
0.280	0.058	0.003	0.464	535.398	12.983	544.746
0.234	0.057	0.003	0.318	527.087	10.517	521.928
0.223	0.058	0.003	0.285	524.116	9.901	518.887
0.231	0.059	0.004	0.404	530.056	10.515	545.340
0.236	0.057	0.003	0.111	539.549	11.125	529.189
0.256	0.057	0.003	0.208	532.431	11.749	526.170
0.298	0.057	0.004	0.159	519.360	12.999	527.982
0.230	0.056	0.003	0.366	531.837	10.513	523.748
0.625	0.114	0.007	0.154	308.379	9.440	579.189
0.417	0.051	0.002	0.322	299.093	5.920	300.953
0.483	0.052	0.002	0.248	286.835	6.304	291.092
0.440	0.060	0.004	0.250	300.385	6.297	338.015
0.485	0.075	0.006	-0.029	299.770	6.927	400.813
4.217	0.069	0.003	-0.196	98.518	6.397	140.675
0.442	0.051	0.003	0.268	296.754	6.173	292.615
0.523	0.048	0.004	0.516	301.616	7.556	281.133
0.485	0.051	0.002	0.065	299.770	6.927	297.172
0.455	0.050	0.002	0.339	295.461	6.300	287.273
0.440	0.053	0.003	0.386	300.385	6.297	306.975
0.618	0.055	0.004	0.317	299.770	8.817	309.224
0.598	0.072	0.005	-0.514	315.136	9.435	421.135
0.670	0.054	0.004	0.297	288.068	8.825	298.686
0.519	0.060	0.002	0.175	302.846	7.555	335.100
0.732	0.091	0.004	0.201	303.461	10.703	492.976
5.443	0.091	0.010	0.925	106.132	9.590	188.505
0.679	0.074	0.004	0.507	286.218	8.826	388.422
0.664	0.093	0.007	0.423	318.204	10.691	517.668
0.781	0.094	0.007	-0.179	318.204	12.577	513.390
0.483	0.058	0.003	0.051	300.385	6.927	327.038
0.425	0.052	0.002	0.532	304.015	6.233	303.216
0.460	0.095	0.007	-0.447	307.765	6.923	509.709
0.428	0.060	0.002	0.388	302.723	6.233	343.098
0.453	0.069	0.003	0.562	296.077	6.300	373.772
0.468	0.283	0.013	-0.232	408.382	12.489	1274.931
2.904	0.076	0.004	0.746	97.185	4.287	152.452
1.280	0.062	0.004	0.426	255.931	13.271	300.198

0.750	0.051	0.003	0.182	299.770	10.706	293.376
0.861	0.099	0.010	-0.006	303.461	12.592	514.002
2.013	0.062	0.002	0.574	204.927	13.323	245.887
0.400	0.051	0.002	0.514	298.601	5.668	288.496
0.548	0.055	0.002	0.171	258.967	5.812	274.181
0.726	0.065	0.004	0.336	276.962	8.832	336.559
0.477	0.050	0.002	0.335	302.231	6.926	294.136
0.524	0.053	0.002	0.471	288.684	6.933	299.442
0.729	0.071	0.005	0.263	304.076	10.702	394.637
1.025	0.081	0.005	0.044	304.691	15.109	431.810
0.670	0.076	0.004	0.319	288.068	8.825	397.387
0.902	0.095	0.007	0.144	296.693	12.598	508.479
1.420	0.164	0.022	-0.685	353.085	28.222	863.229
0.829	0.064	0.003	0.277	293.614	11.341	341.648
0.543	0.055	0.002	0.385	296.077	7.559	309.224
0.688	0.062	0.004	0.246	294.230	9.451	340.197
1.016	0.087	0.007	0.008	305.921	15.107	457.368
0.773	0.054	0.002	0.428	286.835	10.086	294.136
0.712	0.055	0.002	0.505	289.301	9.454	295.655
0.898	0.055	0.003	0.288	289.917	11.975	301.708
0.901	0.054	0.003	0.244	281.900	11.352	288.038
0.794	0.053	0.002	0.479	299.770	11.336	302.462
0.753	0.054	0.004	0.306	307.765	11.329	322.614
1.086	0.053	0.003	0.150	296.077	15.119	291.854
1.001	0.051	0.005	0.363	288.684	13.237	293.376
0.451	0.055	0.003	0.287	310.837	6.921	318.170
0.429	0.052	0.003	0.332	304.076	6.296	300.953
0.628	0.053	0.003	0.460	297.308	8.818	297.929
0.470	0.053	0.003	0.336	304.691	6.925	304.721
0.876	0.088	0.009	0.066	315.136	13.838	462.532
0.494	0.052	0.003	0.265	297.308	6.929	297.929
0.483	0.069	0.004	0.203	300.385	6.927	380.775
0.432	0.051	0.002	0.264	290.718	5.798	289.566
0.472	0.058	0.003	0.346	304.076	6.925	335.829
0.435	0.053	0.002	0.205	297.554	6.110	303.969
0.547	0.092	0.009	-0.151	318.204	8.804	491.726
0.634	0.056	0.003	-0.045	296.077	8.819	318.170
0.355	0.053	0.003	-0.287	297.000	4.976	305.473
0.322	0.054	0.002	0.342	307.580	4.846	317.428
0.481	0.054	0.002	0.303	301.001	6.927	308.475
0.579	0.075	0.005	0.140	320.045	9.432	417.776
0.428	0.100	0.007	0.364	318.818	6.917	538.193
1.757	0.220	0.008	0.785	146.651	5.927	530.996
1.125	0.090	0.003	0.495	168.606	5.026	289.566
0.839	0.362	0.017	-0.476	374.409	18.783	1427.727
0.423	0.055	0.002	0.395	298.478	5.983	300.198
0.586	0.107	0.009	-0.355	318.204	9.433	582.055
0.367	0.056	0.002	0.160	294.045	5.040	305.473
0.608	0.050	0.003	0.419	302.231	8.815	289.566

0.486	0.065	0.003	0.298	359.794	10.029	421.135
0.364	0.076	0.004	0.075	329.239	6.283	446.306
0.417	0.054	0.003	0.345	305.060	6.169	313.707
0.481	0.059	0.004	-0.086	301.001	6.927	332.907
0.454	0.061	0.003	0.424	309.608	6.922	347.434
0.451	0.339	0.011	-0.569	480.585	16.765	1560.509
1.016	0.084	0.006	0.342	198.179	6.284	310.720
1.879	0.065	0.003	-0.092	201.804	12.057	257.772
1.156	0.074	0.003	0.299	220.520	8.871	312.215
0.875	0.084	0.003	0.536	293.614	11.971	439.084
0.850	0.068	0.003	0.583	265.218	9.472	325.565
0.543	0.054	0.002	0.507	296.077	7.559	304.721
0.564	0.054	0.003	0.444	302.231	8.185	310.720
1.131	0.072	0.003	0.542	164.962	4.837	234.022
1.148	0.091	0.009	-0.060	299.770	16.374	463.819
0.426	0.122	0.009	-0.271	319.431	6.917	620.800
0.487	0.296	0.015	-0.321	419.264	13.726	1344.793
0.580	0.055	0.002	0.308	286.835	7.565	302.462
0.766	0.057	0.002	0.100	288.068	10.086	305.473
0.329	0.060	0.002	0.452	306.351	4.910	341.648
0.706	0.055	0.002	0.177	299.770	10.076	310.720
0.634	0.077	0.004	0.226	285.601	8.196	389.115
0.725	0.152	0.007	0.437	286.835	9.456	671.835
2.964	0.253	0.017	0.523	68.674	2.180	321.135
3.810	0.296	0.019	0.780	103.595	6.395	496.719
5.147	0.326	0.024	0.801	119.435	11.496	616.936
12.391	0.359	0.022	0.830	42.022	3.405	284.975
4.018	0.149	0.006	0.326	78.298	3.844	224.136
0.760	0.055	0.002	-0.065	314.522	11.952	320.394
0.425	0.055	0.002	0.165	305.306	6.295	312.215
1.892	0.092	0.003	0.696	134.415	5.359	237.564
4.102	0.188	0.007	0.762	92.675	5.504	323.353
0.500	0.106	0.004	0.190	281.900	6.306	507.247
0.490	0.060	0.002	-0.379	298.539	6.928	331.443
0.464	0.053	0.002	0.541	344.535	8.786	340.197
0.436	0.053	0.002	0.412	342.701	8.160	349.595
0.317	0.052	0.001	0.296	340.072	5.838	335.465
0.284	0.053	0.001	0.376	333.281	5.025	340.850
0.470	0.053	0.002	0.231	354.305	9.406	348.875
0.322	0.053	0.001	0.389	335.484	5.778	338.525
0.483	0.053	0.002	0.666	349.422	9.410	348.155
0.432	0.053	0.002	0.489	356.745	8.778	345.268
0.320	0.053	0.001	0.372	342.029	5.963	340.923
0.477	0.053	0.002	0.643	351.864	9.408	344.545
0.419	0.054	0.002	0.384	349.422	8.155	345.991
0.283	0.052	0.001	0.248	341.846	5.273	335.829
0.477	0.053	0.001	0.550	351.864	9.408	350.314
0.334	0.053	0.002	0.481	343.313	6.276	341.648
0.358	0.054	0.002	0.223	347.590	6.902	347.434

0.473	0.053	0.001	0.606	353.085	9.407	344.256
0.459	0.054	0.002	0.396	346.368	8.785	350.314
0.257	0.054	0.001	0.183	338.972	4.709	342.228
0.410	0.052	0.002	0.369	353.085	8.153	346.712
0.425	0.054	0.002	0.456	346.979	8.157	350.314
0.421	0.055	0.003	0.369	419.264	11.854	417.776
0.370	0.054	0.004	0.515	410.802	9.989	403.547
0.362	0.055	0.003	0.224	415.035	9.986	416.430
0.329	0.056	0.003	0.324	407.172	8.743	411.025
0.267	0.055	0.003	0.272	418.660	7.487	416.430
0.344	0.055	0.003	0.374	425.302	9.978	421.806
0.299	0.056	0.002	0.419	426.509	8.730	425.819
0.278	0.056	0.002	0.308	410.197	7.492	419.121
0.278	0.054	0.002	0.207	426.509	8.106	419.793
0.290	0.056	0.002	0.158	417.452	8.112	423.814
0.279	0.053	0.003	0.182	425.906	8.107	413.731
0.354	0.056	0.003	0.358	406.567	9.368	406.953
0.356	0.054	0.003	0.082	418.056	9.983	403.547
0.297	0.055	0.004	0.358	413.221	8.115	411.702
0.329	0.055	0.003	0.196	421.076	9.357	415.756
0.282	0.057	0.003	0.090	407.172	7.494	418.449
0.324	0.056	0.003	0.370	424.095	9.355	420.464
0.355	0.056	0.003	0.429	405.962	9.368	422.476

Error 2σ	FinalAge ^{207}Pb	Error 2σ
23.376	452.368	21.003
24.171	464.219	23.087
25.614	529.762	27.401
28.217	428.402	23.972
21.875	499.252	23.566
24.878	491.533	25.870
23.384	491.533	25.008
24.163	537.299	30.465
23.315	522.189	26.200
26.390	499.252	25.312
23.999	578.128	30.223
24.757	503.098	27.218
26.086	544.801	27.986
22.524	503.098	23.706
24.894	529.762	26.488
30.680	563.402	35.392
28.626	499.252	26.185
30.997	487.660	29.140
34.838	503.098	33.364
27.157	456.328	23.589
36.152	1859.376	106.297
12.213	258.809	10.574
11.398	302.904	12.139
19.682	603.575	38.226
28.156	1068.502	82.631
8.993	904.708	39.221
13.141	249.844	12.687
17.626	94.333	6.893
12.236	227.214	10.756
12.299	190.338	9.155
15.653	311.581	16.586
16.504	404.072	25.808
36.050	988.765	71.312
18.340	379.369	25.198
13.713	585.440	17.711
26.818	1454.950	55.715
9.240	1446.603	158.967
16.670	1044.192	50.730
34.252	1496.011	105.714
44.473	1502.075	112.215
18.073	533.535	27.549
10.456	298.548	12.558
40.652	1518.127	106.028
8.535	607.177	18.185
15.119	895.748	44.202
76.191	3379.560	155.245
5.646	1097.702	59.140
18.326	670.656	46.588

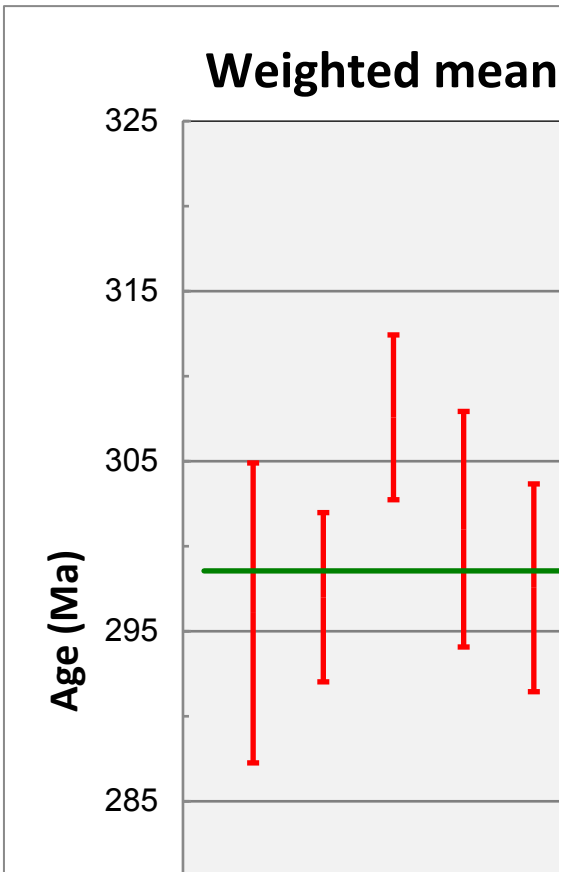

18.391	240.830	14.639
61.618	1605.366	162.158
12.564	667.195	25.910
7.375	222.650	7.040
8.845	416.283	14.355
15.415	787.231	42.130
11.380	204.264	7.731
10.476	337.336	12.682
25.755	951.645	61.830
34.219	1223.869	72.436
21.570	1081.843	50.152
43.025	1535.984	106.263
193.260	2497.323	335.007
18.791	725.019	38.820
13.029	404.072	16.959
22.224	677.554	45.825
44.210	1367.125	114.319
12.256	366.874	14.974
12.246	395.880	17.401
15.696	391.768	17.971
14.051	358.489	16.689
13.075	333.072	13.800
25.016	371.050	28.859
14.899	307.249	16.387
22.769	245.343	22.086
19.021	408.153	25.277
16.574	272.164	15.793
13.979	315.902	19.182
13.930	333.072	15.681
48.097	1373.727	147.409
15.726	302.904	16.764
20.085	901.727	48.283
12.285	254.333	11.899
14.564	537.299	27.696
13.065	315.902	13.787
48.147	1457.030	144.907
19.886	456.328	25.216
22.628	307.249	19.313
11.244	387.646	14.252
12.165	358.489	16.022
28.727	1073.852	74.256
36.957	1622.222	115.293
12.367	2982.154	108.343
9.652	1433.994	46.002
139.064	3758.268	176.493
8.727	395.880	11.601
54.897	1750.645	143.844
10.444	440.430	15.024
14.040	208.880	11.628

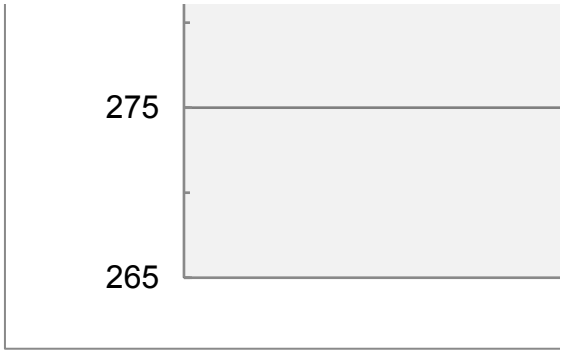

16.387	784.017	30.016
21.022	1102.953	50.594
13.865	375.215	18.726
19.734	578.128	34.122
13.625	642.756	29.455
98.333	3658.268	118.705
18.227	1283.261	87.495
23.191	761.336	37.713
18.213	1027.771	46.145
14.609	1283.261	52.190
10.335	853.240	36.658
10.448	375.215	13.871
13.887	350.061	18.321
6.681	985.941	38.342
48.064	1452.868	144.809
55.231	1979.834	153.046
92.576	3449.416	174.801
11.331	420.333	13.707
12.184	483.777	19.590
9.395	603.575	19.113
14.755	404.072	16.959
18.331	1108.185	50.701
25.785	2373.031	102.769
16.402	3203.637	215.264
26.765	3449.416	221.415
36.898	3598.375	264.911
14.073	3745.628	229.537
12.704	2339.070	100.201
14.681	404.072	15.485
10.407	391.768	12.939
6.399	1467.386	43.065
13.796	2722.990	97.146
18.004	1738.633	58.826
17.173	596.346	23.934
11.967	311.581	10.070
11.058	337.336	12.048
7.798	276.591	7.475
7.947	345.831	8.419
11.913	315.902	9.591
7.785	337.336	7.609
9.364	341.589	10.254
11.083	320.212	11.523
8.544	311.581	7.108
9.381	333.072	11.291
11.079	350.061	11.123
8.567	298.548	6.850
9.353	333.072	8.782
10.249	333.072	10.036
13.625	383.513	13.419

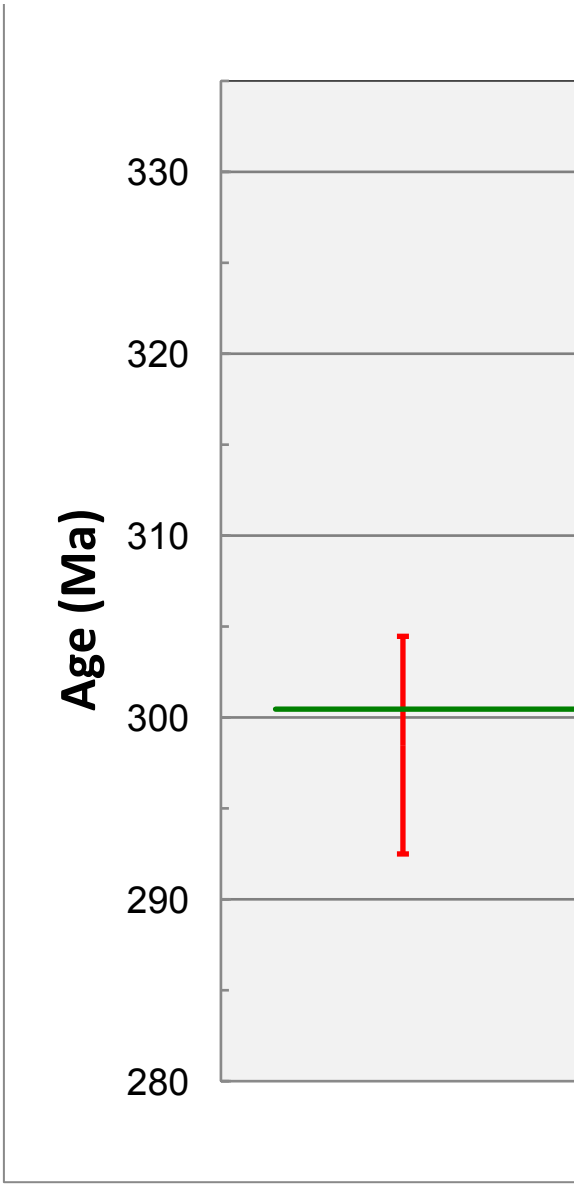

8.359	333.072	8.782
11.904	383.513	14.126
7.856	366.874	8.168
10.222	289.801	8.344
10.203	383.513	12.713
21.340	408.153	23.047
24.808	366.874	25.865
20.534	408.153	20.073
20.592	432.421	22.595
21.355	399.981	19.743
22.114	404.072	22.121
17.164	432.421	17.920
14.764	444.419	15.929
16.398	366.874	14.294
18.818	460.278	19.656
23.031	341.589	19.226
18.986	436.431	21.194
23.154	362.687	20.898
23.879	408.153	28.251
26.293	412.223	25.483
20.512	499.252	24.439
18.032	436.431	21.194
21.288	464.219	23.087

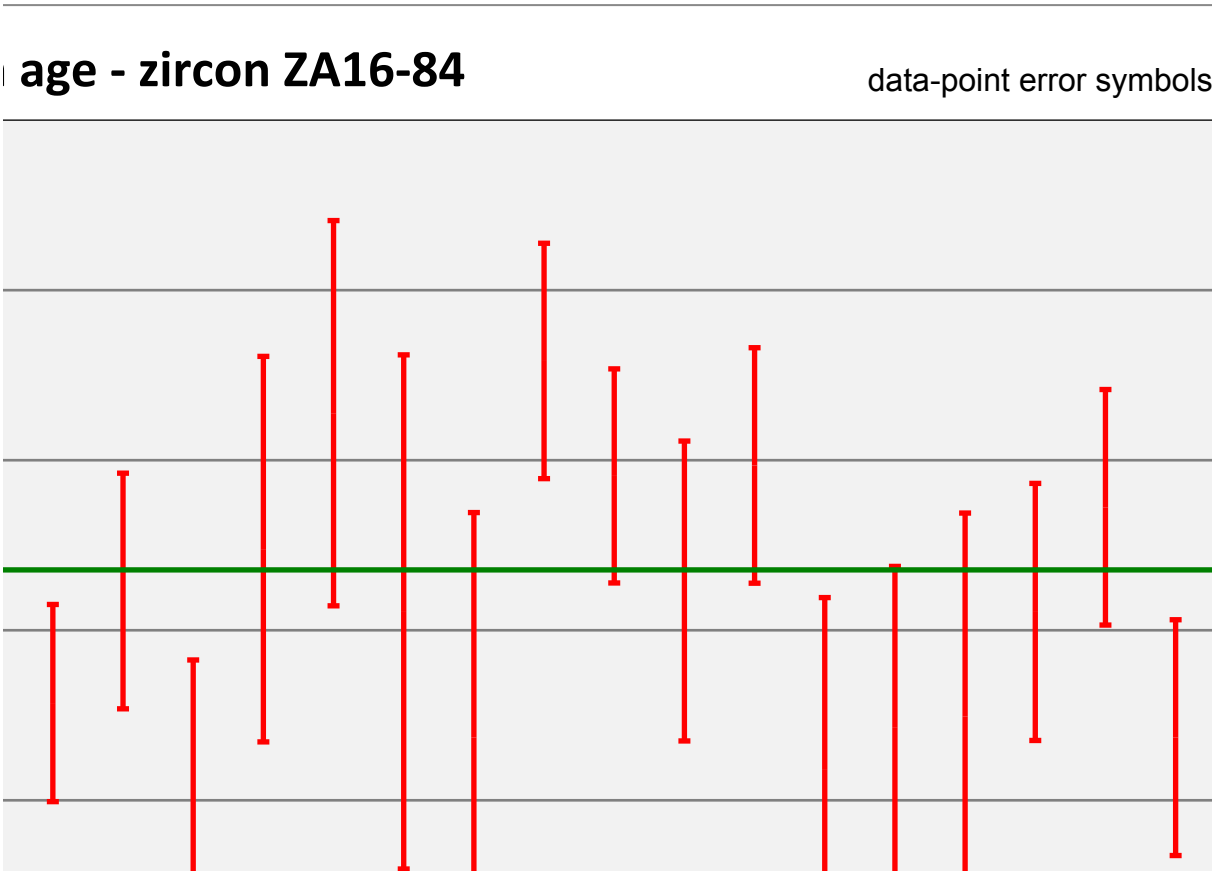
age - zircon ZA16-84
data-point error symbols

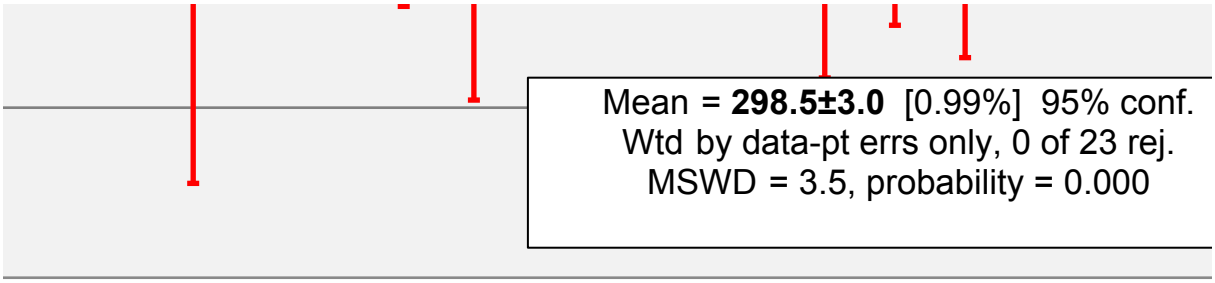

Analyses

Weighted mean age - zircon ZA16-119

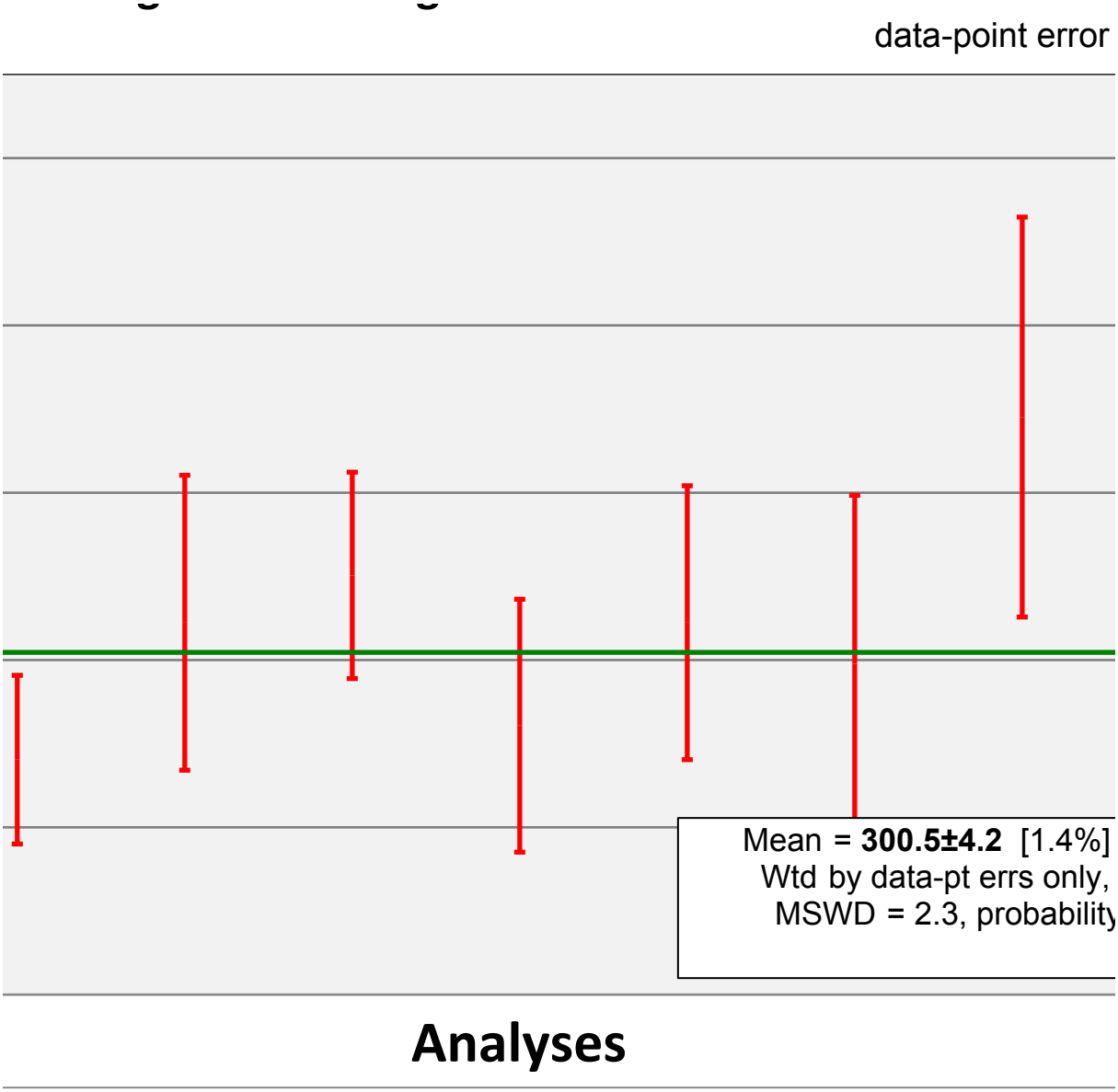
data-point error
Mean = 300.5±4.2 [1.4%]
Wtd by data-pt errs only,
MSWD = 2.3, probability
Analyses

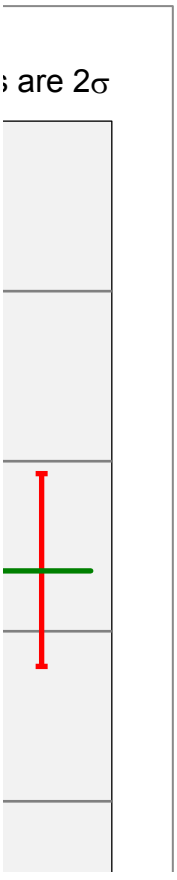
s are 2σ

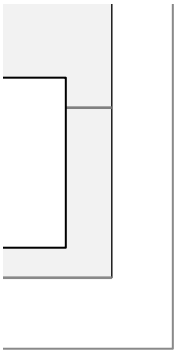

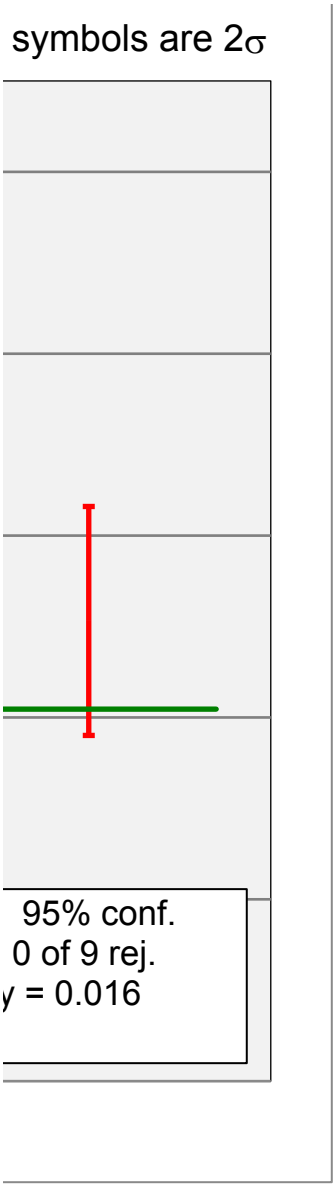
symbols are 2σ
95% conf.
0 of 9 rej.
y = 0.016

Pre-orogenic upper crustal softening by lower greenschist-facies metamorphic reactions in granites of the central Pyrenees

Laura Airaghi[1*], Nicolas Bellahsen[1], Benoît Dubacq[1], David Chew[2], Claudio Rosenberg[1], Emilie Janots[3], Maxime Waldner[1], Valérie Magnin[3]

[1] Sorbonne Université, CNRS-INSU, Institut des Sciences de la Terre de Paris, ISTeP UMR 7193, F-75005 Paris, France

[2] Department of Geology, Trinity College Dublin, Dublin 2, Ireland

[3] Université Grenoble Alpes, CNRS, IRD, IFSTTAR, ISTerre, 38000 Grenoble, France

*corresponding author:laura.airaghi@univ-orleans.fr, now at: Université d'Orléans, CNRS-INSU, Institut des Sciences de la Terre d'Orléans, ISTO, UMR7327, Orléans, France

Short title: Pre-kinematic metamorphism in Pyrenees

ABSTRACT

Pre-kinematic greenschist-facies metamorphism is often observed in granites and basement units of mountains belts, but rarely dated and accounted for in orogenic cycle reconstructions. Studying pre-kinematic alteration is challenging because of its usual obliteration by subsequent syn-kinematic metamorphism often occurring at conditions typical of the brittle-ductile transition. It is however to be expected that pre-kinematic alteration has major implications for the rheology of the upper crust. In the 305 Ma-old Variscan basement of the Bielsa massif (located in the Axial Zone of the Pyrenees), successive fluid-rock interaction events are recorded in granites at temperatures below 350°C. Combined microstructural and petrographic analysis, low-temperature thermobarometry and *in situ* U-Th/Pb dating of anatase, titanite and monazite show extensive pre-orogenic (pre-Alpine) and pre-kinematic alteration related to feldspar sericitization and chloritization of biotite and amphibole at temperatures of 270-350°C at 230-300 Ma. This event is followed by a second fluid-rock interaction stage marked by new crystallisation of phyllosilicates at temperatures of 200-280°C and associated with the formation of mylonitic shear zones and fractures parallel to the shear planes. U-Pb anatase and monazite ages as well as the microtextural relationships of accessory minerals suggest an age for this event at 40-70 Ma, consistent with independent regional geology constraints. The Variscan basement was therefore softened at late- to post Variscan time, at least 150-200 Ma before the main Alpine shortening while Alpine-age compression lead to the formation of a dense net of mylonites. The associated deformation, both distributed at the scale of the Bielsa massif and localized at decametric scale in mylonitic corridors, precedes the strain localization along the major thrusts of the Axial zone. The Bielsa massif is a good example where, inherited, pre-orogenic upper crustal softening controls the deformation patterns in granitic basement units through low-grade metamorphic reactions.

Key words**:** U-Th/Pb anatase-titanite-monazite dating, mylonites, chlorite-white mica thermobarometry, Bielsa, Axial zone

1. INTRODUCTION

Granites deformed at the brittle-ductile transition show mineral assemblages characteristic of low-grade metamorphism. Greenschist-facies metamorphic reactions often result in the growth of phyllosilicates (e.g. white mica, chlorite) whose presence strongly affect the rheological behaviour of the upper crust through softening, strain localization and fluid migration (Tullis, Yund, & Farver, 1996; Ingles, Lamouroux, Soula, Guerrero, & Debat, 1999; Jackson, Austrheim, McKenzie, & Priestley, 2004; Wintsch, Christoffersen, & Kronenberg, 2005; Goncalves, Oliot, Marquer, & Connolly, 2012). The breakdown of 80 % of feldspar into white mica, for example, reduces the depth of the brittle-ductile transition by two thirds (Gueydan, Leroy, Jolivet, & Agard, 2003). Reactions forming low-grade mineral assemblages responsible for crustal softening are generally observed to be syn-kinematic, occurring during the major deformation phases of an orogenic cycle (Wayne & McCaig, et al., 1998; Gueydan et al., 2003; Mansard, Raimbourg, Augier, Précigout, & Le Breton, 2018). Static or quasi-static hydrothermal alteration is also observed in granites and has been widely documented, especially in large igneous provinces (e.g. Parneix, Beaufort, Dudoignon, & Meunier, 1985; Cathelineau et al., 1986; Yuguchi, Sasao, Ishibashi, & Nishiyama, 2015). However static alteration is rarely characterised, and hardly ever dated and placed in a regional orogenic context. Indeed, low-grade metamorphic reactions often leave tenuous fingerprints only hinted at by equivocal microtextural relationships, especially in granites (e.g. Airaghi et al., 2017b), which are generally considered poorly reactive rocks at temperatures below 400°C.

At a microscopic scale, pre-kinematic and syn-kinematic transformations are difficult to distinguish, particularly so if the rocks have been deformed through several orogenic cycles.

78 The timing and conditions of pre-kinematic metamorphic reactions and their effects on (i) the
79 syn-kinematic transformation and (ii) the rheological response of the upper crust to successive
80 compressive phases remain therefore poorly constrained. This study addresses these issues by
81 focussing on the Bielsa massif, a Variscan granite located in the Axial Zone of the central
82 Pyrenees (Figure 1a). This massif is an excellent natural laboratory to study how granitic rocks
83 record distinct low-grade metamorphic events. The massif is part of the central Pyrenean belt,
84 which experienced at least two well-known deformation phases (Late Variscan and
85 Alpine/Pyrenean, Cochelin et al. 2017), which are difficult to distinguish in the Axial zone
86 (Cochelin et al, 2017). The Bielsa massif is located in the most external basement domain of
87 the Pyrenees (implying it experienced the lowest peak metamorphic temperatures with respect
88 to Alpine tectonics), south of the zones of large-scale shear bands that have affected other
89 granitic basement units of Pyrenees (e.g. Maladeta, Néouvielle; Wayne & McCaig, 1988). In
90 addition, structural and microstructural studies show significant distributed shortening at the
91 scale of the massif (Román-Berdiel et al., 2004; Bellahsen et al., 2019), raising questions about
92 the link between low-grade metamorphism and strain accommodation mechanisms. Early
93 feldspar destabilisation has been proposed to have a major control on subsequent mechanical
94 softening in Bielsa (Bellahsen et al., 2019), but the conditions and the age of such reaction still
95 remains unconstrained.

96 In this contribution we estimate the conditions of crystallization of both pre-kinematic and syn-
97 kinematic greenschist-facies mineral assemblages in the Bielsa granite and its Triassic
98 sedimentary cover. Microstructural and petrographic analyses were combined with low-
99 temperature thermobarometry and *in situ* U-Th/Pb dating of zircon, titanite and monazite.
100 Attempt to date anatase (polymorph of rutile) by the U/Pb method were also undertaken. The
101 implications for the timing of crustal softening relative to the major shortening phases are
102 discussed with respect to their associated mineral assemblages. Results suggest that pre-

kinematic (pre-Alpine) alteration controls the deformation pattern and strain localisation in the Bielsa granite during Alpine shortening.

2. THE BIELSA MASSIF IN THE AXIAL ZONE (CENTRAL PYRENEES)

The Axial zone (central Pyrenees) is part of a S-verging thrust system made of imbricated thrust units stacked during the Late Cretaceous-Early Miocene collision of the Iberian and European plates (Figure 1a). The plutons of the Axial zone (i.e. Bielsa, Neuville, Maladetta massifs etc., Figure 1a) were emplaced into Paleozoic sediments during Late-Variscan (320-300 Ma, e.g. Paquette, Gleizes, Leblanc, & Bouchez, 1997; Vacherat et al., 2017). These plutons and their Paleozoic sedimentary cover constitute the basement to the Permian and Mesozoic sedimentary units (Fig. 1a). Several tectono-metamorphic stages are documented in the metasedimentary units Axial zone but are difficult to distinguish within the basement. Recent studies have proposed that the majority of the deformation in the Axial zone is of Variscan age (Cochelin et al., 2017). Cretaceous hydrothermal events have been identified in the eastern Axial zone (Fallourd et al., 2014; Boutin et al., 2015) and related to extensive tectonics centered on the SE Bay of Biscay. Basement thrusts in the central-western Pyrenees (named Gavarnie and Guarga thrusts) were (re)activated during the Eocene to Miocene (20-30 and 32-36 Ma respectively, Jolivet et al., 2007; Elmola et al., 2018 and references therein). In the hanging wall of the Gavarnie thrust, an older deformation event (*c.* 48 Ma) is recognised in the massifs of Néouvielle and Eaux Chaudes. It has been associated with the activation of mylonitic shear bands (e.g. Wayne & McCaig, 1998).

This study focusses on the Bielsa massif, mainly constituted by a pluton emplaced at *c.* 305 Ma (Vacherat et al., 2017), in the S-verging thrust system structurally located between the Gavarnie and Guarga thrusts (Figure 1b). Close to Lake Urdiceto (Figure 1c-d), granitic to granodioritic rocks (Román-Berdiel et al., 2004) are unconformably overlain by Triassic continental red

128 sandstones and pelites. The basement and its sedimentary cover were deformed (folded) during
129 the Alpine compressional phase (Figure 1d, Casas et al., 2003; Román-Berdiel et al., 2004,
130 Bellashen et al., 2019) with a wavelength of ~1 km. Several sub-vertical S- or N-dipping normal
131 or reverse steep faults bound the antiforms and synforms (Figure 1d). In the core of the synforms,
132 Triassic sediments crop out. They exhibit a sub-vertical to N-dipping cleavage (e.g. Figure 2b
133 and 3c), with nord side up sense of shear kinematic indicators above the sediment-cover
134 interface (Bellahsen et al., 2019). The granitic basement is heterogeneously deformed. At the
135 decametric scale, undeformed and weakly deformed granitic rocks alternate with zones of
136 distributed ductile deformation, zones of fracturing and faulting and mylonites (Figures 1c-d
137 and 2a-f). A pervasive N-dipping schistosity is widespread in the basement (Figure 2a-c and e).
138 Mylonitic corridors, with 1-2 m wide, are observed within the basement and at its boundary
139 with the Triassic sedimentary cover (Figure 2a-c). Mylonitic corridors alternate with less
140 deformed rocks with a wave length of ~100 m (Figure 1c) and they are characterized by
141 pervasive schistosity (S) and steep, N-dipping (45-70°) and S-dipping (55-70°) shear planes (C)
142 associated either with a north or with a south-verging movement (Figure 2a-e). In some shear
143 zone, the dips of mylonitic planes varies from S-dipping to N-dipping, with an apparent sense
144 of shear from top-to-north to top-to-south (Figure 2b-d). Some of the shear bands at the
145 boundary between the Triassic sediments and the late Variscan granite (regionally trending
146 N110, Figure 1c) contain deformed fragments of the Triassic red sandstone (Román-Berdiel et
147 al., 2004; Figure 2b), indicating that they are post-Triassic. The high density of mylonitic
148 corridors and the pervasive schistosity development result in a distributed deformation pattern
149 (as observed in other crystalline units as the Aar massif, Wehrens et al., 2017). The
150 granitic/granodioritic basement (regardless of the intensity of the strain) is pervasively hydrated
151 and the original magmatic mineral assemblage is partly to totally replaced by greenschist-facies
152 minerals. The steep topography of the massif allows one to infer that the latter replacement

affects the pluton at least over a topographic vertical profile of 2 km from the lowest outcrop of the massif (yellow stars in Figures 1b).

At the boundary between the Triassic sediments and the granite/granodiorite, sub-horizontal quartz and chlorite-bearing veins which are 1-5 cm-wide are observed (yellow square in Fig. 3b). Fifty meters from the contact, Triassic sediments show two generations of chlorite- and quartz-bearing veins: (1) sub-horizontal veins parallel to the ones observed at the contact between the basement and the sedimentary rocks produced by vertical extension, locally folded and associated with a crenulation cleavage (N184S) and (2) sub-vertical veins (Figure 3c).

3. SAMPLE DESCRIPTION AND CHRONOLOGY OF MINERAL ASSEMBLAGES

Twenty-seven samples were collected along two transects east and west of Lake Urdiceto, from the undeformed granite (e.g. ZA16-84 and B11-16, Figure 4a, b) up to the zone of intense mylonitisation (e.g. ZA16-96, ZA16-98; Figures 1c, 4g). One sample (ZAL18-11) was collected at the contact between the Triassic sandstones and a basement-hosted vein (Figures 3b). Two samples (ZA16-12 and ZA16-13) were collected in the Triassic sediments (Figures 3c).

3.1 Samples from the basement

In the basement unit, we distinguished the following rock fabrics: *Undeformed* samples (e.g. ZA16-84, Figure 4a), where the magmatic, euhedral shape of grains is still preserved. *Weakly deformed* rocks (e.g. Figure 2f and 4c) exhibiting a weak yet pervasive schistosity (at an outcrop scale: S in Figure 2a). In some of those samples the schistosity is associated to mm-scale fractures (e.g. ZA16-82, ZA16-78, ZA16-128, Figure 4e-f and h) that are parallel to the subvertical shear planes observed at an outcrop scale in mylonites (C in Figure 2a). *Mylonites* showing S and C planes (e.g. ZA16-133, Figure 4g), where the C planes are as pervasive as S.

178 In the samples defined as mylonite, both brittle and ductile deformation features are identified,
179 with the brittle ones underlined by fractures parallel to the shear planes C (Figure 4g).
180 All samples, regardless of the degree of the strain, exhibit extensive alteration of the
181 magmatic mineral assemblage originally defined by quartz, K-feldspar and plagioclase, biotite
182 ± amphibole, apatite, zircon (all in textural equilibrium, Figures 4a-b) and ilmenite preserved
183 as inclusions in the less altered amphibole and biotite grains (Figure 5a-b). The alteration is
184 comprised by the breakdown of plagioclase and K-feldspar into white mica (10-30 μm in size)
185 + albite + calcite ± rare epidote (Figure 4a, c, e-f). Biotite and amphibole break down to chlorite
186 flakes (ChlA, abbreviations are from Whitney & Evans, 2010) ± white mica (20-100 μm in
187 size) ± prehnite (Figure 4a) and a Ti-bearing phase (anatase or titanite or both, Figure 4b, d, f
188 and g). In the paragraph below, mineral assemblages are described in relation to their
189 microstructural evolution from the undeformed granites and granodiorites to mylonites.
190 In the undeformed samples, relicts of feldspar, biotite and amphibole are still visible and their
191 euhedral magmatic grain shapes are preserved (Figure 4a). Chlorite flakes (ChlA) grow at the
192 grain boundaries of parent minerals and along biotite cleavages, and they are associated with a
193 Ti-bearing phase (see below) ± prehnite ± K-feldspar (Figure 4a-b). Ilmenite grains are
194 preserved in unaltered biotite and amphibole domains (Figure 5a). Quartz grains contain sparse,
195 micrometric fluid inclusions and are cross-cut by microcracks. Allanite is locally observed in
196 textural equilibrium with the magmatic minerals. Euhedral magmatic zircon grains are found
197 within relicts of feldspar or at the boundaries between feldspar and amphibole.
198 Cathodoluminescence imaging of zircon in samples ZA16-84 and ZA16-119 typically reveals
199 primary oscillatory growth zoning without internal complexity. However, some zircon grains,
200 especially in sample ZA16-119, show metamictization with porous domains and lobate rims 5-
201 20 μm thick, and very low cathodoluminescence emission (Figure 5d). In the weakly deformed
202 samples, feldspar is pervasively sericitized (up to 80-90%). Original biotite grains are

chloritized between 70-90% (Figure 4c). Chlorite flakes (ChlA) and secondary reaction phases (quartz, Ti-phase ± white mica) are oriented parallel to the main schistosity and tightly folded to form kinks (Figure 4d). Quartz grains partly preserve their magmatic texture, but are fractured, with fractures subparallel to the kink axes. Grains are cross-cut by fluid inclusion trails. Originally euhedral grains of ilmenite are first altered to aggregates of anatase + calcite then to titanite (Figure 5a-b), following the reaction proposed by Hansen, Reimink, & Harlov (2010) for low temperature conditions. Anatase is itself replaced by titanite, in textural equilibrium with chlorite flakes (Figures 5a-b). Anatase and titanite are systematically aligned with the chlorite flakes, within the S-planes. When they are folded to form kinks, anatase relicts are mainly preserved in the microfold hinges (Figure 5c). In some of the weakly deformed samples, titanite is the major Ti-bearing phase preserved (samples ZA16-119, B11-16, ZA16-77 and ZA16-84).

In weakly deformed samples showing millimetric fractures, biotite deformation and stretching along the main schistosity S is more pronounced (e.g. Figure 4e). Calcite is present in the matrix. Fractures 1-3 mm thick displace the folded chlorite flakes to form en-echelon microstructures (Figure 4e). These fractures are filled with secondary chlorite (ChlB) ± white mica (Figure 4f). Sheets of ChlB are oriented parallel to the fracture walls in contrast to ChlA grains which are mainly perpendicular (Figure 4f). Furthermore, ChlB is rarely associated with biotite breakdown products as prehnite and Ti-bearing phases (Figure 4f). Quartz grains are both fractured and stretched, they exhibit undulose extinction and abundant fluid inclusion trails. Titanite is observed in the same microstructural position as in undeformed samples (folded within ChlA flakes). The microstructural position of anatase is instead more variable. Anatase is observed: (1) as ~70 μm sub-euhedral relicts in titanite cores at the rims of the ChlA flakes (as in the undeformed samples, type-1 Ant, Figure 4h, 5b-c, f-h and Figure S1) and (2) as grains 20-30 μm in size not associated with titanite within ChlA flakes along the ancient biotite

cleavages (type-2 Ant, e.g. Figure 4h, 5f-h and Figure S1). Locally, type-2 anatase is observed within ChlB-bearing fractures (e.g. ZA16-73, Figure 5i). Type-2 anatase of type 2 is often observed close to type-1 anatase. Magmatic accessory minerals such as apatite and zircon are fragmented and stretched along the S planes.

In mylonitic samples, the schistosity is defined by folded chlorite + white mica flakes and interconnected layers of white mica (Figure 4g). Flakes are folded up to kinks. Shear planes (C) form at high angle with the main schistosity S (Figure 4g-h). The kink axes are kinematically compatible with shear movement on the C planes. Quartz grains are partially stretched and most of them are fractured, with cracks subparallel to the C planes (Figure 4g). Within the grains, evidences of ductile deformation are observed such as deformation lamellae. A larger amount of fluid inclusions in quartz are observed with these samples compared to weakly deformed samples. In mylonites (ZA16-96, ZA16-98), only one type of anatase is observed (small anatase grains of type 2 predominate). In these samples, monazite grains, 10-40 μm in size, were identified in mylonites (sample ZA16-98 and ZA16-88). These monazite grains are wrapped by secondary chlorite and white mica (suggesting post-magmatic origin). The largest grains of monazite (20-40 μm) (Mnz1) are lobate, and stretched along the C planes with fractures perpendicular to them and exhibit irregular grain boundaries, micrometric large fractures, patchy textures with bright and dark spots in BSE images and 'inclusion-like dissolution figures' (as described by Grand'Homme et al., 2018; Airaghi, Janots, Lanari, de Sigoyer, & Magnin, 2018, Figure 5c). Small monazite grains (~10 μm) with rounded shape share features with that of ZA16-88, aligned along the main foliation or within alteration halos marking the reaction front along secondary fractures subparallel to the C (Figure 5j). In sample ZA16-98 monazite is locally Th and Si-enriched (tending towards a thorite composition, inset in Figure 5i).

In summary, the granitic rocks experienced a first transformation of the original magmatic mineral assemblage of Qz + Fs + Pl + Bt ± Amph (+ Ilm + Ap + Zr ± Aln) to Qz + ChlA + Ti-phase (Ttn or Ant then Ttn) ± Pr ± KFs. Zircon and titanite grains with anatase core (type-1 Ant) are stretched in the main schistosity and folded during shearing. They therefore predate any deformation stage. ChlB is rarely associated with secondary reaction products and helps to define the C-parallel fractures. It is considered to precipitate from a fluid during a second syn-kinematic (syn C planes) alteration event. The varying characteristics of anatase, only found in deformed samples, suggest that in these samples two generations of anatase may be preserved. That type-2 anatase is located within ChlA flakes along former biotite cleavage suggests that type-2 Ant grew after type-1 Ant on ChlA rims. The chloritization reaction front and replacement is indeed expected to progress from the grain boundaries to the core, along the biotite cleavages. The proximity of type-2 anatase to type-1 anatase grains indicates however transport scale of the anatase-forming elements limited to some dozen of µm. In sample ZA16-73 (discretely deformed). Type-2 Ant is observed in C-parallel fractures (Figure 5i). Type-2 Ant may have crystallized during the shearing. Mnz1 is affected by deformation and mainly observed within the main schistosity, while Mnz2 (and type-2 Ant, see below) are associated with C parallel fractures. Mnz2 is therefore syn C planes forming stage.

3.2 Samples from Triassic sediments and at the boundary between sediments and the granodiorite

At the brecciated contact between the Triassic sediments and the chlorite-quartz bearing vein in contact with the basement (Figure 6a), the Triassic sediments are composed of quartz, chlorite, white mica, Fe-oxides and clasts in a calcite matrix (sample ZAL18-11). The vein is composed of mm-size quartz grains recrystallized by bulging and hosting a dense net of fluid inclusions, interlayered with elongate chlorite and white mica (± calcite) (Figure 6b). Along

chlorite grain boundaries, abundant Fe-oxides, 20-40 μm large anatase grains, monazite, REE-bearing carbonates and tourmaline are occasionally observed (Figure 6b). The textural aspect of monazite in sediments is similar to that of monazite in the basement (inset in Figure 6b).

The red-coloured, foliated pelitic rocks are comprised of white mica, chlorite and quartz grains on the scale of tents of microns (± detrital monazite, apatite and anatase, samples ZAL18-12 and ZAL18-13). The veins are approximately 100 μm thick, they opened at high angle with the foliation and are filled by elongate grains of quartz rich in fluid inclusions (in the core of the vein). Chlorite developed along the vein-host rock interface with long axes parallel to the vein opening direction (Figure 6c). Veins are stretched and displaced by 30-50 μm secondary chlorite and quartz-bearing layers cross-cutting the foliation, forming 'en échelon' fractures (Figure 6c-d). Monazite in pelites forms euhedral grains 5-10 μm in diameter, sometimes in association with Fe-oxides and xenotime at the interface between the veins and host-rock.

4. ANALYTICAL AND COMPUTATIONAL METHODS

The chemical composition of metamorphic chlorite and white mica has been analysed with a CAMECA SX-FIVE electron probe micro-analyser (EPMA) at ISTeP (Sorbonne Université). Point measurements were made under a 15 kV acceleration voltage and 10 nA beam current with a ~1μm beam size, in wavelength-dispersive spectroscopy (WDS) mode, using diopside (Ca, Mg, Si), $MnTiO_3$ (Mn, Ti), orthoclase (K, Al), hematite (Fe), albite (Na) and Cr_2O_3 (Cr) as standards for measuring the elements written in parentheses. The compositional variability of chlorite and white mica in different microstructural sites was characterised by element mapping using both the EPMA and a Zeiss SUPRA-55VP scanning electron microscope (SEM) at ISTeP (Sorbonne Université). EPMA elemental maps were acquired in WDS mode at 100 nA beam current, 15 keV acceleration voltage with a 200 ms dwell time. SEM maps were acquired in energy-dispersive spectroscopy (EDS) mode at 15 keV acceleration voltage, 30 nA

beam current with a dwell time of 256 μs. SEM and EPMA maps were quantified with the software XMapTools (Lanari et al., 2014). The U, Th, Pb and REE contents of monazite were analysed with the JEOL-JXA-8230 EPMA at ISTerre (University of Grenoble), at 15 keV acceleration voltage, 200 nA beam current with a spot beam size. For each monazite analysis, a chemical U-Th/Pb age was determined and the average age of different populations of monazite (identified on the base of compositional criteria) was calculated with the software NiLeDAM. The analytical protocol and data processing are detailed in Appendix 1.

Titanite, anatase and zircon were dated *in-situ* by the U-Pb LA-ICP-MS technique at Trinity College, Dublin (Ireland), on the same thin sections as used for the microstructural and petrological studies. U-Pb ages were determined using a Photon Machines Analyte Exite 193 nm ArF Excimer laser-ablation system with a Helex 2-volume ablation cell coupled to an Agilent 7900 ICPMS. For titanite, zircon and anatase, 300 shots were ablated per analysis with a laser spot size of 24 μm (Figure S1). The laser repetition rate and fluency were set at 15 Hz, 1.60 J/cm^2 and 11 Hz and 2.25 J/cm^2 for anatase/titanite and zircon respectively, and typically 50 analyses were obtained on each sample (usually 1-2 spots per grain) and plotted on a Tera-Wasserburg diagram (Tera and Wasserburg, 1972) with 2σ error ellipses, allowing determination of the initial Pb intercept on the $^{207}Pb/^{206}Pb$ axis.

The raw titanite and anatase isotope data were reduced using the "VizualAge UcomPbine" data reduction scheme (DRS) of Chew, Petrus, and Kamber, (2014). The "VizualAge" DRS was employed for zircon data reduction. Common Pb in the titanite and rutile standards was corrected using the ^{207}Pb-based correction method. For unknowns, the initial Pb in titanite and anatase was determined from the upper intercept (y-intercept on the $^{207}Pb/^{206}Pb$ axis) of the discordia line defined by the analyses on Tera-Wasserbutg Concordia. The age for each population of grains was calculated from the lower intercept of the discordia line on Tera-Wasserburg Concordia. line with the Pb evolution model. Zircon ages were instead

estimated by calculating the weighted average of $^{206}Pb/^{238}U$ corrected ages (Table S3). The primary standards employed, the secondary standard ages and further details on the analytical procedure are reported in Supplementary Material S1. Titanite and anatase included in ilmenite were not dated due to their small size. When anatase core relicts were preserved in titanite grains (type-1 Ant), it was rarely possible to ablate separately relicts of anatase and their titanite host due to the small grain size (e.g. Figure S1). In anatase-dominated samples, where the bulk of grain was anatase, these analyses were classified and processed as anatase, in titanite dominated samples with only minor relict anatase the analyses were classifies as titanite. The contribution of relicts of anatase to the calculated age was estimated by comparison with results from samples where the only anatase or titanite only were sampled. In sample where two types of anatase were observed, all anatase data were processed together. The existence of one or two population(s) of anatase based on the data interpretation was compared to microstructural observations.

Monazite ages were calculated from the EPMA U, Pb and Th contents. The associated detection limits were 90 ppm for Pb, 120 ppm for U and 115 ppm for Th. For each monazite analysis, a chemical U-Th-Pb age was determined (see Montel et al., 1996). When the Pb content was lower than the EPMA detection limit, a value of 90 ppm was used to estimate a maximum age.

The crystallization temperature and the minimum content of XFe^{3+} ($Fe^{3+}/(Fe^{2+} + Fe^{3+})$) of each generation of chlorite in 23 selected samples were estimated using the Chl-Qz-H_2O thermodynamic model of Vidal et al. (2006) from element abundances at a reference pressure of 3 kbar and H_2O activity at fixed unit value. The absolute uncertainty on the crystallization temperature estimates is around 50°C (Vidal et al., 2006; Dubacq, Soret, Jewison and Agard, 2019), although the relative uncertainty between samples is likely lower (10-20°C). The semi-

empirical thermometer of Bourdelle, Parra, Beyssac, Chopin, and Vidal (2013) formulated for low-temperature chlorite was used for comparison.

5. RESULTS

5.1 Composition of pre-kinematic and syn-kinematic chlorite and white mica

Chlorite generally exhibits compositional variation at the μm-scale with high variability in Fe, Mg and Al contents (especially in discretely deformed granites), as shown in Figure 7 (and Table S1). In samples collected east of Lake Urdiceto, two groups of chlorite are recognized. The first, named Chl1, is ubiquitous from undeformed granites (pre-kinematic) to mylonites, and mainly observed in ChlA flakes (Figure 7a). It should be noted that Chl1 refers to a chemical composition while ChlA refers to the microtexture of chlorite (which do not necessarily correspond, e.g. Vidal et al., 2006; Airaghi et al., 2017). Chl1 is Al-poor (2.2-2.4 apfu) and Mg-rich (1.7-2.5 apfu). The second group of chlorites, Chl2, is mainly observed in syn-kinematic ChlB (Figure 7a, c-d) and exhibits higher Al content (Al= 2.5-2.86 apfu) and lower Mg content (Mg= 1.5-1.7 apfu). The Fe content increases slightly from Chl1 (2.15-2.3 apfu) to Chl2 (2.4-2.5 apfu). In undeformed samples, only homogeneous Chl1 in chlorite flakes is observed (e.g. sample ZA16-84). In the most deformed samples, chlorite flakes (ChlA) exhibit μm-scale Mg and Al zoning and portions of Chl1 are pseudomorphically replaced by Chl2. Chl1 is also found as relicts in ChlB in fractures, wrapped by Chl2 (Figure 7a). In samples collected west of Lake Urdiceto, Chl1 in flakes is Fe-rich (1.97-2.13 apfu) and Mg-poor (2.18-2.47 apfu) compared to Chl2 in veins and along fractures (Fe= 1.39-1.50 apfu, Mg= 2.83-2.95 apfu) (Figure 7b, c, e) while the Al content is typically constant (Table S1). A micron-scale zoning within Chl1 flakes is observed miming cleavage planes of the original magmatic crystal (biotite or amphibole) in discretely deformed samples, while Chl2 within ChlB within fractures

376 is homogeneous (Figure 7b). In mylonites, chlorite shows intermediate compositions (e.g.
377 sample ZA16-96 in Figure 7c) difficult to relate to a specific microtextural sequence due to
378 extensive deformation. In the Triassic sediments, chlorite is Al-enriched compared to chlorite
379 in the basement, but exhibits similar compositional trends (Figure 7c-e). Two groups are
380 recognized in samples ZAL18-13 and ZAL18-12: one is Mg-depleted (1.7-1.97 apfu) and Al-
381 enriched (2.90-2.92 apfu) and is observed in veins, the other is Mg-enriched (2.18-2.40 apfu)
382 or Al-depleted (2.68-2.78 apfu) and is observed within the matrix (Figure 7c-e). Only the
383 second group of chlorite is observed in sample ZAL18-11 (Table S1).
384 White mica in the granitic basement shows 55-80 % muscovite (*Ms*), pyrophyllite (*Prl*)
385 content in the 0-20% range and up to ~30 % celadonite content (*Cel,* Figure 8a). White mica in
386 fractures, veins and in the deformed matrix (syn-kinematic) exhibits lower muscovite (55-70 %)
387 and higher (or similar) celadonite content (20-30 %) than white mica in chlorite flakes (pre-
388 kinematic, 70-80 % muscovite, 10-20 % celadonite, Figure 8a). The composition of white mica
389 in sedimentary samples is similar to that of white mica from feldspar in basement samples
390 (Figure 8b), but with lower variability. While in samples ZAL18-12 and ZAL18-11 one single
391 group of white mica is observed, in sample ZAL18-13 two groups are identified: white mica in
392 the veins have higher celadonite contents (18-28%) than in the matrix (10-18%).

393

394 **5.2 Thermobarometry of low-grade fluid-rock interaction events**

395 Thermodynamic modelling was combined to empirical thermobarometry to distinguish the
396 conditions of crystallisation of the different generations of chlorite and white mica possibly
397 recorded by the restricted range of compositional variations. Crystallisation temperature
398 calculated with the chlorite thermometers of Vidal et al. (2006) and Bourdelle et al. (2013) are
399 reported in Figure 9a, and range between 180 and 350°C. The minimum content of XFe^{3+} in
400 chlorite calculated with the method of Vidal et al. (2006) ranges between 0.1 and 0.55, which

401 is realistic for low-T chlorite (Masci et al., 2019). The entire iron content was considered
402 divalent for the thermometer of Bourdelle et al. (2013) as recommended in that study.
403 Calculated temperatures for all groups of chlorites are in the same range, with small but
404 systematic differences between Chl1 and Chl2. In samples recording two compositional groups
405 of chlorites (that correspond to pre and syn-kinematic grains), where Fe variations prevail on
406 other element variations (ZA16-82, B11-19, ZA16-78), Chl1 records higher temperatures (220-
407 320°C) than Chl2 (180-250°C). In samples where dominant chemical variations involve Al and
408 Mg (ZA16-126, ZA16-73, B10-32), Chl1 records lower temperatures (170-280°C) than Chl2
409 (230-350°C, Figure 8a). In other samples (ZA16-133, B10-31), where two compositional
410 groups of chlorite were observed, calculated temperature cover the entire temperature range
411 estimated for all samples. Undeformed granite samples preserving only Chl1 (e.g. ZA16-79,
412 B11-16, ZA16-117) record the highest range of temperatures (280-350 °C). Crystallisation
413 temperatures calculated for chlorite in mylonites (e.g. ZA16-96, ZA16-98, ZA16-128, ZA16-
414 97) are intermediate between the Chl1 and Chl2 crystallisation temperatures. Two ranges of
415 temperatures were also obtained for chlorite in sedimentary samples (ZAL18-12). The highest
416 temperatures (240-350°C) are generally associated with chlorite in veins, while lowest
417 temperatures (180-280°C) are mostly associated with chlorites in C planes (with variability,
418 especially for samples collected Est and West of the Lake of Urdiceto, Fig. 1c). Only one range
419 of chlorite temperatures (Chl2, 200-300°C) is observed within the vein of sample ZAL18-11.
420 To test for the statistical validity of the two temperature intervals (240-350°C and 180-280°C),
421 3000 temperatures were randomly sampled from the dataset calculated with the thermometer
422 of Vidal et al. (2006) assuming a Gaussian error of ± 30°C (Figure 9b). In the basement, two
423 main peaks at 260 and 330°C persist. Scattered values at low-T conditions are attributed to
424 modelling artefacts due to Fe^{3+} overestimation and/or to departure of some chlorite
425 compositions from equilibrium with assumed unit activity for quartz and water.

426 The moderate celadonite contents of white mica (accounting for the Tschermark substitution
427 only) suggest crystallization pressures in the range 1-4.5 kbar following the calibration of
428 Massone and Schreyer (1988) (Figure 9c), as opposed to sub-surface hydrous alteration of
429 feldspar only, which would favour pyrophyllitic substitution (Dubacq, Vidal, & De Andrade,
430 2010). Following this calibration, the higher celadonite content (and Si apfu content) of white
431 mica in fractures, veins and shear bands indicates higher pressure conditions than in white mica
432 growing from feldspar or from biotite (white mica in flakes, Figure 9c).
433
434 **5.3 *In situ* U-Th/Pb dating of magmatic zircon and hydrothermal anatase, titanite and**
435 **monazite**
436 Results for titanite, anatase and monazite dating are shown in Figure 10a-c and summarized in
437 Table 1; the raw isotopic ratios and age data for zircon, titanite and anatase are provided in
438 Table S3. The entire geochronological dataset is combined with previous literature age
439 constraints of metamorphic events, derived from other localities of the Axial zone in Figure
440 10d. The composition of monazite together with all concordias for zircon, titanite and anatase
441 are provided in Figure S2. Zircon analyses yield weighted mean Concordia ages at 300-310 Ma
442 (Figure 10d and f). Some zircon analyses, especially in sample ZA16-119, exhibit Pb loss and
443 broadly define a discordia line intercepting the Concordia at c. 285-290 Ma (see Figure S1).
444 Titanite grains contain on average 16 ppm of U, 1.7 ppm of Th and 50 ppm of common
445 Pb, and exhibit a Th/U ratio of 0.1 with ages spanning from 336 ± 12 to 313 ± 11 (Figure 10a
446 and d). Titanite in ZA16-84 provides the age constraint with the lowest uncertainty (313 ± 11,
447 MSWD of 1.1, Figure 10a) and exhibits the lowest common Pb content (10 ppm) and the highest
448 Th/U ratio (0.20). Anatase contains on average lower amounts of U (8 ppm) and common Pb
449 (24 ppm), and higher Th contents (3.4 ppm) than titanite, with Th/U ratios of 0.4, with ages
450 from 301 to 48 Ma (Figure 10b and d). The age of anatase is difficult to constrain because of

high common Pb and low radiogenic Pb contents. When possible, two Tera-Wasserburg concordia lower intercepts for anatase U-Pb age data were defined for each sample, delimiting the possible youngest and oldest grain populations (e.g. Figure 10b). In this case, youngest ages cluster at *c.* 30-80 Ma while oldest ages cluster at *c.* 240-280 Ma (Figure 10b, d). The mylonitic granite ZA16-96 exhibits the young age population only (Tera-Wasserburg concordia lower intercept of 39 ± 8 Ma, Figures 10c and S1), despite the low variability of the radiogenic U/Pb ratio.

Patchy monazite in samples ZA16-98 and ZAL18-11 shows low and variable U and Th contents (Figure 10e and Table S2), typical of low-temperature secondary monazite (Rasmussen & Muhling, 2007; Janots, Berger, & Engi, 2011). The U-Th/Pb ages (with Pb > EPMA detection limits of ~100 ppm) range between 180 and 325 Ma (Figure 10c). In both samples, Pb-depleted domains (Pb < EPMA detection limits despite Th contents up to few wt%, Table S2) are observed within Th-depleted monazite grains, indicating late partial replacement of monazite grains by recrystallization and dissolution-reprecipitation (Figure 10e). The oldest ages generally correspond to monazite with relatively high Th content (ThO_2 > 2.4 wt %) and variable U content (0.04 wt% < UO_2 < 1.0 wt %). They cluster around 254 ± 6 Ma. A second group of monazite has a lower Th content (ThO_2 < 1.9 wt%), variable U content (0.01 wt% < UO_2 < 1.9 wt%) and provides an age of 196 ± 18 Ma. In both samples ZA16-98 and ZAL18-11 young ages are estimated from the Pb-depleted domains (Pb < detection limits). Assuming a Pb content equal to the EPMA detection limit (~90 ppm), a maximum age for this late stage crystallisation has been calculated at *c.* 100 Ma in sample ZA16-98 and at *c.* 20 Ma in sample ZAL18-11 for the domains with the highest Th (ThO_2=7.6 wt.%) and U contents (UO_2=0.9750 wt.%) (Figure 10c). Cenozoic ages of *c.* 50 Ma have also been estimated in sample ZA16-98 from thorite-monazite domains. No ages could be obtained for monazite from the sedimentary samples due to their low U, Th and Pb contents.

476

477 **6. DISCUSSION**

478

479 **6.1 Evaluation of geochronological results**

480 Estimated crystallisation temperatures are far below the closure temperature of Pb diffusion in
481 rutile (580-630°C), titanite (575-700°C), monazite (~800 °C) and zircon (~900 °C, Rubatto,
482 2017; Engi, 2017 and references therein). Therefore, U-Th/Pb dates are interpreted as
483 crystallisation ages. Zircon is dominantly of magmatic origin as attested by its microtextures.
484 Concordant zircon ages, inferred to bracket the timing of the Bielsa pluton emplacement at 300-
485 310 Ma (Figure 10d and Table 1), are in agreement with previously published ages (Vacherat
486 et al., 2017). Zircon ages therefore constrain the upper limit of the first alteration event.
487 Discordant ages defining a chord with an intercept at *c.* 290 Ma in sample ZA16-119 (Figure
488 S1) derive from sampling of metamictic zircon domains, characterized by decreasing
489 crystallinity, Pb loss and variable incorporation of common Pb. Since metamict domains show
490 typical textures of dissolution-reprecipitation under low-T conditions (Geisler et al., 2003) and
491 are observed in undeformed samples, the c. 290 Ma age may indicate re-opening of the system
492 during the early pre-kinematic fluid-rock interaction, started shortly after the pluton
493 emplacement, in Late Variscan times.

494 Titanite ages are less accurate but cluster within uncertainty of the zircon ages, at *c.* 300
495 Ma (Late Variscan) (Figure 10d and Table 1). Some of the titanite ages are older than the
496 corresponding zircon ages from the same sample. The titanite Discordia line on Tera-
497 Wasserbourg Concordia diagram is well constrained due to the large variation in U:Pb ratio of
498 the titanite grains (Figure 10a and Figure S2). Therefore, the titanite ages marginally older than
499 their corresponding zircon ages may originate from local incorporation of radiogenic PB at the
500 time of titanite crystallization (see also Essex and Gromet, 2000). The $^{207}Pb/^{206}Pb$ initial ratio
501 of metamorphic titanite has been shown to vary up to 2% in the same sample (Kohn, 2017), and

502 is often significantly lower (i.e. more radiogenic) than the crustal evolution model of Stacey
503 and Kramers (1975). This signs the incorporation of radiogenic Pb from the breakdown of a U-
504 rich mineral phase such as rutile or anatase, anatase being observed here as the most common
505 titanite precursor.

506 The U/Pb ages obtained for anatase are less well constrained than the titanite due to
507 higher common Pb, lower radiogenic Pb contents and the smaller spread in U-Pb ratio of the
508 anatase grains. Calculated ages range between 40 Ma and 280 Ma. Anatase does not record the
509 magmatic stage since it is observed to replace magmatic ilmenite. If type-1 Ant or titanite
510 recrystallize into type-2 Ant, inter and intra-grain variations in the radiogenic Pb and U content
511 could be inherited from the parent mineral given the small transport scales for anatase-forming
512 elements deduced from microtextural evidence (see section 3.1). Such variations and possible
513 incorporation of type-1 Ant in spot ablations of titanite (see section 4) contribute to the large
514 spread of the anatase ages (e.g. samples ZA16-79, ZA16-73). However, a recurrently young
515 signal of *c.* 40-80 Ma is exclusively observed only in samples with both types of anatase and in
516 mylonites. As solid-state Pb diffusion can be excluded due to the low metamorphic grade, the
517 youngest U-Pb anatase ages likely indicate partial (re-)crystallization of the smallest anatase
518 grains (type-2 Ant), in agreement with microtextural observations. In addition, the upper limit
519 of the range of anatase ages is the youngest in samples with both types of anatase: This suggests
520 mixing at a smaller scale than laser beam size between older titanite-anatase and new anatase.
521 The two age end-members are shown on Figure 10d for all anatase-bearing samples.

522 Monazite is unlikely to record the magmatic stage since (1) magmatic allanite and apatite
523 incorporate the rare earth elements and phosphorous necessary for monazite crystallization, (2)
524 monazite is observed to replace magmatic allanite or apatite and (3) the oldest monazite ages
525 are younger than the zircon ages. Monazite ages in both samples ZA16-98 and ZAL18-11
526 indicate a series of events at *c.* 250 Ma, 200 Ma, and possibly < 50 Ma. This range of ages

527 suggests successive episodes of partial dissolution-reprecipitation, as also shown by the patchy
528 textures and the dissolution figures of monazite grains (Figures 5c and 6b). The mineral
529 assemblage corresponding to the monazite ages of *c.* 200 Ma remains difficult to identify as
530 textural and chemical evidences is lacking. The ages of 190-250 Ma obtained in monazite of
531 chlorite-bearing veins in sediments indicate that monazite grains were likely inherited from the
532 underlying basement and partially re-crystallized during vein opening and fluid circulation soon
533 after sediments deposition in Triassic times.
534
535 **6.2 Timing and conditions of fluid-rock interactions and deformation**
536 Detailed microstructural and petrological observations show a poly-phase alteration history in
537 the Bielsa basement at temperatures below 350°C. Within this temperature range, a first fluid-
538 rock interaction event is related to the breakdown of the original magmatic assemblage and the
539 growth of Ttn, Chl1, anatase (type-1 Ant) at 270-350°C. This alteration event predates all
540 deformation stages since the earliest deformation phase deforms this mineral assemblage and
541 the alteration event is also observed in undeformed samples (e.g. Figure 4a-b). During the first
542 alteration event, the source of Al and Ca for chlorite and titanite (± prehnite) growth is the
543 contemporaneous breakdown of plagioclase and the albitization of alkali-feldspar (always
544 largely consumed), irrespective of the strain intensity. Calcium may also derive from external
545 fluids as attested by calcite growth within weakely deformed granite matrix. Titanite, zircon,
546 anatase and oldest monazite ages allow bracketing the timing of the early alteration(s) to 230-
547 300 Ma (late to post-Variscan). This age range is in agreement with $^{40}Ar/^{39}Ar$ ages of biotite of
548 *c.* 280 and 250 Ma obtained in the Bielsa and Maladeta massifs respectively (Jolivet et al., 2007).

549 The second fluid-rock interaction event is related to the syn-kinematic growth of Chl2
550 during the formation of C-S structures (see section 3) at ~200-280°C. The pervasive schistosity,
551 kinking, shearing and fracturing are likely to have occurred at the same time since they are

552 kinematically compatible. The S planes are observed in both the basement and in the Triassic
553 sediments (see section 2). The S-forming stage is therefore post-late Triassic in age at least.

554 In such deformed samples, the youngest ages are yielded by anatase (in samples bearing
555 both types of anatase) and by monazite; this suggests that deformation triggered the partial re-
556 crystallization of anatase and monazite. The youngest anatase ages only (*c.*40 Ma) and the
557 youngest monazite ages (*c.* 50 Ma) are obtained in mylonites (ZA16-96 and ZA16-98). This
558 observation suggests that the mylonitization related to the deformation stage likely occurred
559 between 40 and 70 Ma. These ages are in agreement with Rb-Sr ages of *c.* 48 Ma obtained for
560 the (re)activation of mylonitic bands in the Néouvielle massif (~ 15 km to the northwest of
561 Bielsa, Wayne & McCaig, 1998). In sample ZA16-79 an age population at *c.* 120 Ma is
562 observed, but no clear textural relationships are identified, while the large uncertainties mean it
563 Eocene ages.

564 Chlorite temperatures calculated with the method of Vidal et al. (2006) and Bourdelle
565 et al. (2013) are consistent despite differences in how they employ the oxidation state of Fe.
566 The calculated range of temperatures (200-350°C) is also consistent with hydrothermal
567 conditions typically associated with the appearance of prehnite and titanite in the cleavages of
568 biotite (e.g. Eggleton & Banfield, 1985; Morad, Sirat, El-Ghali, & Mansurbeg, 2011; Yuguchi
569 et al., 2015) and with temperatures calculated for the overlying sediments, suggesting that fluids
570 were freely circulating between the basement and the overlying sediments. In details,
571 thermometric results indicate that the pre-kinematic greenschist-facies metamorphism occurred
572 at higher temperature (270-350°C) than later syn-kinematic fluid-rock interaction (200-280°C,
573 Figure 9b), with spatial variations (east and west of Lake Urdiceto, Figure 9a) due to local
574 variations in fluid composition. The systematic differences between temperatures estimated for
575 Chl1 and Chl2 support however the existence of two different fluid-rock interaction events.

The moderate celadonite content of white mica, especially in fractures, veins and shear bands (Figure 8a and c) suggests crystallization at a pressure of 1-5 kbar (1 - 4.5 kbar, following the formulation of Massone and Schreyer, 1988, Figure 9c and below 3 kbar according to Cathelineau et al., 1986 for hydrothermal alteration in granites). No paragonite nor margarite components are observed within our white mica dataset. Pyrophyllite substitution, which increases the Si content of muscovite, is not predominant compared to the Tschermak substitution (Figure 8a). Increasing pyrophyllite content in sample B11-31 implies crystallization during continuous cooling (Dubacq et al., 2010). Fluid inclusion trapping pressures in the range 2-5 kbar are reported by Henderson and McCaig (1996), consistent with pressure estimates from white mica in mylonite veins (Wayne & McCaig, 1998). The lowest pressure values of ~ 2 kbar are consistent with the maximum burial depth estimated for the Bielsa (Jolivet et al., 2007; Bellahsen et al., 2019).

This low-grade petro-chronological dataset allows the timing of low-grade metamorphism and deformation to be discussed in the light of the Variscan and Alpine orogenic cycles, with major implications for the crustal rheology and the evolution of the deformation style in granites.

6.3 Pre-orogenic alteration and implications for crustal softening prior to shortening

Petro-chronological results and microstructural analyses show that Late to post-Variscan lower greenschist-facies metamorphism in the Bielsa massif transformed an initially strong assemblage made of plagioclase, K-feldspar (forming together close to half of the primary modal composition) and amphibole into weaker, hydrated minerals such as white mica and chlorite, without associated deformation (as suggested by Bellashen et al., 2019). The breakdown of feldspar to white mica decreases by up to two orders-of-magnitude the sustained shear stress (at a constant strain rate) at 400°C, lowering the depth of the brittle-ductile

601 transition by at least a third (Wintsch et al., 1995; Gueydan et al., 2003). In the Bielsa massif,
602 pre-orogenic sub to lower greenschist-facies metamorphic reactions have two effects: they
603 enhance grain size reduction (e.g. from magmatic feldspars to minute white micas) and also
604 replace strong minerals such as feldspar and amphibole with mechanically weaker
605 phyllosilicates (e.g. Shea & Kronenberg, 1993). Both processes are known to result in enhanced
606 softening of the granitic rocks (e.g. Fitz Gerald & Stünitz, 1993; Wintsch et al., 1995; Oliot,
607 Goncalves, Marquer, 2010). Early pre-kinematic alteration therefore considerably softened the
608 granite at least 150 Ma before the major Alpine shortening phases. Furthermore, the massive
609 growth of pre-kinematic and pre-Alpine white mica and chlorite indicates high fluid-rock ratios
610 during Late-to post-Variscan times and may strongly influence the water availability in the
611 rocks at the grain boundaries during deformation. This has been shown to have major effects
612 on the mechanisms of strain accommodation in other major phases as quartz (e.g. Palazzin et
613 al., 2018) and hence impact the deformation style.

614 Sericitisation of feldspar and chloritisation of biotite is observed to increase with
615 deformation. This suggests that granite alteration continued during syn-kinematic Alpine
616 shortening. In mylonites, syn-kinematic chlorite and white mica partly replace the pre-
617 kinematic chlorite and mica grains, this time without needing huge supplementary amounts of
618 external fluid. Consequently, in the latter fluid-rock interaction event, there is no evidence for
619 additional large-scale reaction-driven softening outside mylonitic zones, consistent with
620 observations reported for the Néouvielle massif (~ 15 km to the northwest, Wayne & McCaig,
621 1998). The crystallisation of new phyllosilicates and the larger amount of fluid inclusions in
622 quartz in fractured and mylonitic samples as well as the partial age resetting up to ~40 Ma close
623 to shear zones also appear to indicate progressive localisation of metamorphism with strain
624 localisation.

Zones of fractures and faults indicate that granitic rocks were also deformed by frictional behaviour, as commonly observed at temperatures of 200-350°C (e.g. Copley, 2017). The crystallization of phyllosilicates during a pre-orogenic alteration event may weaken fault zones by at least 30% as phyllosilicates have much lower coefficients of friction than undeformed and unaltered crystalline rocks (e.g. Kaduri, Gratier, Renard, Çakir, & Lasserre, C., 2017; Copley, 2017). The pre-existence of phyllosilicate in the Bielsa basement therefore appears to have generated a network of weak rocks with low friction coefficient resulting in their distributed deformation.

6.4 Effect of the early alteration on deformation patterns at field scale

The pervasive schistosity (S) observed within the Bielsa massif along the studied transects indicates that the deformation is distributed at the scale of the massif (Figure 1b). The existence of mylonitic corridors shows a phase of strain localization with variations in the sense of shear at the kilometric to decametric scale, but their high density also results in a distributed deformation at the massif scale. At Bielsa, both S and C forming stages post-date the Late to post-Variscan pervasive alteration that softened the basement. In the Maladeta massif, (50-60 km to the northeast), less pervasive pre-kinematic alteration is observed as well as localized deformation and lower density of mylonitic corridors (Leblanc, Gleizes, Lespinasse, Olivier, & Bouchez, 1994). This indicates that pre-orogenic crustal softening controlled the deformation patterns observed on a outcrop scale, in particular the frequency of mylonitic bands the location of faults and of fractures.

In the Bielsa massif, strain localization in mylonitic bands may have occurred during the intense folding of the basement and the sedimentary cover in the Eocene as indicated by the young ages from the mylonites. During this stage, the re-activation of steep faults may have served as fluid pathways and triggered alteration. Interfaces between differently-altered

650 domains formed different phase strength contrasts. Consequently, ductile strain and reactions
651 interacted positively to produce narrow ductile shear zones (as described by Holyoke & Tullis,
652 2006). Furthermore, deformation at this stage may strongly influence the breakdown on residual
653 feldspar to muscovite (e.g. Knipe & Wintsch, 1985), as attested by the greater amount of white
654 mica observed in mylonites compared to weakly and undeformed samples.

655 The youngest ages obtained in this study (*c.* 40 Ma) are older than the activation of the
656 Gavarnie and Guarga thrusts (Figure 1b), in the hanging and footwall of the Bielsa unit, dated
657 at 32-36 Ma et 20-30 Ma respectively (e.g. Bosch et al., 2016; Elmola et al., 2018) and similar
658 to the age of mylonitization in the Néouvielle massif (Wayne & McCaig, 1998). This may
659 indicate that the distributed shortening in Bielsa and at a larger scale predates the localization
660 of the strain along some of the major thrust of the Axial zone. These findings are consistent
661 with the distributed / localized modes of shortening documented in the external Western Alps
662 (Bellahsen et al., 2014), in the central Alps (Wehrens, Baumberger, Berger & Herweg, 2017)
663 and in the Longmen Shan where pre-kinematic and a syn-kinematic greenschist-facies
664 metamorphic events were also recognized (Airaghi et al., 2017b), indicating that they might be
665 typical of the evolution of basement massif in the external domains of the orogenic wedges.
666

667 **6.5 Onset and preservation of early alteration in granitic basement**

668 Late to post-Variscan fluid-rock interaction took place on the scale of the Axial zone as
669 metamorphic reactions similar to those observed in the Bielsa massif are found in other
670 crystalline massifs in the Pyrenees (e.g. Maladeta, Néouvielle, Col de Jau; Cathelineau, 1986;
671 Boutin et al., 2016). The early alteration stages may be linked to protracted magmatic activity
672 recorded in the Pyrenean domain throughout the entire Permian (Denèle, Paquette, Olivier, &
673 Barbey, 2012). Late Variscan magmatic activity has also been invoked as the cause of
674 hydrothermal alteration in the French Massif Central (Cathelineau, 1986; Turpin, Leroy, &
675 Sheppard, 1990). Permian to Triassic ages similar to those obtained for fluid-rock interaction

676 events in the Bielsa massif have also been documented in the Variscan basement of the Eastern
677 Iberian Central System and in NE Spain by fluid inclusion and isotopic studies (Tornos,
678 Delgado, Casquet, & Galindo, 2000 and references therein). The associated hydrothermal
679 alteration in these cases is related to hydrothermal cells formed during extensional tectonic
680 events rather than to plutonism (Tornos et al., 2000; Cardellach, Canals, & Grandia, 2002). In
681 the Bielsa massif, high fluid-rock ratios have been proposed to result from ingress of seawater
682 and meteoric fluids during the extensional phase following the Variscan orogeny (McCaig,
683 Tritlla, & Banks, 2000). This is consistent with the fact that the Bielsa basement was exposed
684 at the surface before or during the Permian, as attested by the erosional unconformity between
685 the basement and its sedimentary cover. The preservation of early alteration features in granites
686 over two orogenic cycles (Variscan and Alpine) implies that the basement remained at low
687 grade conditions for over 200 Ma. In the Pyrenees, the main post-Variscan metamorphic phase
688 related to fluid circulation is dated at 110 Ma (e.g. Boutin, 2016). Although Cretaceous ages
689 were obtained for samples which contain both types of anatase, the large U/Pb age uncertainties
690 for this time period in our petro-chronological dataset mean that strong evidence for extensive
691 fluid circulation, mineral replacement and deformation during Cretaceous times is lacking. This
692 is in contrast to the eastern Pyrenees where a hydrothermal event characterized by newly formed
693 rutile and titanite associated with Cretaceous rifting overprints the 'post'-Variscan
694 hydrothermal alteration assemblages (Figure 10d; Boutin et al., 2016; Fallourd et al., 2014).
695 This may indicate that, within the Pyrenean belt, metamorphism related to rifting has only
696 weakly affected the southern part of the Axial zone.
697
698 **7. CONCLUSIONS**
699 The granitic basement rocks in the southern Axial zone of the Pyrenees (Bielsa massif) acted
700 as reactive rocks at low temperatures (T < 350 °C) over a long (*c.* 300 Ma) polyphase history.

701 At an outcrop scale, the Bielsa pluton and the Triassic sedimentary cover exhibit a pervasive
702 N-dipping schistosity, folded or associated to steep C planes localized within a dense network
703 of mylonitic bands. Within the granitic basement, partial mineral replacement and
704 compositional variations at the micron-scale record an extensive fluid-rock interaction event at
705 ~270-350°C in Late to post-Variscan times (230-300 Ma), as indicated by the titanite, anatase
706 and zircon U/Pb ages dataset. This event is ubiquitous and particularly well preserved in the
707 less deformed areas of the massif. It is responsible for pre-kinematic (pre-Alpine) plagioclase
708 and amphibole replacement with growth of phyllosilicates, some tens of million years after
709 pluton emplacement. A second syn-kinematic fluid-rock interaction event is marked by the
710 (re)crystallisation of phyllosilicates at ~200-280°C and is related to the formation of mylonitic
711 corridors and fractures parallel to the C shear planes. In the most deformed samples, despite the
712 low radiogenic Pb content, monazite and anatase U-Th/Pb ages systematically show a young
713 age component at 40-70 Ma, coeval with the Alpine/ Pyrenean deformation in the southern
714 Axial zone and related to the second alteration event. As the strength of phyllosilicate-rich
715 material is lower by up to an order-of-magnitude than that of the original granite, the granitic
716 massif was significantly softened (and hydrated) at least 150-200 Ma before the major Alpine
717 shortening phase. The dense network of mylonites in the Bielsa pluton resulted in distributed
718 deformation at the massif scale before the localization of the strain along the major thrusting
719 systems of the Axial zone. Pre-orogenic crustal softening controlled the deformation patterns
720 where strain and shortening localized during successive deformation events. Pre-orogenic
721 greenschist-facies metamorphism is often poorly characterized compared to higher-grade
722 metamorphic domains in mountain belts. The case of the Bielsa massif shows that moderate
723 analytical effort can provide valuable information allowing for a better constraints on the
724 rheological and thermobarometric evolution of basement rocks during the orogenic cycle, even
725 at low-grade conditions.

ACKNOWLEDGEMENTS

This study was founded by the CNRS-BRGM-TOTAL 'OROGEN' project. We acknowledge Prof. S. Duchene and the anonymous review for their constructive comments and remarks. We thank Michel Fialin, Nicolas Rividi and Omar Boudouma for their help with the electron microscopy at ISTeP. DC acknowledges support from Science Foundation Ireland grants 12/IP/1663, 15/IA/3024 and 13/RC/2092 (iCRAG Research Centre). iCRAG is funded under the SFI Research Centres Programme and is co-funded under the European Regional Development Fund. We also thank Gary O'Sullivan (Trinity College) for his support with the LA-ICP-MS analysis. Authors have no conflict of interest to declare.

REFERENCES

Airaghi, L., Janots, E., Lanari, P., de Sigoyer, J. & Magnin, V. (2018). Allanite petrochronology in fresh and retrogressed garnet-biotite metapelites from the Longmen Shan (eastern Tibet), Journal of Petrology, in press.

Airaghi, L., de Sigoyer, J., Lanari, P., Guillot, S., Vidal, O., Monié, P., … Tan, Xibin (2017). Total exhumation across the Beichuan fault in the Longmen Shan (eastern Tibetan plateau, China) : Constraints from petrology and thermobarometry. Journal of Asian Earth Sciences, 140, 108-121.

Bellahsen, N., Mouthereau, F., Boutoux, A., Bellanger, M., Lacombe, O., Jolivet, L., … Rolland, Y. (2014). Collision kinematics in the western external Alps, Tectonics, 33.

Bellahsen, N., Bayet, L., Denele, Y., Waldner, M., Airaghi, L., Rosenberg, C. … Vacherat, A. (2019). Shortening of the axial zone, Pyrenees: Shortening sequence, upper crustal mylonties and crustal strength. Tectonophysics, 766, 433-452.

750 Bosch, G. V., Teixell, A., Jolivet, M., Labaume, P., Stockli, D., Domènech, M., …Monié, P.
751 (2016). Timing of Eocene-Miocene thrust activity in the Western Axial Zone and
752 Chaînons Bérnais (west-central Pyrenees) revealed by multi-method thermochronology.
753 Comptes Rendus Geoscience, 348(3-4), 246-256.
754 Bourdelle, F., Parra, T., Beyssac, O., Chopin, C. & Vidal, O. (2013). Clay minerals as geo-
755 thermometer: A comparative study based on high spatial resolution analyses of illite
756 and chlorite in Gulf Coast sandstone (Texas, U. S.A.). American Mineralogist, 98, 914-
757 926.
758 Boutin, A., de Saint Blanquat, M., Poujol, M., Boulvais, P., de Parseval, P., Rouleau,
759 C., …Robert, J.-F. (2016). Succession of Permian and Mesozoic metasomatic events in
760 the eastern Pyrenees with emphasis on the Trimouns talc-chlorite deposit. International
761 Journal of Earth Science, 105, 747-770.
762 Cardellach, E., Canals, A. & Grandia, F. (2002). Recurrent hydrothermal activity induced by
763 successive extensional episodes: the case of the Berta F-(Pb-Zn) vein system (NE
764 Spain). Ore Geology Reviews, 22, 133-141.
765 Casas, A.M., Oliva, B., Román-Berdiel, T. and Pueyo, E. (2003). Basement deformation:
766 tertiary folding and fracturing of the Variscan Bielsa granite (Axial zone, central
767 Pyrenees). Geodinamica Acta, 16(2-6), 99-117.
768 Cathelineau, M. (1986). The Hydrothermal Alkali Metasomatism Effects on Granitic Rocks :
769 Quartz Dissolution and Related Subsolidus Changes. Journal of Petrology, 27, 945-965.
770 Chew, D. M ;, Petrus, J. A. & Kamber, B. S. (2014). U-Pb LA-ICPMS dating using accessory
771 mineral standards with variable common Pb. Chemical Geology, 363, 185-199.
772 Cochelin, B., Lemirre, B., Denèle, Y., de Saint Blanquant, M., Lahfid, A., & Duchene, S.
773 (2017). Structural inheritance in the Central Pyrenees : the Variscan to Alpine

774 tectonometamorphic evolution of the Axial Zone. Journal of the Geological Society,
775 175(2), 336.
776 Copley, A. (2017). The strength of earthquake-generating faults. Journal of the Geological
777 Society, 10.1144/jgs2017-037.
778 Denèle, Y., Paquette, J.-L., Olivier, P. & Barbey, P. (2012). Permian granites in the Pyrenees:
779 the Aya pluton (Basque Country). Terra Nova, 24, 105-113.
780 Dubacq, B., Soret, M., Jewison, E., Agard, P. (2019). Early subduction dynamics recorded by
781 the metamorphic sole of the Mt Albert ophiolitic complex (Gaspé, Quebec). Lithos, 334
782 – 335, 161 – 179, doi: 10.1016/j.lithos.2019.03.019.
783 Dubacq, B., Vidal, O., De Andrade, V., 2010. Dehydration of dioctahedral aluminous
784 phyllosilicates: thermodynamic modelling and implications for thermobarometric
785 estimates. Contributions to Mineralogy and Petrology 159, 159–174.
786 Eggleton, R. A. & Banfield, J., F. (1985). The alteration of granitic biotite to chlorite. American
787 Mineralogist, 70, 902-910.
788 Elmola, A. A., Buatier, M., Monié, P., Labaume, P., Trap, P., & Charpentier, D. (2018).
789 40Ar/39Ar muscovite dating of thrust activity: a case study from the Axial Zone of the
790 Pyrenees. Tectonophysics, in press.
791 Engi, M. (2017). Petrochronology Based on REE-Minerals: Monazite, Allanite, Xenotime,
792 Apatite. In: Petrochronology: Methods and Applications, Kohn, M. J., Engi, M. &
793 Lanari, P. Reviews in Mineralogy & Geochemistry.
794 Fallourd, S., Poujol, M., Boulvais, P., Paquette, J.-L., de Saint Blanquant, M., & Rémy, P.
795 (2014). In situ LA-ICP-MS U-Pb titanite dating of Na-Ca metasomatism in orogenic
796 belts: the North Pyrenean example. International Journal of Earth Science, 103, 667-
797 682.

798 Fitz Gerald, J. D. & Stünitz, H. (1993). Deformation of granitoids at low metamorphic grade.
799 I: Reaction and grain size reduction. Tectonophysics, 221 (3-4), 269-297.
800 Geisler, T., Rashwan, A. A., Rahn, M. K., Poller, U., Zwingmann, H., Pidgeon, R.
801 T., …Tomaschek, F. (2003). Low-temperature hydrothermal alteration of natural
802 metamict zircon from the Eastern Desert, Egypt. Mineralogical Megazine, 67(3), 485-
803 508.
804 Goncalves, P., Oliot, E., Marquer, D. & Connolly, J. A. D. (2012). Role of chemical processes
805 on shear zone formation: an example from the Grimsel metagranodiorite (Aar massif,
806 Central Alps). Journal of Metamorphic Geology, 30(7), 703-722.
807 Grand'Homme, A., Janots, E., Seydoux-Guillaume, A.M., Guillaume, D., Magnin, V.,
808 Hövelmann, J., …Boiron, M.C. (2018) Mass transport and fractionation during
809 monazite alteration by anisotropic replacement. Chemical Geology, 484, 51–68.
810 Gueydan, F., Leroy, Y.M., Jolivet, L., & Agard, P. (2003). Analysis of continental midcrustal
811 strain localization induced by microfracturing and reaction-softening. Journal of
812 Geophysical Research, 108(B2), 2064.
813 Henderson, I. H. C. & McCaig, A.M. (1996). Fluid pressure and salinity variations in shear
814 zone-related veins, central Pyrenees, France: Implications for the fault-valve model.
815 Tectonophysics, 262, 321-348.
816 Hansen, E., Reimink, J. & Harlov, D. (2010). Titaniferous accessory minerals in very low-grade
817 metamorphic rocks, Keweenaw Peninsula Michigan, USA. Lithos, 116, 167-174.
818 Ingles, J., Lamouroux, C., Soula, J.-C., Guerrero, N. & Debat, P. (1999). Nucleation of ductile
819 shear zone in a granodiorite under greenschist facies conditions, Néouvielle massif,
820 Pyrenees, France. Journal of Structural Geology, 21, 555-576.
821 Jackson, J. A., Austrheim, H., McKenzie, D. & Priestley, K. (2004). Metastability, mechanical
822 strength, and support of mountain belts. Geology, 32(7), 625-628.

823 Janots, E., Berger, A. & Engi, M. (2011). Physico-chemical control on the REE minerals in
824 chloritoid-grade metasediments from a single outcrop (Central Alps, Switzerland).
825 Lithos, 121, 1-11.
826 Jolivet, M., Labaume, P., Monié, P., Brunel, M., Arnaud, N., & Campani, M. (2007).
827 Thermochronology constraints for the propagation sequence of the south Pyrenean
828 basement thrust system (France-Spain). Tectonics, 26, TC5007.
829 Kaduri, M., Gratier, J.-P., Renard, F., Çakir, Z., & Lasserre, C. (2017). The implications of
830 fault zone transformation on aseismic creep: Example of the North Anatolian Fault,
831 Turkey, Journal of Geophysical Research : Solid Earth, 122, 4208-4236.
832 Knipe, R. J. & Wintsch, R. P. (1985). Heterogeneous, deformation, foliation development, and
833 metamorphic processes in a polyphaser mylonite. In: Thompson, A. B., Rubie, D. C.
834 (Eds.), Advances in Physical Chemistry, 4, Springer-Verlag, New York, 180-210.
835 Kohn, M. J. (2017). Titanite petrochronology, In: Petrochronology: Methods and Applications,
836 Kohn, M. J., Engi, M. & Lanari, P. Reviews in Mineralogy & Geochemistry.
837 Lanari, P., Vidal, O., De Andrade, V., Dubacq, B., Lewin, E., Grosch, E., …Schwartz, S.
838 (2014). XMapTools: a MATLAB-based program for electron microprobe X-ray image
839 processing and geothermobarometry. Computers & Geosciences 62, 227–240.
840 Leblanc, D., Gleizes, G., Lespinasse, P., Olivier, Ph. & Bouchez, J.-L. (1994). The Maladeta
841 granite polydiapir, Spanish Pyrenees : a detailed magneto-structural study. Journal of
842 Structural Geology, 16(2), 223-235.
843 Mansard, N., Raimbourg, H., Augier, R., Précigout, J. & Le Breton, N. (2018). Large-scale
844 strain localization induced by phase nucleation in mid-crustal granitoids of the south
845 Armorican massif. Tectonophysics, 745, 46-65.
846 Masci, L., Dubacq, B., Verlaguet, A., Chopin, C., De Andrade, V., & Herviou, C. (2019). A
847 XANES and EPMA study of Fe^{3+} in chlorite: importance of oxychlorite and

implications for cation site distribution and thermobarometry. American Mineralogist. 104(3), 403-417.

Massonne, H-J. & Schreyer, W. (1987). Phengite geobarometry based on the limiting assemblage with K-feldspar, phlogopite, and quartz. Contributions to Mineralogy and Petrology, 96, 2, 212-224, doi: 10.1007/BF00375235.

McCaig, A. M., Tritlla, J. & Banks, D.A. (2000). Fluid mixing and recycling during Pyrenean thrusting: evidence from fluid inclusion halogen ratios. Geochimica et Cosmochimica Acta, 64,(19), 3395-3412.

Morad, S., Sirat, M., El-Ghali, M. A., K. & Mansurbeg, H. (2011). Chloritization in Proterozoic granite from the Äspö Laboratory, southeastern Sweden: record of hydrothermal alterations and implications for nuclear waste storage.Clay Minerals, 46, 495-513.

Oliot, E., Goncalves, P. & Marquer, D. (2010). Role of plagioclase and reaction softening in metagranite shear zone at mid-crustal conditions (Gotthard Massif, Swiss Central Alps). Journal of Metamorphic Geology, 28, 849-871.

Palazzin, G., Raimbourg, H., Stünitz, H., Heilbronner, R., Neufald, K., & Précigout, J. Evolution in H_2O contents during deformation of polycrystalline quartz : An experimental study. Journal of Structural geology, 114, 95-110.

Parneix, J. C., Beaufort, D., Dudoignon, P. & Meunier, A. (1985). Biotite chloritization process in hydrothermally altered granites. Chemical Geology, 51, 89-101.

Paquette, J.-L., Gleizes, G., Leblanc, D. & Bouchez, J.-L. (1997). Le granite de Bassiès (pyrénées) : un pluton syntectonique d'âge Westphalien. Géochronologie U-Pb sur zircons. Compte Rendus de l'Académie des Sciences de Paris 324, 387-392.

Rasmussen, B. & Muhlig, J. R. (2007). Monazite begets monazite: evidence for dissolution of detrital monazite and reprecipitation of syntectonic monazite during low-grade regional metamorphism. Contribution t Mineralogy and Petrology, 154, 675-689.

873 Román-Berdiel, T., Casas, A. M., Oliva-Urcia, B., Pueyo, E. L. & Rillo, C. (2004). The main
874 Variscan deformation event in the Pyrenees: new data from the structural study of the
875 Bielsa granite. Journal of Structural Geology, 26, 659-677.
876 Rubatto, D. (2017). Zircon: The Metamorphic Mienral, In: Petrochronology: Methods and
877 Applications, Kohn, M. J., Engi, M. & Lanari, P. Reviews in Mineralogy &
878 Geochemistry.
879 Shea, W. T.J., Kronenberg, A.K. (1993). Strength and anisotropy of foliated rocks with varied
880 mica contents. Journal of Structural Geology, 15, 1097-1121.
881 Stacey, J. S. & Kramers, J. D. (1975). Approximation of terrestrial lead isotope evolution by
882 two-stage model. Earth and Planetary Science Letters, 26, 207-221.
883 Tera, F. & Wasserburg, G. J. (1972). U-Th-Pb systematics in lunar highland samples from the
884 Luna 20 and Apollo 16 missions. Earth and Planetary Science Letters, 17, 36-51.
885 Tornos, F., Delgado, A. Casquet, C. & Galindo, C. (2000). 300 Million years of episodic
886 hydrothermal activity: stable isotope evidence from hydrothermal rocks of the Eastern
887 Iberian Central System. Mineralium Deposita, 35, 551-569.
888 Tullis, J., Yund, R. & Farver, J. (1996). Deformation-enhanced fluid distribution in feldspar
889 aggregates and implications for ductile shear zones. Geology, 24(1), 63-66.
890 Turpin, L., Leroy, J. L. & Sheppard, S. M. F. (1990). Isotopic systematics (O, H, C, Sr, Nd) of
891 superimposed barren and U-bearing hydrothermal system in a Hercynian granite,
892 Massif Central, France. Chemical Geology, 88, 85-98.
893 Vacherat, A., Mouthereau, F., Pik, R., Huyghe, D., Paquette, J-L., Christophoul, F., …Tibari,
894 B. (2017). Rift-to-collision sediment routing in the Pyrenees: A synthesis from
895 sedimentological, geochronological and kinematic constraints. Earth-Sciences Reviews,
896 172, 43-74.

Vidal, O., De Andrade, V., Lewin, E., Munoz, M., Parra, T., & Pascarelli, S. (2006). P-T deformation-Fe3+/Fe2+ mapping at the thin section scale and comparison with XANES mapping. Application to a garnet-bearing metapelite from Sambagawa metamorphic belt (Japan). Journal of Metamorphic Geology 24, 669–683.

Wayne, D. M. & McCaig, A. M. (1998). Dating fluid flow in shear zones: Rb-Sr and U-Pb studies of syntectonic veins in the Néouvielle Massif, Pyrenees. Geological Society, London, Special Publications, 144, 129-135.

Wehrens, P., Baumberger, R. Berger, A. & Herweg, M. (2017). Journal of Structural Geology, 94, 47-67.

Wintsch, R.P., Christoffersen, R. & Kronenberg, A.K. (1995). Fluid-rock reaction weakening of fault zones. Journal of Geophysical Research, 100(B7), 13021-13032.

Withney, D., & Evans, B. (2010). Abbreviations for names of rock-forming minerals. American Mineralogist, 95, 185-187.

Yuguchi, T., Sasao, E., Ishibashi, M. & Nishiyama, T. (2015). Hydrothermal chloritization processes from biotite in the Toki granite, Central Japan: Temporal vairations of the composition of hydrothermal fluids associated with chloritization. American Mineralogist, 100, 1134-1152.

SUPPORTING INFORMATION

Additional Supporting Information may be found online in the supporting information tab for this article.

Description Supinfo.doc/x

Appendix S1. Analytical methods for geochronology and monazite analysis

Figure S1. Example of location of laser spot for zircon, anatase and titanite dating.

921 **Figure S2.** Tera-Wasserburg diagrams for all analysed anatase, titanite and zircon. Concordia-
922 discordia diagrams for zircon.
923 Dataset.xls/x
924 **Table S1.** Rapresentative chemical composition of chlorite and white mica.
925 **Table S2.** Representative chemical composition of monazite in samples ZA16-98 and ZAL18-
926 11.
927 **Table S3.** Original istopic data for zircon, titanite and anatase. Graphs represents weighted
928 mean zircon ages.
929
930 **FIGURE CAPTION**
931 **Figure 1** Geological maps and cross section. (a) Schematic structural map of the Pyrenees,
932 modified from Román-Berdiel, Casas, Oliva-Urcia, Pueyo, and Rillo, 2004. Red square: Bielsa,
933 N: Néouvielle, M: Maladeta, J: Jau. (b) Schematic structural cross section of the Axial Zone
934 (modified from Jolivet et al., 2007). Yellow stars indicate limits of the area where pervasive
935 alteration of the original granite has been documented. Black rectangle denotes the studied area.
936 (c) Geological map of the studied area. (d) Cross sections along transects AA' and BB'.
937
938 **Figure 2** Field structures around Lake Urdiceto. (a) Mylonitic corridor along the transect BB'
939 of Figure 1c. White: schistosity (S), yellow: shear planes (C). (b) Second example of mylonitic
940 corridor a few hundred meters eastward of transect BB', at the contact with the Triassic
941 sediments. Schistosity (S, filled white lines) is subparallel to S-dipping shear planes (C, marked
942 in yellow) due to high strain. (c) Mylonitic bands within the basement with C planes varying
943 from S-dipping to N-dipping. (d) N-dipping shear planes in a mylonite at the contact between
944 the basement and the sedimentary cover. (e) Enlarged view of mylonitic granite (see panel a for
945 location). (f) Enlarged view of weakly deformed (but altered) granite (see panel a for location).

946

947 **Figure 3** Field structures in the Triassic sediments. (a) Unconformity between the basement
948 and the Triassic sediments. (b) Chlorite-quartz bearing veins at the contact between the
949 basement and the basal breccia in the Triassic sediments. (c) Two generations of chlorite-quartz
950 bearing veins within Triassic sandstones and pelites.

951

952 **Figure 4** Photomicrographs (a, c, e and g) and backscattered electron images (BSE) (panels b,
953 d, f and h) of granitic basement with increasing deformation. Abbreviations are from Whitney
954 & Evans (2010), except Wm: white mica; (a) Undeformed but altered granite; (b) BSE image
955 of a Chl + Wm + Ttn pseudomorph after Bt; (c) weakly deformed and altered granite with dark
956 Chl-Wm pseudomorphs after Bt folded to form kink bands; (d) BSE images of a kinked Chl
957 flake; (e) weakly deformed sample with opening fractures. Chlorite flakes are cross cut by
958 secondary mm-size fractures. (f) BSE image of a Chl + Ttn flake after Bt (Bt relicts still visible),
959 cross cut by a fracture filled with secondary chlorite; (g) mylonite; (h) folded Chl + Wm + Ant
960 flake cross cut by a secondary fracture in a highly deformed sample. Two types of anatase grains
961 are recognized.

962

963 **Figure 5** Backscattered images of accessory minerals in the granitic basement. (a) and (b)
964 magmatic Ilm breaking down to Ant + Cal, then to Ttn. (c) Anatase 1 folded within a Chl flake
965 and replaced by Ttn. (d) Magmatic zircon (core) with metamict rims (low CL intensity) in
966 sample ZA16-119. (e) Chlorite flakes (ChlA) with type-1 Ant cross cut by ChlB-bearing
967 fractures with type-2 Ant (sample ZA16-73). (f) Type-2 Ant rimming titanite after anatase
968 (type-1 Ant, preserved in the core of titanite). (g) Chlorite flake (ChlA) in sample ZA16-79
969 with both types of anatase. (h) Relationships between titanite and anatase in sample ZA16-128.

970 (i) Monazite in sample ZA16-98. The inset image shows the patchy and porous aspect of the
971 monazite grains. (j) Monazite in reaction halos around fractures in sample ZA16-88.
972
973 **Figure 6** Macro- and micro-scale petrography of the Triassic sediments. (a) Hand sample
974 collected at the boundary between sediments and the granitic basement (ZAL18-11). (b)
975 Backscattered electron image of panel a, showing the occurrence of anatase, Fe-oxides and Mnz
976 within neocrystallized Chl and Wm. The inset show the patchy texture of monazite grains. (c)
977 Chlorite-bearing veins and shear planes forming 'en-echelon' microstructures in sample ZA16-
978 12. (d) Two generations of chlorite (in veins and shear planes) in samples ZA16-12 (zoom of
979 panel c). ChlA and ChlB refer to chlorite flakes and chlorite in fractures/veins respectively but
980 may be different in origin to ChlA and ChlB observed in the basement.
981
982 **Figure 7** Chemical composition of chlorite. (a) Quantified SEM map of Al_2O_3 content in
983 chlorite in sample B10-31 (mylonite). (b) Quantified SEM map of FeO content in chlorite of
984 sample ZA16-82 (fractured sample). (c) Elementary Al vs Mg (%) content of all analysed
985 chlorites; (d) Trends and compositional groups identified in chlorite in samples collected east
986 of Lake Urdiceto; (e) Trends and compositional groups identified in chlorite in samples
987 collected west of Lake Urdiceto.
988
989 **Figure 8** Chemical composition of white mica. (a) Compositional triangular plot and trends for
990 white mica in the basement. (b) Compositional ternary diagram of white mica in the
991 sedimentary samples. Mus: muscovite, Cel: celadonite, Pyr: pyrophillite.
992
993 **Figure 9** Thermobarometric results. (a) Chlorite temperatures calculated with the method of
994 Vidal et al. (2006) (circles) and Bourdelle et al. (2013) (rectangles). (b) Monte Carlo simulation

for the temperature dataset calculated for basement chlorite (3000 iterations, see the text for details). (c) Pressure range estimated from the celadonite content in white mica, following the calibration of Massonne and Schreyer (1988). This calibration does not consider the pyrophillite content in white mica, as it is the case in the Bielsa granite. Pressure values should therefore be considered as minimum values.

Figure 10 Geochronology results. (a) Representative Tera-Wasserburg concordia lower intercept age defined by titanite analyses in an undeformed sample (ZA16-84). (b) Tera-Wasserburg Concordia lower intercept ages defined by various anatase populations (red: old, blue: young) in a deformed sample (ZA16-128). (c) Frequency distribution of monazite ages. Note that youngest monazite ages are estimated from Pb depleted domains (Pb < EPMA detection limits of ~100 ppm) and monazite-thorite domains (see the text for details). Note the ages calculated for domains where Pb is below the EPMA detection limit are maximum ages. (d) Summary of geochronological results (this study) integrated with previously published data for metamorphic events in the Axial zone. U-Pb Ant-Ttn indicate the ages obtained for analysis where a titanite locally preserved anatase cores (type-1 Ant, see the text for details). (e) U and Th content of monazite in sample ZAL18-11. (f) Probability density plot of all zircon ages for samples ZA16-84 and ZA16-119 (2σ error).

Table 1 Summary of sample descriptions and ages.